Isolation of Fundamental Parameters Contributing to Particulate Formation in a Spark Ignition Direct Injection (SIDI) Engine

By

Mitchell D. Hageman

A dissertation submitted in partial fulfillment of
the requirements for the degree of

Doctor of Philosophy

(Mechanical Engineering)

at the

UNIVERSITY OF WISCONSIN–MADISON

2014

Date of final oral examination: 10/23/14

The dissertation is approved by the following members of the Final Oral Committee:

David A. Rothamer, Associate Professor, Mechanical Engineering

Christopher J. Rutland, Professor, Mechanical Engineering

Jaal B. Ghandhi, Professor, Mechanical Engineering

Rolf D. Reitz, Professor, Mechanical Engineering

James J. Schauer, Professor, Civil & Environmental Engineering

© Copyright by Mitchell D. Hageman 2014

All Rights Reserved

To Holly

ABSTRACT

Particulate formation studies have been conducted under both direct-injected (DI) operation and a new experimental operation that ensures a fully premixed flame in-cylinder. By vaporizing the fuel and preparing the air-fuel mixture well upstream of the intake port, a fully premixed and pre-vaporized (PMPV) fuel-air charge was ensured in-cylinder. Using the PMPV technique, the effects of fuel chemistry, mixture enrichment, pressure, temperature, and residence time have been characterized for in-cylinder premixed flames. A non-fuel related baseline (NFB) particulate size distribution (PSD) was demonstrated using gasoline (EPA Tier II EEE), methanol and E100 that was insensitive to fuel composition and enrichment below a critical enrichment level. The PMPV technique was then used to determine the enrichment needed to generate significant soot above the NFB as a function of fuel type and operating condition. The enrichment level where significant soot is first produced above the NFB level is the critical enrichment threshold, and can be quantified as a critical sooting equivalence ratio (Φ_C), a critical effective equivalence ratio (Ψ_C), or a critical carbon-to-oxygen ratio (C/O_C).

A toluene reference fuel (TRF30: 50% iso-octane, 20% n-heptane, 30% toluene) was demonstrated to match the in-cylinder chemical sooting tendencies of EEE well under PMPV operation due to matching of the EEE's aromatic fraction and carbon to hydrogen ratio (C/H). Additional blends spanning the range of toluene fractions at the chosen octane rating show a sensitivity of the sooting tendency to aromatic fraction. Matching the aromatic fraction, octane rating and C/H ratio of

a 3-component surrogate to the real fuel of interest was shown to be sufficient for achieving similar sooting characteristics.

The ideal temperature range for particulate formation in a premixed flame is 1400 K to 1900 K. The bulk gas temperature falls into this region well after the main combustion event has passed. A PMPV combustion phasing sweep confirmed that extreme changes in the main combustion event temperature and pressure result in minor changes in particulate formation. This supports the hypothesis that late cycle thermodynamics corresponding to the aforementioned temperature range may be responsible for particle formation trends. Equivalence ratio sweeps at various loads and two speeds demonstrated that both high pressure and high in-cylinder residence time contribute to a lower critical sooting enrichment threshold and increased particulate formation above that threshold under premixed conditions.

Injection timing sweeps using EEE and TRF30 under SIDI operation showed that TRF30 performs differently from EEE with respect to particulate formation under SIDI operation because the high boiling point components in EEE prevent full vaporization from chamber surfaces before ignition. This gave an indication of the effects of both fuel volatility and diffusion-limited combustion. Comparing the SIDI results to the PMPV results showed that SIDI cases produced more large particles and it is concluded that high numbers of large particles are a sign of diffusion-limited combustion.

Under SIDI operation, lower speed reduced particulate number but produced similar particulate mass. This is attributed to a tradeoff between increased mixing time before ignition, and increased residence time after the main combustion event.

Increased load under stoichiometric SIDI operation was shown to increase particulate with a dependence similar to the one seen for PMPV operation at the richest mixtures. Comparisons between the PMPV and SIDI cases provide a method for interpreting the relative importance of various chemical and physical parameters in an SI engine at different operating conditions by providing a separation of the effects of rich premixed and diffusion-limited combustion.

ACKNOWLEDGMENTS

Isaac Newton once wrote "If I have seen further it is by standing on the shoulders of giants." Newton's meaning was that his own discoveries were only possible due to the work of those who came before him. However, my giants are not my predecesors. My giants are the family, students, and faculty who worked by my side for the last four years, directly contributing to my discoveries, and helping me through my struggles. It feels almost disingenuous to put one name on a thesis when so many contributed to the work. Although there are too many people to list whose contributions were invaluable in helping me complete this work, I would like to acknowledge at least a few of them here.

To begin, I would like to express my deep appreciation for all the graduate students who have shared the B131 SIDI lab with me during my time at the ERC. In particular, Matt Coyne shouldered most of the burden of maintenance and troubleshooting during my first year here. Axel Maier provided most of the preparation for the first PNNL collaboration, and provided many interesting inputs throughout his tenure here. Steve Sakai may be the most competent and multi-talented lab mate I have ever had. He has made too many contributions to mention. The two most notable are his updating of the data acquisition and his constantly calm demeanor throughout our many shared troubleshooting episodes. I'd also like to thank Steve for skipping out of the laboratory to go sailing with me on many breezy summer afternoons. Sandeep Viswanathan has also been an excellent lab mate. His continuously cheery demeanor and constant willingness to lend a hand made several projects easier and more enjoyable. Sandeep and Steve were indispensable

in ensuring the continued operation of the lab through various lab issues over the past two years, and I feel extremely lucky to have shared my time here with them.

I would also like to thank all of the ERC support staff for their help with various issues. Ralph Braun was always available and willing to dispense advice on all things laboratory and engine-related, and provided moral support as well when things didn't go according to plan. Josh Leach efficiently and patiently helped me through dozens of IT issues no matter how big or small they might have been. I've never asked a question he wasn't able to answer. Mike Andrie, Roger Krieger, Todd Fansler, and Dave Foster all offered many useful inputs on research directions and technical issues throughout this project. Additionally, several undergraduate student hourly workers completed various fabrications needed throughout the project.

I am indebted to the University of Wisconsin and all the professors and students in the ERC for both their guidance and their friendship. The students that I shared my classes, research, struggles and personal time with were by far my favorite thing about the ERC and I'm not sure I'll ever find a better group of people to work with. In particular, I'd like to thank Martin Wissink for constantly fielding my Matlab questions and letting me sleep on his futon, Ryan Walker for his guidance in finding jobs in Colorado, Dustin Witkowski for always making me feel better about how much I had accomplished, Varun Ramesh, Lu Qiu, and Eric Gingrich for the late night study sessions that helped me survive our first combustion course, and Allison Ferris and Matt Labaza for respecting our shared emissions bench.

I would like to thank the many collaborators I have had from outside the ERC. General Motors funded the project, and the GM research staff, specifically Paul Najt, Kushal and Narayanaswamy, and Arun Solomon helped guide the research and provided important replacement parts. Alla Zelenyuk from Pacific Northwest National Labs made two 10-14 day visits with her SPLAT instrument, which provided valuable information on particle morphology. Alla and her post-doctoral researchers (Paul Reitz, Jacqueline Wilson, and David Bell) displayed incredible work ethic during the very long days we spent collecting their data. Keyong Lee and He Jee Seong also deserve recognition for their collaborations with us on our shared SAE particulate morphology visualization paper.

My entire family deserves a huge round of thanks for supporting me throughout my life and especially throughout this process. My two brothers Matt and Adam are two of my best friends and have listened to many of my complaints over the past few years. My parents, Dan and Deb are responsible for every good thing I've ever done, and have given me more than I can possibly describe. My wife, Holly has given me more love, support and understanding over the past three years than anyone else. She has shared all of my frustrations and celebrated all of my successes. I owe her more than I can repay.

Finally, I would like to thank my adviser, Professor David Rothamer for all of his advice and support. He has given me dozens of great ideas in the last four years, and has guided my research while allowing me freedom to pursue my own ideas. He has been patient, offered encouragement, helped me to refine my arguments and held me to high standards. His flexibility allowed me to spend far more time with

Holly after she moved away from Madison, which was critical for maintaining our shared happiness. He has spent countless hours helping to make this dissertation a work that I can be extremely proud of, and I am indebted to him for all his help.

Although many individuals lent their time and talents to the completion of this work, there will inevitably be some mistakes and I am solely responsible for them.

CONTENTS

Abstract ii

Contents ix

List of Tables xvii

List of Figures xix

Nomenclature xl

1 Introduction 1

2 Literature Review 5

2.1 Direct Injection: Benefits and Drawbacks 7

2.2 Processes of Soot Formation and Growth 10

2.2.1 Formation 11

2.2.2 Surface Growth 14

2.2.3 Coagulation 15

2.2.3.1 Coalescence 15

2.2.3.2 Agglomeration 16

2.3 Particulate Morphology 17

2.4 Particulate Matter Composition 17

2.5 Particulate Measurement Technique: SMPS 19

2.6 PMP Protocol 22

2.7 Fundamental Flame Theory 24
2.7.1 Metrics for Describing Mixture Enrichment 25
2.7.2 Laminar Premixed Flames 29
2.7.2.1 Flame Structure 29
2.7.2.2 Effect of Mixture Chemistry 30
2.7.2.3 Effect of Temperature 35
2.7.2.4 Effect of Pressure 38
2.7.3 Turbulent Premixed Flames 39
2.7.4 Laminar Diffusion Flames 40
2.7.4.1 Flame Structure 40
2.7.4.2 Effect of Mixture Chemistry 40
2.7.4.3 Effect of Temperature 43
2.7.4.4 Effect of Pressure 45
2.7.5 Summary of Laminar Premixed and Diffusion Flame Dependencies 46
2.8 Surrogate Fuels 47
2.9 SI Engine Particulate Trends - Effects of Operating Conditions 48
2.9.1 Engine Load 49
2.9.2 Engine Speed 50
2.9.3 Combustion Phasing 50
2.9.4 Mixture Preparation 51
2.9.5 Mixture Enrichment 54
2.9.6 Engine Parameters Summary 54

3 Experimental Setup 57

3.1 Engine . . . 57

3.2 Particulate Sampling System . . . 61

3.3 Controls and Data Acquisition Systems . . . 66

3.4 Premixed, Pre-vaporized (PMPV) Method . . . 69

4 Premixed Pre-Vaporized (PMPV) Method Development 71

4.1 Volatile Particle Removal . . . 72

4.1.1 Effect of Thermodenuder . . . 73

4.2 Non-Fuel Baseline (NFB) Particle Size Distribution . . . 75

4.3 Critical Enrichment Level (C/O_C & Φ_C) . . . 78

4.3.1 Matching of Engine Operating Conditions . . . 78

4.3.2 Particulate Data . . . 81

4.4 Discussion . . . 86

4.5 Summary . . . 89

5 PMPV Study of Fuel Chemistry Effects 90

5.1 Fuels and Operating Conditions . . . 90

5.2 PSDs as a Function of Fuel and Φ . . . 97

5.2.1 Comparison of All Fuels . . . 97

5.2.2 Comparison of EEE and TRF30 . . . 101

5.2.3 Behavior of Non-Aromatic Fuels . . . 102

5.3 Metrics for Describing Mixture Enrichment (Φ, Ψ, & C/O) . . . 104

5.3.1 Gaseous Emissions Trend Comparisons . . . 106

5.3.2 Temperature Comparisons 108
5.3.3 Fuel Carbon Mass Comparisons 112
5.3.4 Particulate Trend Comparisons 114
5.3.5 Discussion of Mixing Metrics 116
5.4 Discussion of Trends 117

6 PMPV Study of Thermodynamic Parameter and Kinetic Timescale Effects 120
6.1 Combustion Phasing Effects on particles 121
6.1.1 Thermodynamic Results 121
6.1.2 Particulate Results 127
6.1.3 Discussion 129
6.2 Engine Load Effects on Thermodynamics and Particles 130
6.2.1 Thermodynamic Results 131
6.2.2 Particulate Results 135
6.2.3 Discussion 143
6.3 Engine Speed Effects on Thermodynamics and Particles 145
6.3.1 Thermodynamic Results 146
6.3.2 Particulate Results 149
6.3.3 Discussion 153

7 Spark-Ignition Direct-Injection Engine Operation: Effects of Fuel Physical Properties 155
7.1 Fuel Properties and Operating Conditions 155
7.2 EEE PMPV vs. EEE SIDI Particulate Data 163

7.3 TRF30 SIDI vs. EEE SIDI Particulate Data 166
7.4 Discussion 173

8 SIDI Study of Pressure and Speed Effects 177
8.1 Effects of Engine Load Under Direct Injection 177
8.1.1 Results 177
8.1.2 Discussion 179
8.2 Effects of Engine Speed Under Direct Injection 182
8.2.1 Results 182
8.2.2 Discussion 185

9 Conclusions and Future Work 188
9.1 Conclusions 188
9.1.1 Premixed Combustion Threshold Sooting Behavior 188
9.1.2 Premixed Combustion Fuel Chemistry Effects 189
9.1.3 Premixed Combustion Thermodynamic Effects 190
9.1.4 Interpreting Differences Between SIDI and PMPV Results . . 191
9.1.5 Summary of Conclusions 192
9.2 Future Work 195

A Ring Pack Crevice Flow Model 197
A.1 Introduction 197
A.2 Assumptions 197
A.3 Model Geometry 198
A.4 Volume Definitions 199

A.5 Pressure Definitions 201

A.6 Mass Flow Directions and Magnitudes 204

B Calculating Crank-Angle-Resolved Thermodynamic Parameters From In-Cylinder Pressure Data 209

B.1 Assumptions 209

B.2 Volume 210

B.3 Trapped Mass 211

B.4 Temperature 214

B.5 Heat Release 218

B.5.1 Closed System Energy Balance 218

B.5.2 Approximation of γ 221

B.5.3 Approximation of δQ_W 223

C Calculations From The Measured Particle Size Distribution (PSD) 227

C.1 Introduction 227

C.2 Errors Associated With Particle Size: D_m 227

C.3 Uncertainties in Particle Counting Techniques 228

C.3.1 Sampling Technique Error Sources 229

C.3.2 Instrument Error Sources 230

C.3.2.1 DMA Voltage 231

C.3.2.2 CPC & DMA Flow Rates 232

C.3.2.3 Scan Time 232

C.3.2.4 Charge Distribution 232

C.3.2.5 CPC Counting Efficiency 233
C.3.2.6 DMA Transfer Function 234
C.3.2.7 Working Gas Parameters 235
C.3.2.8 Diffusion Losses 235
C.3.3 Thermodenuder Correction 237
C.3.4 Dilution Ratio Correction 239
C.4 Total Number Concentration 240
C.5 Geometric Mean Diameter 241
C.6 Total Mass Concentration 241
C.7 Soot Volume Fraction 242

D Mass vs Mobility Diameter (D_m) Relationship 243

E Determination of Uncertainty 248
E.1 Introduction 248
E.2 Independent Variable Uncertainty Calculation 249
E.3 Dependent Variable Uncertainty Calculation 251
E.4 Uncertainty in the Average of Multiple Runs 252

F Indicated Specific Particulate Number Emissions Calculated for $D_m \geqslant 23$ nm 255

G Gaseous Emissions Plots 258

H PMPV Thermodynamics Plots 271

I Blank Data Sheet 275

J Haltermann Fuel Data Sheets 277

K EEE Composition Analysis 284

Bibliography 288

LIST OF TABLES

2.1 Summary of parameter dependencies of soot formation in laminar premixed and diffusion flames 46
2.2 Effects of engine operating parameters on particulate formation in SI engines 56

3.1 Engine geometry specifications. Valve timings are based on a lift of 0.5 mm. 58
3.2 Intake, block, and exhaust temperatures and pressures 61
3.3 Recorded raw data and acquisition systems 69

4.1 Properties of research fuels 76

5.1 Aromatics in EEE certification gasoline 91
5.2 TRF blend fractions 92
5.3 Fuel enrichment level comparisons and ranges tested 93
5.4 Properties of research fuels 93
5.5 Critical sooting thresholds 114

6.1 PMPV thermodynamics study operating conditions 120
6.2 Critical sooting thresholds 139
6.3 Speed-dependent critical sooting thresholds 149

7.1 EEE, surrogate component, and TRF30 physical properties 156
7.2 SIDI injection timing and fuel effects study parameters 160

8.1 Gaseous emissions comparisons between 334 kPa and 550 kPa cases . . 178
8.2 Summary of literature results for dependence of soot formation in diffusion flames 181
8.3 Total particulate comparisons between 1050 rpm and 2100 rpm cases . 183
8.4 Gaseous emissions comparisons between 334 kPa and 550 kPa cases . . 185

9.1 Effects of engine operating parameters on particulate formation in SI engines 194

A.1 Possible combinations of the pressure balance in the ring gaps. 201
A.2 Sign conventions for mass flow rates 202
A.3 Crevice pressure roles for pressure balance combinations 204
A.4 Measured crevice dimensions 207

D.1 Conditions for which particle mass vs D_m relationship was measured . 244

LIST OF FIGURES

1.1 The current state of GDI technology as it relates to proposed emissions standards. Modified from [90]. Horizontal red lines represent European number standards. Vertical blue lines represent U.S. mass standards . 3

2.1 Sampling theory based on D_m. Particle trajectory is determined by the combination of the migration velocity and the bulk flow velocity. E = electric field strength, q = charge, (+) = positive charge, (-) = negative charge. 21

2.2 PMP recommended particulate sampling system. PSP = particulate sample probe, PCF = preclassifier, VPR = volatile particulate remover, PND = particulate number diluter, ET = evaporation tube, PTT = particulate transfer tube. Modified from [1]. 22

2.3 Laminar premixed flame temperature and species profiles [52]. 29

2.4 Critical sooting effective equivalence ratio (Ψ_C) as a function of the number of C-C bonds in the fuel from premixed Bunsen flames at a calculated adiabatic flame temperature of 2200 K. The calculated temperature was controlled by varying the N_2 / O_2 ratio [45]. 34

2.5 Threshold for soot formation (threshold determined visually by soot luminosity) as a function of temperature (T_M, measured 10 mm above burner) and presssure for C_2H_4-air flat flames [16]. 36

2.6 Final soot volume fraction (f_v^∞) as a function of temperature (T_M, measured 10 mm above burner) and mixture enrichment (C/O) for a C_2H_4-air flat flame at atmospheric pressure. The broad solid line that borders the base of the dome is the threshold for soot formation [19]. 37

2.7 Radial dimensionless temperature (T') and species profiles in a burning droplet diffusion flame. $T' = T/T_{ad,\Phi=1}$, S = droplet surface, f = flame front. Modified from [47]. 41

2.8 Radial measurements of temperature and scattered light from soot particles in an ethylene-air co-flow diffusion flame. The scattered light peaks correspond to regions containing significant amounts of soot [105]. . . 44

2.9 PSD changes (a) and the resulting total particulate number concentration (b) with changes in intake-stroke injection timings for 100 rpm at a 3-bar IMEP engine load [54]. 53

2.10 PSD plots for EEE (gasoline) Φ sweep. Numbers quoted in the legend are Φ. Modified from [101] 55

3.1 Major components of pressurized fuel system. PG = pressure gage, PXD = pressure transducer, S = Solenoid valve. In this depiction, the right fuel accumulator is pressurized, and is sending fuel through the flow meter to the premixing injector. 60

3.2 Operation of EC and long DMA. Modified from [34]. 62

3.3 Dekati microdiluter cross section. Modified from [6]. Thermocouple (TC) numbers correspond to those in Figure 3.4. PXD = pressure transducer 64

3.4 Experimental setup showing the engine intake system with the premixing chamber and visualization port, exhaust system, micro-diluter, SMPS, and exhaust emissions bench. The engine is operated with either the DI injector or the premixed injector. ESC = electrostatic classifier, DMA = differential mobility analyzer, CPC = condensation particle counter, EP = electrostatic precipitator, TC = thermocouple. 65

3.5 Photo of the PMPV visualization port in the intake system. The intake surge tank is located just above the picture edge, and the engine is located just to the left of the picture edge. Wide arrows denote direction of air/fuel mixture flow. The white wrapping around the visualization port and intake runner is heating tape. 70

4.1 PSDs for EEE at $\Phi = 1.35$ with varying DR. Note error bars/markers are only shown for every 10th point. 73

4.2 Effect of using a thermodenuder (TD) to remove volatile particles at different dilution ratios versus using dilution ratio (DR) alone. 74

4.3 Non-fuel baseline (NFB) PSD demonstrated for EEE, methanol, and E100. Methanol and E100 PSDs are shown for $\Phi = 0.98$ and $\Phi = 1.5$, EEE is only shown at $\Phi = 0.98$. Note error bars/markers are only shown for every 10th point. 77

4.4 Non-fuel baseline (NFB), ambient laboratory air, and intake air PSDs. Note error bars/markers are only shown for every 10th point. 77

4.5 Average pressure traces for Φs close to onset of sooting for EEE. 79

4.6 Average in-cylinder temperature (left) and apparent heat release rate (right) for Φs close to the onset of sooting for EEE. 80

4.7 Average in-cylinder temperature traces adjusted so that time and CAD start at 1900 K for each trace. The time in the critical temperature range is very similar between cases for Φs close to the onset of sooting for EEE. 80

4.8 PSDs for EEE for $0.98 \leqslant \Phi \leqslant 1.49$ at the standard operating condition. Note error bars/markers are only shown for every 10th point 82

4.9 Total concentrations of particles normalized by the NFB average total concentration vs. Φ for EEE fuel at the standard operating condition. Exponential function best fit line also shown with 10X NFB and 1X NFB intercepts and the corresponding best fit equations. Error bars are 95% confidence intervals. 83

4.10 Total particulate number concentrations normalized by the NFB average total concentration (left axis) and indicated specific concentrations (right axis) vs. Φ for EEE fuel at the standard operating condition. Indicated specific concentrations are calculated from PSDs including particle sizes from D_m = 10 nm to 289 nm (dashed red line) and D_m = 23 nm to 289 nm (solid blue line). The Euro 5 regulation counts particles with D_m = 23 nm and above. The dashed horizontal black line is the Euro 5 regulation converted to particles/kw-hr, and the dashed horizontal green line is the converted Euro 6 regulation. Error bars are 95% confidence intervals. For better graph clarity, confidence intervals are not given for the indicated specific particulate number counts. 85

4.11 Total particulate mass concentration (left axis, black symbols) and indicated specific mass emissions (right axis, dashed red line) vs. Φ for EEE fuel at the standard operating conditions. Error bars are 95% confidence intervals. For better graph clarity, confidence intervals are not given for the indicated specific particulate mass calculations. 86

5.1 Adiabatic flame temperature as a function of Φ for the fuel blends tested here. Data for the three pure components is also shown for comparison. Data was calculated with Cantera using the 103 species mechanism developed by Ra [95]. 94

5.2 Calculated AHRR and temperature traces at $\Phi \approx 1.35$ for all fuels. Subscripts denote the number of separate runs used to calculate the average and confidence bounds. 95

5.3 Average temperature (left axis) and time spent (right axis) between 1900 K and 1400 K late in the cycle. For cases where temperatures did not reach 1400 K before EVO, the times and average temperatures recorded are those between 1900 K and EVO. The Aromatic Fraction = 0 data point is iC_8H_{18}. PRF86 was not studied at $\Phi = 1.35$ 96

5.4 Measured pressure traces at $\Phi \approx 1.35$ for all fuels. Subscripts denote the number of separate runs used to calculate the average and confidence bounds. 97

5.5 Comparison of PSDs for different fuels at $\Phi \approx 1.35$. NFB trace matches that from [50]. Note error bars/markers are only shown for every 10th point. 98

5.6 Comparison of PSDs for different fuels at $\Phi \approx 1.50$. NFB trace matches that from [50]. Note error bars/markers are only shown for every 10th point. 99

5.7 Total particulate number concentrations normalized by the NFB (left axis, symbols) and indicated specific particulate number emissions (right axis, dashed lines) vs. Φ. Vertical arrows denote approximate x-axis locations of Φ_C based on the 1X NFB results. For graph clarity, uncertainty bounds are only applied to the concentration data. 100

5.8 Integrated particulate mass concentrations (left axis, symbols) and indicated specific particulate mass emissions (right axis, dashed lines) vs. Φ for the 2100 rpm and 1050 rpm cases. Note that values are absolute, rather than normalized. Vertical arrows denote location of Φ_C based on 1X NFB results. For graph clarity, uncertainty bounds are only applied to the concentration data. 100

5.9 EEE vs. TRF30 PSDs at selected Φ. Subscripts in the legend denote the total number of scans used to calculate the averages and confidence bounds. NFB trace matches that from [50]. Note error bars/markers are only shown for every 10th point. 102

5.10 iC_8H_{18} PSDs at selected Φ. NFB trace matches that from [50]. Note error bars/markers are only shown for every 10th point. 103

5.11 PRF86 PSDs at all enrichment levels studied. NFB trace matches that from [50]. Note error bars/markers are only shown for every 10th point. 104

5.12 Gaseous emissions as a function of Φ, Ψ, C/O for EEE. CO and CO_2 are measured emissions, whereas H_2O and H_2 are calculated using Equations 5.4 and 5.5 respectively. 107

5.13 Adiabatic flame temperature as a function of C/O for the fuel blends tested here. Temperature data is the same as that in Figure 5.1, and mixture data was calculated from Φ based on Equation 5.1. Solid black vertical line denotes approximate location of EEE C/O_C. Note that PRF86 and iC_8H_{18} data overlap closely. 108

5.14 Adiabatic flame temperature as a function of Ψ for the fuel blends tested here. Temperature data is the same as that in Figure 5.1, and mixture data was calculated from Φ based on Equation 5.2. Solid black vertical line denotes approximate location of EEE Ψ_C. Note that PRF86 and iC_8H_{18} data overlap closely. 109

5.15 Calculated AHRR and temperature traces at $C/O \approx 0.48$ for all fuels. Subscripts denote the number of separate runs used to calculate the average and confidence bounds. 110

5.16 Average temperature (left axis) and time spent (right axis) between 1900 K and 1400 K late in the cycle at C/O = 0.48. For cases where temperatures did not reach 1400 K before EVO, the times and average temperatures recorded are those between 1900 K and EVO. 111

5.17 Calculated AHRR and temperature traces at $\Psi \approx 0.71$ for TRF75 and iC_8H_{18}. Subscripts denote the number of separate runs used to calculate the average and confidence bounds. 111

5.18 Calculated carbon mass per cycle as a function of Φ for all fuels. 112

5.19 Calculated carbon mass per cycle as a function of Ψ for all fuels. 113

5.20 Calculated carbon mass per cycle as a function of C/O for all fuels. . . 113

5.21 Total particulate number concentrations normalized by the NFB (left axis, symbols) and indicated specific particulate number emissions (right axis, dashed lines) vs. C/O. Vertical arrows denote approximate x-axis locations of C/O_C based on the 1X NFB results. For graph clarity, uncertainty bounds are only applied to the concentration data. 115

5.22 Total particulate number concentrations normalized by the NFB (left axis, symbols) and indicated specific particulate number emissions (right axis, dashed lines) vs. Ψ. Vertical arrows denote approximate x-axis locations of Ψ_C based on the 1X NFB results. For graph clarity, uncertainty bounds are only applied to the concentration data. 115

6.1 Averaged main combustion event data from $\leqslant 3$ runs of each combustion phasing based on CA50 timing. All cases are set to IMEP = 334 kPa, Φ = 1.35 and 2100 rpm. Markers are drawn every 20 data points. Vertical dashed lines represent approximate location of CA90 for each case. . . 122

6.2 Averaged late-cycle data from $\leqslant 3$ runs of each combustion phasing based on CA50 timing. All cases are set to IMEP = 334 kPa, Φ = 1.35 and 2100 rpm. Markers are drawn every 20 data points. Time and CAD are adjusted to begin where temperature = 1900 K for all cases. Vertical dashed lines denote the EVO timing for each case. 123

6.3 Average temperature (left axis) and time spent (right axis) between 1900 K and 1400 K late in the cycle for the $\Phi = 1.35$ CA50 sweep. For cases where temperatures did not reach 1400 K before EVO, the times and average temperatures recorded are those between 1900 K and EVO. . . 124

6.4 Averaged main combustion event data from $\leqslant 2$ runs of each combustion phasing based on CA50 timing. All cases are set to IMEP = 334 kPa, Φ = 1.40 and 2100 rpm. Markers are drawn every 20 data points. Vertical dashed lines represent approximate location of CA90 for each case. . . 125

6.5 Averaged late-cycle data from $\leqslant 2$ runs of each combustion phasing based on CA50 timing. All cases are set to IMEP = 334 kPa, Φ = 1.40 and 2100 rpm. Markers are drawn every 20 data points. Time and CAD are adjusted to begin where temperature = 1900 K for all cases. Vertical dashed lines denote the EVO timing for each case. 126

6.6 Average temperature (left axis) and time spent (right axis) between 1900 K and 1400 K late in the cycle for the $\Phi = 1.40$ CA50 sweep. For cases where temperatures did not reach 1400 K before EVO, the times and average temperatures recorded are those between 1900 K and EVO. . . 127

6.7 Averaged PSDs from $\leqslant 14$ scans of each CA50 timing at Φ = 1.35. Subscripts denote the number of scans used to determine the average. Markers are drawn every 10 data points. 128

6.8 Averaged PSDs from $\leqslant 14$ scans of each CA50 timing at Φ = 1.40. Subscripts denote the number of scans used to determine the average. Markers are drawn every 10 data points. 129

6.9 Averaged main combustion event data for each load from a single run at $\Phi = 1.35$. Markers are drawn every 20 data points. Vertical dashed lines represent approximate location of CA90 for each case. 132

6.10 Averaged late-cycle data for each load from a single run at $\Phi = 1.35$. Markers are drawn every 20 data points. Data comparison is representative of the matching acheived at all Φ. Vertical dashed lines denote the EVO timing for each case. 133

6.11 Average temperature (left axis) and time spent (right axis) between 1900 K and 1400 K late in the cycle for the $\Phi = 1.35$ load sweep. For cases where temperatures did not reach 1400 K before EVO, the times and average temperatures recorded are those between 1900 K and EVO. . . 134

6.12 Baseline (BL) PSDs for each load from $\leqslant 3$ runs of each at $\Phi < \Phi_C$. Subscripts denote the number of scans used to determine the average. Markers are drawn every 10 data points. NFB trace matches that from [50] 135

6.13 Averaged PSDs for each load from $\leqslant 21$ scans of each at $\Phi = 1.35$. Subscripts denote the number of scans used to determine the average. Markers are drawn every 10 data points. NFB trace matches that from [50] 136

6.14 Averaged PSDs for each load from $\leqslant 21$ scans of each at $\Phi = 1.45$. Subscripts denote the number of scans used to determine the average. Markers are drawn every 10 data points. NFB trace matches that from [50] 137

6.15 Averaged PSDs for 334 kPa IMEP and 550 kPa IMEP cases from seven scans of each at $\Phi = 1.50$. Subscripts denote the number of scans used to determine the average. Markers are drawn every 10 data points. NFB trace matches that from [50] 138

6.16 Integrated particulate number concentrations normalized by the non-fuel baseline (left axis, symbols) and indicated specific particulate number emissions (right axis, dashed lines) vs Φ as a function of load (IMEP). Vertical arrows denote location of Φ_C based on 1X NFB results. Solid horizontal lines denote the baseline particle number for each load. For graph clarity, uncertainty bounds are only applied to the concentration data. 141

6.17 Integrated particulate mass concentrations (left axis, symbols) and indicated specific particulate mass emissions (right axis, dashed lines) vs Φ as a function of load (IMEP). Note that values are absolute, rather than normalized. Vertical arrows denote location of Φ_C based on 1X NFB results. For graph clarity, uncertainty bounds are only applied to the concentration data. 141

6.18 Geometric Mean Diameter (GMD) as a function of Φ for all engine loads. Dashed lines are intended only to guide the eye. 142

6.19 Ratio of total fuel carbon returned from the crevice after CA90 to the total mass of particles formed in the cycle as a function of Φ. Dashed lines are intended only to guide the eye. 142

6.20 Soot volume fraction (f_v) dependence on IMEP, assuming a $f_v \propto P^n$ relationship, as a function of Φ. 144

6.21 Average temperature (left axis) and time spent (right axis) between 1900 K and 1400 K late in the cycle as a function of Φ for the speed study. For cases where temperatures did not reach 1400 K before EVO, the times and average temperatures recorded are those between 1900 K and EVO. 147

6.22 Averaged thermodynamic data from $\leqslant 3$ runs of the 1050 rpm and 2100 rpm cases. Markers are drawn every 20 data points. Vertical dashed lines represent approximate location of CA90 for each case. Data comparison for the $\Phi = 0.98$ case is representative of the matching achieved at all Φ. 148

6.23 Averaged PSDs from $\leqslant 21$ scans of 2100 rpm and 1050 rpm cases at selected Φ. Markers are drawn every 10 data points. 150

6.24 Integrated particulate number concentrations normalized by the NFB (left axis, symbols) and indicated specific particulate number emissions (right axis, dashed lines) vs Φ for the 2100 rpm and 1050 rpm cases. Vertical arrows denote approximate x-axis locations of Φ_C based on 1X NFB results. For graph clarity, uncertainty bounds are only applied to the concentration data. 151

6.25 Integrated particulate mass concentrations (left axis, symbols) and indicated specific particulate mass emissions (right axis, dashed lines) vs Φ for the 2100 rpm and 1050 rpm cases. Note that values are absolute, rather than normalized. Vertical arrows denote location of Φ_C based on 1X NFB results. For graph clarity, uncertainty bounds are only applied to the concentration data. 151

6.26 Geometric Mean Diameter (GMD) as a function of Φ for both engine speeds 152

6.27 Ratio of the fuel carbon crevice mass returned after CA90 to the total particulate mass per cycle as a function of Φ for the 1050 rpm and 2100 rpm cases. Dashed lines are intended only to guide the eye. 154

7.1 Comparison of EEE and TRF30 distillation curve comparison. EEE curves are measured using both equilibrium and ASTM D86 methods [37]. TRF30 curve is calculated according to an equilibrium method. . . 157

7.2 Approximate piston surface positions for the EOI timings studied here. For a downward moving piston the top of the rectangles represent the top of the piston surface at SOI, and the bottom of the rectangles represent the piston position at EOI. Distances quoted are distance from the position of the piston face at the top of its stroke. Gray rectangles represent cases where only EEE was tested. Blue rectangles represent cases where EEE and TRF30 were tested. 159

7.3 EEE comparisons of thermodynamic parameters for the four EOI cases that were matched with TRF30 EOI cases. Markers are drawn every 20 data points. Vertical dashed lines represent approximate location of CA90 for each case. 160

7.4 TRF30 comparisons of thermodynamic parameters for the four EOI cases that were matched with TRF30 EOI cases. Markers are drawn every 20 data points. Vertical dashed lines represent approximate location of CA90 for each case. 161

7.5 Average temperature (left axis) and time spent (right axis) between 1900 K and 1400 K late in the cycle as a function of EOI for TRF30 and EEE. For cases where temperatures did not reach 1400 K before EVO, the times and average temperatures recorded are those between 1900 K and EVO. 162

7.6 EEE SIDI EOI sweep cases plotted along with the extremes of the EEE PMPV Φ sweep. Few PMPV cases resulted in PSDs outside of the NFB or the $\Phi = 1.47$ PSD. Therefore, the gray area between the two marks the range of PSDs present for PMPV cases when operating using EEE with Φ between 0.98 and 1.47. Markers are drawn every 10 data points. 165

7.7 PSDs for EEE SIDI EOI sweep cases and EEE PMPV Φ sweep extreme cases normalized by their respective peak particulate numbers . A y-axis value of 1.0 denotes the location of the peak particulate number for each case. The gray area between the two PMPV cases marks the range of PSDs present for PMPV cases when operating using EEE with Φ between 0.98 and 1.47. Markers are drawn every 10 data points. . . . 165

7.8 Integrated particulate number concentrations (left axis, symbols) and indicated specific particulate number emissions (right axis, dashed lines) vs. EOI for TRF30 and EEE SIDI cases. For graph clarity, uncertainty bounds are only applied to the concentration data. 167

7.9 Integrated particulate mass concentrations (left axis, symbols) and indicated specific particulate mass emissions (right axis, dashed lines) vs. EOI for TRF30 and EEE SIDI cases. For graph clarity, uncertainty bounds are only applied to the concentration data. 168

7.10 EEE PSDs as a function of EOI. Markers are drawn every 10 data points. NFB trace matches that from [50]. 170

7.11 TRF30 PSDs as a function of EOI. Markers are drawn every 10 data points. NFB trace matches that from [50]. 170

7.12 EEE and TRF normalized gaseous emissions concentrations as a function of EOI timing. Each species is normalized by the EEE TRF -340 CAD case concentration. 171

7.13 TRF30 PMPV Φ = 0.98, and SIDI EOI = - 340 CAD Φ = 0.98 thermodynamic comparisons. Markers are drawn every 20 data points. Vertical dashed lines represent approximate location of CA90 for each case. . . 172

8.1 EOI 220 (334 kPa) vs 550 kPa case PSDs. Markers are drawn every 10 data points. NFB trace matches that from [50]. 178

8.2 EEE 550 kPa IMEP and 334 kPa IMEP thermodynamic parameters at EOI = -220 CAD, and 2100 rpm. Markers are drawn every 20 data points. Vertical dashed lines represent approximate location of CA90 for each case. 179

8.3 EOI 220 (2100 rpm) vs 1050 rpm case PSDs. Markers are drawn every 10 data points. NFB trace matches that from [50]. 183

8.4 EEE 1050 rpm and 2100 rpm thermodynamic parameters at EOI = -220 CAD. Markers are drawn every 20 data points. Vertical dashed lines represent approximate location of CA90 for each case. 184

A.1 Sample ring geometry depicting ring gap where mass flow occurs. Modified from [103]. 198

A.2 Generic schematic of volumes formed between the piston and cylinder bore and separated by the piston rings and the associated pressures and mass flows (not to scale) [103]. 199

A.3 Selected example of crevice pressure balances. 203

A.4 Selected example of flow rates from all three crevices. 207

A.5 Measured chamber and crevice dimensions for the engine used in this study. 208

B.1 Generic cylinder geometry. Modified from [55]. 211
B.2 Calculation of average MW (W here) resulting from use of reactant species MW and product species MW for an air/iso-octane mix [43]. . 218
B.3 Closed system cylinder energy flows. 219
B.4 Approximations of γ_{eq} for various fuels as a function of Φ. Calculations and plot courtesy of Prof. David Rothamer. 223

C.1 Uncertainty in D_m as a function of D_m for the SPMS range and resolution used for this study. 228
C.2 Counting efficiency curve for CPC model 3010 [2]. 234
C.3 Penetration of particles through a circular tube as a function of tube length, diffusion coefficient, and flow rate [49]. 236
C.4 SMPS flow paths considered in the AIM calculation of diffusion losses through the SMPS system [5]. 237
C.5 Sample flow path cross-section of the Dekati thermodenuder [3]. . . . 238

D.1 Particle mass measurements [fg] at a range of D_m [nm] for all fuels and conditions. PMPV cases are marked by symbols while SIDI cases are marked by lines with a | at each data point. Fuel name text colors indicate the color used to mark each fuel. No further distinctions are made between cases due to the number of cases and the close agreement between cases. The exception is the EEE SIDI EOI -250 CAD case, which is marked here because it is a slight outlier compared to the remaining data. 245

D.2 Pooled particle mass measurements [g] vs D_m [nm] measured data plotted with a curve fit to the data. Note that the curve is fit to the data beginning at $D_m = 30$ nm because the measurements became less reliable below this range. 246

D.3 Pooled particle mass calculations [g] vs D_m [nm] used for calculations of particle mass from the PSD. Note that the curve is fit from the measured data is used for $D_m \geqslant 30$ nm, and $\rho_{particle} = 2$ g/cm^3 is used for $D_m < 30$ nm because the measurements became less reliable below this range. 247

F.1 Indicated specific particulate number emissions as a function of Φ for all fuels under PMPV operation. Horizontal dashed line denotes the Euro 5 number standard ($6(10^{13})$ particles/km) converted to particles/kw-hr based on the assumption of a 4000 lb vehicle traveling at 50 mph. . . . 255

F.2 Indicated specific particulate number emissions as a function of Φ for all loads under PMPV operation. Horizontal dashed line denotes the Euro 5 number standard ($6(10^{13})$ particles/km) converted to particles/kw-hr based on the assumption of a 4000 lb vehicle traveling at 50 mph. . . . 256

F.3 Indicated specific particulate number emissions as a function of Φ for the 2100 rpm and 1050 rpm cases under PMPV operation. Horizontal dashed line denotes the Euro 5 number standard ($6(10^{13})$ particles/km) converted to particles/kw-hr based on the assumption of a 4000 lb vehicle traveling at 50 mph. 256

F.4 Indicated specific particulate number emissions as a function of EOI for the EEE and TRF30 cases under SIDI operation. Horizontal dashed line denotes the Euro 5 number standard ($6(10^{13})$ particles/km) converted to particles/kw-hr based on the assumption of a 4000 lb vehicle traveling at 50 mph. 257

G.1 CO emissions as a function of Φ for all fuels under PMPV operation. . 258

G.2 CO emissions as a function of Φ for all loads under PMPV operation. . 259

G.3 CO emissions as a function of Φ for 2100 rpm and 1050 rpm under PMPV operation. 259

G.4 CO emissions as a function of CA50 for $\Phi = 1.35$ and $\Phi = 1.40$ under PMPV operation. 260

G.5 CO_2 emissions as a function of Φ for all fuels under PMPV operation. . 260

G.6 CO_2 emissions as a function of Φ for all loads under PMPV operation. 261

G.7 CO_2 emissions as a function of Φ for 2100 rpm and 1050 rpm under PMPV operation. 261
G.8 CO2 emissions as a function of CA50 for $\Phi = 1.35$ and $\Phi = 1.40$ under PMPV operation. 262
G.9 O_2 emissions as a function of Φ for all fuels under PMPV operation. . . 262
G.10 O_2 emissions as a function of Φ for all loads under PMPV operation. . 263
G.11 O_2 emissions as a function of Φ for 2100 rpm and 1050 rpm under PMPV operation. 263
G.12 O_2 emissions as a function of CA50 for $\Phi = 1.35$ and $\Phi = 1.40$ under PMPV operation. 264
G.13 H_2 emissions as a function of Φ for all fuels under PMPV operation. . . 264
G.14 H_2 emissions as a function of Φ for all loads under PMPV operation. . 265
G.15 H_2 emissions as a function of Φ for 2100 rpm and 1050 rpm under PMPV operation. 265
G.16 H_2 emissions as a function of CA50 for $\Phi = 1.35$ and $\Phi = 1.40$ under PMPV operation. 266
G.17 HC emissions as a function of Φ for all fuels under PMPV operation. . 266
G.18 HC emissions as a function of Φ for all loads under PMPV operation. . 267
G.19 HC emissions as a function of Φ for 2100 rpm and 1050 rpm under PMPV operation. 267
G.20 HC emissions as a function of CA50 for $\Phi = 1.35$ and $\Phi = 1.40$ under PMPV operation. 268

G.21 Combustion efficiency as a function of Φ for all loads under PMPV operation. 268
G.22 Combustion efficiency as a function of Φ for 2100 rpm and 1050 rpm under PMPV operation. 269
G.23 Combustion efficiency as a function of CA50 for $\Phi = 1.35$ and $\Phi = 1.40$ under PMPV operation. 269
G.24 Gaseous emissions as a function of EOI for EEE and TRF under SIDI operation. 270
G.25 Gaseous emissions as a function of EOI for EEE and TRF under SIDI operation. 270

H.1 Averaged main combustion event thermodynamic data for all PMPV loads at Φ = 0.98. Markers are drawn every 20 data points. 271
H.2 Averaged main combustion event thermodynamic data for all PMPV loads at Φ = 1.45. Markers are drawn every 20 data points. 272
H.3 Averaged main combustion event thermodynamic data for all Φs for EEE at the standard operating condition (334 kPa, 2100 rpm and CA50 = 8). Markers are drawn every 20 data points. 273
H.4 Averaged main combustion event thermodynamic data for all Φs for EEE at the low speed condition (334 kPa, 1050 rpm and CA50 = 8). Markers are drawn every 20 data points. 274

DISCARD THIS PAGE

NOMENCLATURE

Abbreviations

A/F - air-fuel ratio

AHRR - apparent heat release rate

AIM - Aerosol Instrument Manager

BC - black carbon

BDC - bottom dead center

BL - baseline

BSFC - brake specific fuel consumption

CA50 - crank angle corresponding to point of 50% heat release

CAD - crank angle degrees

CARB - California Air Resources Board

C/O - carbon to oxygen ratio

CI - compression ignition

COV - coefficient of variance

CPC - condensation particulate counter

CR - compression ratio

CVS - constant volume sampler

DAQ - data acquisition system

DI - direct injection

DISI - direct injection spark ignition

DMA - differential mobility analyzer

DR - dilution ratio

E100 - unblended ethanol with denaturant

EC - elemental carbon

ECM - engine control module

EEE - EPA Tier II research grade gasoline from Haltermann Products

EOI - end of injection

EEPS - engine exhaust particulate sizer

EP - electrostatic precipitator

EPA - Environmental Protection Agency

ESC - electrostatic classifier

ET - evaporation tube

EVC - exhaust valve closed

EVO - exhaust valve open

FID - flame ionization detector

FPS - fine particle sampler

FTP - federal test procedure

GCMS - gas chromatography / mass spectrometry

GDI - gasoline direct injection

gIMEP - gross indicated mean effective pressure

GMD - geometric mean diameter

H/C- hydrogen to carbon ratio

HC - hydrocarbon

HEPA - high efficiency particulate air

IMEP - indicated mean effective pressure

IVC - intake valve closed

IVO - intake valve opened

LEV - low emission vehicle

LII - laser induced incandescence

LIF - laser induced flouresence

LOSA - line of sight attenuation

MAP - manifold absolute pressure NA - not applicable

NEDC - New European Drive Cycle

NFB - non-fuel baseline

NI - National Instruments

OC - organic carbon

P - pressure

PC - personal computer

PFI - port fuel injection

PID - proportional-integral-derivative

PM - particulate matter

PMP - Particulate Measurement Programme

PN - particulate number

PNC - particle number counter

PND - particulate number diluter

PNNL - Pacific Northwest National Lab

PRF - primary reference fuel

PSD - particulate size distribution

PSP - particulate sample probe

PTT - particulate transfer tube

PXD - pressure transducer

RSR - resonantly stabilized radical

SI - spark ignition

SIDI - spark ignition direct injection

SMD - sauter mean diameter

SMPS - Scanning Mobility Particulate Sizer

SOC - standard operating condition

SOF - soluble organic fraction

SPLAT - Single Particle Laser Ablation Time-of-Flight Mass Spectrometer

SSE - spectral soot emission

T - temperature

t - time

TC - thermocouple

TD - thermodenuder

TDC - top dead center

TRF - toluene reference fuel

PCF - preclassifier

UBHC - unburned hydrocarbons

VOC - volatile organic content

VPR - volatile particulate remover

Elements and Molecules

C - carbon

CO - carbon monoxide

CO_2 - carbon dioxide

CH_3OH - methanol

C_2H_2 - acetylene

C_2H_4 - ethylene

C_2H_5OH - ethanol

C_3H_3 - propargyl

C_6H_5 - phenyl

C_6H_6 - benzene

C_7H_8 - toluene

C_7H_{16} - n-heptane

H_2 - hydrogen

H - atomic hydrogen

H_2O - water

iC_8H_{18} - iso-octane

K - potassium

Li - lithium

N_2 - nitrogen

Na - sodium

NO_X - oxide of nitrogen

O - atomic oxygen

O_2 - oxygen

OH - hydroxide

S - sulfur

Symbols

dN/dlog(Dp) - derivative of number concentration with respect to the logarithm of the particulate diameter

D_p - particle diameter

D_m - mobility diameter

$\dot{m}$ - mass flow rate

q - charge

E - electric field strength

F - force

ve - steady state migration velocity

Φ - equivalence ratio

Ψ - effective equivalence ratio

Δ - change

f_v^∞ - soot volume fraction far downstream

Units

C - Celcius

g - grams

Hz - Hertz

J - Joule

K - Kelvin

kHz - kilohertz

km - kilometers

kWh - kilowatt-hour

kPa - kilopascal

m - meters

mm - millimeters

mg - milligram

mi - mile

MPa - Megapascals

MU - million units

μm - micrometers

nm - nanometers

pC - picoculombs

psi - pounds per square inch

rpm - rounds per minute

s - seconds

v - volts

1 INTRODUCTION

Particulate formation in internal combustion engines has been studied at great length for several decades. Most of the work up until the late 1990s focused more on compression-ignition (CI) diesel combustion than on spark-ignition (SI) gasoline combustion. Diesel engines have historically suffered from higher particulate mass in their exhaust when compared to SI engines. However, particulate mass is not necessarily indicative of particulate number. Beginning in the 1990s, epidemiological, toxicological, and phenomenological studies [28, 63, 84, 106] have produced increasing evidence that particle size and number are perhaps of greater importance than mass to the influence of particulate matter on human health. This is due to longer ambient air residence time, greater surface-to-volume ratio, and higher respiratory tract deposition of particles smaller than 1 μm. Higher retention in the lungs at lower diameters can cause particles that are non-toxic in the micrometer size range to be toxic in the nanometer size range [106]. Medical findings indicate that adverse health effects are caused by ultrafine ($<$ 100 nm diameter) particles for which internal combustion engines are a significant source [28, 83, 84]. Nanometer-sized particles may contribute to only 1-20% of the particulate mass, but over 90% of the particulate number [63]. Therefore, these smaller particles may pose a greater health risk than larger, more massive particles.

The European Union instituted the Particulate Measurement Programme (PMP) to validate new particle measurement methods that can offer data on particle number emissions as well as mass-based emissions [1]. The PMP is used to measure particulate emissions over the New European Driving Cycle (NEDC). The Euro

5 regulation specifies a particle number limit for gasoline direct injection (GDI) vehicles of $6.0(10^{12})$ particles/km and will become effective for models introduced between September 2014 and September 2015. The Euro 6 regulation specifies a limit of $6.0(10^{11})$ particles/km and will become effective three years later (September 2017- September 2018) [54].

In North America, the current Tier 2 Low Emission Vehicle II (LEV II) PM limit is mass-based at 10 mg/mi for the federal test procedure (FTP)-75 test cycle [21]. However, the California Air Resources Board (CARB) has proposed that vehicles subject to the LEV III regulation should comply with the FTP-weighted particulate mass emission limit of 3 mg/mi which goes into effect in 2017 [8].

Although SI engine emissions are currently well below mass-based regulations, SI engines with direct injection (DI) generate higher particulate numbers than port fuel-injected (PFI) SI engines, and may have trouble meeting the number-based regulations. Figure 1.1 from Piock et al [90] represents the state of GDI and PFI technologies relative to the proposed Euro 6 particulate standards as of 2011. Horizontal red lines have been added to the original graph to represent the 2014 and 2015 European number standards, and vertical blue lines have been added to represent the proposed 2017 and 2025 US mass standards.

Significant research effort has been focused on investigating the operating conditions that affect particulate number emissions from GDI engines. The literature regarding effects of various operating conditions and fuels in a variety of GDI engine geometries is extensive, but little quantitative information has been offered in the literature explaining the contribution of fundamental parameters towards

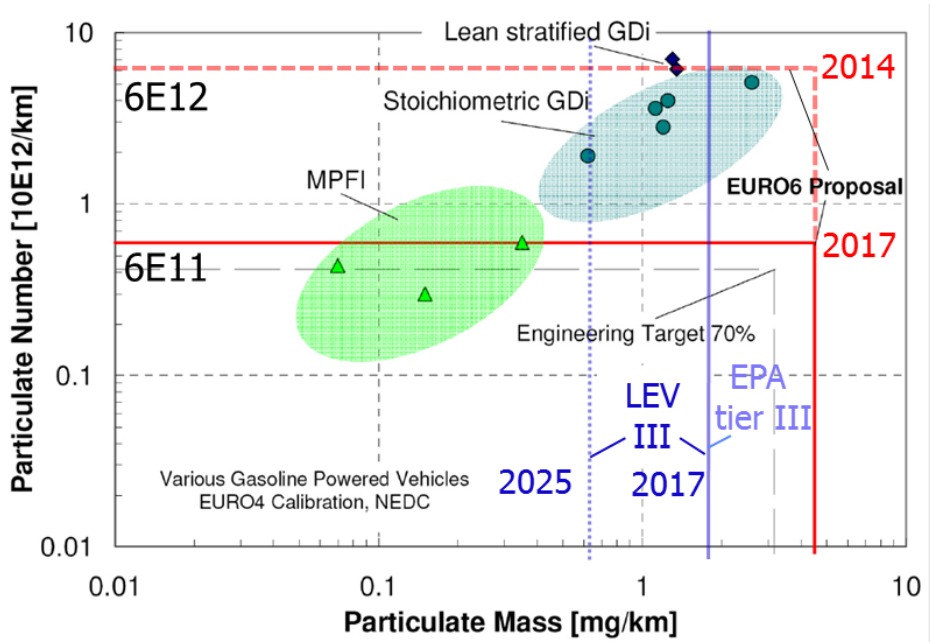

Figure 1.1: The current state of GDI technology as it relates to proposed emissions standards. Modified from [90]. Horizontal red lines represent European number standards. Vertical blue lines represent U.S. mass standards

particulate formation in these studies. Due to a shifting focus on alternative fuels for SI engines that have traditionally run on gasoline, the more-general term "spark ignition direct injection" (SIDI) will be used to describe the engine and combustion strategies in this work. While the term GDI can be used almost interchangeably with the term SIDI or the term DISI (direct injection spark ignition), the term SIDI more accurately describes the fuel-neutral nature of this study.

This work focuses on filling the gap in the understanding of the relative contributions of fundamental parameters towards particulate formation in SIDI engines. The work begins with a validation of the premixed, pre-vaporized (PMPV) method. The PMPV method is then used to validate that a 3-component surrogate fuel is

an appropriate surrogate for a research-grade gasoline for in-cylinder premixed flames. The role of fuel aromatic fraction in particulate formation is then characterized under PMPV operation. The main combustion event is shown to have little effect on particulates under PMPV operation through a combustion phasing sweep. This result allows for better characterization of the effects of cylinder pressure and residence time, which are investigated under PMPV operation here using engine load and speed, respectively. Finally, SIDI injection timing sweeps as well as SIDI speed and load studies are compared to the PMPV results to help better understand the sources and effects of diffusion-limited burning in SIDI particulate formation. This also allowed a comparison of the relative effects of fuel chemical properties vs fuel physical properties. The results provide an understanding of the interactions between the fundamental sources and parameters affecting particulate formation in all SIDI operating conditions. For any operating condition where multiple variables are changing simultaneously, it is now possible to interpret the most likely sources of the particles. It is also easier to pinpoint the source of differences between operating conditions.

2 LITERATURE REVIEW

This work investigates the basic physical parameters that lead to particulate matter formation and growth in SIDI engines. A complete understanding of this problem requires an understanding of the current state of SI engine technology, in-cylinder flame development, the kinetics and physical processes that drive particulate formation and growth in different types of flames, available methods for quantifying particulate emissions, and the interdependencies of physical parameters as they are encountered in the engine. Each of these topics will be discussed separately in the literature review. The relationships between the topics will also be discussed when possible so that a cohesive description of the complete problem can be constructed.

First the current state of the art of SIDI technology will be discussed, including the benefits of utilizing direction injection and the unresolved issues associated with DI operation, focusing on those related to particle formation.

Second, the physical processes of particulate formation and growth will be discussed. This discussion begins with the particle origins as a fuel molecule and follows the chemical and physical progression up to the final stages of agglomeration, accounting for the constant destruction of particles by oxidation.

Third, the various methods for measuring and quantifying particulate emissions will be discussed. There are several ways to characterize and quantify particulate emissions, many of which have been utilized in this study. The available methods will be presented along with their associated benefits and drawbacks, and the primary technologies used for this study will be discussed.

Fourth, trends of particle formation in laboratory flames will be discussed. The simplicity of laboratory flames allows easier isolation of fundamental parameters, and knowledge of the particle formation behavior in these simplified flame environments provides significant guidance in interpreting the behavior of in-cylinder flame development. The two most basic and widely studied cases of laboratory flames are laminar premixed flames and laminar diffusion flames. Decades of experimentation, modeling, and theoretical effort has produced a wealth of knowledge regarding both of these flame types. The response to different variables changes based on the flame type. Globally, SI combustion can be described as a premixed flame environment. However, diffusion-limited combustion can occur locally in the form of liquid fuel burning as a result of spray impingement and incomplete vaporization and is often cited as the primary source of in-cylinder particle formation for SIDI engines [54, 90, 125]. The literature review will discuss these two flame types separately, focusing on the behaviors of each with respect to particle formation as a function of temperature, pressure, and mixture chemistry.

Finally, significant experimentation and modeling of both DI and port fuel injection (PFI) SI engines has resulted in a basis of practical knowledge of the sooting effects of different engine operating parameters, The literature review will conclude by revisiting the topic of SIDI engines, focusing on the documented trends in sooting and identifying gaps in the understanding of the role of the fundamental parameters that cause these trends.

2.1 Direct Injection: Benefits and Drawbacks

The benefits of SIDI engines over PFI engines are well documented and widely recognized [125]. Direct injection allows induction throttling to potentially be significantly decreased, particularly when operating at a globally lean equivalence ratio with stratified operation, minimizing energy losses from the pumping loop. DI engines also exhibit an improved tolerance for lower octane fuels, allowing them to run on a wider range of fuels [125] and for a given octane number can operate at a higher compression ratio (CR). Time lags associated with fuel delivery under PFI operation are avoided with direct injection, and this allows for more accurate fuel metering, better transient response, reduced over-fueling during startup, quicker startup, and less cylinder-to-cylinder variation in the air-fuel ratio (A/F). After startup, combustion with leaner mixtures can be achieved by aligning the fuel injector in a position relative to the spark plug that allows a local equivalence ratio that is sufficient for ignition, while maintaining a globally lean mixture [125]. Additionally, DI operation provides more options for fuel delivery timing and the option of cutting off fueling upon deceleration. These improvements result in the potential for lower unburned hydrocarbon (UBHC) emissions upon startup, a more responsive engine, more potential for optimization, a greater power-to-weight ratio, and lower brake specific fuel consumption (BSFC) as compared to PFI engines. Because of these advantages, estimates indicate that up to 60% of the light-duty automotive market in the United States will utilize DI engines by 2016 [21].

There are several challenges associated with SIDI engine systems. The most noteworthy challenge is the one addressed here: increased particulate emissions

relative to PFI engines. The time available for mixture preparation is reduced from PFI to DI operation, and the potential for in-cylinder fuel impingement is increased. Reduced mixture preparation time can lead to poor fuel vaporization and inhomogeneous mixing. Liquid fuel burning from incomplete vaporization and fuel impingement increases diffusion burning, while inhomogeneous mixing leads to local pockets of overly-rich premixed flames, both of which can lead to higher particulate number and mass.

An SIDI engine operating map may include both homogeneous and stratified charge operating points [66]. Homogeneous charge refers to early fuel-injection timings corresponding to a downward-moving piston and coinciding with air intake, and stratified charge refers to late injection timings corresponding to an upward-moving piston. A late injection timing results in a local equivalence ratio favorable for ignition near the spark plug, creating a flame that propagates into a progressively leaner or "stratified" air-fuel charge. The term "homogeneous," as it is used with respect to DI operation is not an absolute term, but rather a relative term used to differentiate the mostly homogeneous fuel-air mixture resulting from early injection from the markedly stratified fuel-air mixture resulting from late injection.

The benefits of charge stratification include the ability to use a globally lean mixture which reduces fuel consumption due to reduced pumping losses associated with throttling, reduced heat loss, reduced chemical dissociation, and an increased cycle specific heat ratio [125]. These characteristics make stratified charge operation optimal for maximum fuel economy and more responsive load transitioning.

However, under higher-load operation the increase in injection duration causes locally overly rich regions and more potential for wall wetting, both of which lead to higher soot emissions [54, 90]. For these reasons, stratified charge operation is not well suited for high-load operation, and the formation of soot is a limiting factor in its use [125]. Additionally, combustion stability is more difficult to achieve with stratified charge operation, and implementation of this strategy can require significant increases in overall system complexity so it is not yet widely used in production engines.

Compared to stratified charge, homogeneous-charge operation allows a slightly higher compression ratio, low cold-start and transient emissions, low particulate emissions, and better combustion stability. Additionally, the near-stoichiometric mixture used under homogeneous operation allows the use of a three-way catalyst, whereas stratified operation using a leaner mixture produces a relatively oxygen-rich exhaust gas causing reduced efficiency of catalytic NO_X conversion.

Particulate formation limits the usefulness of stratified operation, but tightening regulations will be difficult to meet using homogeneous DI strategies as well. Homogeneous operation is the focus of the current study. The primary contributors to particulate formation under homogeneous charge have been consistently identified as mixture inhomogeneity and liquid fuel burning. This is because incomplete mixing and fuel impingement are inherent under DI operation regardless of the injection strategy. For this reason the potential sources of particulate emissions under homogeneous and stratified operation are similar and the results of this

study also provide significant insight into particulate formation during stratified operation.

2.2 Processes of Soot Formation and Growth

In this section, the basic model of soot formation and growth will be discussed. There is no complete or universal model of soot formation and growth. However, it is well accepted that particle inception begins with the formation of chemical precursors, which grow initially by chemical processes. Inception is followed by coagulation, which includes both coalescence and agglomeration, and surface growth. Particle formation and growth are limited at all stages by destruction of both soot precursors and soot via oxidation [38, 39, 45, 53, 59, 60, 110, 115]. An understanding of the details of each step can aid in understanding changes in particle size distribution (PSD) shapes, and the effects of certain operating conditions on the PSD.

It should be noted that most combustion literature on particulate matter formation utilizes the term "soot" to refer to any particulate matter formed in the flame, which is the appropriate term when the particles are known to originate from combustion of fuel under rich conditions. Nominally soot refers to combustion formed particulate with a high C/H ratio. However, soot composition varies throughout a flame and C/H ratio varies as a function of residence time. When the term soot is used in the current work it is meant to refer to this classic definition. This term will be maintained where the cited literature uses it and where its use is appropri-

ate. The term "particulate matter" (PM) is more universal because it accounts for other potential particle sources. Particulate matter is the most appropriate term to use when referring to all of the particles emitted by an engine since not all of the particulate is due to combustion generated soot. In many cases, the two terms are somewhat interchangeable because soot is a subset of the PM emitted by engines.

2.2.1 Formation

The first step in the formation of soot that is common among all fuels is the formation of polycyclic aromatic hydrocarbons (PAHs) [12, 39, 45, 53, 80, 115, 121]. Other non-aromatic species, most notably acetylene (C_2H_2), are often designated as soot precursors as well. However, aromatic hydrocarbon rings are widely identified as the building blocks of soot [12, 31, 39, 45, 53, 115], and their formation may be a rate limiting step [45, 53]. Most notably, benzene (C_6H_6) and naphthalene ($C_{10}H_8$) formation rates have been closely tied to soot formation rates [79, 119]. Growth begins chemically as single or double aromatic-ring structures develop into larger multiple-ring structures. Physical growth also occurs as molecules collide and stick to one another. The simplest instance of physical growth is the case of two PAH molecules sticking together, referred to as a dimer. Pyrene ($C_{16}H_{10}$) is often assumed to be the smallest aromatic compound that is capable of forming PAH dimers [13, 108] and Pyrene dimerization is used often in modeling as the soot particle inception step.

Although a universal transition point from molecules to soot particles is not well established, dimerization of pyrene and larger aromatics is a commonly accepted

transition point [12, 13, 39, 108]. This transition has been referred to as both particle nucleation [39, 45] and particle inception [13, 53, 108]. Here, the term "particle inception" will be used. The inception mode particles are known to have many radical sites and are highly reactive [39, 53] leading to rapid initial chemical growth.

The H-abstraction-C_2H_2-addition (HACA) model of chemical PAH growth developed by Frenklach et al. [39–41] was first conceptualized in 1984 (The term HACA was first used in 1991 [40]) and is now used frequently in modeling of PAH growth. The HACA mechanism describes a two-step, repetitive reaction sequence. The first step, abstraction of a hydrogen atom (H) from an aromatic molecule (A_i) to form a radical aromatic (A_{i-}) is currently believed to be dominated by reactions with gaseous hydrogen in the representative reaction [39]

$$A_i + H \rightarrow A_{i-} + H_2 \tag{2.1}$$

that is followed by addition of acetylene to the new radical site [39]

$$A_{i-} + C_2H_2 \rightarrow products. \tag{2.2}$$

The subscript (i) denotes the number of aromatic rings present in the structure, which may be any number for these representative reactions. Initial formation of the aromatic ring may proceed through various reaction pathways that are fuel and condition dependent. A few of the most common initial pathways are listed below. However, numerical simulations suggest that each of these initial pathways lead quickly to the HACA sequence described above.

Some of the most common pathways to formation of the initial aromatic rings involve acetylene, propargyl (C_3H_3), and cyclopentadienyl (C_5H_5). These reaction types can be further categorized as follows [39]:
even carbon atom pathways involving the addition of acetylene

$$n - C_4H_3 + C_2H_2 \rightarrow C_6H_5(phenyl)$$
$$n - C_4H_5 + C_2H_2 \rightarrow C_6H_6 + H\ ,$$

and odd carbon atom pathways involving propargyl and the cyclopentadienyl radical

$$C_3H_3 + C_3H_3 \rightarrow C_6H_6(or\ C_6H_5 + H)$$
$$C_5H_5 + CH_3 \rightarrow C_6H_6 + 2H$$
$$C_5H_5 + C_5H_5 \rightarrow C_{10}H_8 + 2H,$$

and the reaction between propargyl and acetylene to form a cyclopentadienyl radical

$$C_3H_3 + C_2H_2 \rightarrow C_5H_5.$$

The pathways are dependent on fuel structure, and certain fuels and intermediates have been shown to more readily decompose to soot precursor species than others. From these reactions, it is clear that two of the most important non-aromatic soot precursors are acetylene and propargyl.

2.2.2 Surface Growth

Chemical and physical growth continues on the surface of particles, and this stage is referred to as surface growth. Although some details of surface growth differ from the initial gas-phase reactions that formed the particle, the primary contributors continue to be PAH collisions and chemical growth of the aromatic rings. The growing particle initially behaves similarly to a large PAH molecule [39], and the HACA model remains relevant [13]. Surface hydrogen abstraction creates reactive radical sites, which encourage further chemical growth. Potential radical sites include carbon atoms saturated with hydrogen, any C-H bonds, and radicals formed through dehydrogenation.

Surface growth refers to separate growth of individual particles, and the collisions referred to in this stage are collisions between particles and molecular hydrocarbons, including aromatics. Surface growth does not include separate particles colliding and sticking together. The majority of the solid-phase material is collected in this stage and the mass of soot increases greatly, but the number of particles is not affected [53]. The rate of surface growth is determined by the competing processes of oxidation via O, O_2 and OH, and growth of the aromatic rings. Aromatic ring growth is assisted or induced by H atom migration [39]. It can occur at temperatures and hydrocarbon concentrations lower than those required for soot inception [53]. Surface growth eventually slows due to surface aging, which is brought about by removal of hydrogen atoms [39, 45], a reduction of active sites, and surface voids left by collisions of growth fronts made up of migrating rings [39].

2.2.3 Coagulation

At this stage, soot particles begin to collide with and stick to each other, forming a reduced number of larger particles. Until this point, the particles are approximately spherical, but as larger particles begin to collide, the aggregates may begin to take on a more branched, or "fractal" structure. The extent of branching is dependent on how well surface growth keeps pace with growth via particle collisions. Chemical growth on the surface of the aggregate has a smoothing effect that increases sphericity, while growth via collisions increases branching. Coagulation has the opposite effect of surface growth on the amount and number of particles. As particles collide and stick together, the overall number of particles decreases, but gas phase molecules are not added via coagulation, so the mass of the soot distribution remains unchanged [53]. Of course, particle inception, surface growth, aging, coalescence and oxidation occur simultaneously so both the number and mass of soot are constantly changing.

2.2.3.1 Coalescence

Coalescent growth refers to collisions of young liquid like soot particles where the two particles coalesce completely with each other forming a single spherical particle. Coalescence does not result in a chain like fractal structure. As is the case with all coagulation processes coalescence preserves particulate mass and decreases particulate number.

2.2.3.2 Agglomeration

In the final stage of soot growth, collisions outpace surface growth, and the aggregate takes on a chain-like structure. This often happens at the same time that the surface growth slows down due to surface aging [39, 53]. Therefore, the start of the agglomeration stage serves as an indicator of the transition from coalescent type growth to chain and branched chain agglomerate growth [39]. Oxidation and particle breakup continue to occur during this step, counteracting its effect on particulate number and mass. As with all other stages, all processes in this stage are dependent on temperature, pressure, and oxygen availability.

The various stages of soot particle growth are often differentiated in the literature by particle size ranges [23, 63, 74, 101]. This can be helpful for quick approximations when analyzing PSDs if no other information on the particulate morphology is available, but there are no exact particle sizes where one growth stage ends and another begins. As will be discussed later, the size of a particle can only be defined with an "equivalent" diameter that represents some correlation to a perfect sphere that would act in the same way as the particle under the same physical conditions. Some significant deviations in particle morphology and mass can exist among particles with the same equivalent diameters, regardless of the size definition used. Furthermore, differing flame types and operating conditions can produce particles with differing morphologies that may not be represented well by the resulting PSDs. For these reasons, it is beneficial to use multiple sampling methods that, when used together, can provide information on particle number, size, and morphology for a given operating condition.

2.3 Particulate Morphology

The results of particle formation and growth processes manifest themselves in the PSD, the particulate morphology, and the particulate composition. While the PSD is the primary metric used here for interpreting particle formation trends, information on the particulate composition and morphology can be a useful supplement in creating a fuller understanding of formation processes. Morphology refers to the extent of branching, primary particle size, apparent density, extent of agglomeration, and other visually distinguishable features.The extent of branching ranges from a perfect sphere (no branching) to a long straight chain [29]. Both branching and internal void spaces reduce the particle density at higher D_m. Therefore an important implication of the particle morphology is changes in the relationship between particle mass and particle number as D_m increases. This relationship can be quantified for a given exhaust sample by sorting the sample by D_m using a DMA, then measuring the mass of the D_m-selected particles. This produces a D_m vs mass relationship that can be used to approximate the mass of the particles in a PSD from the same sample.

2.4 Particulate Matter Composition

Composition refers to the chemical constituents that make up the particle, and can provide information on particle origins. The various particulate sources, compositions, and measurement techniques have resulted in a body of terminology with overlapping definitions due to the tests used to gather compositional information.

Understanding the basic differences between compositional definitions and realizing that the definitions may overlap is important for interpretation of reported results, so the various definitions are introduced briefly. Terms used to describe particulate composition include soluble organic fraction (SOF), elemental carbon (EC), volatile organic content (VOC), black carbon (BC), organic carbon (OC), and ash. The SOF is made up of unburned fuel and lubrication oil, and is composed of PAHs containing oxygen, nitrogen, and sulfur [63]. Elemental carbon (EC) is typically thought of as the fraction of C atoms bonded to other carbon atoms. In the context of particulate matter, OC consists of compounds containing predominantly carbon and hydrogen but may also include partially oxidized species. Volatiles, or VOC are liquid or gas-phase molecules found either alone or condensed on the surface of solid particles. Ash typically refers to inorganic metals and non-metals that may be present alone or within carbon-containing particles.

The measured compositional fractions often overlap due to the fact that the true definition of the quantities is based on the tests used to measure them. For example, the California Air Resources Board (CARB) defines BC as light-absorbing carbon and it is measured using light attenuation techniques [87]. However, BC may contain both EC and OC. Elemental carbon is defined by CARB as the carbon mass left on a particulate filter after the OC fraction has been removed by stepwise heating of the filter [87].

In this work, the compositional information provides a way of interpreting the sources of non-fuel particles, which are likely to be present in the form of SOF, ash, and metallic species. Common sources of ash include phosphates and sulfates

[120]. These may come from fuel impurities, engine wear particles, oil films, and potentially from particles in the intake air. The portion of the ash due to oil films comes from additives such as detergents, antioxidants, and antiwear agents [120]. Some SOF from the oil films is also expected [63]. While the hydrocarbon portion of the oil contribution is not easily separated from the fuel contribution, the non-hydrocarbon ash allows for some distinction between particles originating from incomplete oxidation of the fuel and particles originating from the non-fuel sources listed above.

2.5 Particulate Measurement Technique: SMPS

The primary particle measurement utilized in the current study is the particle size distribution (PSD). The PSD provides information on the number concentration of particles as a function of the particle size. There are relatively few systems available for this type of measurement that have suitable resolution and measurement speed to enable online measurements. For steady-state particle sizing applications, where highly time-resolved measurements are not needed, the scanning mobility particulate sizer (SMPS) is widely used due to its relatively high-diameter resolution. The SMPS system software reports the particle size distribution in terms of $dN/dlog(D_P)$, which is the derivative of the number concentration (N [$1/cm^3$]) with respect to the logarithm of the particle diameter (D_P). The motivation for reporting PSDs in terms of $dN/dlog(D_P)$ stems from the fact that many aerosol size distributions exhibit a lognormal form and as such will resemble a normal

distribution when plotted versus $\log(D_p)$. Plotting the derivative accounts for instrument resolution.

The particle diameter measured by the SMPS is the mobility diameter (D_m) such that $D_P = D_m$. As with all aerodynamic based diameter measurements this is an equivalent diameter. The equivalent mobility diameter is defined as the diameter of a sphere with the same terminal migration velocity in the applied electric field.

Determination of D_m is as follows: a particle with a charge (q) in an electric field of strength (E) experiences a force ($F = qE$). The particles quickly obtain a steady-state migration velocity (v_e) relative to the gas motion. In the SMPS, the strength E of the electric field is changed based on the desired D_m and the known charge distribution that is applied to the sample before size selection. The sample is introduced in a laminar sheath flow perpendicular to the force of the electrical field. The combination of electrical mobility and the field strength determine the migration velocity across the electric field. The bulk fluid motion produces a second velocity component that is perpendicular to the migration velocity. The combination of the velocity vectors and the instrument geometry allow particles within a narrow range of electrical mobility to arrive at a predetermined sampling point while all other particles miss this point. A simplified sketch of this process is shown in Figure 2.1.

Two additional systems that measure the mobility-based PSDs include the DMS 500 manufactured by Cambustion and the engine exhaust particulate sizer (EEPS) manufactured by TSI. Both of these systems are more useful for transient measurements than the SMPS, but less precise during steady-state operation. Due

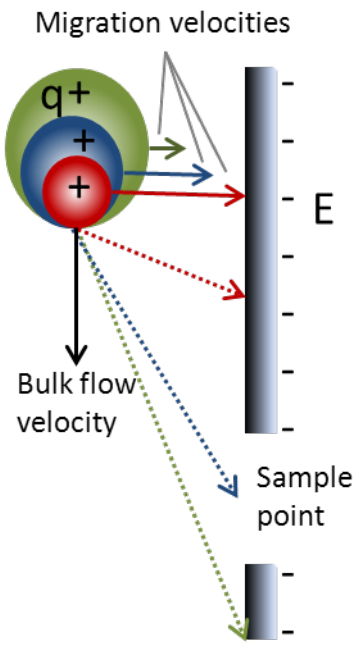

Figure 2.1: Sampling theory based on D_m. Particle trajectory is determined by the combination of the migration velocity and the bulk flow velocity. E = electric field strength, q = charge, (+) = positive charge, (-) = negative charge.

to the drawbacks of lower diameter resolution and lower particulate counting sensitivity of the DMS 500 and EEPS the SMPS was used for the current study.

2.6 PMP Protocol

The Particle Measurement Programme (PMP) defines the standards for particle number measurements that will be used to determine compliance with the Euro 5 and Euro 6 PM number standards. The specifications for PMP compliant measurement systems are discussed in United Nations Regulation 83 [1]. The PMP measurement specifications are designed for sampling from vehicles but they are also an example of good sampling practices, and it is worth noting the conditions particles will be sampled under for the Euro 5 and Euro 6 emissions regulations. A primary goal of the PMP specifications is to eliminate volatile particles from the exhaust since the number count of these particles is difficult to replicate.

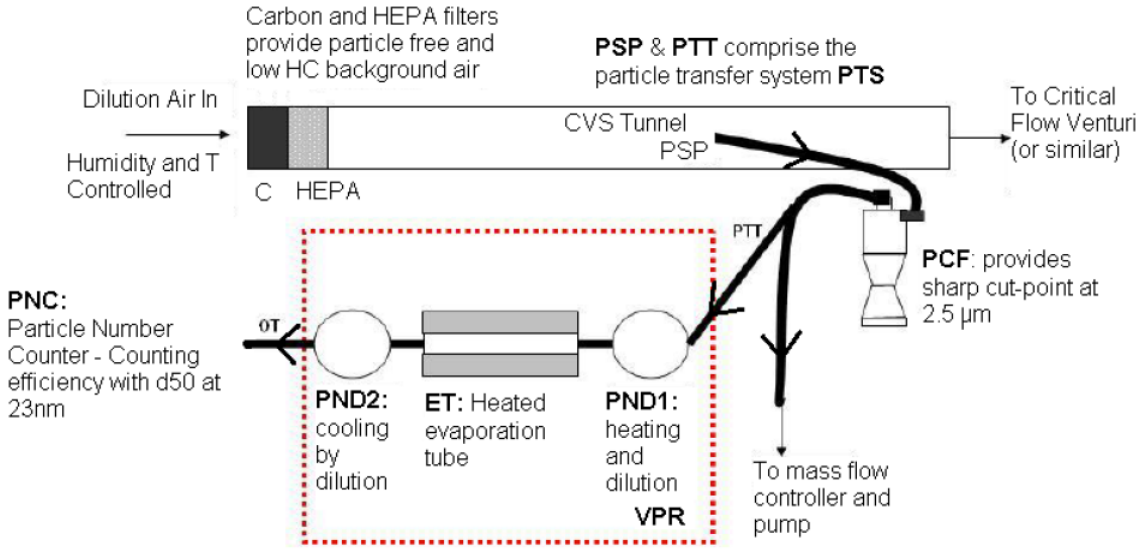

Figure 2.2: PMP recommended particulate sampling system. PSP = particulate sample probe, PCF = preclassifier, VPR = volatile particulate remover, PND = particulate number diluter, ET = evaporation tube, PTT = particulate transfer tube. Modified from [1].

A diagram of the recommended sampling system for the PMP is shown in Figure 2.2. The PMP specifies that the particulate number counting system should receive the exhaust gas sample from a constant volume sampler (CVS) [1]. This offers the advantage of intrinsic determination of emissions on a specific basis (/km or /kWh). A particle pre-classifier (PCF) is recommended to remove particles with aerodynamic diameters > 2.5 μm. Particles below this cutoff are considered to be the most harmful fine fraction [1]. A volatile particulate remover, or VPR is required to evaporate liquid and volatile exhaust gas components while properly transmitting solid particles to the number counter [1]. The recommended VPR system consists of two diluters (PND1 & PND2 in Figure 2.2) with a heated evaporation tube (ET) between them. The first PND is heated to 150 °C and reduces the concentration of all particles and droplets. The ET accelerates vaporization by heating the sample to 300 °C. The second PND cools the sample in order to avoid thermophoretic particulate losses. The dilution air should be filtered with HEPA filters.

Finally, a particle number counter (PNC) is required to determine the particle concentration in the sample. The instrument of choice for this measurement is a condensation particle counter (CPC), which detects particles by light scattering. The CPC does not differentiate between solid and volatile particles, so the VPR is necessary upstream to allow the total number concentration of solid, non-volatile particles to be determined. This should be accomplished with a time resolution of approximately 1 second.

Several best practices for any particle sampling system are also specified. The entire system including dilution air and sampling systems should be air tight.

The sampling system components should minimize deposition or alteration of the particles by using electrically conductive and grounded tubing with a minimized total system length. The system length should be kept below 3.6 meters if not insulated, or 6.1 meters long if heat-insulated. Finally, the system should avoid sharp bends and abrupt changes in cross section, smooth surfaces should be used, and overall length should be minimized [1].

Previous researchers have noted critical considerations for PMP measurements, particularly regarding the identification of volatile particles in the PSD. Chan [21] noted that for distributions of solid soot particles, differences in VPR performance have little impact on the measured number concentration, but if the distribution contains a significant number of liquid particles, a more effective VPR system may result in lower measured number concentrations. He et al. [54] also pointed out that inception mode particles, as defined by a low mobility diameter, are more sensitive to humidity, dilution, and sampling system factors, most likely due to the larger fraction of volatile material in the smaller size range.

2.7 Fundamental Flame Theory

The formation of soot in internal combustion engines is dependent on several fundamental variables: temperature, pressure, mixture chemistry, mixture homogeneity, and flame structure. These factors are often interdependent and can be difficult to isolate in an engine, especially when using direct fuel injection. Premixed and diffusion flames occur simultaneously in modern DI engines and have substantially

different sooting tendencies. While it is difficult to isolate individual variables in a DI engine, this can be more easily accomplished in a laboratory flame. A wealth of knowledge has been produced for bench-scale premixed and diffusion flames regarding the dependence of soot formation on the fundamental variables of interest. This section first discusses metrics for mixture enrichment commonly used in laboratory flame studies, then the effects of the fundamental variables on premixed flames, and, finally, their effects on diffusion flames.

2.7.1 Metrics for Describing Mixture Enrichment

Because mixture enrichment is a controlling variable for particle formation in all flames, it is important to note the different methods for describing enrichment before discussing its effects in specific combustion setups. Three metrics are discussed in this work. The conventional metric for mixture enrichment in engine experiments is the equivalence ratio (Φ), which assumes a stoichiometric condition where the products are CO_2 and H_2O. Normalizing a given A/F against the stoichiometric A/F to obtain Φ implies that combustion at that A/F follows a similar tendency towards CO_2 and H_2O production.

Alternatively, many premixed flame studies have expressed mixture enrichment using the ratio of carbon atoms to oxygen atoms (C/O) present. Zero soot would be formed for a C/O ratio of 1 if the combustion products were composed solely of CO and H_2. This would imply that richer conditions with a C/O ratio > 1 would be likely to form soot [45]. Glassman suggested that at the rich mixtures required for sooting in premixed flames, neither Φ nor C/O account well for the

combustion chemistry because excessively rich mixtures favor production of CO and H_2O rather than CO_2 or H_2. Therefore, the equilibrium balances for Φ and C/O do not necessarily capture the chemical balance of rich mixtures and may not be an appropriate basis for comparison or normalization beyond a certain level of mixture enrichment.

To address this issue, a third metric for mixture enrichment, the "effective equivalence ratio (Ψ)," was proposed by Takahashi and Glassman [112], which defines a stoichiometric condition where the reactants are converted to CO and H_2O. The equilibrium balances for Φ, C/O and Ψ are presented in Equations 2.3, 2.4, and 2.5 respectively.

$$C_mH_n + \left(m + \frac{n}{4}\right)(O_2 + 3.76N_2) \rightarrow mCO_2 + \frac{n}{2}H_2O + \left(m + \frac{n}{4}\right)3.76N_2 \qquad (\Phi = 1) \quad (2.3)$$

$$C_mH_n + \frac{m}{2}(O_2 + 3.76N_2) \rightarrow mCO + \frac{n}{2}H_2 + \frac{m}{2}(3.76N_2) \qquad \left(\frac{C}{O} = 1\right) \quad (2.4)$$

$$C_mH_n + \left(\frac{m}{2} + \frac{n}{4}\right)(O_2 + 3.76N_2) \rightarrow mCO + \frac{n}{2}H_2O + \left(\frac{m}{2} + \frac{n}{4}\right)(3.76N_2)$$
$$(\Psi = 1) \quad (2.5)$$

The balance used for normalization to calculate Ψ is more representative of rich mixture chemistry, and the balance used for normalization to calculate Φ is more representative of near-stoichiometric mixture chemistry. The C/O metric accounts for fuel-bound oxygen and allows a more direct comparison of oxygen availability between hydrocarbon and oxygenated fuels. The balance used for C/O becomes more representative as C/O approaches 1.0. In this study the mixture was swept from slightly lean to very rich for a variety of fuels, so the dependence of soot on all three metrics is presented and compared.

A method for comparing the three metrics using common parameters is useful for interpreting data. Each metric can be expressed as a balance of C, H, and O molecules in the mixture. This allows for mathematical relationships between the metrics to be determined for a given fuel. The balance for C/O is self-apparent and independent of H, but is presented along with the balances for Φ and Ψ in Equations 2.6 and 2.7.

$$\Phi \equiv \frac{\left[2C + \frac{H}{2}\right]}{O} \quad (2.6)$$

$$\Psi \equiv \frac{\left[C + \frac{H}{2}\right]}{O} \quad (2.7)$$

$$C/O \equiv \frac{C}{O} \tag{2.8}$$

For hydrocarbon fuels the relationship between C/O and Φ is described by Equation 5.1, which shows that fuels with a lower C/H have a lower C/O at the same Φ. Similarly, the relationship between Ψ and Φ for hydrocarbon fuels is described by Equation 5.2, which shows that fuels with a lower C/H have a higher Ψ at the same Φ. For a given $\Delta\Phi$, as C/H decreases $\Delta(C/O)$ increases and $\Delta\Psi$ decreases. Finally, Equation 5.3 shows a direct correlation between C/O and Ψ for hydrocarbon fuels.

$$C/O = \Phi \left(\frac{1}{2\left(1 + \frac{4}{(C/H)_{fuel}}\right)} \right) \tag{2.9}$$

$$\Psi = \Phi \left(1 - \frac{1}{2\left(1 + \frac{4}{(C/H)_{fuel}}\right)} \right) \tag{2.10}$$

$$C/O = \Psi \left(\frac{1}{1 + \frac{2}{(C/H)_{fuel}}} \right) \tag{2.11}$$

Most engine studies use Φ as the mixture metric, but many of the laboratory flame studies cited in the following sections utilize C/O as the metric. A small number of studies use Ψ [45, 112]. All three metrics are used in the literature and the discussion of laboratory flames, so it is important to understand the relationships between the three.

2.7.2 Laminar Premixed Flames

2.7.2.1 Flame Structure

In a premixed flame, the fuel and oxidizer enter the reaction zone as a homogeneous mixture and combustion is limited by chemical reaction rates. The flame exhibits zones of preheating, reaction, and recombination. The reaction zone can be divided into a very thin region of fast chemistry, followed by a region of slower chemistry [47, 115]. The recombination zone may also be referred to as the post-flame zone. Figure 2.3 is an example of a premixed laminar, low-pressure flat flame on a Mckenna burner used in [52]. The quartz nozzle is a sampling apparatus, and can be ignored for the current discussion.

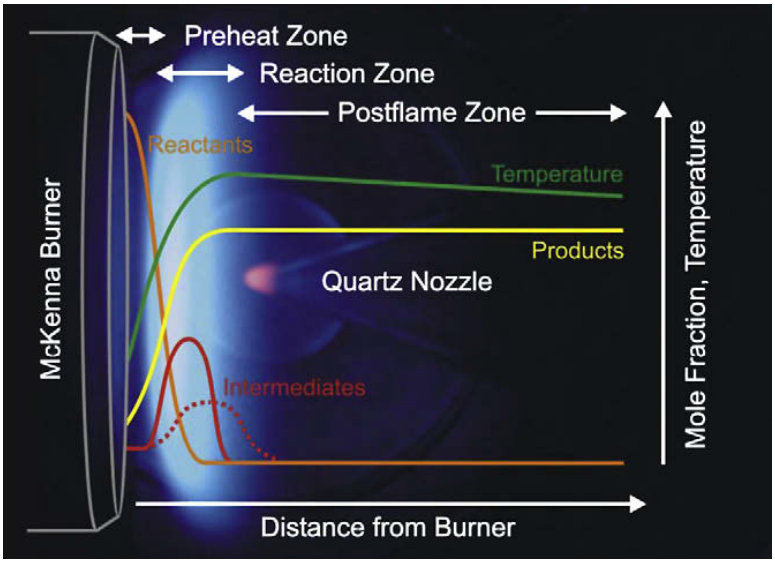

Figure 2.3: Laminar premixed flame temperature and species profiles [52].

As shown in Figure 2.3, the temperature rise rate reaches a maximum in the fast chemistry region of the reaction zone, which is also where the greatest rates

of fuel decomposition and CO_2, CO, H_2O and H_2 production occur [47, 53, 115]. In the slower chemistry region of the reaction zone, CO_2, CO, H_2O and H_2 reach equilibrium values [47, 115], but oxidation and pyrolysis continue. Figure 2.3 shows that destruction of intermediates continues even into the post-flame zone. Reactions leading to particle formation and oxidation begin in the fast chemistry region of the reaction zone and can continue through the post-flame zone. While gaseous emissions come to a near equilibrium at the end of the slow-chemistry region, H radicals and oxidizing agents continue to decrease in the post-flame zone [47].

2.7.2.2 Effect of Mixture Chemistry

Mixture chemistry can be defined by the oxidizer, the fuel, and the relative proportions of the two in the reaction chamber. Here, filtered air was used as the oxidizer so oxidizer chemistry won't be discussed. Fuel chemistry parameters that have been shown to affect soot formation include the C/H ratio, the number of carbon atoms, the number of carbon-carbon bonds, bond strengths, and unique elements of molecular structure that provide fast pathways to PAH formation [45, 79, 97, 112]. Finally, the proportion of fuel to oxidizer strongly affects the onset of particle formation and the total particle concentration [31, 45, 50, 53].

The oxidation of carbonaceous species directly opposes the formation of soot precursors, soot inception, and soot particle growth. Oxidation is accelerated by high temperatures, pressures, and oxygen concentrations. Given a sufficient supply of oxygen and the appropriate thermodynamic conditions, a premixed flame will not produce soot [31, 45, 50, 53] because the oxidation rate of gaseous

hydrocarbons is high enough to prevent particle inception. However, there is a fuel-specific critical enrichment threshold, that is temperature and pressure dependent, above which an enriched premixed flame begins to soot [31, 45, 50, 53]. Soot yield is known to increase with mixture enrichment above this critical enrichment threshold [31, 45, 50, 53] because there is not enough oxygen to convert all of the carbon to gaseous combustion products such as CO and CO_2. Once particles have formed, oxidation at all stages of particle growth becomes important. Oxidation at the early stages of aromatics growth, specifically at the phenyl stage is critical because as aromatics growth progresses, it depletes the supply of O_2 by reaction of O_2 with H atoms [39]. As surface aging increases, oxidation becomes more prevalent and despite decreasing supplies of oxygen, oxidation dominates over pyrolysis in older particles [39]. These effects are decreased as the mixture is enriched.

The formation of the intermediate species that lead to aromatics growth tends to be the rate-limiting step in particle formation and it depends on the initial fuel chemistry [45, 53, 79, 119]. The sooting properties of low carbon number single-component fuels are well-documented, but the chemical mechanisms leading from large hydrocarbon fuels to aromatics are still not well understood [79, 119]. This is an important distinction because real fuels are multi-component mixtures that include large hydrocarbons with elements of molecular structure such as aromatic rings that are not present in low carbon-number fuels.

Early studies [111] had shown a sooting dependence on fuel structure in premixed flames, with aromatics having the highest tendency to soot, followed by alkanes, alkenes, and alkynes [45, 53]. Glassman and coworkers demonstrated a

strong sooting dependence on flame temperature and pointed out that adiabatic flame temperature is a function of fuel structure. The earlier results had been gathered without controlling the flame temperature [45, 112], resulting in observed changes in sooting that were convolved with changes in flame temperature. Therefore, chemical fuel sooting tendencies must be compared at similar temperatures.

Glassman [45, 112] indicated that the C/H ratio and number of carbon atoms are the primary fuel chemistry parameters affecting soot formation characteristics in a premixed flame, while fuel structure (chain, branched, cyclic) appeared to have little impact. A higher C/H ratio and a larger number of carbon atoms both resulted in a lower threshold for soot with all other factors held constant, but they argued that the two factors increased sooting tendency through separate means. They stated that a high C/H causes lower OH concentrations, increasing soot by decreasing the rate of oxidation. A large number of carbon atoms increases the Arrhenius pre-exponential term in the global pyrolysis reaction, thereby increasing soot by accelerating pyrolysis rates. Those studies noted that the number of carbon atoms correlates to the number of C-C bonds, and the C/H ratio correlates to the C-C bond strength, so the number of C-C bonds was used to capture the effects of both parameters with a single metric. Using this reasoning, they studied the threshold for soot onset for various pure fuels using soot luminosity in atmospheric pressure premixed flames at a constant calculated adiabatic flame temperature of 2200 K, and reported a linear correlation between $\log(\Psi_C)$ and the number of C-C bonds. [112]. A plot of these results is shown in Figure 2.4.

This linear relationship becomes less reliable for small hydrocarbons, most notably acetylene, due to the nonlinear relationship between C/H and the number of C-C bonds [112]. Additionally, the C/H, the number of carbon atoms, and the number of C-C bonds are related to fuel structure. For example, aromatic molecules have a higher C/H than most aliphatics, and a higher number of C-C bonds than alkanes for a given number of carbon atoms due to the alternating single and double C-C ring structure. Therefore the individual contributions of these parameters is not clear from this study.

More recent studies have suggested that pyrolysis pathways may be dependent on fuel structure, although the mechanisms for large hydrocarbons and real fuels are still not well understood [79, 119]. This is due to the large number of possible chemical pathways a large hydrocarbon molecule can follow to form aromatic rings [79, 119]. However, a few important features of fuel structure have been identified for their importance in soot precursor formation. First, molecular bond strengths can determine the preferred decomposition route, because weaker bonds are broken first. Second, a given fuel molecule's tendency towards formation of certain stable aromatic species may cause it to soot more readily. Specifically, resonantly stabilized free-radicals (RSRs) are known to play a critical role in aromatics formation, and fuels with chemical structures that preferentially decompose to these RSRs will have a greater propensity to soot [79, 97, 119]. Finally, the effect of multiple constituents, as opposed to a pure fuel has not been well-documented for premixed flames but is of interest because real fuels and the surrogates used to model them are multi-component mixtures.

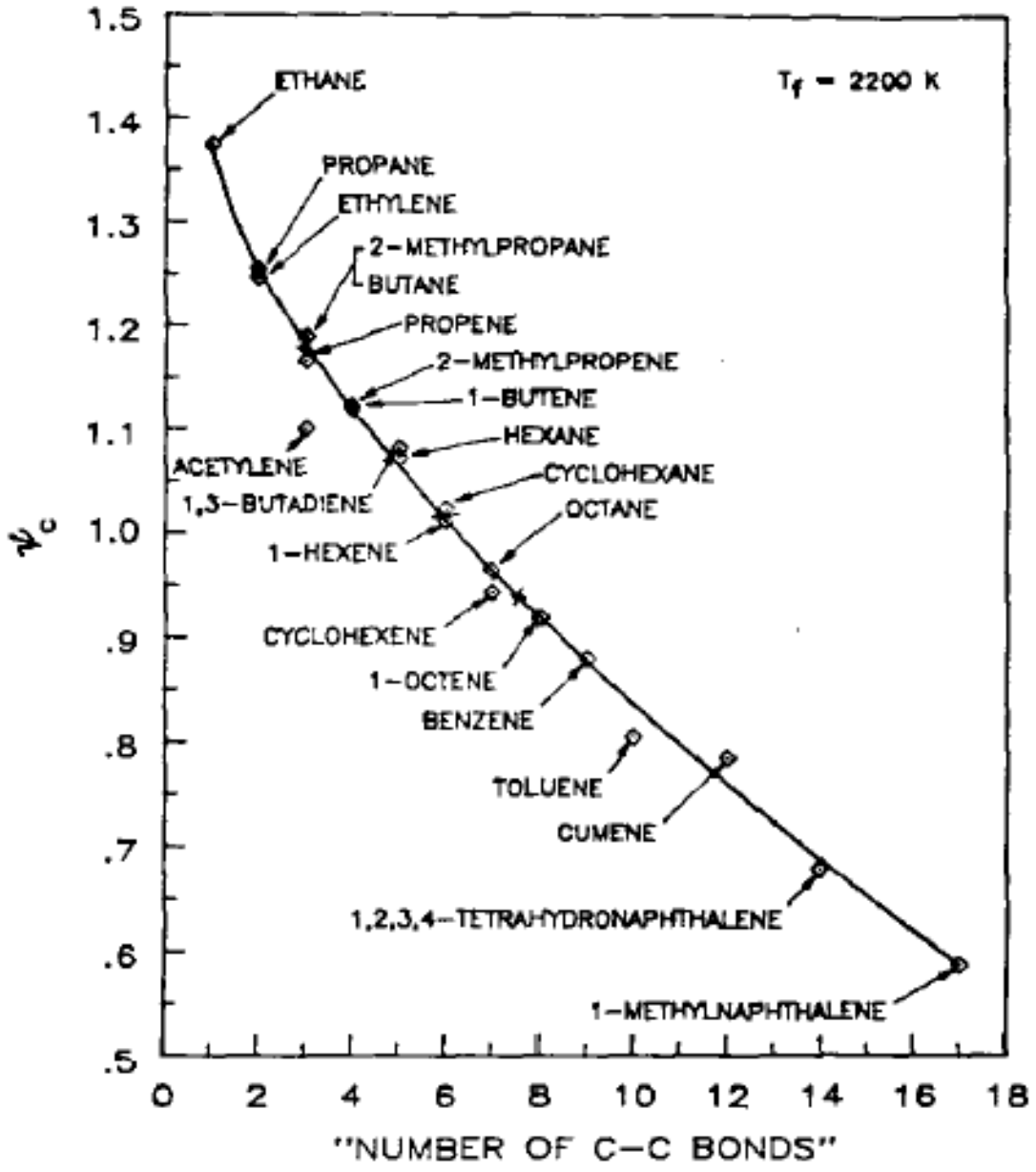

Figure 2.4: Critical sooting effective equivalence ratio (Ψ_C) as a function of the number of C-C bonds in the fuel from premixed Bunsen flames at a calculated adiabatic flame temperature of 2200 K. The calculated temperature was controlled by varying the N_2 / O_2 ratio [45].

2.7.2.3 Effect of Temperature

"The most dominant physical characteristic that affects soot formation is the temperature" [45]. Temperature accelerates pyrolysis and oxidation kinetics, creating competition between particle formation and destruction. Effects of flame type, mixture chemistry, and pressure help to determine which of the competing processes dominates. Two effects of temperature on soot formation are particularly important: the effect on soot onset, and the effect on the maximum soot formation.

The temperature range where soot formation has been shown to occur for laboratory flames is approximately 1300 K to 2600 K [45, 46, 53, 96]. However, the range where soot formation is most likely is much smaller. Böhm et al. [19] showed a strong dependence of C/O_C on temperature for C_2H_2, C_2H_4 (ethylene) and C_6H_6. All three fuels showed a maximum propensity to soot at temperatures between 1500 K and 1600 K with C/O_C increasing rapidly for C_2H_4 and C_6H_6 at temperatures below 1450 K. Bönig et al. extended the C_2H_4 results for several pressures at a similar temperature range, and the results for this study are shown in Figure 2.5.

For mixtures richer than the critical enrichment threshold in premixed flames, it is well established that soot formation follows a bell-shaped dependence on temperature, where the maximum soot formation and the minimum enrichment threshold occur within a similar temperature range [19, 25, 45, 81, 124]. One measure of the maximum soot formation is the soot volume fraction far downstream of the flame (f_v^∞). A bell-shaped dependence of f_v^∞ for C_2H_2-air flames on temperature has been shown between 1300 K and 2000 K at both 1 bar [19, 76] and 10 bar [16, 76], and total soot volume fraction decreases rapidly with temperature above 1900 K [45, 53]. The

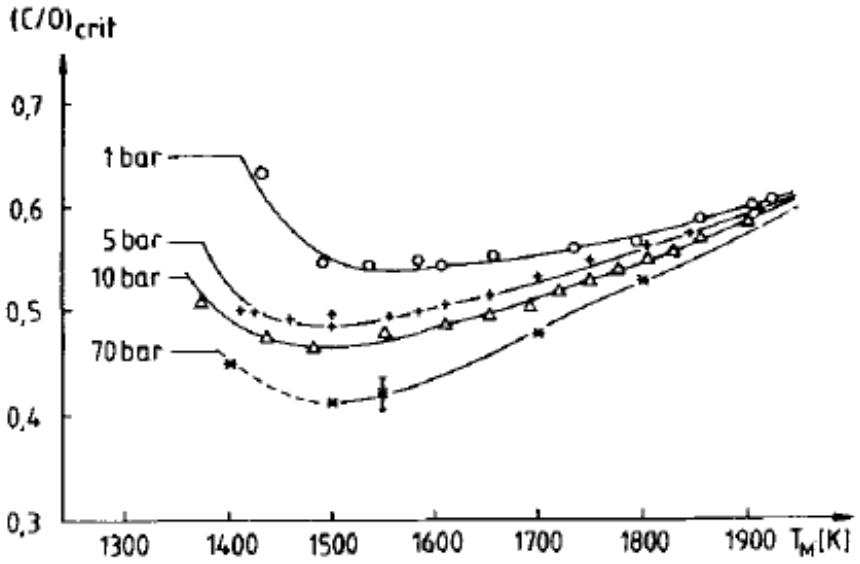

Figure 2.5: Threshold for soot formation (threshold determined visually by soot luminosity) as a function of temperature (T_M, measured 10 mm above burner) and presssure for C_2H_4-air flat flames [16].

1 bar results are shown in Figure 2.6. Note that f_v^∞ increases as a function of both temperature and mixture enrichment (C/O), but even at the richest mixtures, there is a temperature below which soot does not form, and even for the temperatures most conducive to soot formation, there is an enrichment threshold below which soot will not form. Figures 2.5 and 2.6 effectively show the relationship between mixture enrichment, temperature, and pressure in premixed flames.

Temperature dependencies are attributed to the differences in the activation energies and reaction rates of the particle-forming and particle-opposing steps in the chemical mechanism [53]. Activation of stable PAHs by hydrogen and reaction with acetylene are crucial to PAH growth, and both have appreciable energy barriers

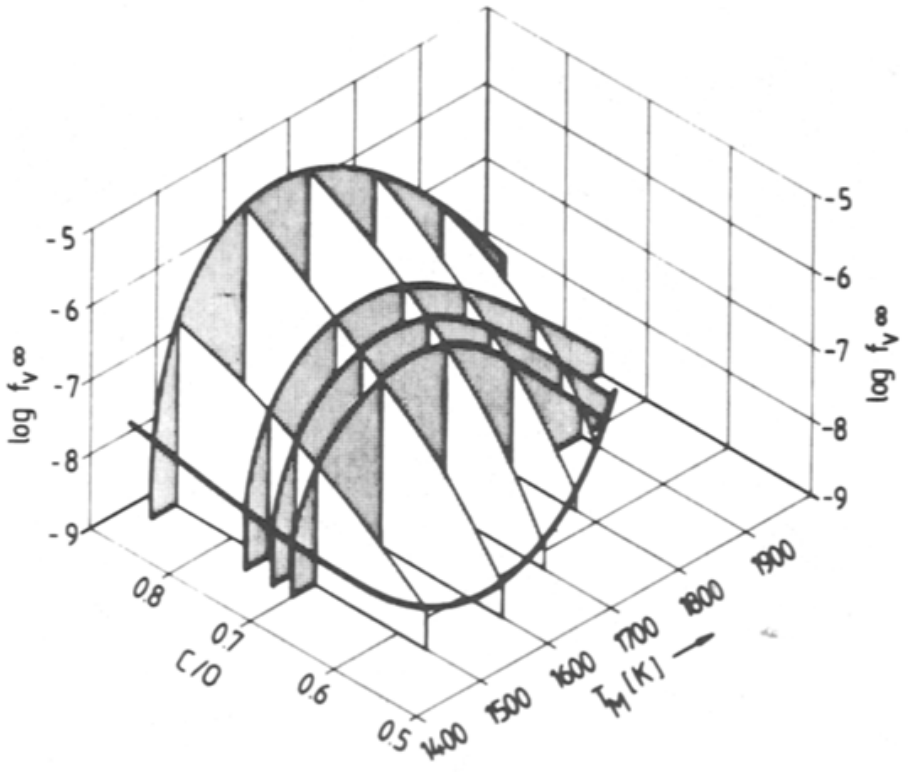

Figure 2.6: Final soot volume fraction (f_v^∞) as a function of temperature (T_M, measured 10 mm above burner) and mixture enrichment (C/O) for a C_2H_4-air flat flame at atmospheric pressure. The broad solid line that borders the base of the dome is the threshold for soot formation [19].

making them temperature-dependent. Particle inception follows an Arrhenius rate that is proportional to the presence of precursors [60]. Therefore, the low temperature limit may not mean that soot will not form below this temperature, but it implies that the kinetic rates may be too slow to form soot in the time provided. Surface oxidation is also exponentially dependent on temperature until the reactive surface sites are depleted, at which point the dependence decreases [53]. Pyrolysis reduction at high temperatures is also due in part to reverse reactions with high

activation energies that cannot occur at lower temperatures [76]. Increases in reverse reactions and oxidation at higher temperatures may help to explain the high temperature limit.

2.7.2.4 Effect of Pressure

As Figure 2.5 demonstrates, the propensity for soot formation increases with pressure as indicated by the reduced C/O_C with increasing pressure. The effect of pressure on soot formation becomes weaker at pressures above 10 bar and for temperatures above 1700 K. Specifically, a power law scaling of soot volume fraction pressure dependence has been commonly observed, i.e., $f_v^\infty \propto P^n$, where $n \approx 2$ for the pressure range from 1-3 bar, $n \approx 1.3$ for 3-5 bar, and $n \approx 1$ above 10 bar [16, 76]. Figure 2.5 also shows that the effect of temperature is slightly greater at increased pressure and that increasing pressure decreases the enrichment threshold and shifts the minimum enrichment threshold to lower temperatures [16]. Mauss et. al. [76] showed that increasing pressure shifts the maximum soot volume fraction to lower temperatures.

The dependence on pressure is linked to the pressure dependence of reaction rates of key species. A sensitivity analysis showed that the gas phase reactions affect the particle inception rates more than surface growth reactions [76]. This suggests that the pressure is a greater factor in particle inception than in particle growth.

2.7.3 Turbulent Premixed Flames

Turbulent premixed flames present in reciprocating engines, locally exhibit characteristics that are similar to their laminar premixed flame counterparts [115]. Turbulent flames have a very similar structure to a laminar flame in that the reaction front is thin, just as in a laminar flame, but with turbulence causing the overall flame front to be significantly more convoluted [115]. The extent to which the flame front is distorted depends on the level of turbulence experienced by the flame, and at extremely high turbulence, the wrinkles in the flame front may become significant enough to create small pockets of unburned gas. However, for the particular engine studied by Turns [115], these pockets were not seen until an engine speed of 2400 rpm, suggesting that below 2400 rpm the turbulent flame front behaves similarly to the laminar flame front. Turns notes that the effect of turbulence is simply to "wrinkle and distort an essentially laminar flame front [115]." McEnelley and Pfefferle [79] note that the relationship between laminar and turbulent premixed flame chemistry has not been closely studied, but that the chemical mechanisms important for soot precursor formation should be similar between the two. Glassman uses similar results between Bunsen flames and stirred reactors to support this claim as well [45]. This lends support to the notion that knowledge of laminar premixed flames can be used to predict the behavior of premixed turbulent flames in this engine.

2.7.4 Laminar Diffusion Flames

2.7.4.1 Flame Structure

In a diffusion flame, the fuel and oxidizer are separate until they enter the combustion zone. They diffuse toward each other in the flame in proportions that are near stoichiometric, independent of the overall mixture strength. Characteristic parameter variations as functions of the flame radius for a burning fuel droplet are shown in Figure 2.7. This is representative of the type of diffusion flame that may be experienced in-cylinder due to incomplete droplet vaporization and wall films. The profiles are applicable to any liquid surface [47]. A critical difference between diffusion and premixed flames is that a diffusion flame is mixing-rate controlled, whereas a premixed flame is reaction-rate controlled [47]. Diffusion burning is therefore highly dependent on the mixing properties [45, 53], and has a greater propensity to soot because of this. Kumfer and Skeen [65] have shown that at a point in the diffusion flame where the fuel and air have mixed sufficiently, C/O_C becomes similar to that of a premixed flame. Diffusion flames also have a wider reaction zone than premixed flames.

2.7.4.2 Effect of Mixture Chemistry

In a premixed flame, the formation of soot precursors by fuel pyrolysis is combatted by the oxidation of the precursors, but there is no such oxidative attack in diffusion flames [45]. The result is that increased oxygen availability does not necessarily lead to greater oxidation and reduced particulate. In fact, oxidation can cause local

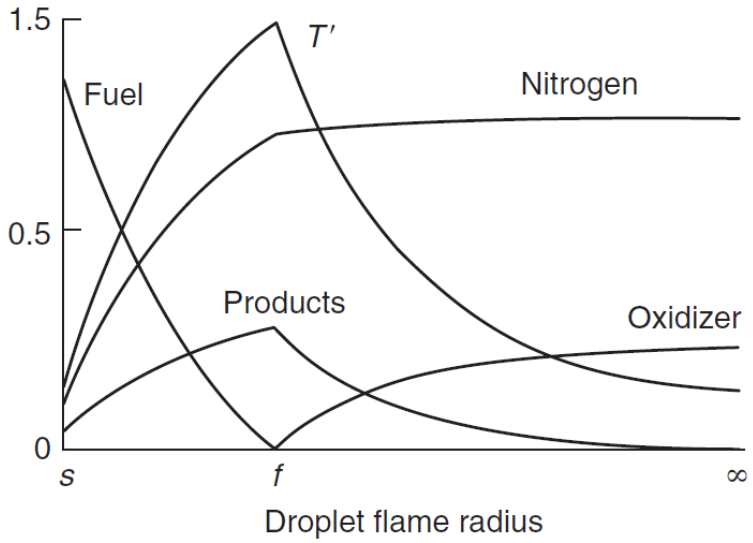

Figure 2.7: Radial dimensionless temperature (T′) and species profiles in a burning droplet diffusion flame. $T' = T/T_{ad,\Phi=1}$, S = droplet surface, f = flame front. Modified from [47].

temperatures to increase in fuel-rich zones, which accelerates the local pyrolysis rates and may actually increase the sooting tendency [45, 53].

Kumfer and Skeen noted that on the fuel side of the reaction zone, initial soot onset is determined by temperature and residence time, but as the fuel mixes with oxidizing species, soot production is limited by the local enrichment level [65]. For a given local enrichment level there is a temperature below which soot will not form due to excessively slow kinetics [65] and a temperature above which soot formation ceases. These observations are similar to those for premixed flames. The difference is that the soot production is dependent on the local enrichment, not the global enrichment, and the level of local enrichment is dependent on mass transfer rates rather than kinetics.

Molecular fuel structure has a more direct effect on soot formation in diffusion flames because the fuel is more likely to directly form aromatics and soot via pyrolysis or for aromatics already present in the fuel to directly contribute [45, 53, 65], whereas in a premixed flame the fuel is assumed to break down in the flame and form soot in the post-flame zone [45]. Soot formation increases with the number of C-C bonds, and with an increasing C/H ratio [45, 53]. Additionally, the general tendency of fuels to soot in a diffusion flame is: aromatics $>$ alkynes $>$ alkenes $>$ alkanes [45, 115]. Formation of the first aromatic ring is again the rate limiting step and sooting tendency is tied to the susceptibility to hydrogen abstraction and the fastest route to the first aromatic ring. Examples of these routes include decomposition of C_4 hydrocarbons to C_4H_5 and the subsequent formation of benzene by C_2H_2 addition, the immediate presence of the napthalene radical in 1-methylnaphthalene [45], and the initial presence of the first benzyl ring in aromatic fuels [79].

Finally, it has also been found that multi-component fuel mixtures can have a synergystic effect that causes greater particle formation in a non-premixed flame than would be expected from a linear blending assumption [24, 79, 97]. Specifically, Choi [24] tested a range of iso-octane/toluene and n-heptane/toluene mixtures and noted maximum soot formation based on laser induced incandescence (LII) and laser induced flourescence (LIF) signals between 60% and 80% toluene for the iso-octane/toluene mixtures. Raj et al [97] were able to predict these same results using a mechanism that was validated for both premixed and non-premixed flames. The effect was less significant for n-heptane / toluene mixtures.

2.7.4.3 Effect of Temperature

As in premixed flames, increasing temperature increases both pyrolysis and oxidation. However, this is dependent on the local enrichment level. In the locally rich zones near the liquid fuel surface, higher temperature increases the rate of pyrolysis [45]. As oxygen enters the mixture, oxidation reactions accelerate with temperature, reducing soot formation [65]. Increased temperature will cause quicker liquid vaporization, which enhances mixing and reduces soot formation. Flame temperature reaches a maximum near the stoichiometric mixture region of the flame front [47].

Critical temperatures for soot onset are near 1300 K in atmospheric pressure flames, and soot is formed over a limited range from the onset temperature up to approximately 1700 K [38, 45, 105]. As in premixed flames, soot formation is possible below the critical temperature, but the kinetic rates are too slow for particles to form in the time provided. Maximum soot formation occurs on the fuel side of the flame, coincident with the maximum temperature, and high rates of particle formation occur in regions with high temperature gradients. Measurements of this relationship performed by Santoro et al. [105] for an ethylene-air co-flow diffusion flame are shown in Figure 2.8.

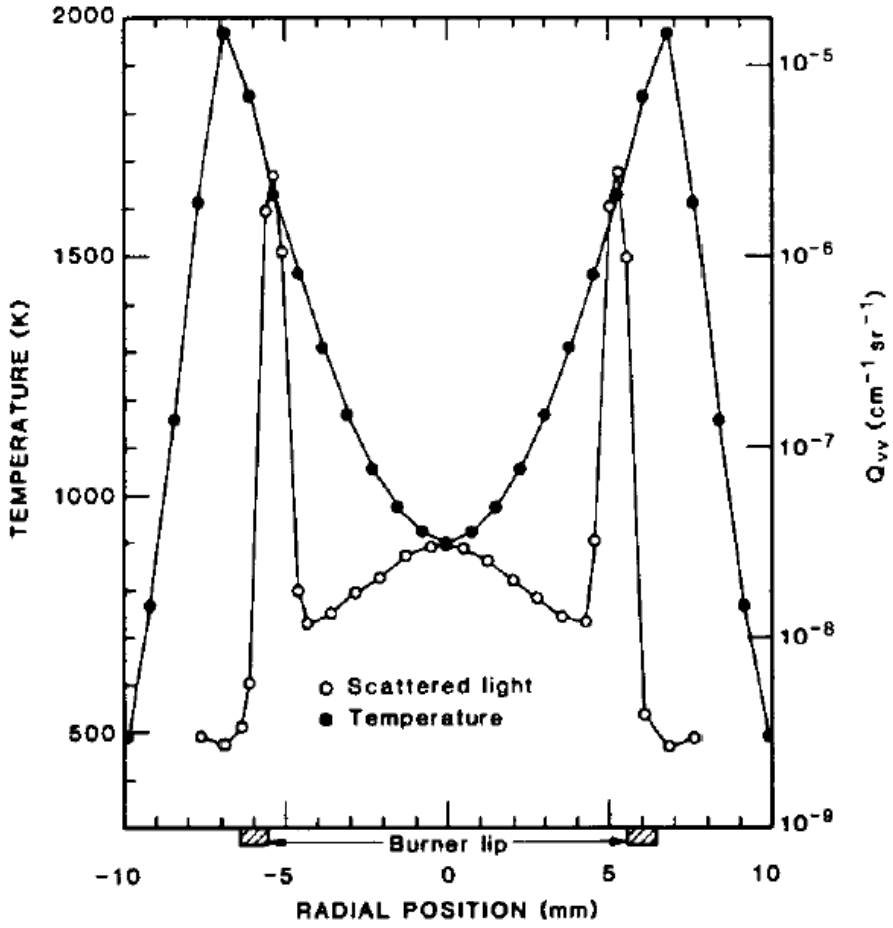

Figure 2.8: Radial measurements of temperature and scattered light from soot particles in an ethylene-air co-flow diffusion flame. The scattered light peaks correspond to regions containing significant amounts of soot [105].

2.7.4.4 Effect of Pressure

Diffusion flames have a dependence on pressure that is similar in magnitude to that for premixed flames [38, 46, 53, 58]. Several studies of diffusion flames have shown a strong direct dependence of soot formation on pressure between 1 and 10 bar [38, 58, 70] ($f_v^\infty \propto P^{1.2-1.7}$), and a weak dependence up to 100 bar that was not fit to the normal $\propto P^n$ relationship [38, 58, 70]. For diffusion flames, global C/O_C is weakly dependent on pressure [38, 53]. Molecular diffusivity decreases with increasing pressure causing the flame diameter to decrease and the radial flame temperature gradients to increase locally increasing the thermal diffusion and pyrolysis rates [38, 47].

Pressure increases enhance reaction rates in a few important ways. Reactions with weak temperature dependence and third-body reactions [69] are affected the most by higher pressures. Radical species such as OH decrease with pressure [70] and oxidation in general decreases as pressure rises [38]. It has been noted [39], that the role of ring-ring reactions and formation of the first aromatic ring via C_6 hydrocarbon species becomes more defined as pressure increases. However, these effects decrease at high pressures. Near 10 bar 40%-50% of carbon was found to be emitted as soot in an axisymetric ethylene-air diffusion flame [38] , at which point the dependence on pressure is forced to decrease due to the reduced carbon fraction available for soot formation. The small dependence of C/O_C on pressure may be due to the fact that most soot inception occurs near the stoichiometric contour where local C/O is mostly independent of global C/O.

2.7.5 Summary of Laminar Premixed and Diffusion Flame Dependencies

Table 2.1: Summary of parameter dependencies of soot formation in laminar premixed and diffusion flames

Parameter	**Premixed Flames**	**Diffusion Flames**
Rate controlling process	Kinetics (reaction rates)	Mixing (heat & mass transfer rates)
Typical lowerbound T_C	1300K-1400K	1300 K
Typical upperbound T_C	1900K-2000K	1700 K
Typical T for $f_{v,max}^{\infty}$	1500K-1700K	1500K-1600K
$f_v^{\infty} \propto P^n$ n value (Valid pressure range [bar])	2 1.3 1 (1-3) (3-5) (>10)	1.2-1.7 <1 (1-10) (>10)
Effect of high global oxygen availability	decreases soot	depends on local T and Φ
Effect of high local oxygen availability	NA	decreases local soot
Effect of high fuel C/H	increases soot	increases soot
Effect of high carbon number	increases soot	increases soot
Effect of high number of C-C bonds	increases soot	increases soot
Effect of molecular structure	aromatics > alkanes > alkenes > alkynes*	aromatics > alkynes > alkenes > alkanes
Effect of unique pyrolysis pathways	Paths to rings may increase soot.*	Paths to rings increase soot.
Critical enrichment threshold	fuel-dependent	fuel-dependent

*Effects of fuel chemical properties in premixed flames is still not fully understood, particularly for large hydrocarbons

Both diffusion and premixed flames have been shown to have dependencies on temperature, pressure, and various aspects of the mixture chemistry. Although the dependencies are similar, the importance of the above parameters is flame

dependent. Table 2.1 summarizes the dependencies of soot formation in both types of flames on the parameters discussed above.

2.8 Surrogate Fuels

Modeling particulate formation requires a suitable surrogate fuel with key properties that cause it to behave similarly to the real fuel in the system of interest [91]. Therefore, identification of the key chemical properties and their relative effects on particulate formation is critical to formulation of a useful surrogate and for accurate particulate modeling.

An acceptable surrogate fuel has a minimal number of components but similar in-cylinder thermodynamic behavior and particulate formation tendencies to the real fuel. Primary Reference Fuel (PRF) mixtures of iso-octane (iC_8H_{18}) and n-heptane (C_7H_{16}) are used to match the octane number of gasoline, and addition of toluene (C_7H_8) allows for matching of the C/H ratio and aromatic content. Blends of iC_8H_{18}, C_7H_{16} and C_7H_8 are referred to here as toluene reference fuels (TRFs). A TRF has several benefits over a 2-component PRF with minimal added complexity. First, fuels with the same C/H ratio can be expected to have similar adiabatic flame temperatures [47], and matching the aromatic content should allow closer approximation of the C-C bond structure. Additionally, toluene is the most abundant aromatic in gasoline [22, 91, 102], and has been shown to suppress the negative temperature coefficient behavior associated with traditional PRFs, which allows closer matching to gasoline auto-ignition behavior [22, 102]. Because the

number of C-C bonds in a real fuel is not readily ascertained, the formulation of a surrogate is more easily defined with respect to C/H ratio and aromatic fraction. The octane number of the TRF can be adjusted independently from the C_7H_8 fraction by changing the ratio of C_7H_{16} to iC_8H_{18} [22]. The well-matched thermodynamic properties that result allow similar Φ, Ψ, C/O, combustion phasing, engine load, and temperature history in-cylinder with similar charge mass and spark timing between the real and surrogate fuels.

Witkowski et al. [122] showed in a laminar co-flow diffusion flame, that by using a TRF mixture (50% iC_8H_{18}, 30% C_7H_8, 20% C_7H_{16}) with an aromatic fraction and C/H approximately equal to that of a research-grade gasoline (EPA TierII EEE), the particulate formation properties of the TRF could be closely matched under the same thermodynamic conditions to those of EEE.

2.9 SI Engine Particulate Trends - Effects of Operating Conditions

The current study investigates PM formation in an SIDI engine at various operating conditions. This is an active area of research, and several other studies have drawn connections between particulate formation and operating parameters such as engine load, mixing time, combustion phasing, equivalence ratio, fuel pressure, and fuel composition for both SIDI engines and PFI SI engines. In general, increased engine temperature has been found to reduce particulate emissions [90]. High loads, aggressive acceleration, and cold start conditions tend to increase emissions [83].

SIDI engines in general produce more PM than PFI SI engines especially during stratified operation [83]. Charge heterogeneity and the combustion of liquid fuel are widely reported as primary particulate sources under all SIDI conditions [31].

These findings are discussed in more depth in the current section along with some explanations of the trends that have been found. However, most explanations in this section fall short of fully describing the fundamental changes that led to particulate trends because there are too many variables changing simultaneously to isolate the effect of just one. In addition, some of these effects will be engine design specific causing differences between studies. One of the most significant confounding factors in studies of SIDI particulate formation is the injection event that can result in incomplete mixing and diffusion flames due to the presence of droplets and fuel films.

2.9.1 Engine Load

The literature generally agrees that increased engine load results in increased particulate number [35, 61, 71]. This increase is primarily attributed to the more massive intake charge and correspondingly higher fuel quantity. Maricq et al. [71] found an exponential dependence of particulate emissions on engine load, as well as a change in the PSD shape. It has been suggested [61, 71] that higher loads result in more efficient combustion, which favors decreased HC concentrations and should reduce adsorption and growth, but higher particulate concentrations and larger particles still result. It is likely that this can be explained by the premixed and diffusion flame pressure dependencies discussed in the preceding sections.

2.9.2 Engine Speed

Increased speed results in less time for fuel evaporation and charge mixing, a shorter time for oxidation and formation of soot, and reduced time for heat transfer, all of which could impact the amount of soot formed. Kayes and Hochgreb [61] suggest that increased engine speed should increase particulate emissions, and Maricq et al. [71] reported similar findings. But the uncertain tradeoff between the effects of chemical timescale versus mixing timescale makes the cause for any changes in particles with speed uncertain.

2.9.3 Combustion Phasing

Spark timing affects both the available mixing time prior to flame arrival and in-cylinder thermodynamic conditions due to changes in combustion phasing, resulting in strong effects on particulate formation in DI engines [54]. Higher particulate formation is associated with advanced ignition [94] and lower particulate formation is associated with retarded ignition [35, 61, 71, 94]. Advancing spark timing reduces the mixing time leading to more local rich pockets [71, 94]. Advancing spark timing also increases the peak combustion temperature and pressure, which has been suggested to result in a competition between increased oxidation and increased inception [54, 59, 61, 71]. A retarded spark will cause a somewhat slower burning flame, decreasing the available reaction time at high temperatures and pressures. Additionally, studies have suggested that, for some engine geometries, mixing is significantly enhanced in the last few degrees before TDC, and a retarded spark timing was shown to result in a more homogeneous mixture at ignition [89].

2.9.4 Mixture Preparation

Mixture preparation is affected by several operating parameters. Engine speed, injection timing, and spark timing determine the time available for mixing in-cylinder. The injection pressure helps to determine fuel atomization and air entrainment, but in a DI engine it may also contribute to wall impingement. Combustion chamber geometry, piston bowl shape, and intake flow motion also affect mixture preparation [21, 92, 107]. Finally, physical fuel properties such as density, and fuel volatility properties, affect vaporization, spray penetration, and mixing.

In-cylinder bulk motion used to enhance mixing is often described in terms of swirl, tumble, and squish flows. Charge motion in-cylinder is generally rotational about some axis that has an angle relative to the cylinder axis. The component of the flow that rotates about an axis parallel to the cylinder axis is called swirl [125]. The component that rotates about an axis perpendicular to the cylinder axis is called tumble [125]. Squish is flow generated near TDC by piston and head geometries designed specifically to squeeze the gasses out of quickly closing spaces and into the main combustion chamber. Numerous combinations of swirl, tumble, and squish have been achieved with different combustion chamber and intake runner designs with varied success in reducing particulate. The primary goal of any of these strategies is to enhance mixing by increasing turbulence. High turbulence intensity and low mean velocity at the spark plug gap contribute to mostly homogeneous combustion, which reduces particulate. In addition, higher turbulence and increased mixing produce a higher turbulent flame speed [31].

The fuel injection strategy also plays a critical role in mixing. Injection timing, pressure, and targeting each contribute to charge mixing. Injection targeting strategies can be classified as spray-guided, wall-guided, or flow-guided (air guided) on the basis of the spray's interaction with the air flow and the cylinder geometry [125]. Spray cone angle has been shown to affect fuel films and soot emissions, where increasing spray cone angles up to about 70 degrees can reduce emissions at a given injection timing [125].

Early injection timings provide more time for mixing than late injection timings, and injections near BDC result in less piston wetting [68]. Multiple studies suggest that the optimal injection timing occurs late in the intake stroke with the piston moving downward, between -280 CAD and BDC [54, 68, 71, 125] due to the tradeoff between mixing time and wall wetting [23, 35, 71, 94]. Shifts in the total concentration are seen in this range, with only small changes in the shape of the distribution, suggesting a change in the inception rate while the relative rates of the other process remain unchanged [54, 59]. Both of these observations are represented in Figure 2.9 from He et al [54].

Strategies using multiple injections have also been shown to provide the benefits of both increased mixing and reduced fuel impingement resulting in reduced particulate [23, 88, 89, 89, 90, 125]. Higher loads and richer mixtures result in decreased sensitivity to injection timing under early injection compared to that under late injection [125]. The impact of injection timing can vary based on the volatility of the fuel used because the optimal EOI changes slightly based on the readiness of the fuel to vaporize [94].

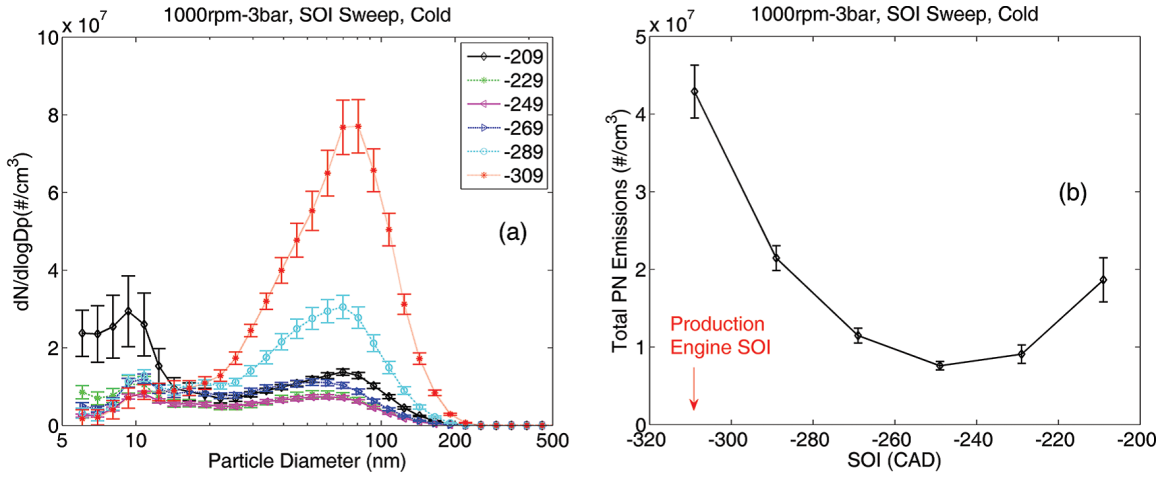

Figure 2.9: PSD changes (a) and the resulting total particulate number concentration (b) with changes in intake-stroke injection timings for 100 rpm at a 3-bar IMEP engine load [54].

High injection pressure leads to better fuel atomization, increased injection velocity, and greater air entrainment. These effects enhance mixing and reduce droplet burning [54, 125]. The high injection pressure required for DI operation results in typical Sauter mean diameter (SMD) of a fuel droplet between 15 μm and 25 μm, whereas the typical SMD from a PFI injector is about 120 μm [125]. However, it is also possible for increased injection pressure to increase wall impingement by increasing spray penetration [93]. Higher injection pressures have been shown to reduce PM emissions when increasing pressure from 24 bar up to 50 bar for a single injection [54, 89]. However, the effect of the injection pressure is dependent on the injection strategy, including the injection timing, injection targeting, and the number of injections. For an early single injection strategy, an injection pressure of 50 bar was found to produce fewer particles than 100 bar and 200 bar injection pressures

because piston impingement dominated the mixing process, whereas when multiple injections were used at the same pressures, the mixing process became dominated by spray atomization and the higher injection pressures produced fewer particles [88].

2.9.5 Mixture Enrichment

Particulate formation generally decreases for lean mixtures and increases for rich mixtures for DI operation [54, 68]. The results of a DI Φ sweep from $\Phi = 0.85$ to $\Phi = 1.15$ showed a consistent trend of increased particulate number and increasing mean particulate size with increased equivalence ratio [101]. An interesting observation regarding the SIDI gasoline Φ sweeps done by Sakai et al. is that the PSD shifts continuously toward larger particle sizes with increasing Φ [101], suggesting a more rapid increase with enrichment in agglomeration mode particles ($\approx$ 50 nm - 250 nm) than inception mode particles ($\approx$ 7 nm - 25 nm). At high enough Φ, the concentration of the smaller particles actually begins to decrease. The decrease in smaller particles at the richest cases suggests that the growth rate has superseded the inception rate, and the larger particles are removing inception mode particles faster than they are being formed. This is shown in Figure 2.10.

2.9.6 Engine Parameters Summary

The various SIDI engine parameters that have been discussed above, their known effects on particulate formation, and the parameters still requiring investigation are summarized in Table 2.2. The table also summarizes the areas where the

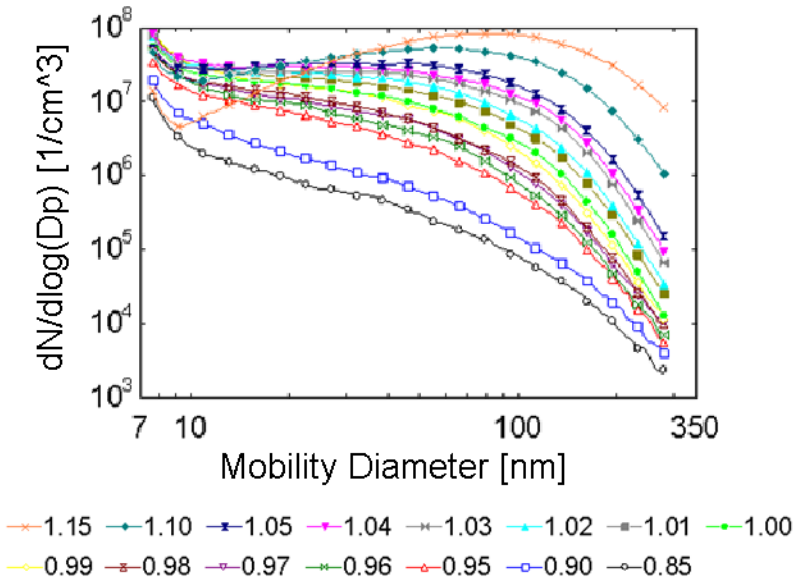

Figure 2.10: PSD plots for EEE (gasoline) Φ sweep. Numbers quoted in the legend are Φ. Modified from [101]

current study contributes. The table is not an exhaustive list, but it summarizes those parameters that are dependent upon the fundamental variables studied here. Note that the effects of injection pressure, the number of injections, and injection targeting were not directly investigated here, but the findings from this study will be useful for interpretting the effects of these parameters better.

Table 2.2: Effects of engine operating parameters on particulate formation in SI engines

Engine parameter	**Parameter change**	**Particulate response**	**Known effects**	**Parameters with poorly understood effects**	**Studied here?**
Load	Increase	Increase	Increased fuel mass	Diffusion $f_v^\infty \propto P^n$ vs. premixed $f_v^\infty \propto P^n$	 Yes
Speed	Increase	Increase	Less mixing time	Residence time for reactions	Yes
Combustion Phasing	Advanced	Increase	Less mixing time	-Main comb. thermodynamics -Postflame thermodynamics -Postflame residence time	Yes Yes Yes
Injection Pressure	Increase	Depends on pressure & injection strategy	-Smaller droplets (less soot) -Better mixing (less soot) -Fuel impingement (more soot)	Mixing / impingement tradeoff	 No
Injection Timing	TDC to -280CAD -280 CAD to ≈BDC ≈BDC to Ignition	High Low High	Fuel impingement vs. charge mixing tradeoff	Tradeoff variables - fuel volatility - turbulence	 Yes No
Number of Injections	2 or 3 (rather than 1)	Decrease	Fuel impingement vs. mixing tradeoff	Mixing / impingement tradeoff	 No
Injection Targeting	Strategies vary	Depends on strategy	Mixture distribution	Mixing / impingement tradeoff	No
Mixture Enrichment	Increase	Increase	Lower oxygen availability	Liquid vs heterogeneity contribution	Yes
Fuel Chemistry	Various parameters	Parameter dependent	Fuel-bound oxygen reduces soot	-C/H, -C-C bonds -# of C atoms -Molecular structure	Yes Yes Yes Yes
Fuel Physical Properties	High volatility	Low	Improved mixing	Physical vs chemical effects tradeoff	Yes

3 EXPERIMENTAL SETUP

In this chapter, the physical lab setup, experimental methods, and data acquisition methods will be discussed. The physical lab setup consists of the air and fuel intake systems, the engine geometry, and the exhaust stream particulate and gaseous emissions sampling equipment. The engine geometry will be discussed first along with the important measurements that define the in-cylinder thermodynamics and the supporting systems that ensure consistent operation. Next, the particulate sampling system will be described. Engine controls and data acquisition systems are discussed next. Finally, the premixed, pre-vaporized (PMPV) method is described.

3.1 Engine

A single-cylinder SIDI engine built on a Ricardo Hydra engine block was used for the current study. The engine features a four-valve over-head camshaft cylinder head with pentroof combustion chamber geometry in conjunction with a flat top piston. The fuel injector, located between the air intake ports, is oriented at a 45° angle to the piston surface and has a 70° spray cone angle. The spark plug is centered at the top of the pentroof between the inlet and exhaust ports. The engine is representative of a modern automotive SIDI engine. For PMPV experiments, the in-cylinder injector was replaced with an identical aluminum blank, and a similar injector was installed upstream of the intake surge tank, $\approx$ 80 cylinder volumes upstream of the intake port. Table 3.1 lists engine specifications of interest. Note timings are referenced to TDC of the compression stroke. Values after TDC are positive and those before TDC are negative.

In-cylinder pressure is measured with a high-speed piezoelectric pressure transducer (Kistler model # 6125B) and is used to determine indicated mean effective pressure (IMEP) and location of 50% cumulative heat release (CA50). These parameters are used to set the operating condition. Pressure data is acquired for 500 cycles and averaged. A Matlab

Table 3.1: Engine geometry specifications. Valve timings are based on a lift of 0.5 mm.

Parameter	Unit	Value
Compression Ratio	[-]	11.97
Bore	[mm]	85.96
Stroke	[mm]	94.6
Intake Valve Lift	[mm]	9.9
Exhaust Valve Lift	[mm]	9.9
Intake Valve Open	[CAD]	350
Intake Valve Close	[CAD]	-140
Exhaust Valve Open	[CAD]	150
Exhaust Valve Close	[CAD]	-355
Displacement	[cm^3]	549.0
Speed	[rpm]	2100

postprocessor was used to calculate cumulative heat release, heat release rate, and mass averaged in-cylinder temperature based on ideal gas assumptions and the method developed by Gatowski et al. [42].

Intake air, oil, and coolant temperatures, as well as fuel, intake, exhaust, and oil pressures were actively controlled to maintain the operating conditions. The values of these pressures and temperatures for different operating modes are given in Table 3.2. The coolant and oil temperatures are representative of the engine block temperature, and are similar to the engine block temperatures of a hot steady-state engine for the baseline case. The exhaust temperature is monitored closely and used to help determine when steady-state operation is achieved. The fuel rail pressure depends on the operational mode (PMPV or SIDI) and the test condition, but in all cases it falls within the range of commonly utilized SIDI fuel rail pressures. Rail pressures from 4.0 MPa [125] up to 20.0 MPa [90] have been studied in the literature, and design rail pressures are typically on the order of 10.0 MPa to 20.0 MPa [125]. The injector used in this study suffers from a rapidly decreasing fuel mass flow rate beyond 11.25 MPa. For these reasons, the baseline SIDI condition utilizes an injection pressure of 11 ± 0.1 MPa. Due to the intake system heating and long mixing time, the injection pressure is a less critical parameter under PMPV operation. The pressure needs to be high enough to ensure sufficient fuel atomization, but can be reduced slightly to

help increase injector lifetime. Therefore, PMPV operating conditions utilized an injection pressure of 10.5 ± 0.25 MPa.

The major components of the fuel system are shown in Figure 3.1. Fuel mass flow rate was measured by a positive displacement piston flow meter (Max Machinery model 213). Fuel pressure wass provided by a piston accumulator pressurized using a high-pressure nitrogen tank. A pressure regulator and pressure gauge at the exit of the nitrogen tank were used to manually set the desired fuel pressure, and when the solenoid valve was activated, the nitrogen pressurized one of the piston-type fuel accumulators. Two identical fuel tanks stored fuel for two identical fuel accumulators. The single difference between the two is that one accumulator was fitted with Viton sealing components while the other was fitted with Buna-N sealing components. The Viton components were more compatible with ethanol and toluene fuels, while the Buna-N components were only acceptable for use with EEE. Only one accumulator and storage tank were used at any given time, and a series of three-way valves allowed the operator to choose which accumulator was pressurized and sending fuel to the injector. The accumulators were filled and drained from the same port, so this port was connected to a three-way valve that either allowed fuel from the storage tank to enter the accumulator when the piston was unpressurized or allowed fuel to flow from the accumulator to the injector when the piston was under pressure. The low-pressure nitrogen system was used to force fuel from the storage tank into the accumulator when filling the accumulator. This system eliminated fuel pressure oscillations that could be encountered when using a fuel pump.

Flow of intake air was controlled by a critical flow orifice rack with an upstream pressure regulator. The operator chose one orifice from a set of five, and set the upstream pressure that provided the desired flow rate. Air mass flow rate was calculated based on the chosen orifice, and the measured upstream pressure and upstream temperature. From the critical flow orifice, the air flow was routed through the heated flow path depicted in Figure 3.4.

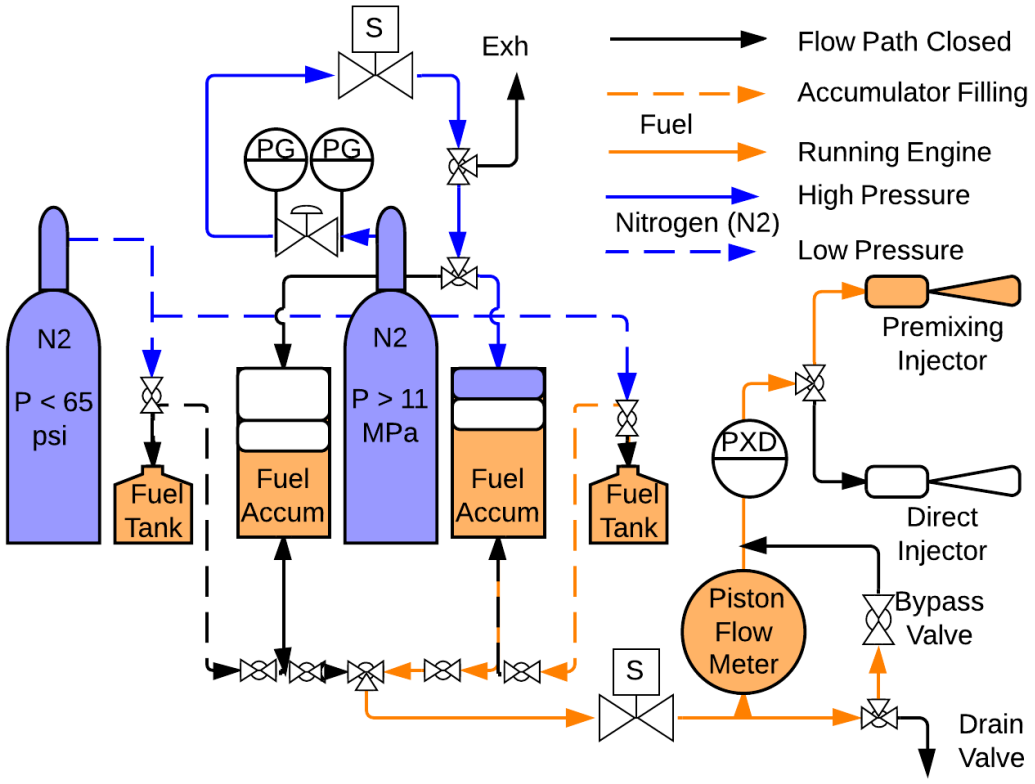

Figure 3.1: Major components of pressurized fuel system. PG = pressure gage, PXD = pressure transducer, S = Solenoid valve. In this depiction, the right fuel accumulator is pressurized, and is sending fuel through the flow meter to the premixing injector.

The oil pressure was maintained at 32 psi ensuring adequate lubrication. The exhaust pressure was maintained just above ambient to ensure adequate exhaust flow to measurement equipment and to ensure that no leakage of ambient air into the exhaust system occurred. The slight back pressure on the engine mimics the exhaust back pressure seen in actual vehicle applications due to the exhaust system. The values of these parameters were kept constant for all SIDI operation conditions. The intake temperature was increased for all PMPV operating conditions to ensure a temperature above the saturation temperature of the mixture, and all PMPV conditions except those listed in Table 3.2 utilized the parameters listed for the PMPV baseline.

Table 3.2: Intake, block, and exhaust temperatures and pressures

Parameter	Unit	SIDI Baseline	PMPV Baseline
Intake Air Temperature	[°C]	45	60
Intake Coolant Temperature	[°C]	90	90
Intake Oil Temperature	[°C]	90	90
Fuel Rail Pressure	[MPa]	11	10.5
Oil Pressure	[psi]	32	32
Exhaust Pressure	[kPa]	102	102
Exhaust Sample Point Temperature	[°C]	>245	>245

3.2 Particulate Sampling System

The primary diagnostic used to determine particle formation tendencies was the engine-out measured particle size distribution (PSD) and particle number (PN) concentration. The scanning mobility particulate sizer (SMPS) and dilution system used to acquire the PSDs are described here. This system has the capability to accurately resolve particle mobility diameters from 10 nm to 289 nm. The concentrations in each bin are measured sequentially and the time required to scan the concentrations of all particle sizes is a function of the number of particle size bins. The bin size resolution of the SMPS system can be changed depending on the precision and speed needed for a particular measurement. The best precision is accomplished with the highest resolution setting, and therefore requires the longest scan duration. Conversely, faster scanning can be accomplished by reducing the bin size resolution at the cost of lower precision.

The SMPS is composed of a long differential mobility analyzer (DMA, TSI model 3081) controlled by an electrostatic classifier (ESC, TSI model 3080) followed by a condensation particulate counter (CPC, TSI model 3010). A diluted exhaust sample of polydisperse aerosol enters the ESC where the randomly charged particles pass through a charge neutralizer, establishing a bipolar equilibrium charge distribution on the particles. The particles receive either a single positive, single negative, or zero charge, which allows the DMA to separate them based on their electrical mobility diameter [10]. The DMA consists of two cylindrical coaxial oppositely-charged stainless steel electrodes, creating an electric field

whose strength is specified by the classifier and which allow the desired particle size to exit the DMA. Particle-free filtered air enters a sheath flow inlet and is fed through a flow-straightening mesh to provide the laminar flow field for the aerosol. As the polydisperse aerosol, which is made up of the diluted exhaust sample with all particle sizes still present, enters the DMA the positively charged particles are attracted radially toward the center electrode with a force proportional to the specified electric field causing a particular mobility diameter to reach a circumferential slit in the center electrode for a given electric field strength. The particles of the selected mobility diameter exit the DMA as a "monodisperse" or single mobility diameter aerosol flow, which is sent to the CPC to be counted [10]. The operation of the classifier and DMA system is depicted in Figure 3.2. The CPC condenses butanol vapor onto the particles, causing them to grow into droplets that can be counted by an optical particle detector.

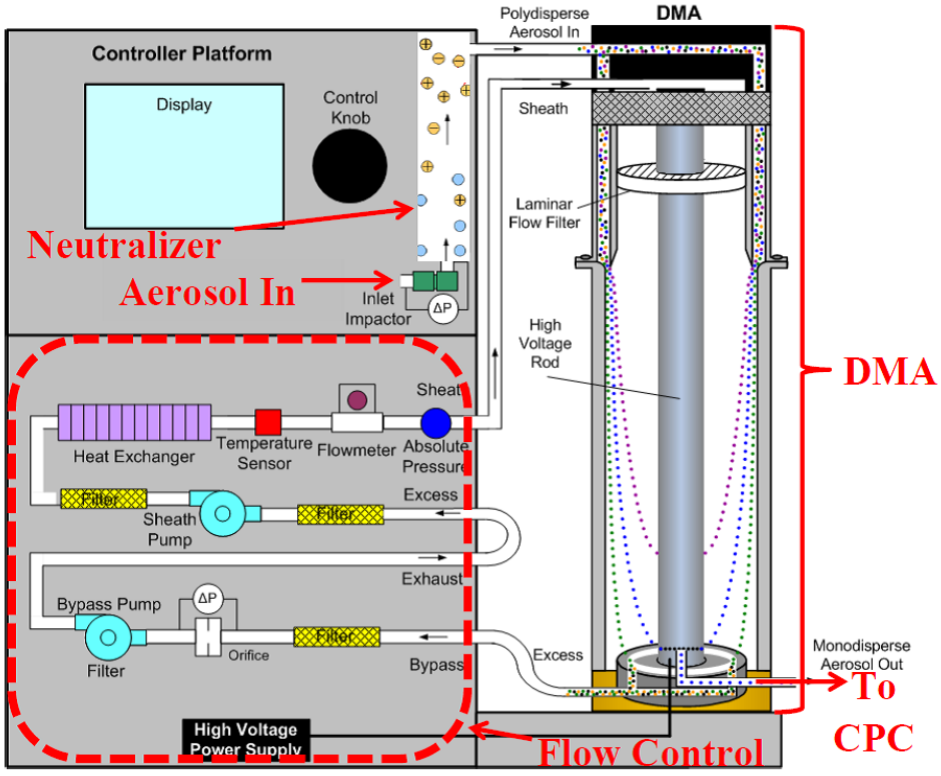

Figure 3.2: Operation of EC and long DMA. Modified from [34].

Because the particle size is sampled by varying the DMA voltage, which is infinitely variable from 0 to 10,000 volts, the number of bins available and therefore the maximum resolution of the SMPS is much higher than other instruments with a fixed number of bins or "channels." The higher available resolution makes the SMPS the instrument of choice for steady-state measurements. However, the sequential bin sampling causes the scan duration to be much higher than instruments that use simultaneous size sampling techniques, causing the SMPS to be less desirable for transient measurements. In this study, the SMPS-generated PSD consists of 102 separate particle size bins or channels. The SMPS system is capable of resolving the particulate data into as many as 167 channels and is the standard method for sub-micrometer particle size measurements for steady state operation [4]. The Aerosol Instrument Manager (AIM) software supplied with the SMPS was used to process the particle data. The AIM reports $dN/dlog(D_p)$ as a function of D_m, which is referred to as the particle size distribution (PSD) throughout.

The AIM software also allows for a set of corrections to be applied to the raw data before outputting the PSD. Loss of particles via diffusion to the walls of the sampling apparatus is of particular concern for particles below 50 nm. The AIM software offers the option of a diffusion correction, which accounts for this issue by identifying critical sections of the sample flow path within the SMPS and utilizing modeling, experimental, and published data as appropriate for each section to approximate the particle penetration in each of these sections and correct for the overall particle diffusion in the reported PSD [5].

The SMPS applies a known charge distribution to the sample before it enters the DMA. A second type of correction is needed because some particles may obtain multiple charges. This increases their mobility and causes them to be counted as smaller particles than they actually are. This issue is most pronounced for particles above 100 nm. The AIM software offers the option of multiple charge correction, which uses an internal algorithm to correct for this issue [5]. All data presented here utilize both the diffusion correction option and the multiple charge correction option.

The dilution of the engine-out exhaust sample is accomplished upstream of the SMPS system by a Dekati microdiluter system. A cross section of this system is shown in Figure 3.3. A probe located upstream of the exhaust surge tank allows a raw exhaust sample to flow into the diluter, where it initially flows through a perforated tube section that allows heated filtered primary dilution air to mix with the sample. The primary dilution air can be heated to a maximum of approximately 450 °C allowing the dilution temperature to matche the typical temperatures. From the perforated tube section, the diluted sample is drawn through an ejector diluter, by a pressure drop caused by the flow of secondary dilution air. The secondary dilution air is filtered but is not heated. The microdiluter receives dilution air from the fine particle sampler (FPS) control unit mounted in the same cart as the SMPS. The control unit connects to a PC and utilizes a graphic user interface that allows the operator to specify the primary dilution air temperatures as well as the dilution ratio, which is controlled by a combination of critical flow orifices inside the unit.

The diluted exhaust at the exit of the microdiluter is sent to both a CO_2 analyzer that is used to determine the dilution ratio and to the SMPS. Additional lines allow excess flow to be directed into the building exhaust system.

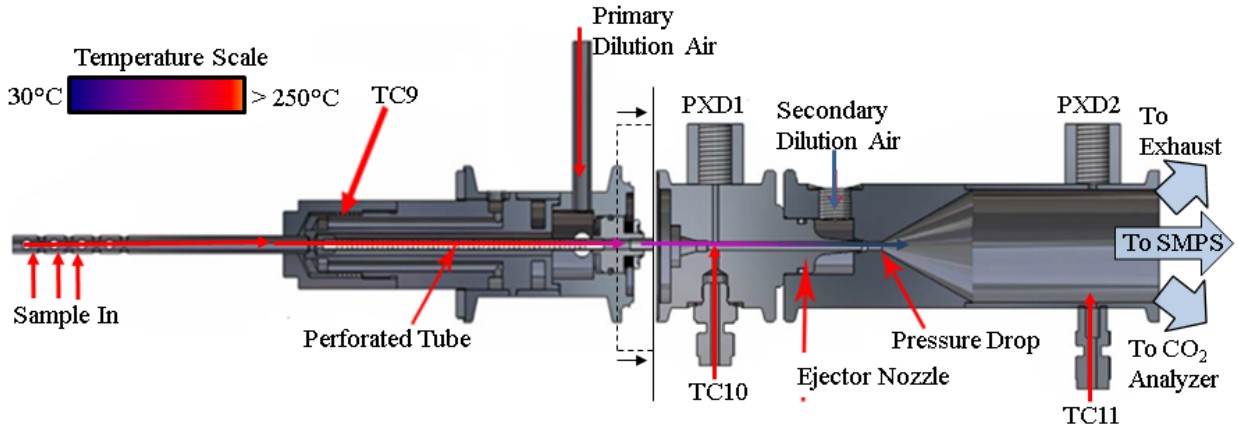

Figure 3.3: Dekati microdiluter cross section. Modified from [6]. Thermocouple (TC) numbers correspond to those in Figure 3.4. PXD = pressure transducer

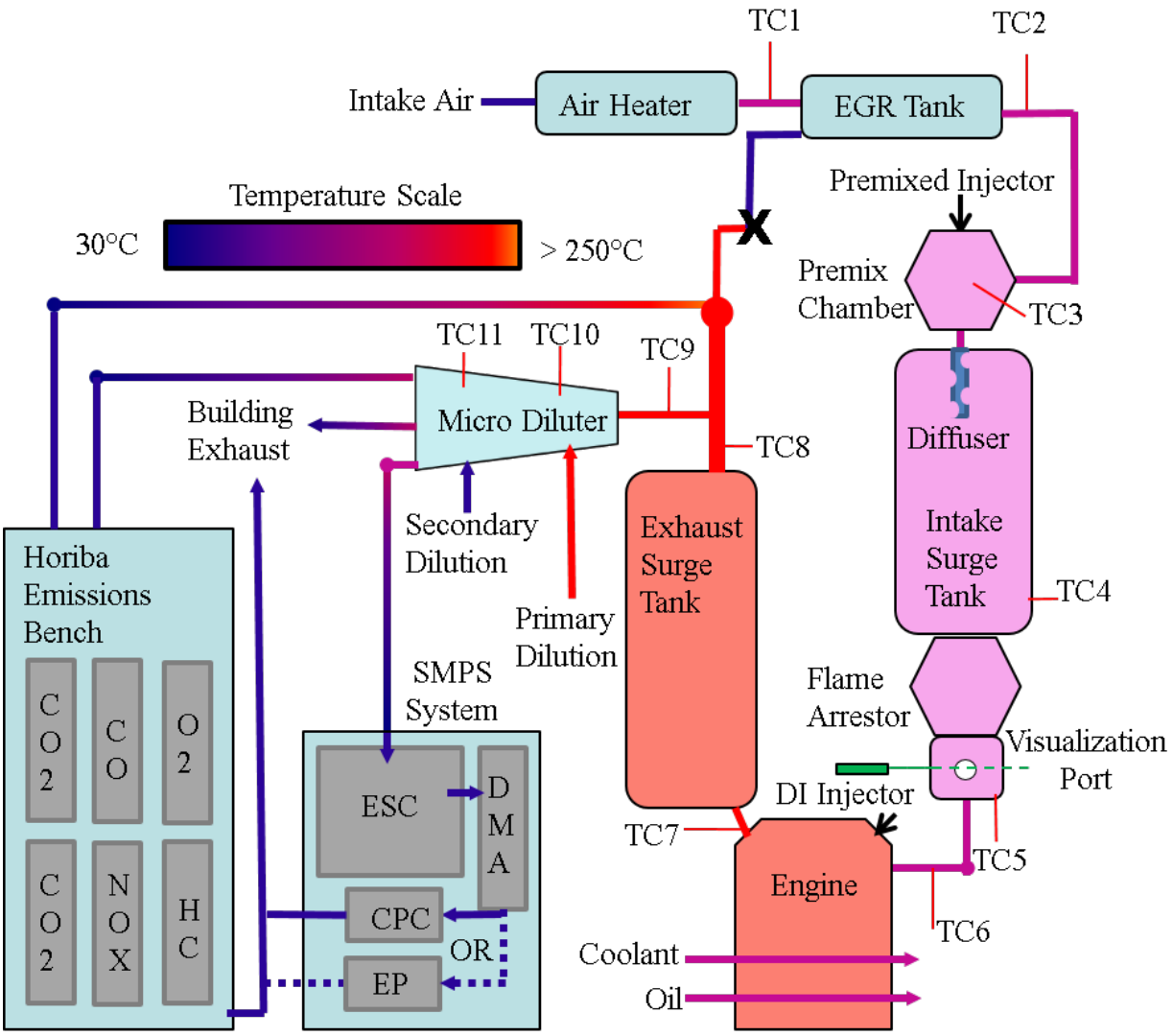

Figure 3.4: Experimental setup showing the engine intake system with the premixing chamber and visualization port, exhaust system, micro-diluter, SMPS, and exhaust emissions bench. The engine is operated with either the DI injector or the premixed injector. ESC = electrostatic classifier, DMA = differential mobility analyzer, CPC = condensation particle counter, EP = electrostatic precipitator, TC = thermocouple.

A Horiba emissions bench is used to sample engine-out undiluted gaseous emissions including CO, CO_2, O_2, NO_X, and HC. The bench includes a Horiba FIAA-23A flame ionization detector (FID) to determine total hydrocarbons, Horiba AIA-23 non-dispersive infrared analyzers to determine both CO and CO_2 concentrations, a Horiba CLA-22A chemiluminescent analyzer to determine NO_X, and a Horiba MPA-21A magnetopneumatic

analyzer to determine O_2. Two CO_2 analyzers are installed. One measures the undiluted CO_2 concentration, and the other measures the CO_2 concentration downstream of the microdiluter. In addition to raw emissions data, these readings are used to determine oxygen- and carbon-based air-fuel ratios. A flow diagram of the full exhaust sampling system is shown in Figure 3.4.

3.3 Controls and Data Acquisition Systems

Several systems were used to control and record critical parameters. The dynamometer controller was used to maintain engine speed. A Mototron ECM-0565-128-0503 engine control module (ECM) was used to control the timing and duration of both the fuel injection and the spark through the Mototune^{TM} user interface. A physical control panel populated with Omega PID controllers was used to control and monitor quantities such as air pressure upstream of the critical flow orifice, oil and coolant temperatures, and intake air heater temperatures. Fuel pressure, exhaust back pressure, and SMPS back pressure were all set manually and monitored on Omega units in the control panel and the SMPS unit display, respectively. Dilution ratio was controlled using the FPS software provided with the microdiluter system.

Determination of thermodynamic data depended on acquisition of high-speed, crank-angle-resolved in-cylinder pressure data. Crank angle readings from A 720 tooth crankshaft encoder paired with the Kistler 6125B pressure readings were acquired by a high-speed National Instruments (NI) data acquisition module, and continuously displayed in Labview. The combination of the physical NI modules and the custom Labview graphical user interface used to record and visualize this data will hereafter be referred to as the Labview Data Acquisition System, or DAQ. The 720 CAD readings per revolution resulted in 1440 pressure data points per cycle, and the DAQ recorded 500 cycles when prompted. The pressure signal was filtered using a SRS Sim965 analog filter before being passed to the

NI module. This module was set to apply a 5.00 kHz low-pass Butterworth filter to the pressure signal before it was sent to the DAQ. The pressure transducer signal was sent first to a Kistler 5010 dual mode charge amplifier with a sensitivity of 20 pC/MU and a scale of 10 MU/volt, then to the filtering module, then to the DAQ. The DAQ was able to average a user-defined number of raw pressure traces, and the average was used to calculate and display crank-angle-resolved temperature, apparent heat release rate (AHRR), cumulative heat release, and dP/d(CAD) as well as cycle-resolved parameters such as gross IMEP, net IMEP, COV of IMEP, peak pressure, location of peak pressure, and CA50 in real time. These outputs were primary metrics for setting most operating conditions. It is critical to note that most of these parameters were recalculated from the raw pressure readings during post-processing using a more detailed Matlab script, so there were slight differences between the DAQ calculations and the final reported data. The postprocessor used slightly more accurate methods for calculation that will be discussed later, while the DAQ calculations were simpler and faster to enable real time data visualization.

The DAQ was used to record most steady state data as well. Fuel and air flow rates were calculated from signals from the intake system instrumentation and used to calculate A/F, temperature, and heat release. Raw emissions data from the Horiba bench were plotted, recorded, and used for calculations of A/F and DR. Finally, most of the Omega units in the physical control panel passed readings into the DAQ, so that data such as intake air temperatures, oil and coolant temperatures, exhaust temperatures and pressures, and manifold absolute pressure (MAP) were all recorded automatically. All of this data was recorded at a frequency of 1 Hz, and will hereafter be referred to as low speed data. The number of readings of each of the low speed parameters was dependent on the sample time. The standard procedure was to record this data as long as the SMPS was recording particulate data, so most conditions have 10-15 minutes of low speed data, resulting in 600-900 readings of each parameter. The postprocessor utilizes the average values of these readings for many of its calculations.

Particulate data was recorded by the SMPS software when prompted. In this work, SMPS was set to scan through the maximum D_m range in 90 seconds with a 30 second scan-down time to return the DMA to a zero voltage, resulting in 120 seconds per scan. The time spent scanning through the D_m range is referred to as the scan-up time, and the time spent returning to a zero voltage is referred to as the scan-down time. Seven scans were used for all data sets, with outlier scans periodically removed in post-processing for various reasons. This combination resulted in approximately 15 minutes of total scan time for each condition recorded. As previously mentioned, multiple charge correction and diffusion correction were applied for all data.

Finally, any data that was not recorded by Labview or the AIM software was manually entered into a standardized data sheet by the operator for each condition. SMPS flow rate and inlet pressure were read from the SMPS display. Torque was read from the dynamometer controller. Engine and dynamometer hours were read from tachometers connected to the dynamometer controller. Ambient pressure was read from a dial pressure gauge. Oil and exhaust pressures were read from Omega units in the control panel. Spark and injection timings were read from the Mototron user interface. The FPS valve combination, sample probe temperature, and temperatures TC9, TC10, and TC11 in Figures 3.4 and 3.3 were read from the FPS user interface. The SMPS inlet line temperature was read from an Omega unit in the particulate cart. Bypass flow out of the SMPS line was read from a rotameter in the particulate cart. Ambient CO_2 was read from the emissions bench before the rest of the recordings by passing ambient air through the bench, and the emissions bench bath temperature was recorded from a display on the Horiba bench front panel. Various other notes on the conditions of the runs were recorded in the data sheets as well. A blank data sheet listing all the parameters recorded can be found in the appendix.

Table 3.3 summarizes the parametric groups, how they were controlled, the method used to record the data, and the frequency at which each group was recorded for each run.

Table 3.3: Recorded raw data and acquisition systems

Parameter	Controlling System	Recording System	Reading Frequency
Cylinder Pressure	NA	LabView	720 readings/rev
Intake Air T/P/$\dot{m}$	Control Panel	LabView	1 Hz
Fuel T/P/$\dot{m}$	MotoTune, Manual Valve	LabView	1 Hz
Oil & Coolant T & P	Control Panel	LabView	1 Hz
Exhaust T & P	Manual Valve	Labview	1 Hz
Gaseous Emissions	NA	Labview	1 Hz
Particulate Emissions	NA	AIM	7 Scans/14 min
Microdiluter Conditions	FPS	Data Sheet	once/condition
Injection & Spark Timing	Mototune	Data Sheet	once/condition
Exhaust Flowrates	Manual Valve	Data Sheet	once/condition

3.4 Premixed, Pre-vaporized (PMPV) Method

The PMPV method has been developed to give repeatable soot measurements when operating over a wide range of Φs for all fuels. The method allows increases in particle number density and changes in the particle size distribution resulting from changes in fuel chemistry, air-fuel mixture composition, and thermodynamic parameters to be measured with high repeatability independently from the confounding effects of the injection event under engine-relevant thermodynamic conditions. The setup for PMPV operation is shown in Figure 3.4. The DI fuel injector is replaced with a geometrically identical aluminum blank and fuel is injected from the premixed injector at 10.5 ± 0.25 MPa into the intake air ≈ 80 cylinder volumes upstream of the intake port, giving the mixture approximately 4.6 s of residence time at 2100 rpm before entering the engine. The mixture is heated uniformly throughout the intake system to 60°C, which is well above the saturation temperature of all the tested Φs, and passes through a cross-drilled cylinder when entering the intake surge tank to enhance mixing. Finally, a visualization port is installed just upstream of the intake port, and vaporization is verified by lack of light scattering of a green laser beam. Fuel droplets and/or condensation could be made to appear or be removed by control of the intake system temperatures. A picture of the visualization port is shown in Figure 3.5

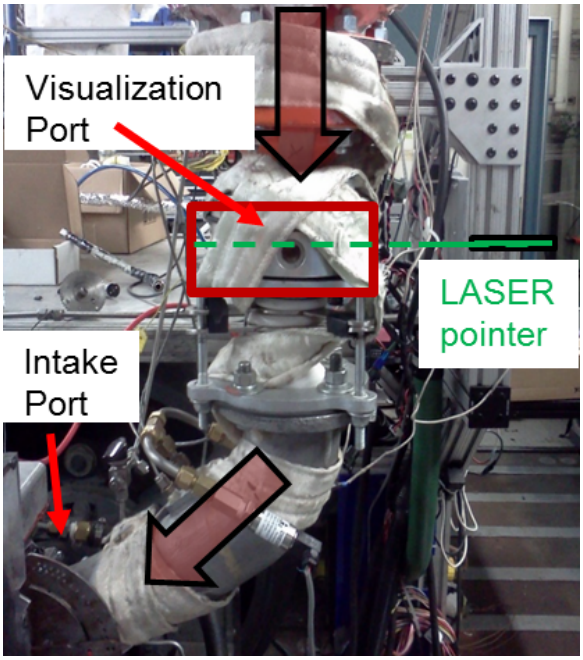

Figure 3.5: Photo of the PMPV visualization port in the intake system. The intake surge tank is located just above the picture edge, and the engine is located just to the left of the picture edge. Wide arrows denote direction of air/fuel mixture flow. The white wrapping around the visualization port and intake runner is heating tape.

Careful exhaust system conditioning and exhaust sample conditioning were needed under PMPV operation because small changes could induce large changes in the number of volatile nucleation mode particles present following dilution. This was particularly true when operating at rich conditions with $\Phi > 1.3$ where unburned hydrocarbon emissions were high and exhaust temperatures were decreasing. For the current study, the goal was to eliminate the volatile nucleation mode particles from the measured PSDs because these particles are difficult to replicate day-to-day. Validation of the PMPV method demonstrated that a dilution ratio greater than 20:1 is required to sufficiently remove volatile particles from the size distribution across the range of fuel-air mixtures studied here. Once the volatile particles are removed, the distribution was shown to be independent of dilution ratio after the appropriate correction was applied, but dilution ratio uncertainty increases quickly above 50:1 due to the resulting low diluted stream CO_2 concentration. Therefore, all scans were taken with a dilution ratio between 20:1 and 40:1.

4 PREMIXED PRE-VAPORIZED (PMPV) METHOD DEVELOPMENT

The literature review discussed the effects of fundamental variables on particle formation and oxidation: temperature, pressure, oxygen availability, fuel chemistry, mixture homogeneity, and flame structure. Much of the fundamental knowledge originates from experiments performed in laboratory flames. To date there have been few studies to isolate the impact of these fundamental variables on particle formation and oxidation for spark-ignition direct-injection engines. The work completed here aims to fill a portion of this knowledge gap by attempting to isolate the fundamental variables (temperature, pressure, residence time, oxygen availability, and fuel chemistry) controlling particle formation in SI engines.

A critical component of this work has been the development of the premixed pre-vaporized (PMPV) system that eliminates the confounding effects caused by the direct-injection event for all SIDI operating conditions, i.e., incomplete mixing and in-cylinder liquid fuel droplets and wall films. Ensuring that a homogeneous mixture of air and fully vaporized fuel enters the combustion chamber provides a high level of certainty that diffusive combustion or other mixing limited non-premixed combustion does not occur. As such, the results can be interpreted in terms of a completely premixed flame enabling comparison of results to laboratory premixed flames. This enables isolation of the effects of fuel chemical properties such as molecular structure and fuel-bound oxygen, isolation of mixture property effects such as differences in Φ and C/O, and isolation of thermodynamic effects such as in-cylinder temperatures, chemical timescales, and pressure free from the confounding effects of the physical mixing process.

The validation of intake conditioning methods for PMPV operation was discussed in the experimental setup, and will not be revisited here. In this section, three of the most important features of PMPV particle size distributions are discussed. First, the motivation and method for removal of volatile particles through exhaust conditioning are discussed

and demonstrated. Second, a non-fuel baseline (NFB) PSD is demonstrated that is specific to this engine, regardless of fuel type. Finally, the NFB is used as a basis from which to demonstrate a critical enrichment threshold that corresponds to the onset of soot formation based on different measures of mixture enrichment (Φ_C, Ψ_C, or C/O_C). Particle formation beyond the critical enrichment threshold is also presented.

4.1 Volatile Particle Removal

Careful exhaust sample conditioning were needed under PMPV operation because small changes in temperature could induce large changes in the number of volatile nucleation mode particles present following dilution. This was particularly true when operating at rich conditions with $\Phi > 1.3$ where unburned hydrocarbon emissions were high and exhaust temperatures were decreasing with increasing Φ. The goal was to eliminate the volatile inception mode particles from the measured PSDs because these particles are difficult to replicate day-to-day. Additionally, the focus for the current work is to measure the onset of formation of carbonaceous soot particles similar to the soot onset measurements performed in premixed laboratory flames. In laboratory flames the temperatures at the soot measurement location are high enough (> 1300 K) that any volatile components are in the non-condensed gas phase. To make measurements analogous to the premixed flame measurements it is necessary to eliminate the volatile mode that can form as the exhaust cools in the exhaust system. Figure 4.1 shows an example of eliminating the volatile particles present at mobility diameters < 50 nm using increased DR. As seen in Figure 4.1, volatile particles are eliminated for DRs $\geqslant 25$. The DRs for all data to be presented were $\geqslant 25$ and the volatile particle mode is not present to any significant level in any of the following results.

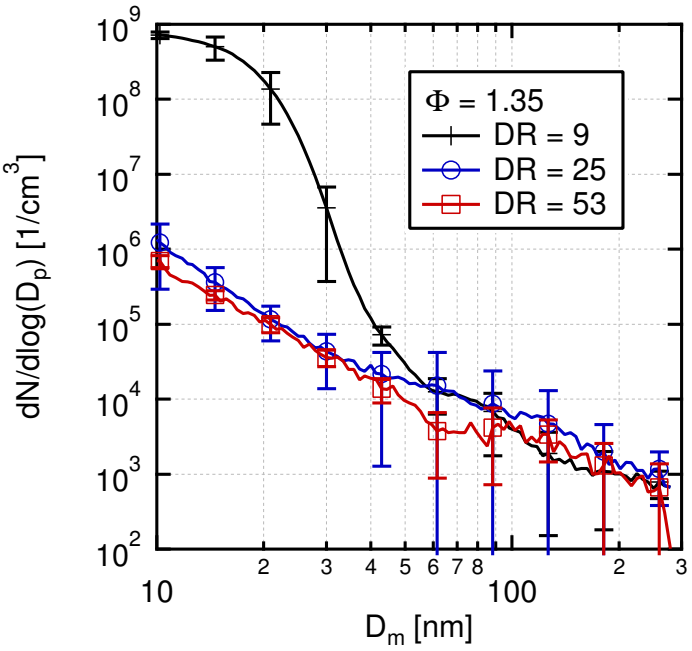

Figure 4.1: PSDs for EEE at $\Phi = 1.35$ with varying DR. Note error bars/markers are only shown for every 10th point.

4.1.1 Effect of Thermodenuder

Although the chosen method for volatile particle removal was to increase the dilution ratio to DR $\geqslant$ 25, another method was available. A thermodenuder (TD) is designed specifically to remove volatile particles from the sample stream using adsorption onto an activated charcoal filter. During validation of the PMPV process, a TD was used to verify that the particles removed by the dilution process were volatile by demonstrating that high DR and use of the TD produced the same effect.

Figure 4.2 compares the effect on volatile particle removal at $\Phi = 0.98$ using the TD to the effect of using dilution ratio (DR). The similar results were obtained for higher Φs as well. The figure shows that volatile particles are present at a low DR with no TD. Using a TD at DR = 9 was equivalent to increasing the dilution ratio to DR = 27 with no TD. Finally, Figure 4.2 shows that once the volatile particles are removed by either method, further

increasing DR has no effect on the DR-corrected PSD. Specifically, note that the DR = 9 PSD with the TD is the same as the DR = 27 PSD with the TD.

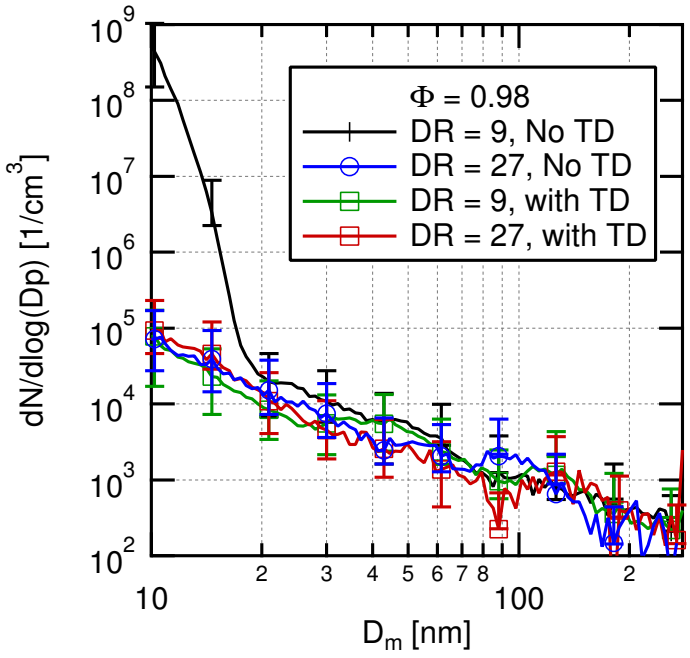

Figure 4.2: Effect of using a thermodenuder (TD) to remove volatile particles at different dilution ratios versus using dilution ratio (DR) alone.

These results lead to the conclusion that high DR and use of the thermodenuder both remove the same type of particles in an equally effective manner. Furthermore, once the volatile particles are removed, neither thermodenuder use nor increased DR has any effect on the final PSD. Therefore, use of one or the other is sufficient.

In all the results reported here, DR $\geqslant$ 25 is the preferred method for removing volatile particles. The thermodenuder requires a transmission correction to be applied to the data, which increases uncertainty. Furthermore, the activated charcoal elements become progressively less effective after only a few hours. The loss of effectiveness is gradual enough that it is not immediately obvious so it could cause the collection of erroneous data near the end of its useful life. The elements can be regenerated by baking them at 250 °C for 12 hours, but the useful life decreases with each regeneration, and they are costly to

replace. For these reasons, the thermodenuder was used only to validate the effectiveness of the DR-controlled volatile particle removal, and was not used again after that.

4.2 Non-Fuel Baseline (NFB) Particle Size Distribution

Unlike a premixed laminar flame, where there may be negligible amounts of particles in the reactant gases and the only source of particles is from flame generated soot, in the engine it was anticipated that some background level of particles would exist in the exhaust. It was also possible that the fuel contributes to particle formation even for $\Phi \leqslant 1$. The validation of the NFB PSD required characterization of the PSD under conditions where contributions from fuel-borne carbon were considered unlikely. This was verified by observing that the PSD was common to all fuels tested (including oxygenates) for enrichment levels below a fuel-specific threshold.

Three fuels were used to establish the non-fuel baseline PSD: a research grade gasoline (EEE) (Haltermann Products, Tier II EEE), methanol (VP racing fuels, $>$ 99.85% purity CH_3OH), and denatured ethanol (E100) (Haltermann Products, 3.27% denaturant). Methanol and ethanol were used due to their low propensity for soot formation. Methanol has been reported to produce negligible soot at Φs as high as 7 [62, 64, 85], so at $\Phi = 0.98$ it is not anticipated to produce any significant amount of soot. It was expected that E100 would also not soot significantly as particle emissions from high-level ethanol blends are generally low even for DI operation [15, 67]. Properties of interest for the fuels are shown in Table 5.4. The range of Φs and C/O ratios tested are also given in Table 5.4. The EEE fuel was tested for C/O ranging from 0.34 to 0.51. Due to low air/fuel ratios needed to reach C/O = 0.51 for the oxygenated fuels, both were tested only up to C/O ratios corresponding to a Φ of 1.5.

The measured PSDs for methanol, E100, and EEE are shown in Figure 4.3. The results for methanol and E100 are shown at Φs of 0.98 and 1.5, whereas the EEE PSD is only shown

Table 4.1: Properties of research fuels

Fuel	Fuel C/O	Fuel H/C	Aromatics vol. [%]	RON/MON	Φs Tested	Mixture C/O tested
EEE[a]	∞	1.840	28	96.6/88.5	0.98 to 1.5	0.335 to 0.514
CH_3OH	1.0	4.0	0.0	108.7/88.6[56]	0.98, 1.35, 1.5	0.245, 0.310, 0.333
E100[b][c]	2.066	2.948	0.92	108.6/89.7 [56]	0.98, 1.35, 1.5	0.283, 0.371, 0.404

[a]All properties for EEE (gasoline) are from the Haltermann Products fuel data sheet unless otherwise noted.
[b]E100 contains 3.27% denaturant and 0.55% water by volume, denaturant assumed to have H/C of EEE.
[c]RON and MON listed for E100 are those for pure ethanol without denaturant.

for $\Phi = 0.98$. The PSDs for all three fuels at the different equivalence ratios agree within the uncertainty of the measurements. The error bars in the figure give the 95% confidence intervals based on the SMPS scans taken for each Φ. The PSDs demonstrate the existence of a baseline PSD for the current operating condition. This PSD is independent of the fuel used and is also independent of Φ for methanol and E100 from 0.98 to at least 1.5. For EEE the distribution is independent of Φ up to at least Φ = 1.25. The insensitivity of the PSD to fuel type and Φ below a critical value indicates that the particles present are not due to conversion of carbon in the fuel to particles. Instead it is concluded that the particulate represented in this PSD is from non-fuel sources. Examples of possible sources include engine oil and engine wear particles [32, 116]. This baseline PSD is referred to throughout the rest of this dissertation as the non-fuel baseline (NFB). The total integrated particle concentration calculated for the NFB used for all graph normalizations is 27,863 $1/cm^3$. It should be noted that the NFB particle concentration is quite low and that particle concentrations in the ambient room air exceed the NFB levels for $D_m > 80$ nm, as shown in Figure 4.4. In contrast, the NFB particle concentrations greatly exceed those in the compressed building air used to supply the intake air for the engine. Figure 4.4 shows that the NFB PSD exceeds the intake air particle concentrations by more than an order of magnitude over the entire D_m range measured.

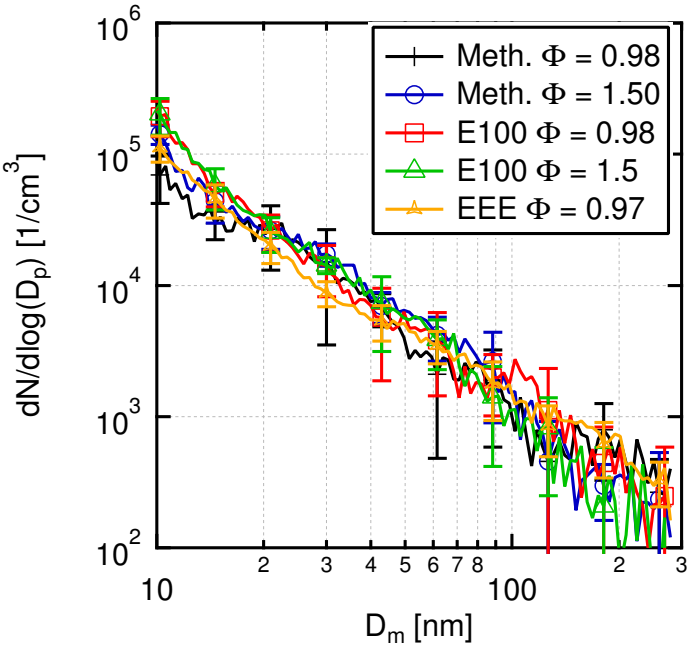

Figure 4.3: Non-fuel baseline (NFB) PSD demonstrated for EEE, methanol, and E100. Methanol and E100 PSDs are shown for $\Phi = 0.98$ and $\Phi = 1.5$, EEE is only shown at $\Phi = 0.98$. Note error bars/markers are only shown for every 10th point.

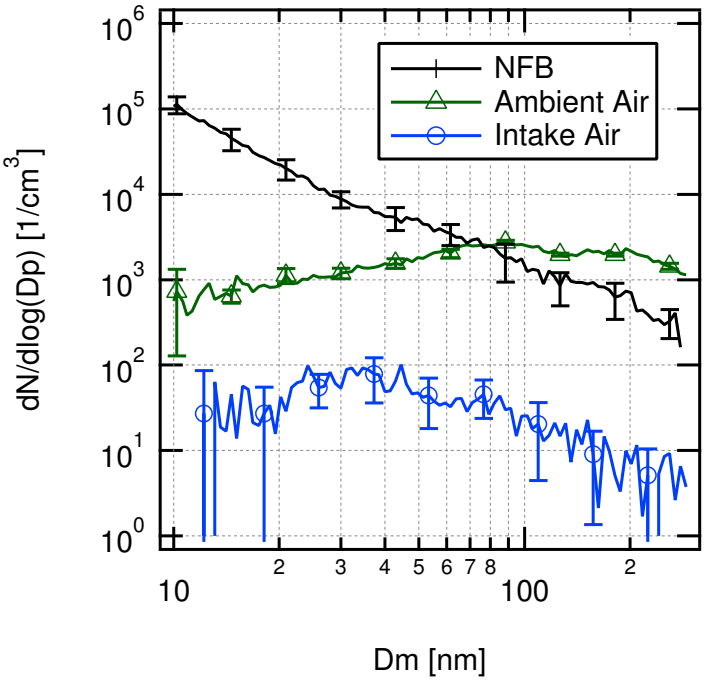

Figure 4.4: Non-fuel baseline (NFB), ambient laboratory air, and intake air PSDs. Note error bars/markers are only shown for every 10th point.

The NFB PSD has several implications. First, it suggests a lower limit for the particle number that can conceivably be obtained for a particular SI engine with perfectly homogeneous charge preparation. Second, the independence of the PSD from fuel chemistry verifies the ability to achieve essentially non-sooting conditions in the engine. Therefore, it provides a baseline PSD that can be used to determine the onset of sooting and the critical level of enrichment (Φ_C and C/O_C).

4.3 Critical Enrichment Level (C/O_C & Φ_C)

With the NFB established, a fuel-dependent critical mixture enrichment level was demonstrated where particles began to form from fuel carbon. Beyond the critical enrichment threshold, particle formation increases rapidly with further enrichment. These two results are demonstrated for EEE at a standard operating condition in this section. Accurate determination of the critical enrichment level required good thermodynamic matching throughout the cycle because the sooting threshold is temperature and pressure dependent [19, 33, 119]. The thermodynamic matching is presented first, and the resulting particle trends are presented second.

4.3.1 Matching of Engine Operating Conditions

Tests were conducted at a standard operating condition characterized by a gross IMEP (gIMEP) of 334 kPa and a CA50 of 8 CAD. The same gIMEP was maintained for all Φs tested. Due to the fixed intake air temperature, the average in-cylinder temperature decreases with increasing Φ above Φ = 1.1 to Φ = 1.2 resulting from decreasing adiabatic flame temperature. This decrease in temperature will impact the results slightly since the critical sooting threshold is temperature dependent [16, 19, 33]. Bönig and Felderman showed that the critical C/O for C_2H_2 - air flat flames decreased linearly as temperature decreased from 1900 K to 1500 K. For pressures of 1 bar and 5 bar, the critical C/O decreased over

this temperature range by approximately 0.08 and 0.12, respectively [16]. If the same temperature dependence existed for EEE, it would correspond to a decrease in Φ_C of between 0.058 and 0.088 for each 100 K decrease in temperature (for pressures between 1 bar and 5 bar). The transition between sooting and non-sooting behavior occurs over a $\Delta\Phi < 0.1$ and the peak temperature changes by less than 100 K with this change in Φ. By the time temperatures in-cylinder reach 1900 K during the expansion stroke, they agree to within 50 K, as shown in Fig. 4.6. The in-cylinder pressure for the same set of Φs is shown in Fig. 4.5. Figure 4.7 compares the late cycle temperatures between the two cases where the x-scale has been adjusted so that time and CAD are at zero where each trace reaches 1900 K. This plotting strategy shows that the time spent in the critical temperature range is very similar between the cases for Φ close to the onset of sooting. Because the gIMEP and combustion phasing are matched the pressure histories match closely.

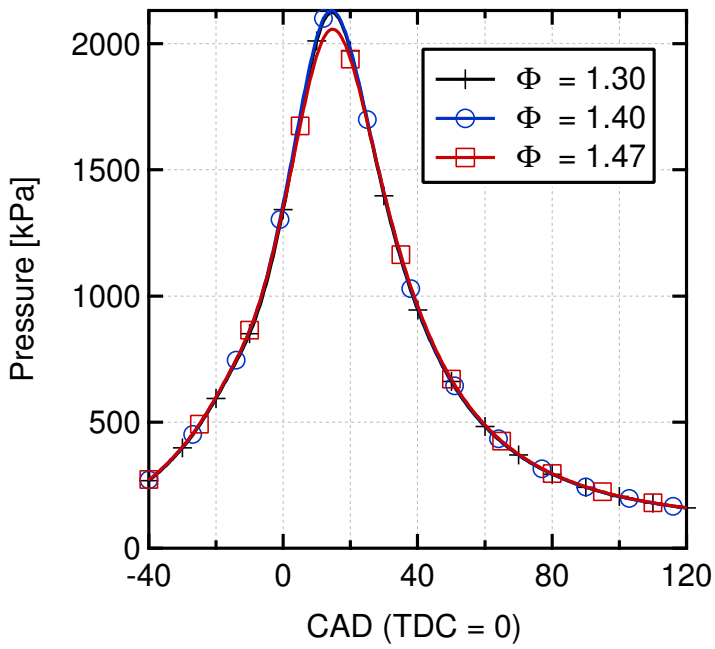

Figure 4.5: Average pressure traces for Φs close to onset of sooting for EEE.

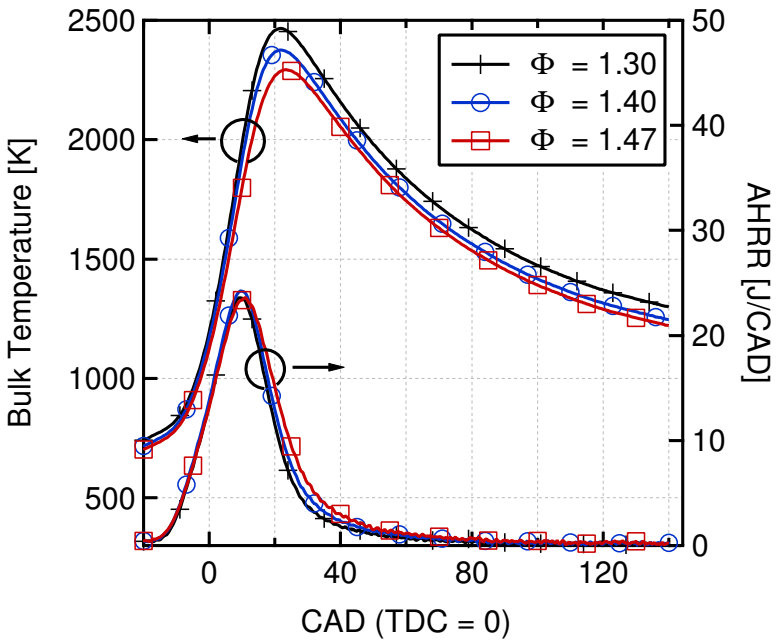

Figure 4.6: Average in-cylinder temperature (left) and apparent heat release rate (right) for Φs close to the onset of sooting for EEE.

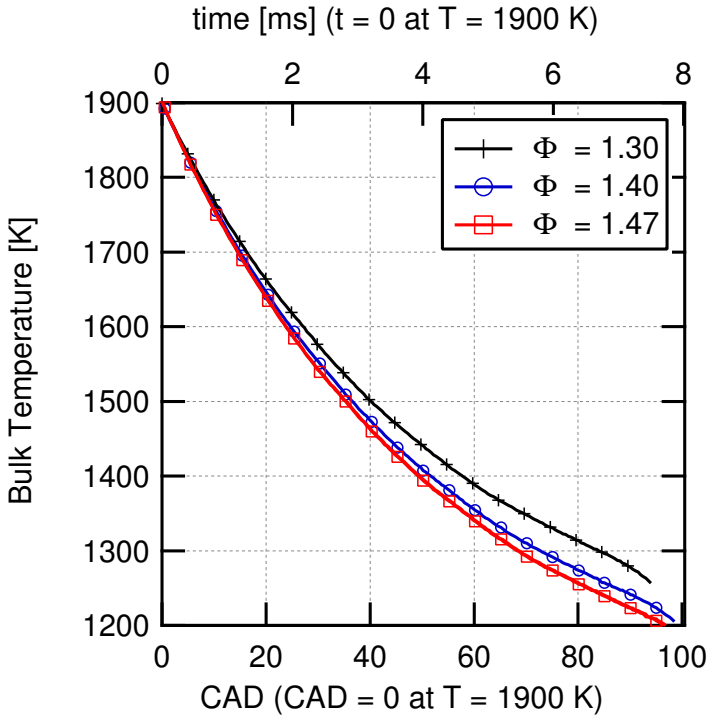

Figure 4.7: Average in-cylinder temperature traces adjusted so that time and CAD start at 1900 K for each trace. The time in the critical temperature range is very similar between cases for Φs close to the onset of sooting for EEE.

4.3.2 Particulate Data

Particulate size distributions were measured for EEE for a range of Φs from 0.98 to 1.49. The evolution of the size distribution with increasing equivalence ratio is depicted in Figure 4.8. For $\Phi < 1.30$ the PSD remains approximately invariant with Φ, i.e., PSDs are within the day-to-day repeatability of the measurements. At Φ = 1.35 a statistically significant increase in particle concentration is seen, most notably for $D_m < 100$ nm. With further increase in Φ the concentrations of small particles continue to increase while a significant increase in larger particles (D_m >100 nm) occurs for $\Phi > 1.40$. The NFB PSD is the dominant particle source for $\Phi \leqslant 1.3$. Beyond this equivalence ratio the inception rate of soot becomes significant as soot onset occurs. As a large number of small particles are formed the rate of coagulation increases and concentrations of larger particles increase at higher equivalence ratios. There is a very large change in the particle concentrations between Φ = 1.3 and Φ = 1.49 with concentrations for D_m from 10 to 100 nm increasing by 3 to 4 orders of magnitude. This is indicative of threshold sooting behavior commonly seen in premixed laboratory flames where soot mass increases rapidly above the critical sooting threshold [72, 75].

Based on the PSD data from Figure 4.8 threshold sooting behavior is apparent. To better determine the actual onset of sooting above the NFB, the measured PSDs were integrated and the total particle number concentrations were determined for each data set. The results were then plotted as the total concentration normalized by the particle concentration for the NFB. The results are shown in Figure 4.9 vs. Φ. The data plotted in this fashion make it readily apparent that the threshold for soot formation occurs between Φ = 1.3 and Φ = 1.4.

A method was developed to quantify the critical equivalence ratio (Φ_C) based on the normalized total particulate number concentration data. The method takes advantage of the fact that the particle number concentration as a function of Φ appears as a nearly straight line on a log-linear plot for a range of Φs above the critical enrichment threshold. This suggests an exponential function for that range of Φ. Therefore, an exponential function with the form shown in Equation 4.1 was fit to the data above the NFB. The beginning

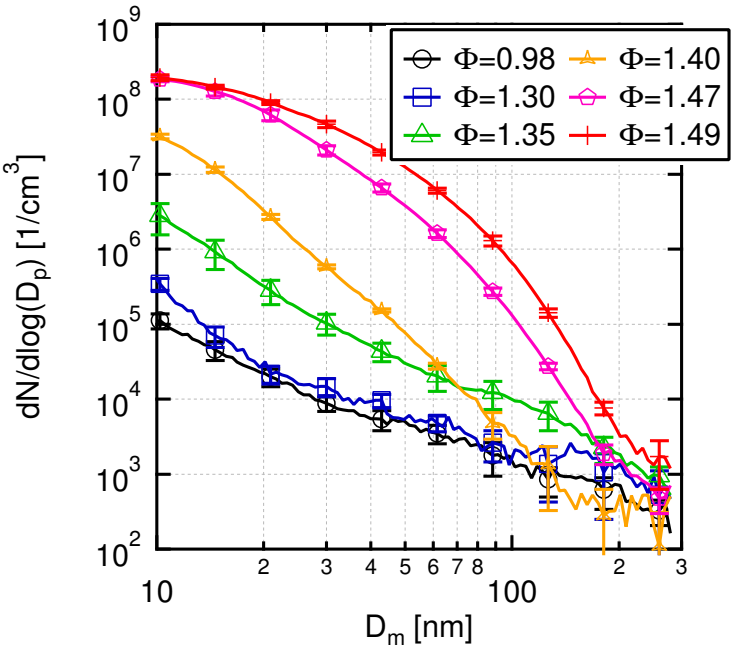

Figure 4.8: PSDs for EEE for $0.98 \leqslant \Phi \leqslant 1.49$ at the standard operating condition. Note error bars/markers are only shown for every 10th point

data point for the curve fit is the first normalized concentration where the exponential dependence appears to become valid. The end data point corresponds to the highest Φ where the exponential dependence appears to remain valid. The dependence becomes weaker at very high Φ, likely due to increases rate of coagulation and surface growth, and the exponential function no longer holds.

$$f(x) = b * exp\,(a * (x - x_0)) \tag{4.1}$$

In Equation 4.1, the coefficient b is the y-intercept and therefore represents the normalized concentration where Φ_C is evaluated. Here, the method was applied twice using two y-intercept values: $b = 1.0$ and $b = 10.0$. This causes x_0 to be calculated where the best fit line intercepts 1X NFB and 10X NFB, respectively. The 1X NFB calculation gives a value slightly closer to the initial onset point whereas the 10X NFB calculation corresponds to a point that has a measurable increase in soot concentration well outside the uncertainty

bands on the total number concentrations. These two results give a range of Φ within which the true Φ_C is likely to fall. The 1X setting gave a result of $\Phi_C = 1.32$ and the 10X setting gave a result of $\Phi_C = 1.36$.

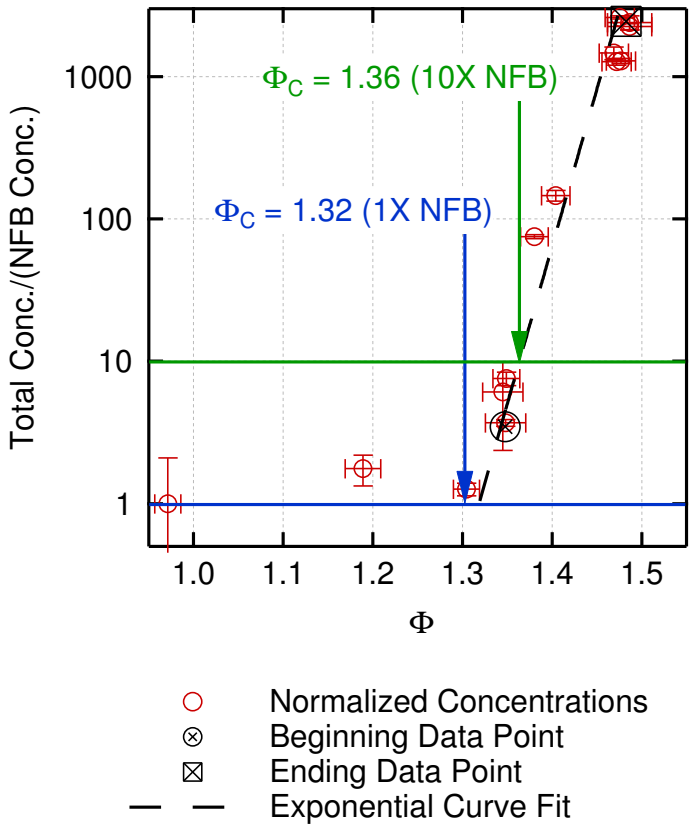

Figure 4.9: Total concentrations of particles normalized by the NFB average total concentration vs. Φ for EEE fuel at the standard operating condition. Exponential function best fit line also shown with 10X NFB and 1X NFB intercepts and the corresponding best fit equations. Error bars are 95% confidence intervals.

Later in this document, Φ_C is calculated twice more for EEE, and the results are slightly different due either to additional data points, or a completely new EEE PMPV Φ sweep data set being used. These slight variations were maintained to provide an idea of how much this calculation method may vary from one data set to the next or with a varying number of data points in the same data set. The results differ by a maximum of ± 0.02 in

Φ. This level of variation is consistent with the uncertainty in determining Φ from the experimental measurements.

The normalized particle concentrations are plotted with the indicated specific particle number emissions as a function of Φ for the EEE standard operating condition in Figure 4.10. Two measures of the indicated specific particle concentrations are shown. The first counts all the particles from D_m = 10 nm to 289 nm. This represents the full range of particle sizes the SMPS is capable of measuring with acceptable accuracy. The second measure counts all the particles from D_m = 23 nm to 289 nm. This is representative of the range of particle sizes that would be counted to determine compliance with the Euro 5 particle number standard. The horizontal dashed lines in Figure 4.10 represent the Euro 5 and Euro 6 particle number limits ($6(10^{12})$ particles/km and $6(10^{11})$ particles/km) converted to particles/kw-hr. This conversion was made assuming a 4000 lb vehicle moving at 50 mph, which has been measured to deliver 85 lbs (378.1 N) of force at the wheels on a chassis dynamometer [113]. Assuming a loss of 20% of the power between the engine and the wheels [27], and an additional mechanical loss of 28% within the engine [44] gives an approximate limit of $3.296(10^{13})$ particles/kW-hr. All other measures of particle number/kw-hr throughout the body of this document will be reported from D_m = 10 nm to 289 nm because using the wider range of sizes allows for better interpretation of potential formation mechanisms. However, the converted Euro 5 limit is still noted on graphs of indicated specific concentrations as a reference. For better comparison of the conditions to the standard, Appendix F includes plots of all the indicated specific number emissions calculated for $D_m > 23$ nm. Note in Figure 4.10 that the trends are nearly the same whether the data is plotted as a normalized concentration or as an indicated specific particle number. Differences between the two methods are due to slight deviations of the measured IMEP and rpm from the nominal IMEP and rpm for each case.

Finally, the total particulate mass concentrations are plotted with the indicated specific particle mass emissions as a function of Φ for the EEE standard operating condition in

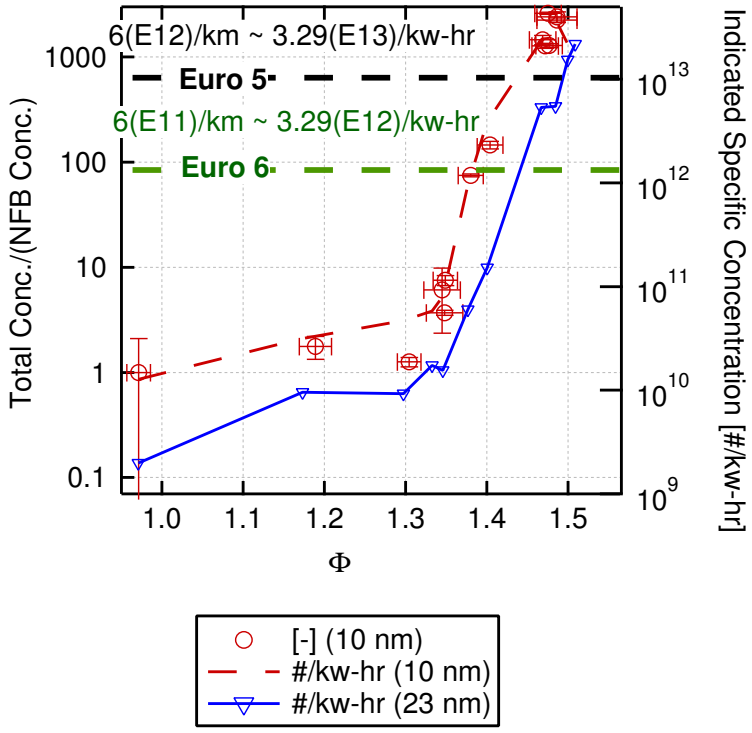

Figure 4.10: Total particulate number concentrations normalized by the NFB average total concentration (left axis) and indicated specific concentrations (right axis) vs. Φ for EEE fuel at the standard operating condition. Indicated specific concentrations are calculated from PSDs including particle sizes from D_m = 10 nm to 289 nm (dashed red line) and D_m = 23 nm to 289 nm (solid blue line). The Euro 5 regulation counts particles with D_m = 23 nm and above. The dashed horizontal black line is the Euro 5 regulation converted to particles/kw-hr, and the dashed horizontal green line is the converted Euro 6 regulation. Error bars are 95% confidence intervals. For better graph clarity, confidence intervals are not given for the indicated specific particulate number counts.

Figure 4.11. The total particulate mass concentration was determined from the integrated number concentrations using a mass vs D_m relationship that was determined from measurements taken by PNNL collaborators during a two week visit during which many of the conditions shown here were repeated to establish this relationship. The mass versus D_m relationship was shown to be nearly independent of fuel and operating condition, so the same relationship was used to calculate the integrated mass for all the conditions in this study. To determine the integrated mass concentration, the number concentration at each D_m was multiplied by the single particle mass associated with that D_m. More information

about the mass vs. D_m relationship used and the methods for determining the relationship are described in Appendix D. The indicated specific particulate mass was calculated from the total mass using the same method used to determine indicated specific particulate number emissions from the total number concentration. The indicated specific particulate mass for each case is indicated on the right axis of Figure 7.9. Based on the assumption of a 4000 lb vehicle driving at 50 mph and assumed losses in the drivetrain and engine, the EPA regulation of 3 mg/mi corresponds to approximately 10 mg/kw-hr. This is noted in all figures where indicated specific mass is reported.

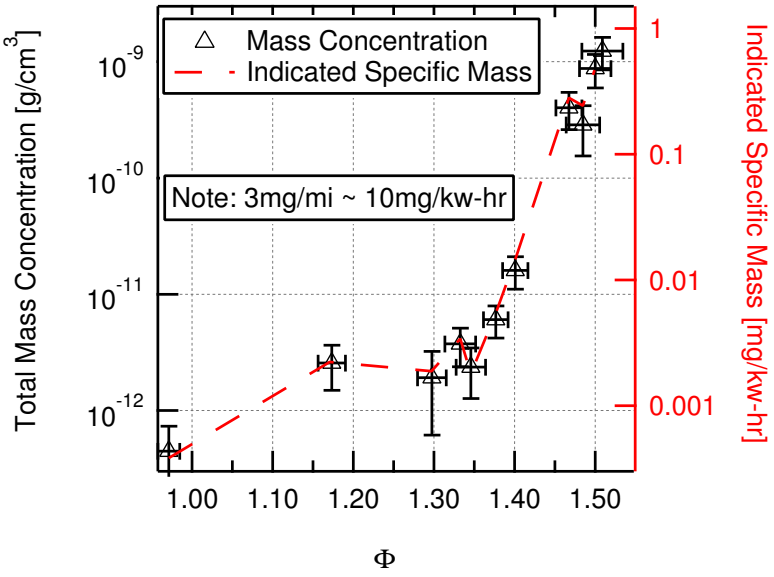

Figure 4.11: Total particulate mass concentration (left axis, black symbols) and indicated specific mass emissions (right axis, dashed red line) vs. Φ for EEE fuel at the standard operating conditions. Error bars are 95% confidence intervals. For better graph clarity, confidence intervals are not given for the indicated specific particulate mass calculations.

4.4 Discussion

These results give useful information for those studying soot formation in SI engines. For the first time, the critical level of enrichment needed to produce soot under typical engine operating conditions with a representative fuel has been identified. However, the

mechanism and formation conditions are still uncertain due to measurements in the engine exhaust without in-cylinder diagnostics. The literature on premixed flame sooting can be used as a guide to help identify the likely scenario.

First, the in-cylinder conditions where soot formation are most likely must be identified. It is well established that soot formation decreases as temperature increases beyond a critical value in premixed flames [19, 33, 45]. Bohm et al. [19] showed the strong dependence of C/O_C on temperature for C_2H_4 and C_6H_6. Both fuels showed a maximum propensity to soot at a temperature of 1500 to 1600 K with C/O_C increasing rapidly for temperature below 1450 K. Bönig et al. [16] also saw that increasing pressure decreased C/O_C and shifted the location of minimum C/O_C to lower temperature. Increasing pressure had a decreasing influence on C/O_C as temperature increased for temperatures > 1700 K in C_2H_4 flames.

The results from premixed laminar flames indicate that soot onset most likely occurs for 1400 K $<$ temperature $<$ 1900 K in the engine. The temperature at the end of combustion (CA95) is $>$ 1900 K for all PMPV conditions tested. This temperature is above the range where soot formation is most favorable, indicating that the onset of soot formation likely occurs near the end of combustion or slightly after main combustion has ended. It is important to note that the air-fuel mixture forced in the crevices during the compression process will begin to flow back into the cylinder once the pressure begins to decrease. This mixture has yet to be reacted and likely enters the cylinder at a location and time where temperature is favorable for soot formation. This an indication why wetting of the piston, liner, and cylinder-head in SIDI engines can lead to significant soot production. Wetting these surfaces places rich pockets at locations with favorable thermodynamic conditions for soot formation. Additionally, little time is available to oxidize this soot because temperature is dropping when it is being formed and oxygen concentrations are low. Based on these considerations, it is expected that during the early part of combustion for the range of equivalence ratios tested soot doesn't form because the combustion gases

are at high temperature $>$ 2200 K for a residence time of a few milliseconds, sufficient to promote oxidation of soot precursor species and inhibit the growth of precursors to soot. The temperature of the products exiting the flame front decreases towards the end of combustion but remains high enough to avoid the formation of soot until right at the end of combustion where quenching of the flame at the walls is occurring.

Based on the information from premixed flames, under PMPV engine operation soot is most likely to form near the walls at the end of combustion up until the time where temperatures drop below 1350 K (the approximate minimum temperature for soot formation [48]) at 120 CAD. The results of a recent SIDI soot modeling study also suggest that soot tends to form near the walls [57]. The residence time from the end of combustion to 120 CAD in the case of EEE at standard operating conditions is $\approx$5.8 ms. The temperature during the exhaust stroke and in the exhaust system are too low for significant oxidation or formation of soot [61] and the amount of soot at EVO can be viewed as being the same as what is measured downstream in the exhaust system. The influence of the elevated pressure on soot formation will be small for temperature $>$ 1900 K. For EEE at standard operating conditions, the pressure at CA95 has dropped to $<$ 800 kPa as seen in Figure 4.5, at the time a temperature of 1700 K is reached the pressure has dropped below 500 kPa.

The elevated pressures during the time with favorable temperatures for soot formation will slightly reduce the Φ_C compared to atmospheric pressure flames. The influence of pressure may be more important for increasing Φ above Φ_C. The point during the combustion where soot starts forming will move earlier with increased Φ. Pressure has been shown to increase soot volume fraction as P^2 for pressure $<$ 10 bar [16]. Therefore, earlier onset of soot will allow for start of formation at higher pressures and potential for higher soot formation rates. Soot formation should also move closer to the center of the cylinder as Φ is increased above Φ_C.

4.5 Summary

The PMPV method has been demonstrated here to produce a completely premixed flame environment in-cylinder that enables comparison of particle formation results to laboratory premixed flame environments. Intake and exhaust conditioning strategies have been discussed that are critical to the repeatability of the data from this method. A non-fuel baseline particle level has been demonstrated that provides a baseline PSD that can be used to determine the onset of sooting and the critical level of enrichment for in-cylinder flames. The method was used here to demonstrate a critical enrichment threshold for a certification gasoline at one set of engine operating conditions. The method will be used in the following chapters to demonstrate the dependence of premixed flame soot formation on fuel type and thermodynamic parameters in-cylinder.

5 PMPV STUDY OF FUEL CHEMISTRY EFFECTS

Having established the usefulness of the PMPV method for identifying soot onset in SI engines, the technique was applied to study the influence of fuel chemistry on soot onset and sooting beyond the critical equivalence ratio. Specifically, the aromatic fraction was varied by changing the volumetric toluene fraction of 3-component toluene reference fuels (TRFs) composed of iso-octane, n-heptane, and toluene. Toluene was the aromatic of choice because it is the most abundant aromatic in the EEE, as discussed below.

Five TRF mixtures were compared to EEE for their soot formation tendencies under PMPV operation. This group included a TRF with a C/H and aromatic fraction that was matched to EEE. The research octane number was maintained among fuels, and a full range of aromatic fractions was tested. Engine thermodynamic conditions were maintained as closely as possible between fuels.

Two important distinctions must be made in order to interpret the effects of fuel chemistry. First, the metrics for quantifying the air-fuel mixture enrichment should be compared. These include Φ, Ψ, and C/O. Second, the metrics for defining soot formation trends must be compared. These include the threshold for soot formation, the particulate number, and the particulate mass.

Finally, relationships between the trends and important fuel chemistry parameters will be discussed. The important chemical parameters include the number of carbon atoms, the C/H ratio, the number of C-C bonds, and the fuel structure. Because the fuels studied here are multiple component mixtures, the potential for synergistic effects will also be discussed.

5.1 Fuels and Operating Conditions

The reference fuel used for the study was an EPA tier II certification grade gasoline (Haltermann Products Tier II EEE). A gas-chromatography mass-spectrometry (GCMS) analysis

was carried out by Southwest Research on one batch of EEE according to ASTM D5769 to determine the composition of the aromatics in the fuel. From this analysis it was determined that the EEE contained 33% by volume total aromatics. More specifically, the analysis showed that it contained 21% by volume toluene, with the next most significant component being 1,2,4-trimethylbenzene at 3.7% by volume. All other aromatic components were in concentrations less than 2% by volume (see Appendix 9.2 for the full results of the analysis). The volume and weight percentages of the major aromatics in the EEE determined from the GCMS analysis can be found in Table 5.1. In comparison, the manufacturer's data sheet specified 28% by volume aromatics fraction based on the ASTM D1319 method.

Table 5.1: Aromatics in EEE certification gasoline

Component	Volume%	Weight%
Total Aromatics	33.08	39.73
Toluene	20.99	25.09
1,2,4-Trimethylbenzene	3.7	4.46
1-Methyl,3-Ethylbenzene	1.83	2.18
1-Methyl,4-Ethylbenzene	1.07	1.27
1,3,5-Trimethylbenzene	1.04	1.24
1-Methyl,2-Ethylbenzene	0.78	0.95
1,2,3-Trimethylbenzene	0.67	0.82
n-Propylbenzene	0.67	0.8
Oxylene	0.42	0.51
Benzene	0.28	0.34
1,4-Diethylbenzene	0.26	0.30
2-Methylnapthalene	0.24	0.34
l-propylbenzene	0.19	0.22
Indane	0.17	0.23
1-Methylnapthalene	0.13	0.18
Other	$\leqslant$ 0.1 each	$\leqslant$ 0.1 each

Based on the reported aromatics a toluene reference fuel was formulated to serve as a gasoline surrogate. The chosen TRF contained 30% aromatics (toluene) by volume with the fractions of iso-octane and n-heptane chosen to match the C/H ratio of EEE. This surrogate has the same composition as that tested by Witkowski et al. [122] in a laminar co-flow diffusion flame. Three additional TRF blends were also tested to develop a broader understanding of the role of aromatic fraction in soot formation under premixed conditions.

The TRF75 mixture is a two-component blend of n-heptane and toluene. Therefore, this set of TRF mixtures spans the full range of toluene volume fractions that are possible at the chosen octane rating. In addition, unblended iso-octane (iC_8H_{18}) was studied due to it's common use in gasoline surrogates. The exact formulations of the TRF blends are given in Table 5.2 on both a volume and molar blending basis.

Table 5.2: TRF blend fractions

	iC_8H_{18}		C_7H_{16}		C_7H_8	
Blend Name	Volume Fraction	Mole Fraction	Volume Fraction	Mole Fraction	Volume Fraction	Mole Fraction
PRF86	0.86	0.85	0.14	0.15	0.00	0.00
TRF15	0.67	0.61	0.18	0.18	0.15	0.21
TRF30	0.50	0.42	0.20	0.19	0.30	0.39
TRF45	0.33	0.26	0.22	0.19	0.45	0.55
TRF75	0.00	0.00	0.25	0.19	0.75	0.81

Fuels were tested under PMPV SI operation at a standard operating condition characterized by a gross IMEP (gIMEP) of 334 kPa, and a CA50 of +8 CAD. This operating condition is the same as that used for the PMPV validation in Chapter 4. Each fuel was tested over a range of air-fuel ratios, specified to result in similar ranges of C/O, Φ and the effective equivalence ratio (Ψ). Due to differences in fuel chemistry and sooting tendencies, the mixture ranges are slightly different for some of the fuels. For example, iC_8H_{18} and PRF86 were both tested at higher Φs than the rest of the fuels due to their higher critical enrichment thresholds. The seven fuels and the enrichment ranges studied for each on a Φ, C/O and Ψ basis are shown in Table 5.3. The table also lists the A/F, C/O, and Ψ at $\Phi = 1$. Note that as aromatic fraction increases, A/F and Ψ at $\Phi = 1$ decrease, and C/O at $\Phi = 1$ increases.

In addition to aromatic fraction, several other physical and chemical fuel properties are of interest. Aromatic fraction, C/H, and the number of C-C bonds are chemical fuel properties that have been shown to affect sooting tendencies [45, 79, 97, 112]. The octane rating was kept within the same range here to ensure similar ignition characteristics and to limit the number of simultaneous variables. The seven fuels and their properties of interest

Table 5.3: Fuel enrichment level comparisons and ranges tested

Fuel	Φ Range Tested	C/O Range Tested	Ψ Range Tested	A/F at $\Phi = 1$	C/O at $\Phi = 1$	Ψ at $\Phi = 1$
EEE	0.97 - 1.51	0.34 - 0.51	0.64 - 1.00	14.57	0.342	0.658
TRF75	0.95 - 1.33	0.35 - 0.50	0.59 - 0.83	13.85	0.373	0.627
TRF45	0.95 - 1.50	0.34 - 0.53	0.63 - 0.97	14.32	0.352	0.648
TRF30	0.98 - 1.52	0.34 - 0.52	0.65 - 1.00	14.57	0.342	0.658
TRF15	1.01 - 1.54	0.34 - 0.51	0.68 - 1.03	14.84	0.331	0.669
PRF86	1.50 - 1.65	0.48 - 0.53	1.02 - 1.12	15.13	0.320	0.680
iC_8H_{18}	0.98 - 1.61	0.31 - 0.52	0.67 - 1.09	15.13	0.320	0.680

are shown in Table 5.4. Note in Table 5.4 that for the five TRF mixtures, the number of C-C bonds and C/H ratio both increase approximately linearly with aromatic fraction.

Table 5.4: Properties of research fuels

Fuel	Fuel C/H	Aromatics [Vol %]	C-C Bond #	Carbon Number	RON/MON	ρ [g/cc]
EEE[a]	0.583	28	Unknown	Unknown	96.6/88.5	0.742
TRF75[b,c]	0.732	75	9.22	7.00	94/85	0.821
TRF45[b,c]	0.597	45	8.44	7.26	89/82	0.772
TRF30[b,c]	0.540	30	7.98	7.42	88/83	0.748
TRF15[b,c]	0.489	15	7.45	7.61	86/83	0.724
PRF86[b,c]	0.443	0	6.85	7.85	86/86	0.699
iC_8H_{18}[d]	0.444	0	7.00	8.00	100/100	0.702

[a] All properties for EEE (gasoline) are from the Haltermann Products fuel data sheet unless otherwise noted. Aromatics volume % listed was determined by ASTM D1319 method. ASTM 5679 method gave aromatics Vol% =33.
[b] TRF properties are based on a mixture of pure components
[c] TRF RON and MON calculated using modified linear-by-volume model from [82].
[d] iC_8H_{18} properties based on pure iso-octane.

As shown in Figure 5.1, the adiabatic flame temperature will change depending on fuel and mixture enrichment, which leads to differences in cylinder temperature histories. In order to properly compare the effect of fuel structure, this difference must be minimized because the critical sooting threshold is temperature dependent [33, 45, 119]. This control is achieved with slight differences in fuel mass and spark timing required to maintain gIMEP and CA50, respectively between fuels. The result of these controls is that the pressure and apparent heat release rate (AHRR) traces are well matched between fuels for all comparable

mixtures. This also results in close temperature history matching between fuels, although the peak temperature does increase with aromatic fraction, as would be expected from the comparison of adiabatic flame temperatures. For mixtures with substantially different C/H ratio the adiabatic flame temperatures are different enough that substantial differences in in-cylinder temperatures can exist.

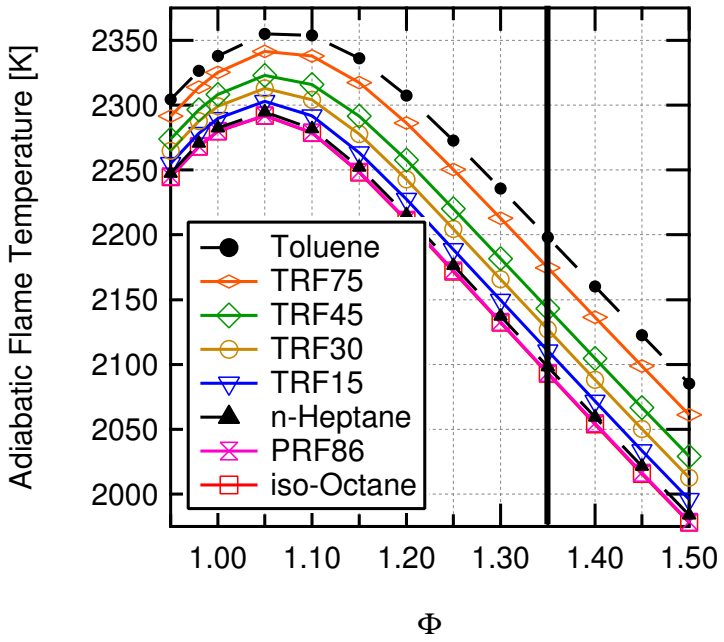

Figure 5.1: Adiabatic flame temperature as a function of Φ for the fuel blends tested here. Data for the three pure components is also shown for comparison. Data was calculated with Cantera using the 103 species mechanism developed by Ra [95].

The average bulk gas temperatures and AHRR for the $\Phi \approx 1.35$ case for all the fuels are shown in Figure 5.2. This case is very near the critical sooting threshold for EEE and is therefore the case where thermodynamic matching is most important. PRF86 is not included in this plot because it was not tested below $\Phi = 1.5$. The difference in peak temperatures between the two most extreme cases are less than 300 K, and the maximum temperature difference after CA95 was less than 150 K. Excluding the TRF75 trace, the difference in temperatures between fuels throughout the cycle is less than 100 K. The TRF75 has the highest peak temperature because it has the highest adiabatic flame temperature

and the shortest combustion duration. The error bars on these plots are a 95% confidence interval with the t-statistic based on the number of runs, but they are smaller than the symbols and are therefore difficult to see.

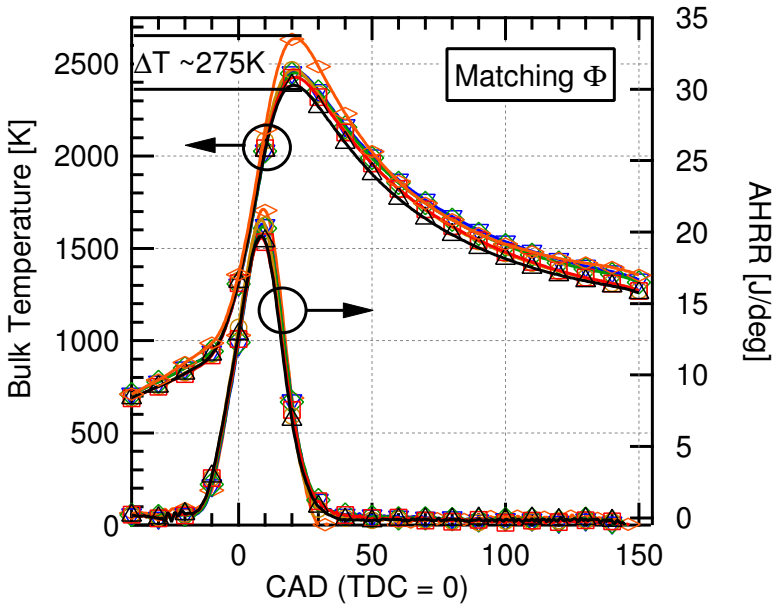

Fuel	Φ	Ψ	C/O
$TRF75_2$	1.33	0.83	0.50
$TRF45_2$	1.35	0.87	0.48
EEE_4	1.35	0.89	0.46
$TRF30_3$	1.34	0.88	0.46
$TRF15_2$	1.34	0.90	0.44
$iC_8H_{18\ 1}$	1.35	0.92	0.43

Figure 5.2: Calculated AHRR and temperature traces at $\Phi \approx 1.35$ for all fuels. Subscripts denote the number of separate runs used to calculate the average and confidence bounds.

The averaged temperature traces were used to determine the average temperature for each trace during the time that it spends between 1900 K and 1400 K late in the cycle. As will be discussed in later chapters, the influence of temperature during the main combustion process on particulate is small and temperatures late during the expansion stroke in the range of 1400 to 1900 K are what drive PM formation. The calculation of the average temperature during this time, and the time spent between 1900 K and 1400 K are plotted in

Figure 5.3. There is about 30 K difference in the average late cycle temperatures between fuels, and about 2 ms of difference between the most extreme cases. However, there is not a clear trend with aromatic fraction. Therefore differences in time and temperature in the critical temperature range are unlikely to be responsible for particulate trends that correlate with aromatic fraction.

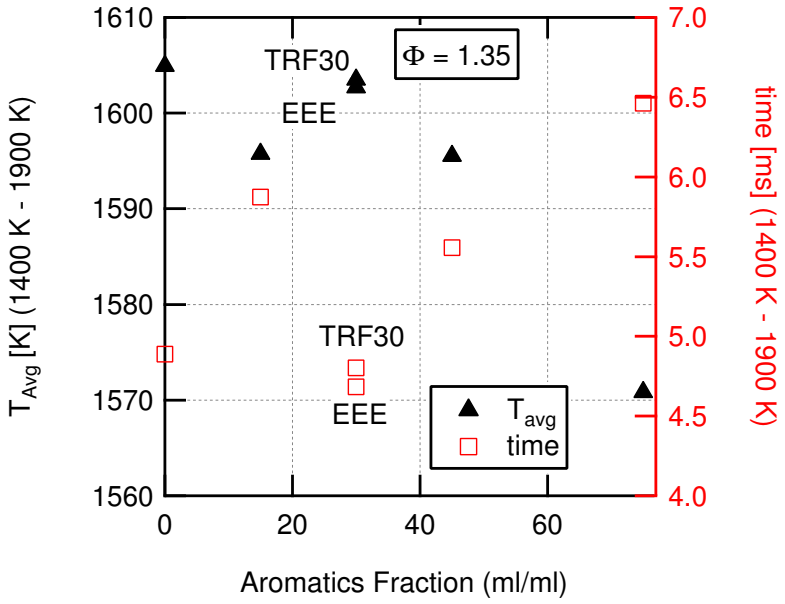

Figure 5.3: Average temperature (left axis) and time spent (right axis) between 1900 K and 1400 K late in the cycle. For cases where temperatures did not reach 1400 K before EVO, the times and average temperatures recorded are those between 1900 K and EVO. The Aromatic Fraction = 0 data point is iC_8H_{18}. PRF86 was not studied at $\Phi = 1.35$

The number of runs used to calculate the averages and confidence bounds for the data throughout this work varies among fuels and mixture settings. Every fuel and mixture was run at least two times, but most cases were run three or more times. Data reported here may include fewer runs than were completed because variations in experimental conditions for some cases were determined to be outside the range specified for a given variable. For this reason, all plots include a subscript for each data set specifying the number of measurement sets used to calculate the average and confidence bounds.

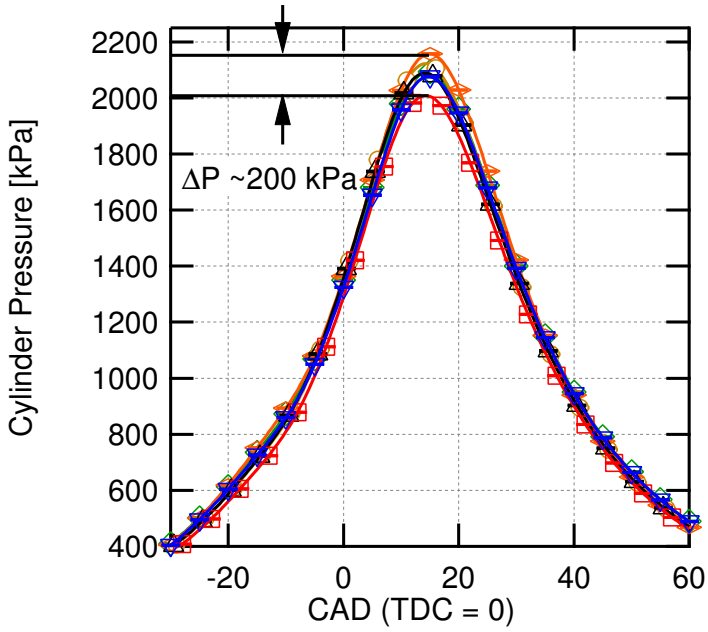

Fuel	Φ	Ψ	C/O
$TRF75_2$	1.33	0.83	0.50
$TRF45_2$	1.35	0.87	0.48
EEE_4	1.35	0.89	0.46
$TRF30_3$	1.34	0.88	0.46
$TRF15_2$	1.34	0.90	0.44
$iC_8H_{18\ 1}$	1.35	0.92	0.43

Figure 5.4: Measured pressure traces at $\Phi \approx 1.35$ for all fuels. Subscripts denote the number of separate runs used to calculate the average and confidence bounds.

5.2 PSDs as a Function of Fuel and Φ

Due to the common use of Φ as the enrichment metric for most engine studies, the soot formation as a function of fuel aromatic fraction will first be compared over a range of Φ.

5.2.1 Comparison of All Fuels

The particle size distributions for EEE, PRF86, TRF15, TRF30, TRF45, and TRF75 are compared at a $\Phi = 1.35$ in Figure 5.5 and $\Phi = 1.50$ in Figure 5.6. Note that PRF86 is missing in Figure 5.5 because it was not tested down to $\Phi = 1.35$ and TRF75 is missing

in Figure 5.6 because it was not tested up to $\Phi = 1.5$. Both figures show a clear trend of increasing particulate number and mobility diameter at the same Φ as the aromatic fraction increases. Throughout this work, the 2013 EEE $\Phi = 0.98$ case is used to represent the NFB. Note that the PRF86 $\Phi = 1.49$ case falls below the NFB, which is a common result for data taken after January 2014 when the NFB decreased for uncertain reasons. The original NFB is used throughout this work for consistency. Finally, all three enrichment metrics are listed for each fuel as a reference, but only Φ remains constant for these comparisons.

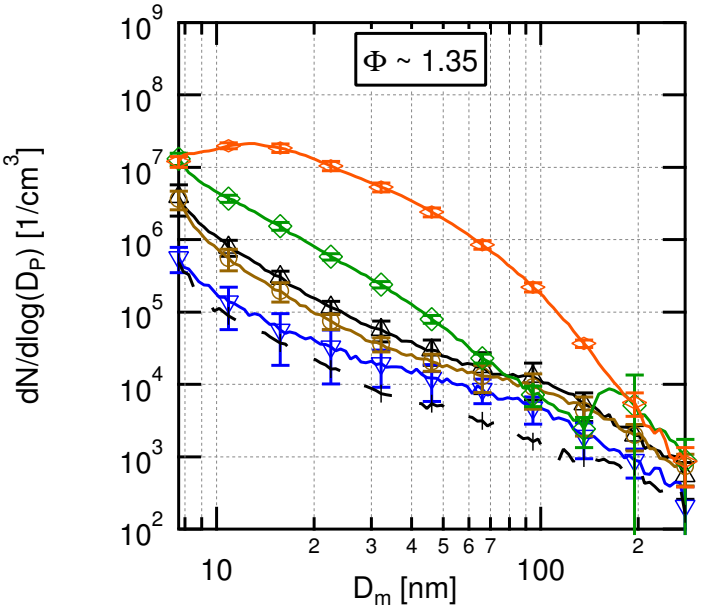

Fuel	Φ	Ψ	C/O
$TRF75_{14}$	1.33	0.84	0.50
$TRF45_{21}$	1.35	0.88	0.48
EEE_{21}	1.35	0.89	0.46
$TRF30_{21}$	1.34	0.88	0.46
$TRF15_{14}$	1.34	0.90	0.44
		NFB	

Figure 5.5: Comparison of PSDs for different fuels at $\Phi \approx 1.35$. NFB trace matches that from [50]. Note error bars/markers are only shown for every 10th point.

For all the fuels, the NFB behavior was present up to a fuel-specific critical enrichment threshold. Above the threshold, PSD development is marked for all fuels by an initial

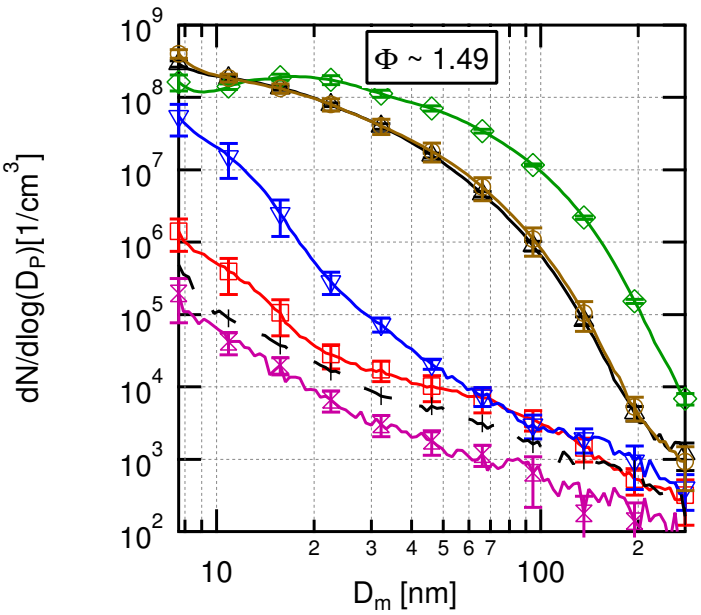

Fuel	Φ	Ψ	C/O
$TRF45_{14}$	1.50	0.97	0.53
EEE_{21}	1.49	0.98	0.51
$TRF30_{21}$	1.49	0.98	0.51
$TRF15_{13}$	1.48	0.99	0.49
$iC_8H_{18\ 21}$	1.50	1.02	0.48
$PRF86_{21}$	1.50	1.02	0.48
	NFB		

Figure 5.6: Comparison of PSDs for different fuels at $\Phi \approx 1.50$. NFB trace matches that from [50]. Note error bars/markers are only shown for every 10th point.

increase in small particles, followed by a continuously larger fraction of large particles as the mixture is enriched. The transition to the larger particles is also fuel-dependent.

For each fuel, the measured PSDs were integrated from 10 nm to 289 nm to obtain the total number concentrations for each data set. The total concentrations were then normalized by the NFB concentration in this diameter range and plotted against Φ for each fuel in Figure 5.7. The y-axis error bars represent a 95% confidence interval based on the repeatability of the SMPS scans for each case. The exact number of scans used for each data point is not listed simply because the large number of points makes this impractical.

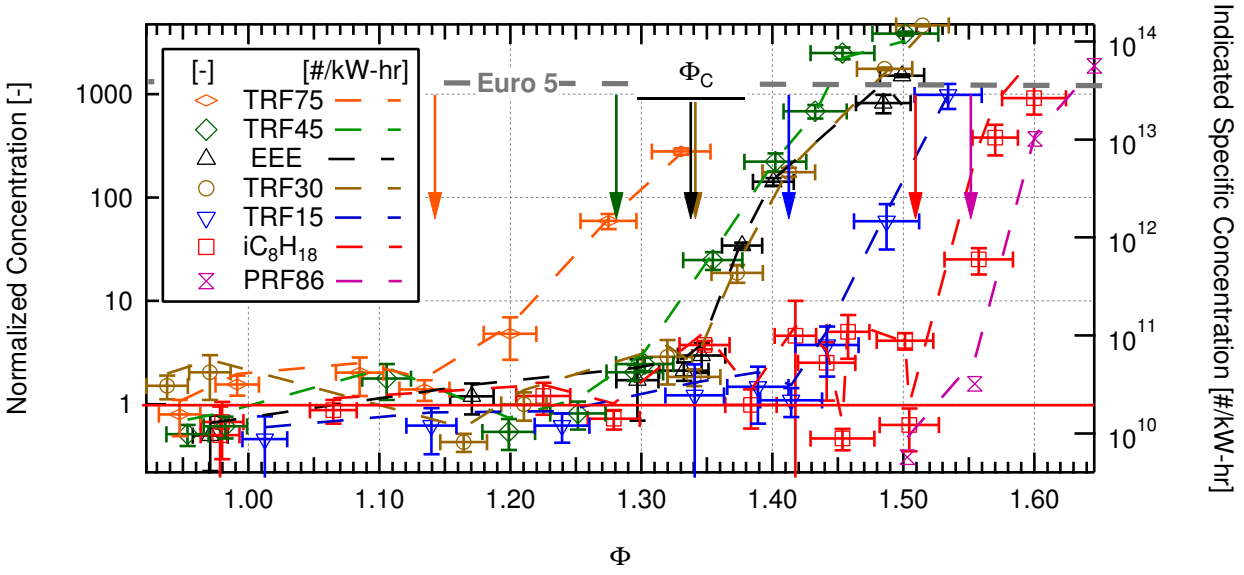

Figure 5.7: Total particulate number concentrations normalized by the NFB (left axis, symbols) and indicated specific particulate number emissions (right axis, dashed lines) vs. Φ. Vertical arrows denote approximate x-axis locations of Φ_C based on the 1X NFB results. For graph clarity, uncertainty bounds are only applied to the concentration data.

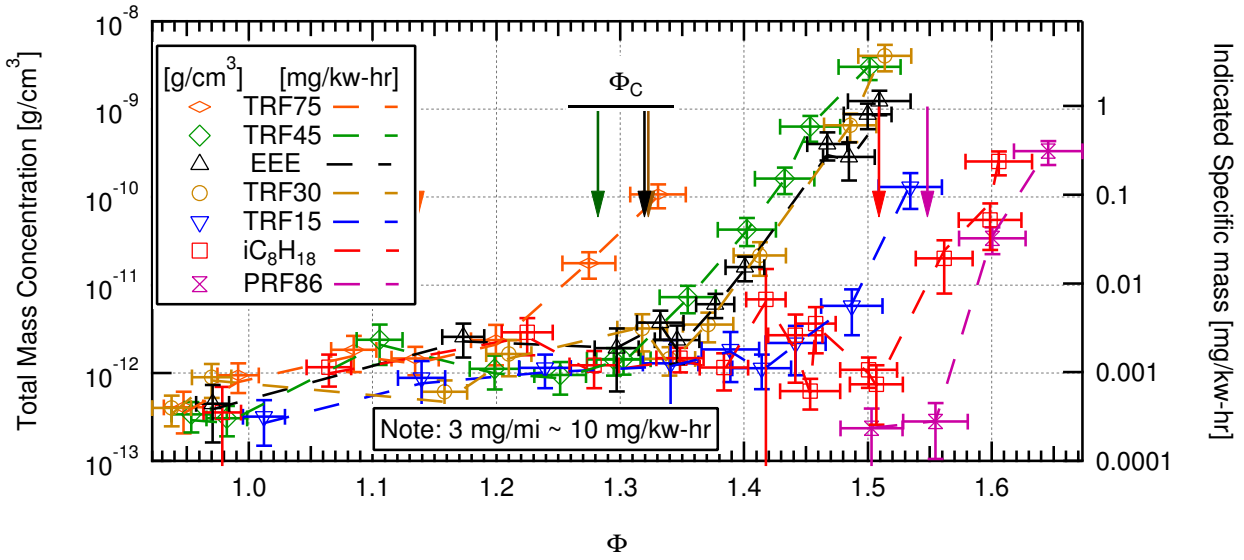

Figure 5.8: Integrated particulate mass concentrations (left axis, symbols) and indicated specific particulate mass emissions (right axis, dashed lines) vs. Φ for the 2100 rpm and 1050 rpm cases. Note that values are absolute, rather than normalized. Vertical arrows denote location of Φ_C based on 1X NFB results. For graph clarity, uncertainty bounds are only applied to the concentration data.

The minimum number of scans averaged for each point is 7, the maximum is 56, and most points are an average of 14-21 scans. The x-axis error bars are based on a 95% confidence interval calculated from the combined measurement uncertainties of the air and fuel flows. The right side y-axis in Figure 5.7 is the indicated specific particulate number emissions and corresponds to the dashed lines. Uncertainty bounds are not plotted for the indicated specific particulate number measurements because doing so would reduce the clarity of the graph. It is apparent from Figure 5.7 that the NFB is the dominant particle source for all fuels up to a fuel-specific threshold mixture (Φ_C). The particulate number concentration increases rapidly beyond this threshold. The total particulate masses and indicated specific particulate masses are shown in Figure 5.8.

Comparison of the mass concentrations and normalized number concentrations shows the result of the transition to accumulation mode particles. At high Φ where the number concentration begins to exhibit a lower dependence on Φ, the mass concentration continues to rise in a log-linear fashion. This shows that particulate mass formation does not slow down as Φ increases, and that increasing agglomeration rates at high Φ cause a decrease in the dependence of particulate number on Φ.

5.2.2 Comparison of EEE and TRF30

The sooting thresholds and concentration trends with enrichment beyond the threshold matched well between TRF30 and EEE, suggesting similar sooting trends between these two fuels. To more closely compare TRF30 and EEE particulate formation trends, PSDs are shown in Figure 5.9 at representative Φs. In Figure 5.9, the $\Phi = 1.35$ case is approximately at Φ_C for both fuels, $\Phi = 1.41$ is just above Φ_C, and $\Phi = 1.48$ is the highest comparable sooting case studied. Because the C/H ratios were matched, the fuels have nearly the same Ψ and C/O at the same Φ. The PSDs show that both the number and size distributions of TRF30 and EEE match well for all the mixtures studied. The well-matched PSD also results in closely matched total particulate mass and mean particle diameters. Because physical

mixing effects have been removed, the results are indicative of well-matched particulate formation chemistry between the two fuels, suggesting that the TRF30 mixture used here is an acceptable chemical surrogate for EEE particulate modeling.

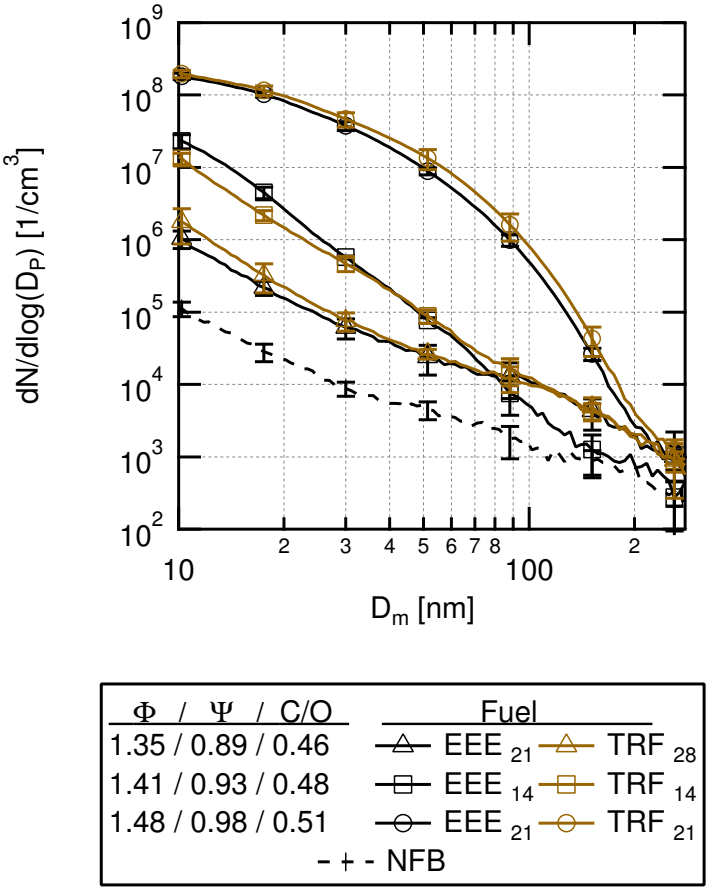

Figure 5.9: EEE vs. TRF30 PSDs at selected Φ. Subscripts in the legend denote the total number of scans used to calculate the averages and confidence bounds. NFB trace matches that from [50]. Note error bars/markers are only shown for every 10th point.

5.2.3 Behavior of Non-Aromatic Fuels

Non-aromatic fuels (iC_8H_{18} and PRF86) follow a slightly different trend than aromatics. Initial soot onset is dominated more strongly by $D_m < 50$ nm particles, and the shift to agglomeration is slower. The iC_8H_{18} and PRF86 PSDs at several Φ are plotted in Figures 5.10 and 5.11.

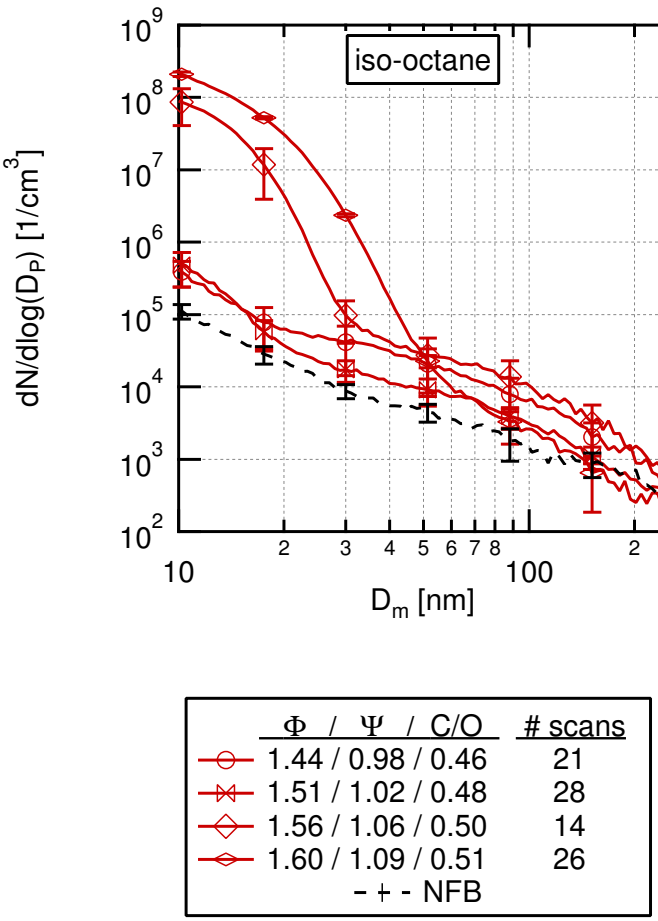

Figure 5.10: iC_8H_{18} PSDs at selected Φ. NFB trace matches that from [50]. Note error bars/markers are only shown for every 10th point.

The domination of the PSD by small particles for iC_8H_{18} and PRF86 is similar to behavior initially witnessed for all fuels and documented in [50]. For the rest of the fuels, those small particles could be removed by careful exhaust conditioning using either increased sample dilution or a volatile particulate remover (VPR). However, these strategies did not remove the large number of small iC_8H_{18} particles seen in Figure 5.10, even when the highest practical sample dilution ratio was combined with use of a VPR (thermodenuder). For the other fuels, removal of the small particles with either dilution or a VPR suggested that these were volatile particles, which were desirable to remove because they are difficult to replicate from one day to the next. To the contrary, the particles produced by iC_8H_{18} are

highly reproducible and do not appear to be volatile. A similar result was recorded for the PRF86 PSDs that are plotted in Figure 5.11. The development of the PSD is very similar to that of iC_8H_{18}, except that the critical enrichment threshold occurs at even higher Φ.

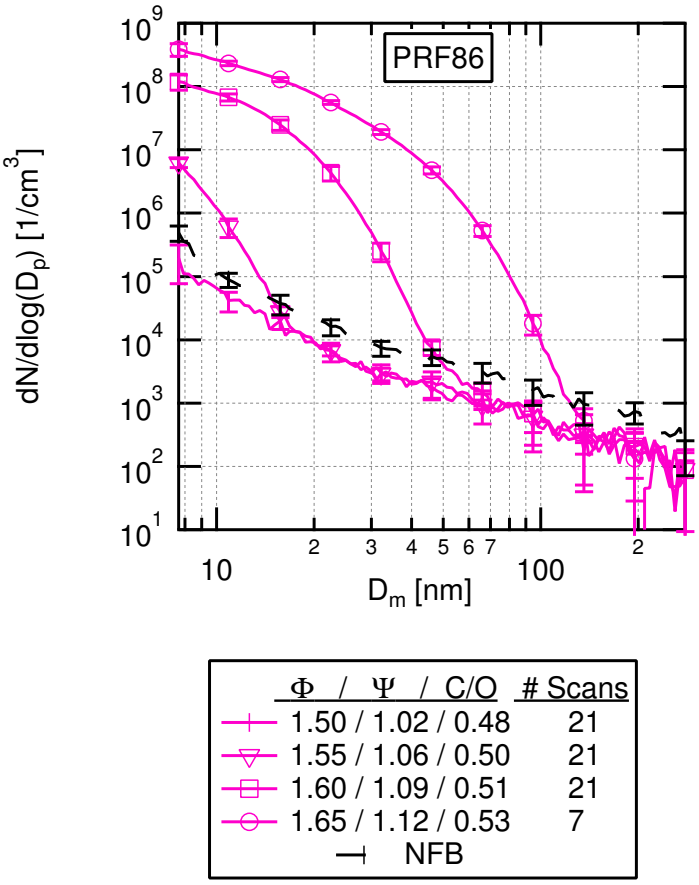

Figure 5.11: PRF86 PSDs at all enrichment levels studied. NFB trace matches that from [50]. Note error bars/markers are only shown for every 10th point.

5.3 Metrics for Describing Mixture Enrichment (Φ, Ψ, & C/O)

Although Φ is an appropriate metric for mixture enrichment near the stoichiometric A/F, the product chemistry at very rich mixtures may not be well represented by the stoichiometric global reaction used to determine Φ. It is desirable to compare sooting tendencies

between fuels using a mixture enrichment metric that allows isolation of fuel molecular chemistry effects. The metrics Φ, Ψ, and C/O are the most appropriate for hydrocarbon fuels. Each of these metrics has benefits and drawbacks that will be discussed here.

For hydrocarbon fuels the relationship between C/O and Φ is described by Equation 5.1, which shows that fuels with a lower C/H have a lower C/O at the same Φ. Similarly, the relationship between Ψ and Φ for hydrocarbon fuels is described by Equation 5.2, which shows that fuels with a lower C/H have a higher Ψ at the same Φ. For a given $\Delta\Phi$, as C/H decreases $\Delta(C/O)$ increases and $\Delta\Psi$ decreases. Finally, Equation 5.3 shows a direct correlation between C/O and Ψ for hydrocarbon fuels.

$$C/O = \Phi \left(\frac{1}{2\left(1 + \frac{4}{(C/H)_{fuel}}\right)} \right) \tag{5.1}$$

$$\Psi = \Phi \left(1 - \frac{1}{2\left(1 + \frac{4}{(C/H)_{fuel}}\right)} \right) \tag{5.2}$$

$$C/O = \Psi \left(\frac{1}{1 + \frac{2}{(C/H)_{fuel}}} \right) \tag{5.3}$$

The three metrics are compared here based on the following criteria:

1. the assumed products should represent the actual products near the critical threshold,
2. the thermodynamic parameters (temperature, pressure, and heat release rate) should match between fuels at each mixture value, and
3. the fuel carbon mass per cycle should match between fuels at each mixture value.

Matching of the first criterion suggests that the theory used to define the stoichiometry or equilibrium chemistry is representative of the actual chemistry. Matching of criteria 2 and 3 ensures that differences in potentially influential variables outside the fuel chemistry were minimized between fuels. Meeting criterion 1 is judged from comparisons of gaseous emissions trends. Meeting criterion 2 is dependent on the adiabatic flame temperature as a

function of the enrichment level, and is judged by comparing in-cylinder temperatures at the same C/O, Φ and Ψ. Meeting criterion 3 is judged by comparing fuel flow measurements as a function of enrichment.

5.3.1 Gaseous Emissions Trend Comparisons

Recall that the determination of Φ assumes that the products are H_2O and CO_2, the stoichiometric equation for C/O assumes the products are CO and H_2, and the determination of Ψ assumes the products are CO and H_2O. The molar fractions of CO, CO_2, H_2 and H_2O are plotted against all three mixture metrics for EEE in Figure 5.12. Similar trends were noted for all fuels. Emissions of CO_2 and H_2O are significantly higher than CO and H_2 emissions near $\Phi = 1$. The mixture range of interest here is at and above the sooting threshold. For all of the fuels studied, CO production is nearly zero for slightly lean mixtures, and increases to nearly 13% of the exhaust products for the richest mixtures. Conversely, CO_2 comprises around 14% of the exhaust products at slightly lean mixtures and decreases to about 5% for the richest mixtures. The crossover between CO_2 and CO occurs when each make up about 8% of the exhaust, which corresponds to $\Phi \approx 1.32$, $\Psi \approx 0.86$ and $C/O \approx 0.45$ for EEE. This is just below the critical mixture threshold. The molar fraction of H_2O remains higher than H_2 for all mixtures.

It is worth mentioning that CO and CO_2 concentrations are directly measured quantities while H_2O and H_2 concentrations are calculated from the measured emissions. The H_2O concentration is assumed to be a function of the CO_2 and CO concentrations, as shown in Equation 5.4. Brackets denote a concentration.

$$[H_2O] = (H/C)_{fuel} * (0.5 * [CO_2] + 0.25 * [CO]) \tag{5.4}$$

The H_2 concentration is determined from the water-gas shift reaction from the number of moles of dry exhaust, CO, CO_2, and H_2O. This relationship is shown in Equation 5.5.

$$[H_2] = \frac{n_{CO} * n_{H2O}/n_{CO2}}{3.8 * n_{dry-exhaust}} \tag{5.5}$$

In Equation 5.5, n stands for the number of moles, and the subscripts are the species.

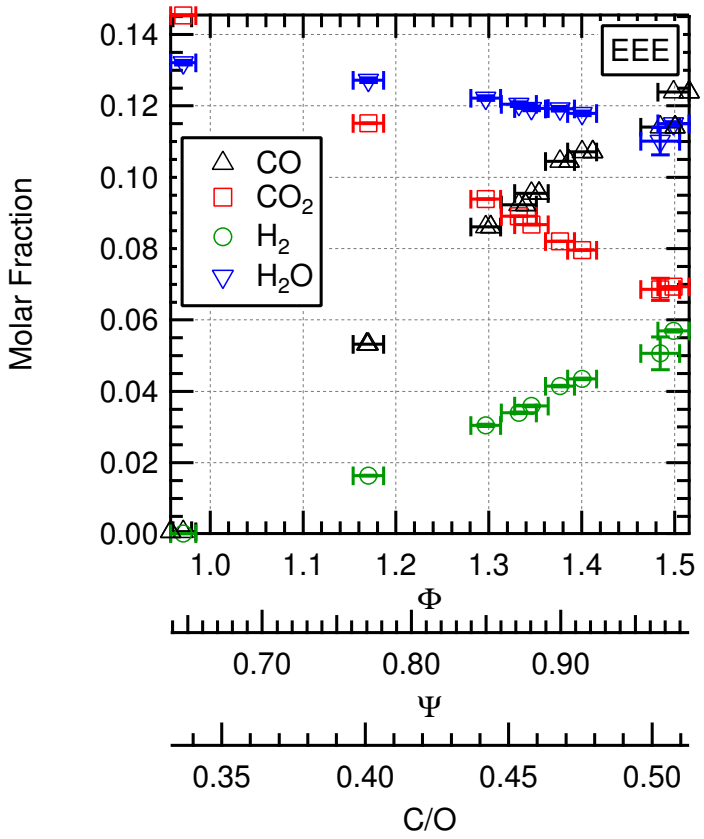

Figure 5.12: Gaseous emissions as a function of Φ, Ψ, C/O for EEE. CO and CO_2 are measured emissions, whereas H_2O and H_2 are calculated using Equations 5.4 and 5.5 respectively.

Near the critical enrichment threshold the stoichiometric product assumptions of both Ψ and Φ are equally appropriate for all fuels because the molar fractions of CO and CO_2 are nearly the same and water is the dominate hydrogen containing product. The molar fraction of H_2O in the exhaust is higher than the molar fraction of H_2 for all fuels even in the richest cases, but the two values are converging. The assumed products for the C/O

metric do not match the measured products as well as Ψ or Φ at the richest conditions tested, which may be due to the fact that all the mixtures are far from C/O = 1.

5.3.2 Temperature Comparisons

Figures 5.13 and 5.14 show the same adiabatic flame temperature data originally presented in Figure 5.1 as a function of C/O and Ψ, respectively. Figure 5.13 shows that the adiabatic flame temperatures between fuels differ more at the same C/O than they did at the same Φ. Conversely, Figure 5.14 shows that the adiabatic flame temperatures between fuels are nearly the same at the same Ψ. From this, it is expected that in-cylinder temperatures will match better at the same Ψ, and worse at the same C/O, as compared to the matching noted earlier at the same Φ.

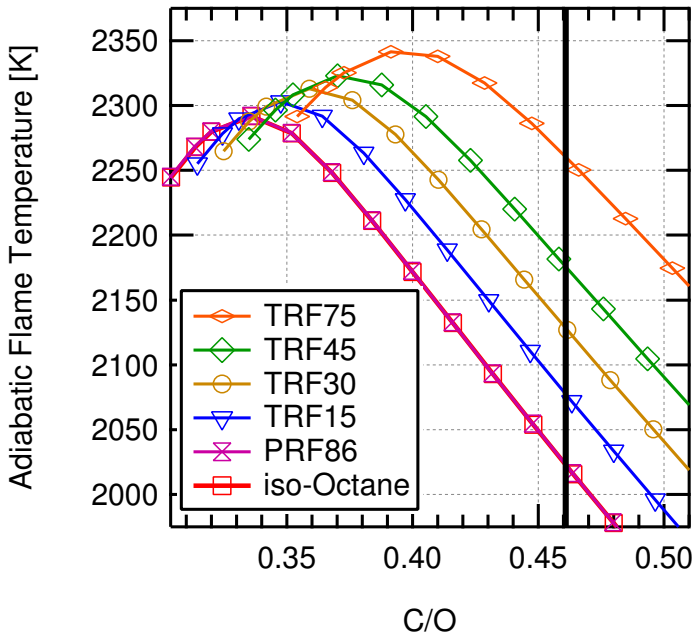

Figure 5.13: Adiabatic flame temperature as a function of C/O for the fuel blends tested here. Temperature data is the same as that in Figure 5.1, and mixture data was calculated from Φ based on Equation 5.1. Solid black vertical line denotes approximate location of EEE C/O_C. Note that PRF86 and iC_8H_{18} data overlap closely.

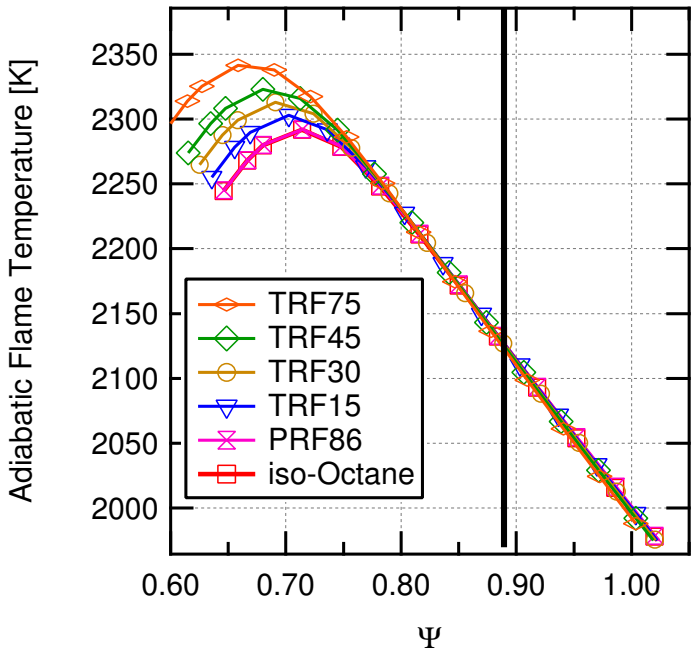

Figure 5.14: Adiabatic flame temperature as a function of Ψ for the fuel blends tested here. Temperature data is the same as that in Figure 5.1, and mixture data was calculated from Φ based on Equation 5.2. Solid black vertical line denotes approximate location of EEE Ψ_C. Note that PRF86 and iC_8H_{18} data overlap closely.

Figure 5.15 compares the in-cylinder temperature traces for all fuels at the same C/O, and Figure 5.17 compares TRF75 and iso-octane at the same Ψ. As noted in Figure 5.15, the maximum difference between peak temperatures at the same C/O is greater than 475 K, whereas the maximum difference between peak temperatures at the same Ψ is closer to 100 K. Late in the cycle at the same C/O the maximum temperature difference remains greater than 150 K, while at the same Ψ, the temperature difference becomes negligible. The temperature difference noted in Figure 5.15 is not the maximum difference. It is the difference between TRF75 and iC_8H_{18} because those two fuels were used to quote the temperature differences at the same Φ and Ψ. Only TRF75 and iC_8H_{18} temperature traces are shown for the $\Psi = 0.71$ case because few other fuels were tested at that Ψ.

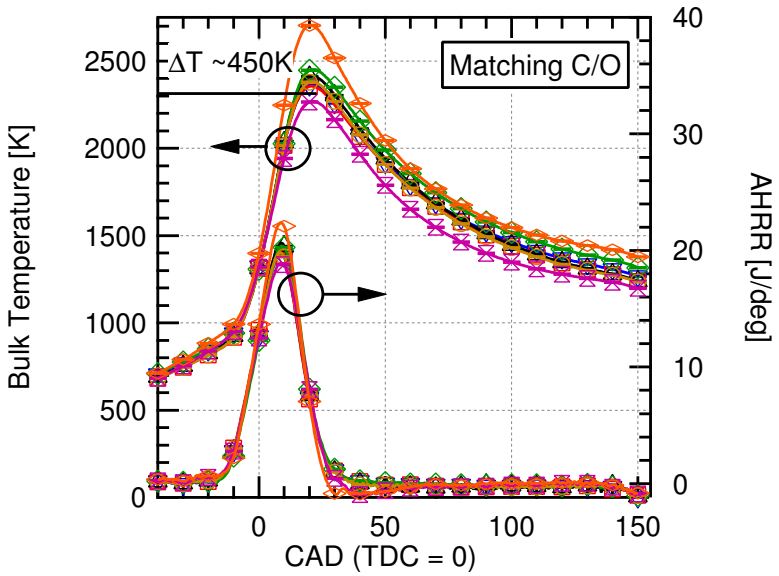

Fuel	Φ	Ψ	C/O
$TRF75_2$	1.28	0.80	0.48
$TRF45_2$	1.35	0.87	0.48
EEE_1	1.40	0.93	0.48
$TRF30_3$	1.41	0.93	0.48
$TRF15_2$	1.44	0.97	0.48
$PRF86_3$	1.50	1.02	0.48
$iC_8H_{18\ 2}$	1.50	1.02	0.48

Figure 5.15: Calculated AHRR and temperature traces at C/O $\approx$ 0.48 for all fuels. Subscripts denote the number of separate runs used to calculate the average and confidence bounds.

Figure 5.16 compares the averaged late cycle temperature and the time spent between 1900 K and 1400 K. The maximum difference in the late cycle temperatures is about 33 K, and the difference in the time is a little less than 3.5 ms.

The trends shown in the adiabatic flame temperature plots agree with those seen in the in-cylinder temperature traces. Both sets of plots show that for the conditions used here, temperature differences are minimized most effectively when fuels are compared at the same Ψ. They are minimized less effectively when compared at the same Φ and are the greatest when compared at the same C/O.

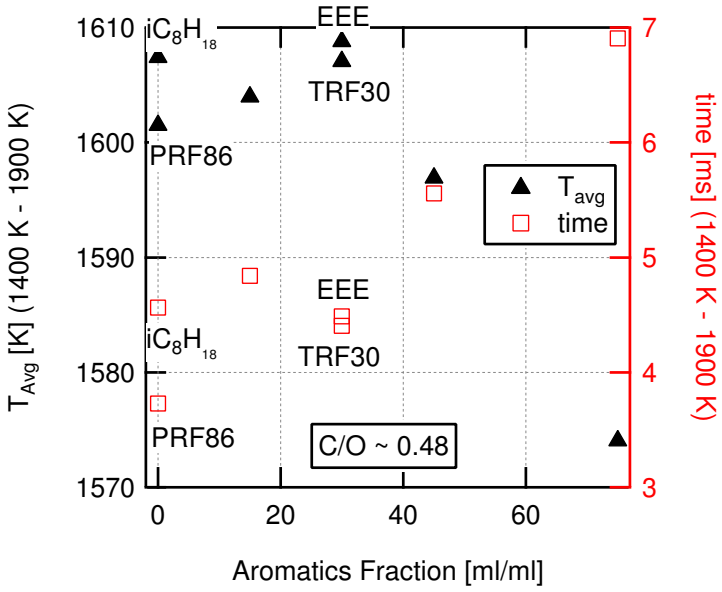

Figure 5.16: Average temperature (left axis) and time spent (right axis) between 1900 K and 1400 K late in the cycle at C/O = 0.48. For cases where temperatures did not reach 1400 K before EVO, the times and average temperatures recorded are those between 1900 K and EVO.

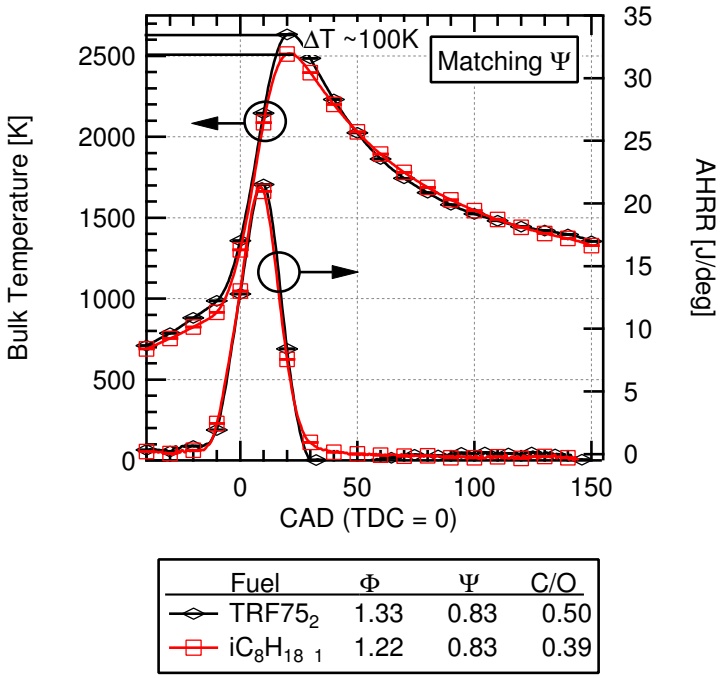

Figure 5.17: Calculated AHRR and temperature traces at $\Psi \approx 0.71$ for TRF75 and iC_8H_{18}. Subscripts denote the number of separate runs used to calculate the average and confidence bounds.

5.3.3 Fuel Carbon Mass Comparisons

The fuel carbon mass per cycle was calculated from the measured fuel mass per cycle. The fuel mass per cycle matches well between fuels when compared at the same Φ and the same Ψ. Increasing H/C decreases the mass of carbon relative to the total fuel mass according to Equation 5.6:

$$\mathrm{Mass_C} = \frac{\mathrm{Mass_{fuel}}}{\left(\frac{\mathrm{H}}{\mathrm{C}}\right)\frac{MW_\mathrm{H}}{MW_\mathrm{C}} + 1} \tag{5.6}$$

Implementation of this equation for each fuel is plotted against Φ, Ψ, and C/O in Figures 5.18, 5.19, and 5.20, respectively.

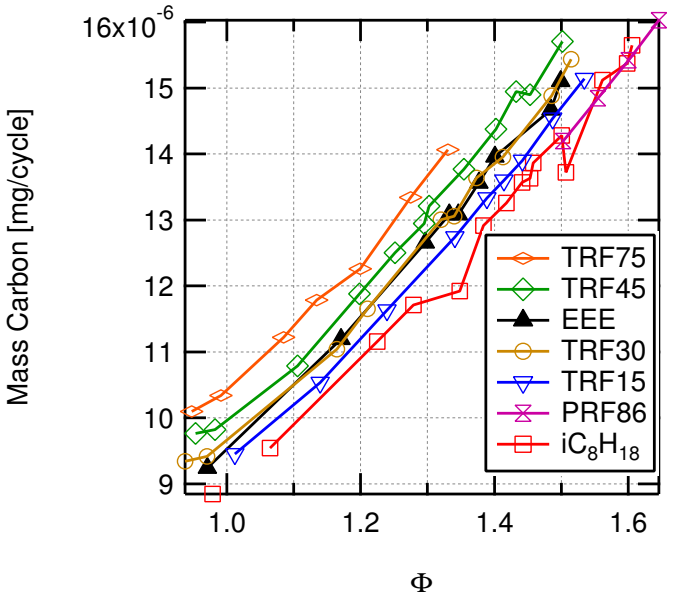

Figure 5.18: Calculated carbon mass per cycle as a function of Φ for all fuels.

The carbon mass per cycle matches very well between fuels when compared at the same C/O. The carbon mass per cycle increased approximately 10% from the lowest to the highest fuel C/H when compared at the same Φ, and increased by almost 20% over the same range when compared at the same Ψ. This means that more carbon is available for particulate formation for fuels with higher C/H at the same Φ and Ψ. This could cause an

increase in particulate formation that is unrelated to fuel chemistry. At the same C/O, the available carbon mass among fuels varies by less than 2% in most cases.

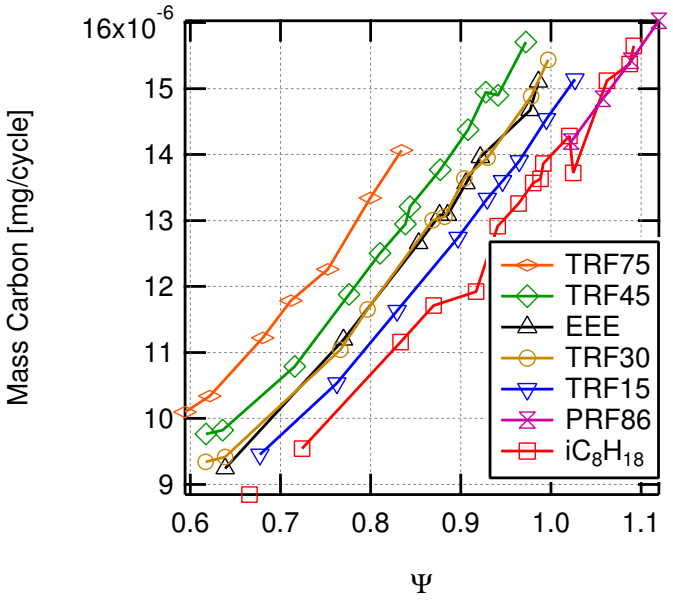

Figure 5.19: Calculated carbon mass per cycle as a function of Ψ for all fuels.

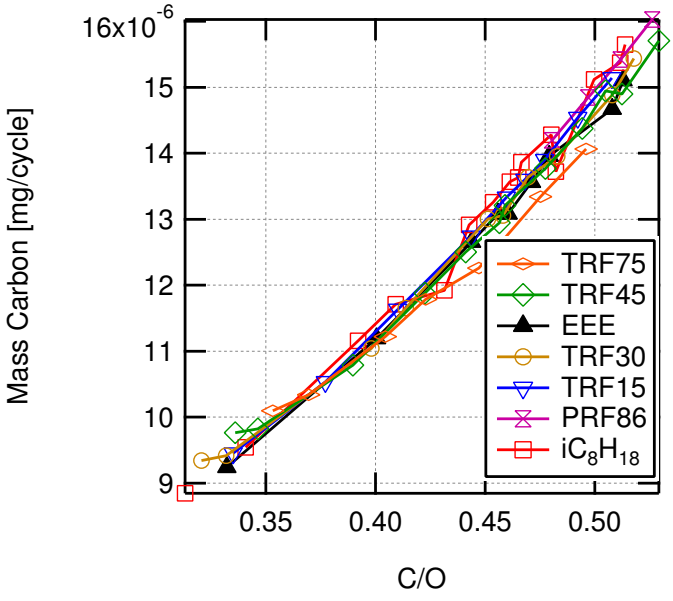

Figure 5.20: Calculated carbon mass per cycle as a function of C/O for all fuels.

Table 5.5: Critical sooting thresholds

Fuel	Ψ_C^{1X}	Ψ_C^{10X}	Φ_C^{1X}	Φ_C^{10X}	C/O_C^{1X}	C/O_C^{10X}
TRF75	0.71	0.76	1.14	1.22	0.42	0.45
TRF45	0.83	0.86	1.28	1.33	0.45	0.47
EEE	0.87	0.90	1.33	1.36	0.45	0.47
TRF30	0.87	0.90	1.33	1.36	0.45	0.47
TRF15	0.95	0.97	1.41	1.46	0.47	0.48
iC_8H_{18}	1.03	1.05	1.51	1.54	0.48	0.49
PRF86	1.05	1.07	1.55	1.58	0.49	0.50

Superscript "1X" refers to the 1X NFB results.
Superscript "10X" refers to 10X NFB results

5.3.4 Particulate Trend Comparisons

The total concentrations are normalized by the NFB concentration and plotted against Ψ and C/O for each fuel in Figures 5.21 and 5.22. Interpretation of the results is dependent on the metric used to describe the enrichment level. The normalized concentration vs. Ψ and normalized concentration vs. Φ plot both show the critical enrichment threshold decreasing as aromatic fraction increases. Beyond the threshold, both show a somewhat similar rate of increase in the number concentration among all fuels as the mixture is enriched. Upon close inspection, the rate of increase seems to increase for fuels with decreasing toluene fraction. This is more obvious when the fuels are compared at the same C/O. The C/O vs. normalized concentration plot also shows that the critical enrichment threshold decreases as aromatic fraction increases. However, beyond the critical enrichment threshold, the dependence of concentration on C/O appears to become weaker as aromatic fraction increases. In particular, TRF45 and TRF75 both produce fewer particles than TRF30 at C/O > 0.475. Also, the dependence of the critical enrichment threshold on aromatic fraction is weaker on a C/O basis.

The 10X NFB and 1X NFB results for all the fuels are tabulated in Table 5.5. The table shows that Φ_C and Ψ_C consistently decrease as aromatic fraction increases, while C/O_C decreases but with a less consistent dependence. In particular, the downward trend of C/O_C is not present between TRF30 and TRF45.

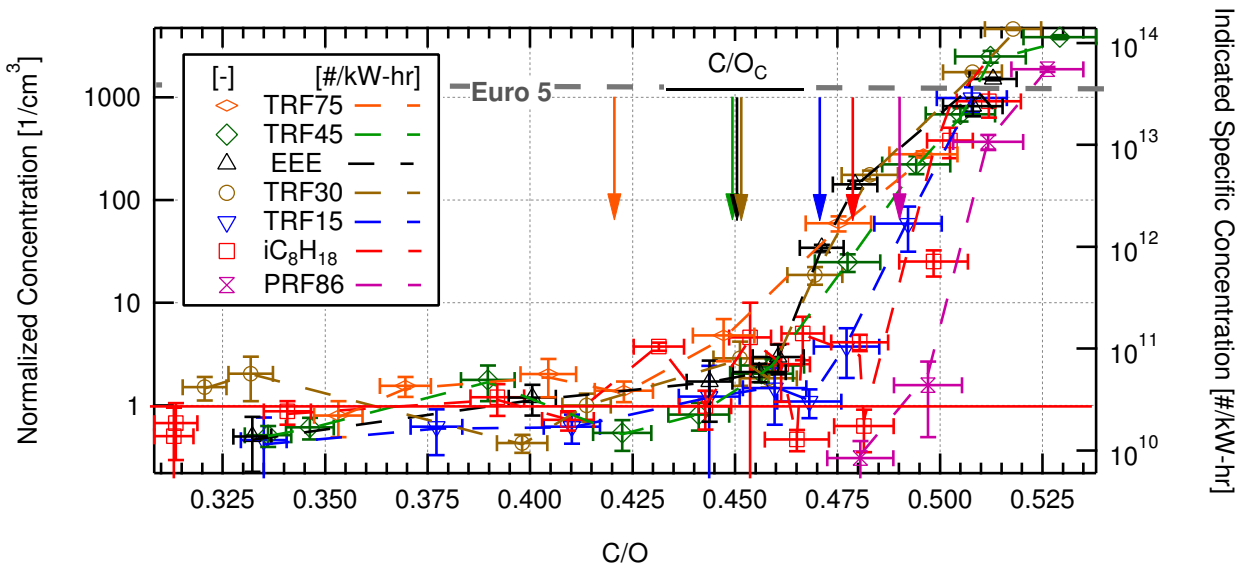

Figure 5.21: Total particulate number concentrations normalized by the NFB (left axis, symbols) and indicated specific particulate number emissions (right axis, dashed lines) vs. C/O. Vertical arrows denote approximate x-axis locations of C/O_C based on the 1X NFB results. For graph clarity, uncertainty bounds are only applied to the concentration data.

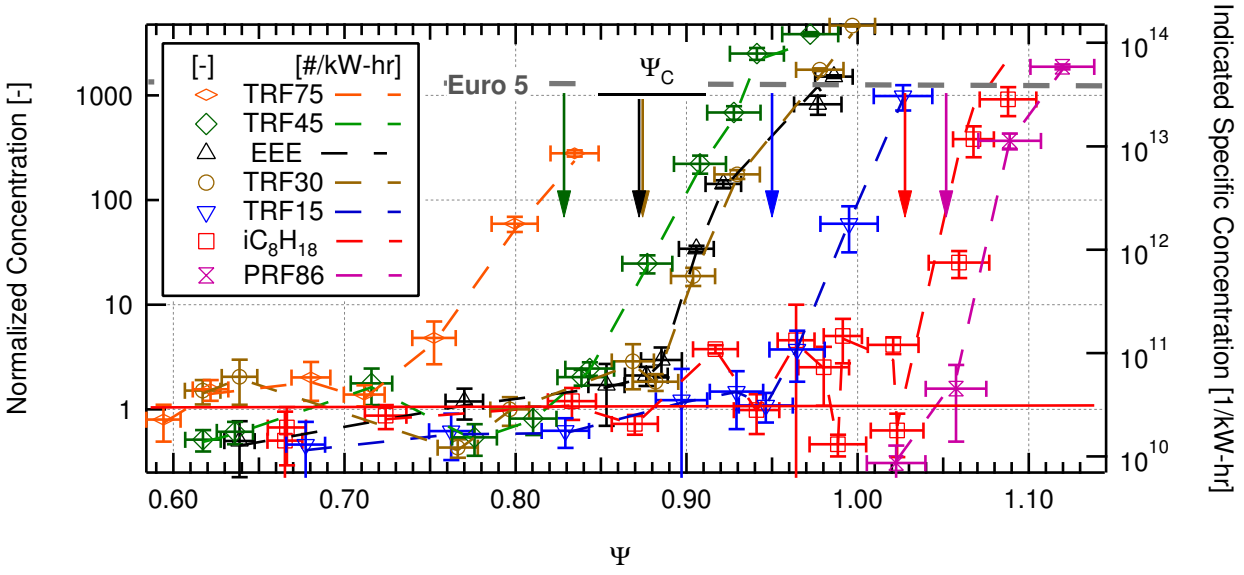

Figure 5.22: Total particulate number concentrations normalized by the NFB (left axis, symbols) and indicated specific particulate number emissions (right axis, dashed lines) vs. Ψ. Vertical arrows denote approximate x-axis locations of Ψ_C based on the 1X NFB results. For graph clarity, uncertainty bounds are only applied to the concentration data.

5.3.5 Discussion of Mixing Metrics

Each enrichment metric was shown to have benefits and drawbacks based on the criteria stated at the beginning of this section. Comparing the fuels at equal Ψ captures the global reaction chemistry near the critical enrichment threshold better than C/O, and ensures the closest thermodynamic condition matching. However, the difference in fuel carbon mass per cycle between fuels is the highest when compared at the same Ψ. This may cause particulate concentration differences that are due to higher carbon concentration, rather than a difference in the kinetic mechanism and chemical fuel structure.

Comparing fuels at equal C/O does not capture the global reaction chemistry well, and results in significant differences in both the peak and late-cycle in-cylinder temperatures. The temperature difference is expected to cause differences in both oxidation and formation reaction rates causing differences in particulate formation that are not directly due to differences in the chemical structure. However, it is the only metric where carbon mass per cycle is well-matched between fuels.

Finally, comparing fuels at equal Φ captures the global reaction chemistry near the critical enrichment threshold approximately as well as Ψ, results in the second best in-cylinder temperature matching, and the second-closest carbon mass per cycle matching. However, at the same Φ, both temperature and carbon mass are potentially significant variables, which results in the highest number of simultaneous variables to consider when interpreting the data.

Due to the inability to fully isolate the fuel chemistry using any of these metrics, the data will be interpretted based on all three methods of comparison, bearing in mind the potential effects of variations in additional variables in each case.

5.4 Discussion of Trends

On both an equal Ψ and equal Φ basis, critical enrichment threshold decreases in the order PRF86 > iC_8H_{18} > TRF15 > TRF30 > TRF45 > TRF75. Above the threshold, the rate at which number concentration increases with further enrichment is similar among fuels. On a C/O basis, there is a less direct dependence on fuel type. The critical enrichment threshold decreases in the order PRF86 > iC_8H_{18} TRF15 > EEE $\approx$ TRF30 $\approx$ TRF45 > TRF75. Particulate number formation increases at a slightly higher rate for low aromatic fraction fuels. The lower rate of particulate number formation for higher aromatic fraction fuels is partially explained by the more rapid shift to agglomeration mode growth, which results in a similar increase in particulate mass concentration as a function of Φ for all fuels.

For these fuels, C/H, number of carbon atoms, number of C-C bonds, and aromatic fraction all increase simultaneously, and they are all expected to increase particulate formation. Therefore, it is difficult to fully understand which elements are most critical to particulate formation. However, based on premixed flame literature, it is possible to consider some likely scenarios.

Fuel decomposition and small aromatics formation are frequently the rate-controlling steps for soot formation in both premixed and diffusion flames [39, 45, 79]. Soot inception must occur before growth modes can begin, so faster precursor formation will lead to earlier inception and quicker agglomeration. Mechanisms for aromatics formation have large uncertainties.Elements of fuel structure that have potential to affect aromatic growth independently from C/H and the number of carbon atoms are the result of molecular bond strengths and unique pathways to known soot precursors. Common pathways for toluene decomposition include dehydrogenation of either the methyl group or the benzene ring including:

$$O_2 + C_6H_5CH_3 \rightarrow HO_2 + C_6H_5CH_2 \tag{5.7}$$

$$HO_2 + C_6H_5CH_3 \rightarrow H_2O_2 + C_6H_5CH_2\,(1) \tag{5.8}$$

$$\rightarrow H_2O_2 + C_6H_4CH_3\,(2) \tag{5.9}$$

$$C_3H_5 + C_6H_5CH_3 \rightarrow C_3H_6 + C_6H_5CH_2 \tag{5.10}$$

Each of these reactions leads to the creation of the resonantly-stabilized benzyl radical [79]. The dehydrogenation of toluene to form benzyl is a well-accepted pathway and toluene is a well-known resonantly-stabalized radical (RSR) precursor [26, 97]. Once formed, RSRs react slowly with O_2 and dissociate slowly, resulting in slow destruction rates [79]. The result of these two factors is that RSRs are instrumental in aromatics formation [79, 119]. It is possible that the benzyl radical is formed from crevice gas sources after the main combustion event and therefore escapes the high temperature of the main combustion event. This pathway may begin to explain the increased soot formation with toluene fraction seen here.

The formation of the benzyl RSR from toluene is one alternative pathway to the H-abstraction C_2H_2 addition (HACA) mechanism. Formation of the first aromatic ring from acetylene is often treated as the rate limiting step [39, 45]. In the case of the non-aromatic fuels, this is likely to be the dominant mechanism. In the case of the aromatic fuels, it is likely that both the HACA mechanism and RSR formation contribute to the additional soot formation. The relative contributions of the two paths is still uncertain. Aromatics formation is highly kinetically controlled and the relative importance of the two pathways is likely to be temperature-dependent [119].

The greatest effect of the aromatic fraction may be the introduction of faster pathways to the formation of stable aromatic species, and the increased number of C-C bonds and C/H ratio inherent to the aromatic ring structure. The synergistic effect of alkane-toluene mixtures is not obvious from this study, which may be due in part to the fact that the study did not extend all the way to 100% toluene.

Although the correlations between the critical fuel chemistry parameters and sooting tendency are not fully isolated in this study, the results demonstrated that matching the C/H and aromatic fraction of the TRF30 to the EEE without knowing the EEE C-C bond number was sufficient to give close agreement in the sooting trends between the two fuels regardless of enrichment or the metric used for comparison. Both the sooting threshold and the PSDs were similar for these two fuels. Because of the close agreement between the PSDs, the two fuels had similar sooting tendencies on both a mass and number basis. Because of the close matching of the C/H ratios, the two fuels had similar sooting tendencies on a Φ, Ψ, and C/O basis. The results suggest that the TRF30 blend is an appropriate chemical surrogate for EEE, and that matching the aromatic fraction and C/H are critical metrics for surrogate fuels to be used for modeling soot formation.

6 PMPV STUDY OF THERMODYNAMIC PARAMETER AND KINETIC TIMESCALE EFFECTS

Thermodynamic effects of various combustion parameters on particulate formation chemistry were tested by testing EEE under PMPV operation. Two engine speeds, four engine loads, and combustion phasing variations from CA50 = 0 to +25 CAD were tested over a range of Φ. This enables the characterization and comparison of the effects of main combustion thermodynamic conditions and late-cycle (CAD $>$ CA90) thermodynamic conditions on particulate formation. Combustion phasing was used as a method to investigate the effects of temperature and pressure during combustion prior to CA95. Engine load variation (gIMEP) was used to isolate the effect of pressure on soot formation. Variation in engine speed (rpm) was used to investigate the influence of the available kinetic timescale. Particular attention was paid to the late-cycle CAD window where ideal particulate formation temperatures occur. The standard operating condition (SC) had a CA50 = +8 CAD, a gIMEP = 334 kPa, and an engine speed of 2100 rpm. The variations in combustion phasing, load, and speed were compared against this condition. Table 6.1 summarizes the variations in engine operation performed to study the impact of thermodynamic parameters and kinetic timescale.

Table 6.1: PMPV thermodynamics study operating conditions

Case Units	Speed [rpm]	IMEP [kPa]	CA50 [CAD]	Φ [-]
SC	2100	334	8	0.98 to 1.50
CA50 0	2100	334	0	1.35, 1.4
CA50 = 13	2100	334	13	1.35
CA50 = 18	2100	334	18	1.35, 1.4
CA50 = 25	2100	334	25	1.35
1050 rpm	1050	305-320	8	0.98 to 1.50
440 kPa	2100	440	8	0.98 to 1.45
550 kPa	2100	550	13	0.98 to 1.50
660 kPa	2100	660	15.5	0.98 to 1.35

6.1 Combustion Phasing Effects on particles

Combustion phasing was used to simultaneously modify the temperature and pressure associated with the main combustion event. Initial studies showed that only extreme changes in the combustion phasing resulted in statistically significant differences in the PSD. The CA50 timing was swept at equivalence ratios of 1.35 and 1.4 to study the effect of combustion phasing and its dependence on Φ. These Φs are just above the critical equivalence ratio for the standard operating condition and were expected to be the most sensitive to changes influencing soot formation. These tests were summarized in Table 6.1.

6.1.1 Thermodynamic Results

The in-cylinder bulk temperature, pressure, AHRR, and crevice flowrate resulting from changes in combustion phasing are shown for the Φ = 1.35 case in Figures 6.1 and 6.2, and for the Φ = 1.40 case in Figures 6.4 and 6.5. In these plots, the step change in the crevice mass flow rate calculation is due to the pressure in the second ring gap becoming greater than the pressure in the first ring gap causing the top ring to shift from the bottom ring land to the top ring land. This results in a step change in the top gap volume that is directly proportional to the change in the mass flow rate out of the crevice due to the ideal gas law relationship between the two quantities. Also, a decrease in the calculated heat release occurs at +140 CAD due to the exhaust valves beginning to open. Finally, note that the late-cycle thermodynamic comparisons, Figure 6.2 and Figure 6.5 have had the horizontal axis shifted so that the parameters can be directly compared based on the time spent in the critical temperature range. In these plots, time (t) = 0 and CAD = 0 when T = 1900K.

The average temperature and time spent between 1900 K and 1400 K are plotted for the Φ = 1.35 case in Figure 6.3 and for the Φ = 1.40 case in Figure 6.6. For the Φ = 1.35 case, as CA50 is increased beyond +8 CAD, the average temperature in the critical range increases, but the time spent in that temperature range decreases. The difference between the average

late cycle temperatures is just over 100 K, and the time spent in the critical temperature range over the same set of cases decreases by about 1.5 ms. For the $\Phi = 1.40$ case, as CA50 is increased beyond +8 CAD, both the average temperature and the time spent in the critical temperature range increase. The temperature increases from +8 CAD to +18 CAD by about 25 K, and the time spent in the critical temperature range increases by about 0.75 ms.

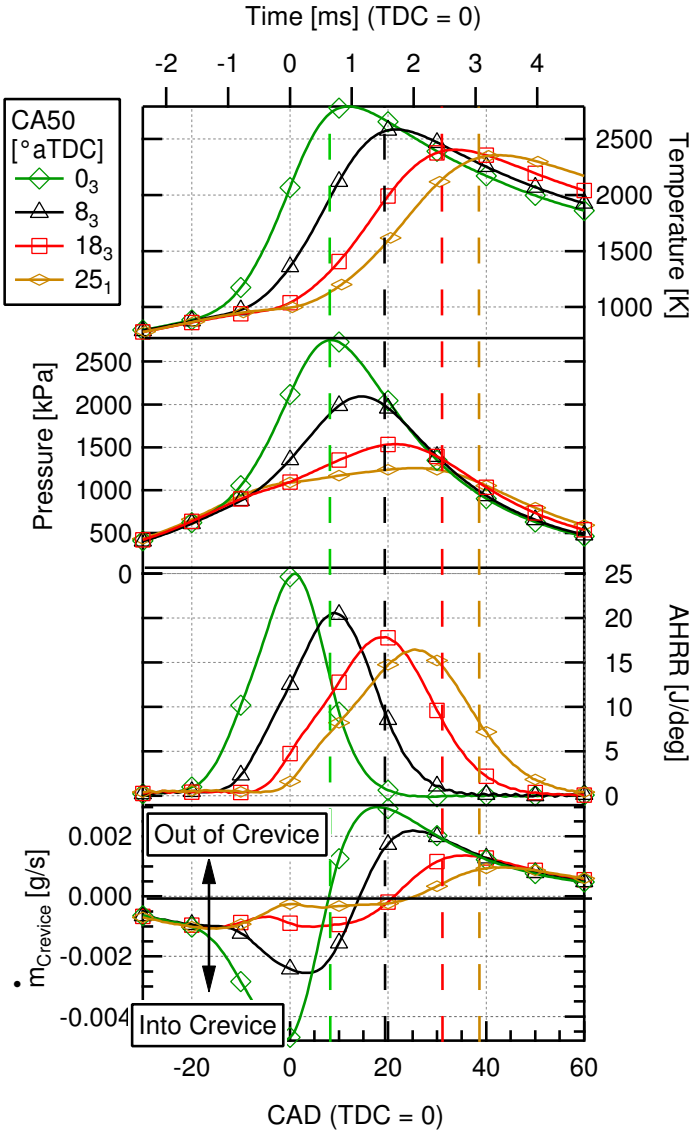

Figure 6.1: Averaged main combustion event data from $\leqslant 3$ runs of each combustion phasing based on CA50 timing. All cases are set to IMEP = 334 kPa, $\Phi = 1.35$ and 2100 rpm. Markers are drawn every 20 data points. Vertical dashed lines represent approximate location of CA90 for each case.

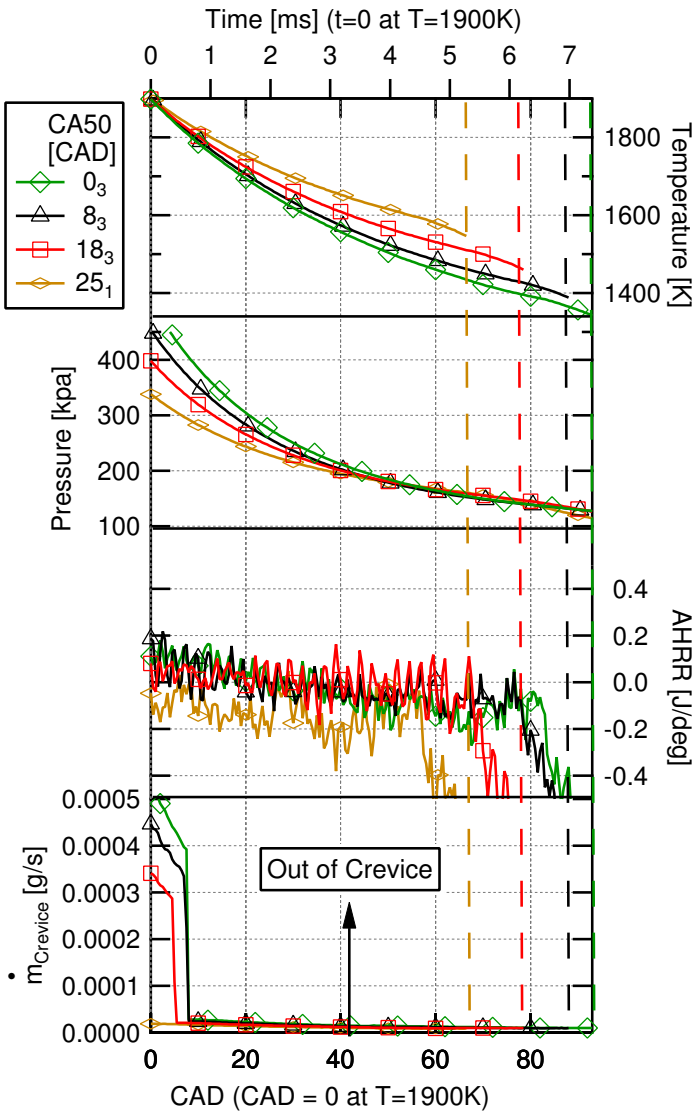

Figure 6.2: Averaged late-cycle data from $\leqslant 3$ runs of each combustion phasing based on CA50 timing. All cases are set to IMEP = 334 kPa, Φ = 1.35 and 2100 rpm. Markers are drawn every 20 data points. Time and CAD are adjusted to begin where temperature = 1900 K for all cases. Vertical dashed lines denote the EVO timing for each case.

In order to maintain the same IMEP between different combustion phasings, the fuel mass flow rate had to be changed to compensate for the differences in combustion phasing. Greater fuel mass flow rates ($\approx$ 6-7%) are required for the CA50 = +18 CAD and +25 CAD cases, while the CA50 = 0 CAD case required an almost identical mass flow rate when compared to the standard operating condition (CA50 = +8 CAD). Because the difference in

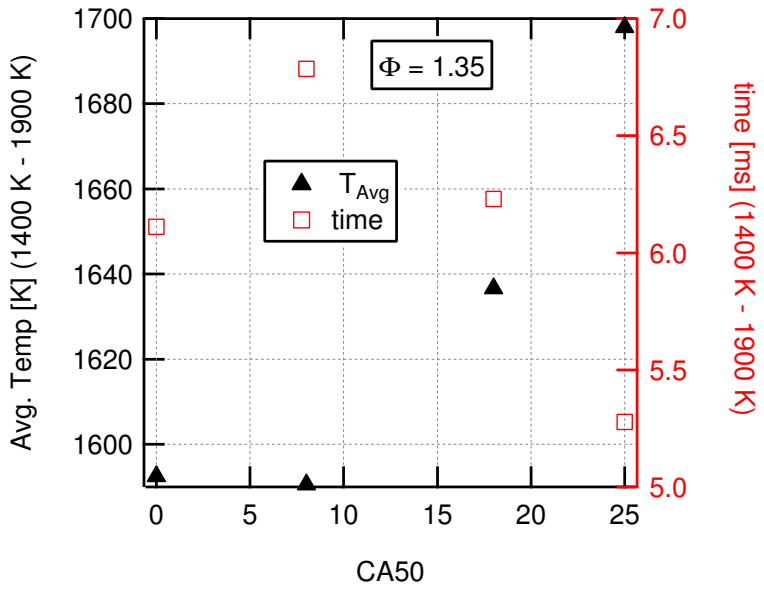

Figure 6.3: Average temperature (left axis) and time spent (right axis) between 1900 K and 1400 K late in the cycle for the $\Phi = 1.35$ CA50 sweep. For cases where temperatures did not reach 1400 K before EVO, the times and average temperatures recorded are those between 1900 K and EVO.

fuel mass has the potential to affect the particulate trends, additional cases were investigated where the CA50 = 0 CAD and +18 CAD cases were compared on the basis of equal fuel mass flow rate. This study produced almost identical results to the cases with IMEP matching, so the IMEP matching strategy was maintained for consistency. A final consideration to keep in mind before analyzing the thermodynamic results is that retarding spark timing reduces combustion stability. The limit for stable combustion in the 334 kPa IMEP case occurs at CA50 = +25 CAD, where the COV of IMEP is nearly 5.0%. For the standard operating condition the COV of IMEP is less than 1.0%

Advancing spark timing results in higher peak temperature, pressure, and crevice flow at the same load. The peak pressures differ by more than a factor of two for the CA50 = 0 CAD and CA50 = +25 CAD cases and the peak bulk average temperature is different by $>$ 400 K for the same two cases. Conversely, after about CA90, temperature, pressure, and crevice flows are greater for the retarded combustion phasings, but differ substantially less than during the main combustion event. If particulate formation is sensitive to the

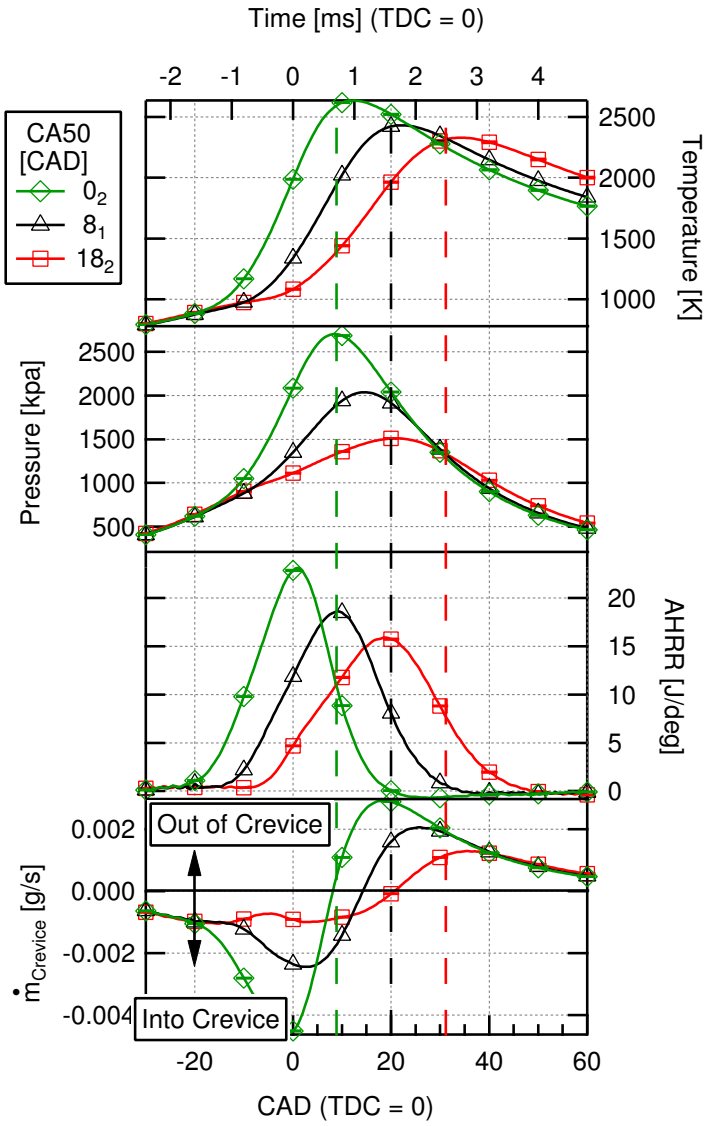

Figure 6.4: Averaged main combustion event data from $\leqslant 2$ runs of each combustion phasing based on CA50 timing. All cases are set to IMEP = 334 kPa, Φ = 1.40 and 2100 rpm. Markers are drawn every 20 data points. Vertical dashed lines represent approximate location of CA90 for each case.

conditions during the main combustion event (CA5 to CA95) one would expect a significant impact on the resulting PSD.

Thermodynamic differences late in the cycle are small compared to the main combustion event but are noteworthy. At a Φ = 1.35, the more advanced spark timings spend slightly more time in the temperature range of 1400 K to 1900 K where soot production is most

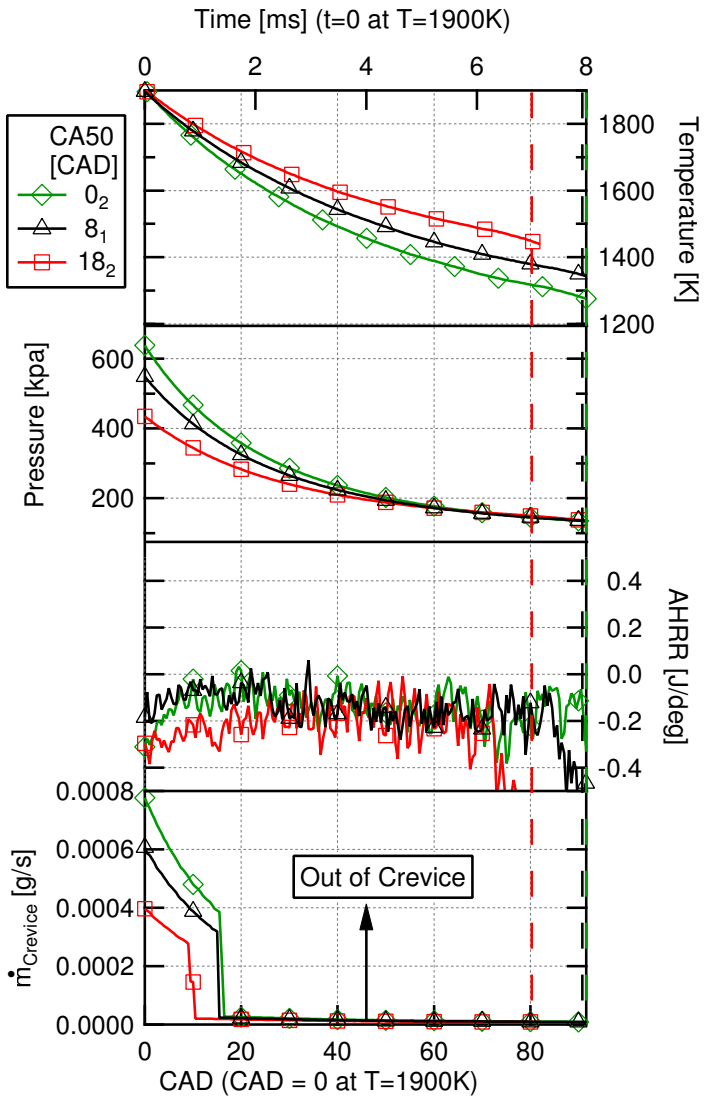

Figure 6.5: Averaged late-cycle data from $\leqslant 2$ runs of each combustion phasing based on CA50 timing. All cases are set to IMEP = 334 kPa, Φ = 1.40 and 2100 rpm. Markers are drawn every 20 data points. Time and CAD are adjusted to begin where temperature = 1900 K for all cases. Vertical dashed lines denote the EVO timing for each case.

likely. The difference between the most extreme cases is approximately 2 ms out of 7 ms, approximately a 30% difference. However, the more retarded cases have a higher average temperature during this time period. The difference is slightly less for $\Phi = 1.4$ case. The more advanced spark timings at both equivalence ratios have a more rapidly decreasing temperature with time causing the charge to spend less time in the temperature range

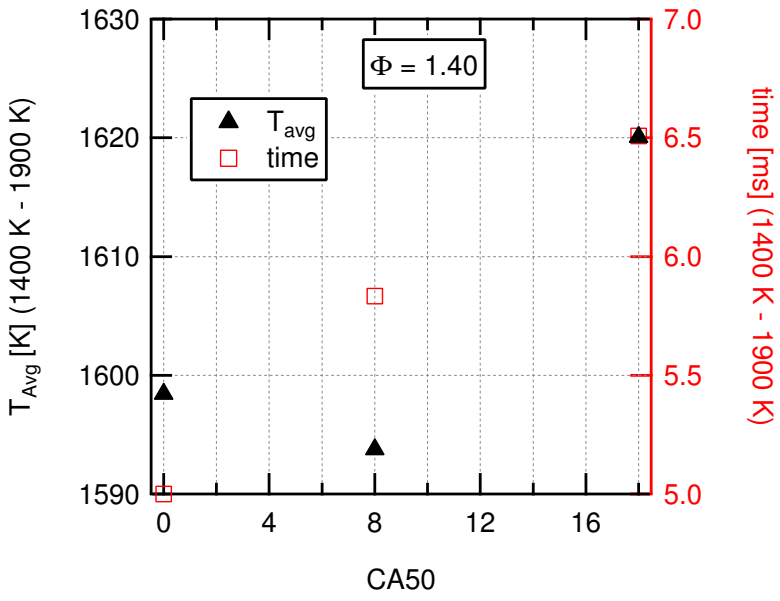

Figure 6.6: Average temperature (left axis) and time spent (right axis) between 1900 K and 1400 K late in the cycle for the $\Phi = 1.40$ CA50 sweep. For cases where temperatures did not reach 1400 K before EVO, the times and average temperatures recorded are those between 1900 K and EVO.

where peak soot formation is expected ($\approx$ 1500 K to 1700 K). Pressures for the retarded cases are lower late in the cycle, but they are converging and differences are relatively small beyond +80 CAD. Due to this the influence of pressure is assumed to have only second order effects on the particulate results to be discussed.

6.1.2 Particulate Results

Figure 6.7 shows that despite the major changes in the combustion event, the resulting PSDs in the $\Phi = 1.35$ case are nearly identical below $D_m = 100$ nm, and only slightly outside each other's error bounds above $D_m = 100$ nm at $\Phi = 1.35$. Advanced combustion phasings appear to consistently produce slightly more large particles than retarded combustion phasings. The significance of this result is somewhat debatable since at the dilution ratios used the actual number of counts measured by the CPC in the large particulate range is quite small. Therefore, it is easy for small variation in the number of counts measured to

result in what appear to be large variations. The differences in the large particulate range are close enough to the error bounds that they are at best just barely significant.

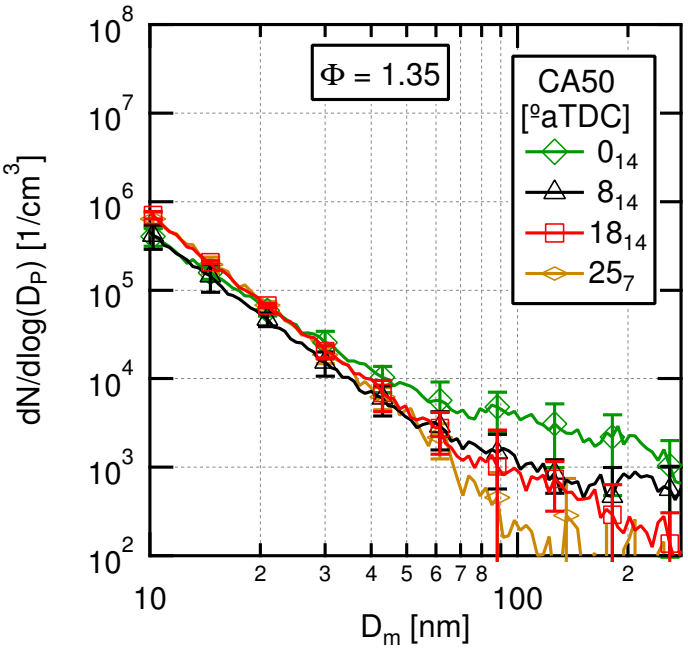

Figure 6.7: Averaged PSDs from $\leqslant$ 14 scans of each CA50 timing at Φ = 1.35. Subscripts denote the number of scans used to determine the average. Markers are drawn every 10 data points.

The PSDs from the Φ = 1.4 test are shown in Figure 6.8. The sensitivity to combustion phasing is clearly higher at Φ = 1.4. The CA50 = 0 and CA50 = +8 PSDs are not statistically different, but the CA50 = +18 case produces substantially more particles with $D_m < 100$ nm, and between one and ten times as many particles up to D_m = 100 nm. Above D_m = 100 nm, differences between the PSDs are small and likely not real, but the most advanced case does again produce the most particles.

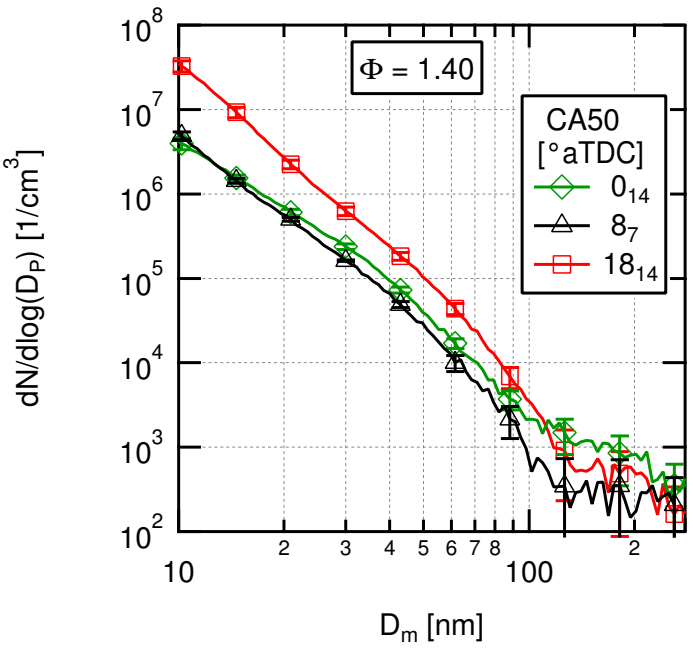

Figure 6.8: Averaged PSDs from $\leqslant 14$ scans of each CA50 timing at $\Phi = 1.40$. Subscripts denote the number of scans used to determine the average. Markers are drawn every 10 data points.

6.1.3 Discussion

Due to the minimal changes in particulate formation near soot onset for large variations in the main combustion event, it is argued that the formation of soot does not occur for equivalence ratios near soot onset until after the main combustion process is essentially complete. This was hypothesized in an earlier Combustion Institute paper by the author [50]. The reasoning for the original hypothesis was based on the argument that soot formation is most likely in the temperature range 1400 K to 1900 K, and that the time spent within this temperature range is the most important variable. Temperatures in-cylinder do not fall below 1900 K until well after the main combustion event has ended. The current results appear to support this conclusion since large variation in main combustion temperature and pressure appear to have little influence on sooting for $\Phi = 1.35$. This is a useful result because it suggests that bulk gas particulate formation tendencies under DI operation are not likely to be affected much by temperature or pressure fluctuations in the main

combustion event. This also supports the suggestion by Pilla [88] that the decreased particle number from retarded spark timings in DI engines is likely due to the increased charge mixing and time for evaporation provided by delaying ignition. The result is also useful in this study because it suggests that differences in the main combustion temperature and pressure can be ignored for the sake of closer late-cycle thermodynamics matching when trying to isolate specific variables.

While the PSDs had low sensitivity to combustion phasing, small but consistent trends were noted. These trends may be explained by differences in late-cycle thermodynamics. For the $\Phi = 1.35$ CA50 sweep no significant change in particulates was seen for $D_m < 100$ nm even though the time spent in the critical temperature range was approximately 1.5 ms shorter for the most retarded condition compared to the +8 CAD condition. This shorter time was potentially offset by the higher average temperature during this time period. In the $\Phi = 1.4$ CA50 sweep, the amount of time spent in the critical temperature range was highest for the most retarded condition due to the overall decreasing temperatures with increasing Φ. This case also had the highest average temperature for the time spent in the critical temperature range. The combination of these two differences are the likely cause of the increase in particle number for $D_m < 100$ nm seen for this sweep. These results suggest that time and average temperature during the time in the critical temperature range influence the production of soot. This idea will be revisited when discussing the results for changing engine speed.

6.2 Engine Load Effects on Thermodynamics and Particles

Load variations were performed at a speed of 2100 rpm, at IMEPs and CA50s of 334 kPa and +8 CAD, 440 kPa and +8 CAD, 550 kPa and +13 CAD, and 660 kPa and +15.5 CAD. The combustion phasing was retarded as the load increased to allow for closer late-cycle temperature matching to the standard operating condition. This is based on the

results of the combustion phasing study where main combustion temperature and pressure were shown to have minimal influence on soot formation and late-cycle temperatures and pressures where shown to have measurable impacts.

6.2.1 Thermodynamic Results

The main combustion event and late-cycle thermodynamics are compared between loads in Figures 6.9 and 6.10. The bulk gas temperatures naturally change very little with increased load, although changes in combustion efficiency and heat transfer do cause slight changes. The average late cycle temperature and time spent between 1900 K and 1400 K are shown in Figure 6.11. Retarding CA50 as load increases, reduces and retards the peak average temperature and increases the late-cycle average temperatures, so the average late cycle temperatures vary by only about 10 K. Neither the time spent in the critical temperature range or the average late cycle temperature changes as a consistent function of IMEP. This strategy successfully isolated the pressure changes from temperature and residence time effects. However, note that because crevice mass flow is directly dependent on cylinder pressure, this variable increases with load.

The combustion phasing used for each load was chosen to achieve the closest late-cycle temperature matching between the 334 kPa Φ = 1.35 case and the Φ = 1.35 case for the higher loads. This phasing was maintained for all Φs to allow for accurate comparison of the effect of Φ at the same load. Because of this, the late cycle temperature matching is optimal between loads for Φ = 1.35, but is acceptable throughout the range of Φs tested. The thermodynamic matching among loads shown in Figures 6.9 and 6.10 is for the Φ = 1.35 case because it is near Φ_C for all the loads, and is the range where thermodynamic matching is most critical.

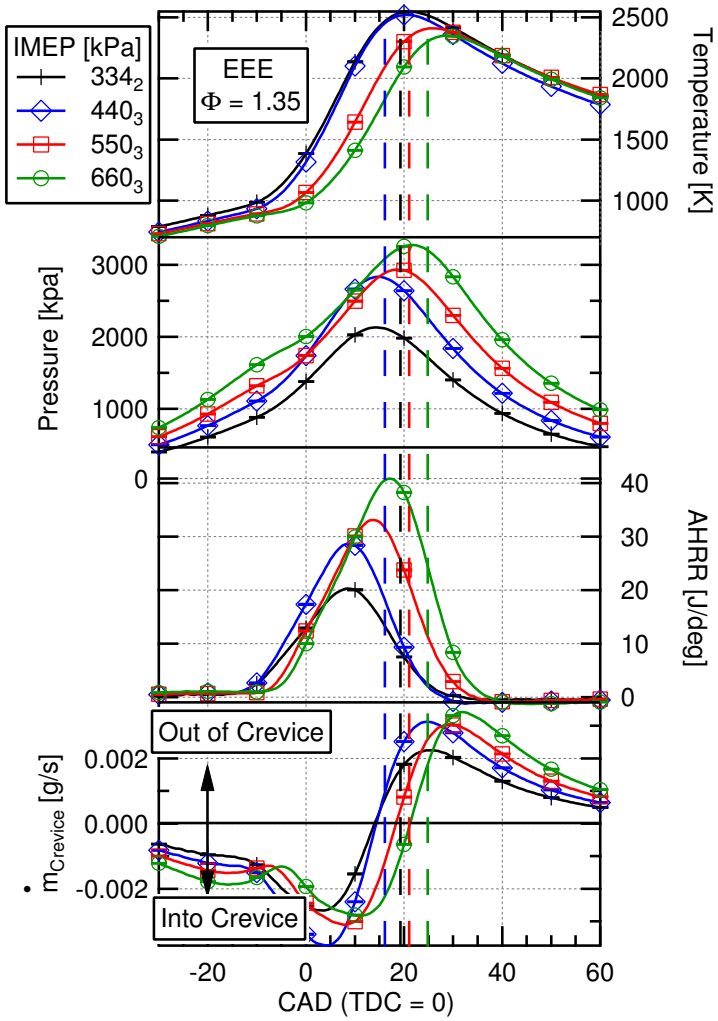

Figure 6.9: Averaged main combustion event data for each load from a single run at $\Phi = 1.35$. Markers are drawn every 20 data points. Vertical dashed lines represent approximate location of CA90 for each case.

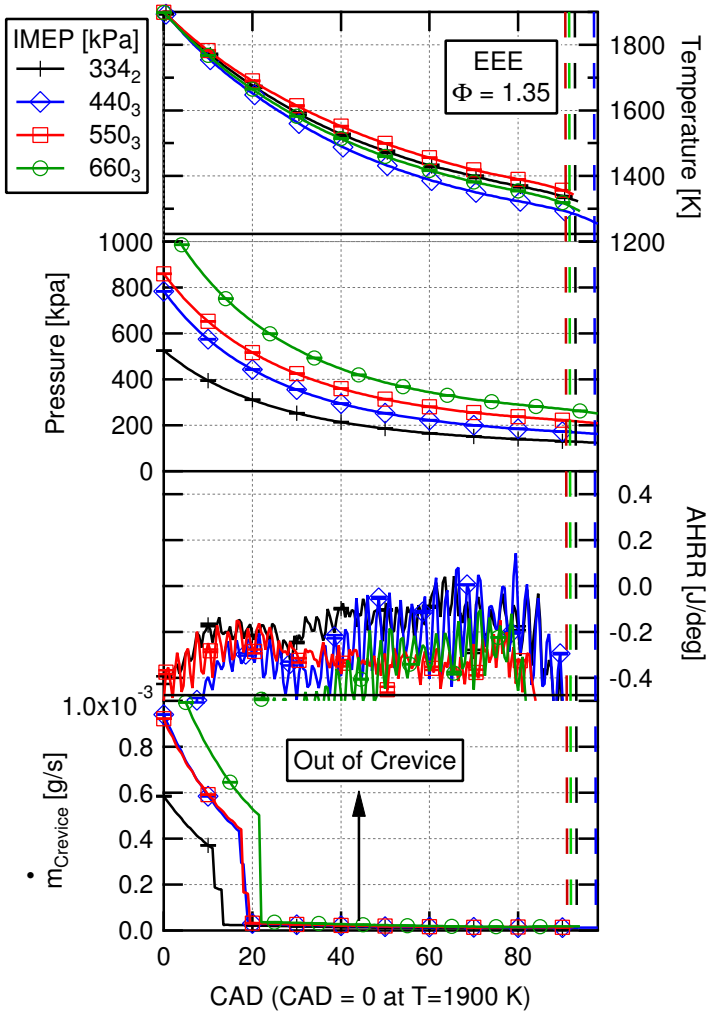

Figure 6.10: Averaged late-cycle data for each load from a single run at $\Phi = 1.35$. Markers are drawn every 20 data points. Data comparison is representative of the matching acheived at all Φ. Vertical dashed lines denote the EVO timing for each case.

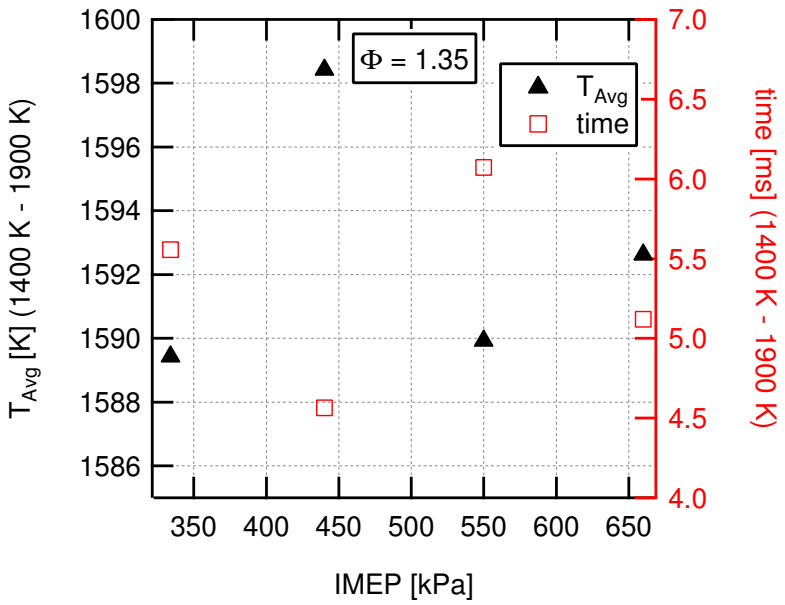

Figure 6.11: Average temperature (left axis) and time spent (right axis) between 1900 K and 1400 K late in the cycle for the $\Phi = 1.35$ load sweep. For cases where temperatures did not reach 1400 K before EVO, the times and average temperatures recorded are those between 1900 K and EVO.

6.2.2 Particulate Results

The PSDs are compared between loads for each equivalence ratio in in Figures 6.12, through 6.15. The baseline PSDs for each load point are shown along with the NFB in Figure 6.12. Note that the EEE data shown here is measurably lower than the original NFB level due to the aforementioned NFB decrease that occurred after January 2014. The 334 kPa Φ sweep was repeated to ensure accurate comparisons between cases, and the new 334 kPa sweep is the one shown. It is important to note that the decrease in particles seen in the NFB was determined to be an absolute change. That is, the drop was not proportional to the total particulate number but is an absolute difference, so for higher particulate cases it is almost negligible because the particulate concentrations for the NFB are so low. First, note that the 334 kPa baseline is similar in shape to the original NFB, but the concentration at each D_m is lower. The shape of the PSD remains similar for all loads as well, but the concentration at each D_m increases with load.

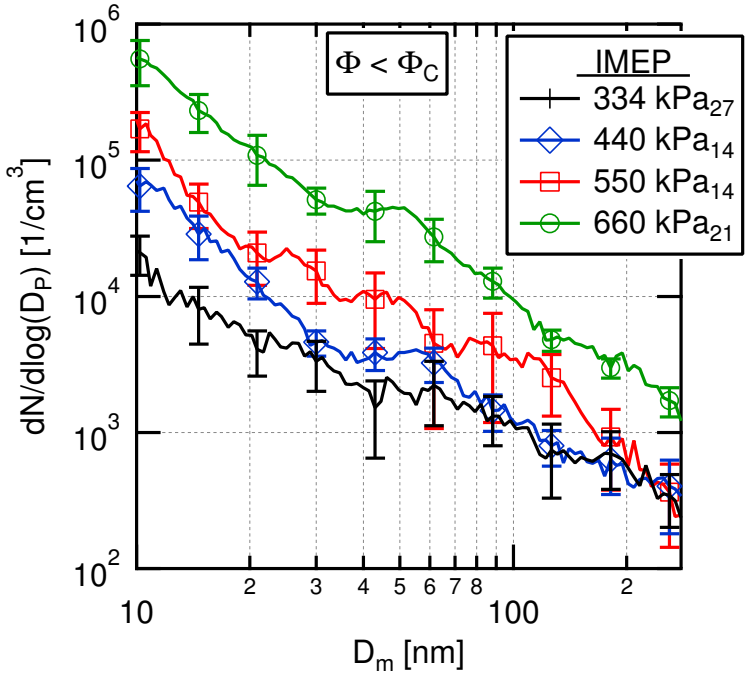

Figure 6.12: Baseline (BL) PSDs for each load from $\leqslant 3$ runs of each at $\Phi < \Phi_C$. Subscripts denote the number of scans used to determine the average. Markers are drawn every 10 data points. NFB trace matches that from [50]

PSD comparisons among load cases at $\Phi = 1.35$, 1.45, and 1.50 are shown in Figures 6.13, 6.14, and 6.15, respectively. The 660 kPa IMEP load was only tested up to $\Phi = 1.35$, and the 440 kPa IMEP case was only tested up to $\Phi = 1.45$. Particle number concentrations increase with Φ, and there is a shift to accumulation mode particles as Φ increases. Additionally, particle number concentrations increase with load, and the shift to accumulation mode particles occurs at leaner mixtures for higher loads.

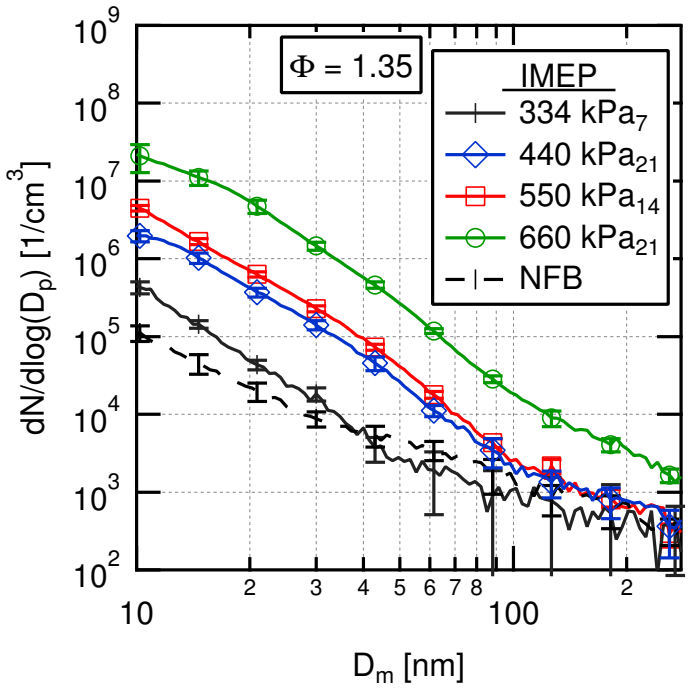

Figure 6.13: Averaged PSDs for each load from $\leqslant 21$ scans of each at $\Phi = 1.35$. Subscripts denote the number of scans used to determine the average. Markers are drawn every 10 data points. NFB trace matches that from [50]

The effect of load on the shift to agglomeration is similar to that of enrichment that has been noted in multiple particle formation studies for both PMPV and DI operating modes [50, 101]. Initial mixture enrichment causes high rates of particle inception leading to large numbers of small particles. Further enrichment causes higher agglomeration rates leading to larger numbers of large particles. This results in increasing GMD, flattening of the PSD, and eventually decreases the number of small particles due to their agglomeration

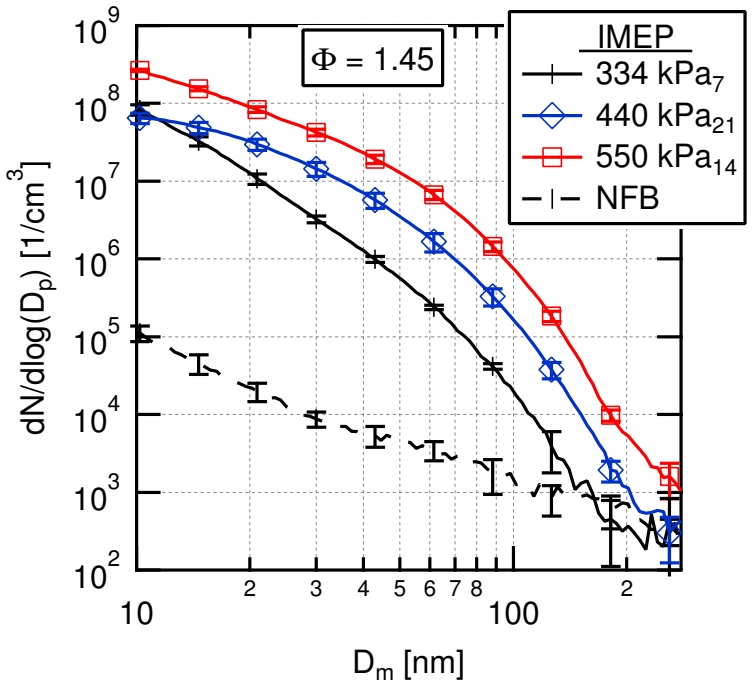

Figure 6.14: Averaged PSDs for each load from $\leqslant 21$ scans of each at $\Phi = 1.45$. Subscripts denote the number of scans used to determine the average. Markers are drawn every 10 data points. NFB trace matches that from [50]

into larger particles. Once agglomeration rates become comparable to inception rates, the total particulate number increases more slowly with Φ, while the total particulate mass continues to increase quickly. Increasing load accelerates this trend. This is most easily seen by comparing the 334 kPa $\Phi = 1.5$ case to the 550 kPa Φ=1.45 case which produce nearly identical PSDs despite a leaner mixture at the higher load. The reason for the only small change between 440 kPa and 550 kPa PSDs in the $\Phi = 1.35$ case is due to the approximate matching of the pressure and temperature during the late cycle period when the curves are shifted to match at 1900 K.

The total normalized particle number concentrations and indicated specific particulate counts at every Φ for all loads are shown in Figure 6.16. The data is normalized against the same NFB total particle number determined in the PMPV validation and used in the fuel chemistry effects study. The total particulate mass concentrations and indicated specific particulate mass emissions for all loads are shown in Figure 6.17. Note that the total mass

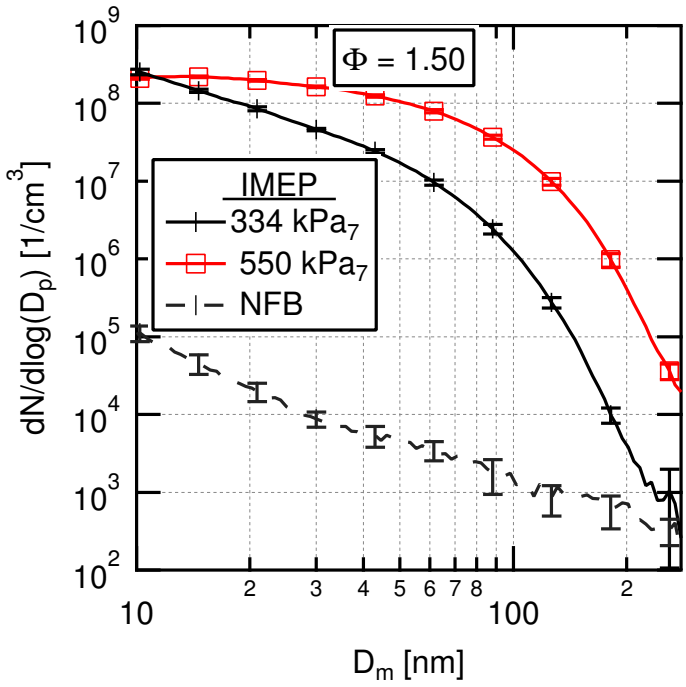

Figure 6.15: Averaged PSDs for 334 kPa IMEP and 550 kPa IMEP cases from seven scans of each at $\Phi = 1.50$. Subscripts denote the number of scans used to determine the average. Markers are drawn every 10 data points. NFB trace matches that from [50]

concentrations are not normalized. The most notable difference between the number and mass concentration graphs is that the dependence of number concentration on Φ becomes weaker at the highest Φ, which is evidenced by the slope of the normalized concentration vs Φ decreasing at the highest Φ. This behavior is caused by a shift to agglomeration mode particles, which have higher mass, so the mass vs Φ slopes do not exhibit this behavior.

Several trends from the PSDs are seen more clearly in Figure 6.16. First, the total particulate concentration at $\Phi < \Phi_C$ increases with load. It is reasonable to believe that particles from oil films, oil mist, and engine wear would all increase as a function of load, so the entire particulate distribution for each load at $\Phi < \Phi_C$ may be from non-fuel sources. However, the increase in particles due to load have not been proven to come from non-fuel sources by testing different oxygenated fuels. Therefore, the particulate levels at each load and $\Phi < \Phi_C$ will be referred to as the "Baseline" (BL) for that load. Only the original 334 kPa baseline will be referred to as the NFB.

Table 6.2: Critical sooting thresholds

Load [kPa]	Ψ_C^{1X}	Ψ_C^{10X}	Φ_C^{1X}	Φ_C^{10X}	C/O_C^{1X}	C/O_C^{10X}	$[\#/cm^3]_{BL}$
334	0.856	0.885	1.30	1.35	0.446	0.461	4450
440	0.847	0.883	1.29	1.34	0.441	0.460	21610
550	0.827	0.856	1.26	1.30	0.431	0.446	19450
660	0.813	0.836	1.24	1.27	0.423	0.435	109910

The NFB total particulate number used for all graph normalizations is 27,863 [$1/cm^3$].
Superscript "1X" refers to the 1X NFB threshold result
Superscript "10X" refers to the 10X NFB threshold result

The second trend seen in Figure 6.16 is that Φ_C decreases with increased load. Because the baseline particulate concentrations changed with load, Φ_C was determined for each load using the baseline particulate concentration for that load. Both the 1X NFB and 10X NFB critical enrichment threshold results are given in Table 6.2. Also note that the baseline total particulate number for each load is given in Table 6.2. The total particulate number given for the 334 kPa IMEP case is from the second 334 kPa Φ sweep.

The third trend seen in Figure 6.16 is that beyond Φ_C, particulate concentration increases with Φ at a similar rate for all loads. The rate of number formation with Φ is slightly lower from $1.4 \leqslant \Phi \leqslant 1.5$. This is due to the shift from inception to agglomeration, which was seen in the PSDs, and is more apparent in Figure 6.18 where GMD is plotted as a function of Φ for all loads. Here, GMD is highly variable below Φ_C, decreases quickly just above Φ_C where increased concentrations are dominated by inception mode particles, then increases rapidly as agglomeration overtakes inception. Close inspection of Figure 6.18 shows that these trends begin sooner as load increases. The rapid rise in inception rate is most clearly seen for the 550 kPa IMEP case because this was the only high load case that was tested at $\Phi = 1.5$. The GMD is variable below the NFB simply due to the higher data variability at very low particulate concentrations.

Although the trends noted above have been tied to cylinder pressure, recall that the crevice mass flow rate also increased with pressure. Because this is considered a potential source of particles, it is worth noting the relationship between the crevice and particulate

masses before discussing the effects of pressure on the particles. In Figure 6.19, the ratio of total mass of fuel carbon returned from the crevice after CA90 to the total cycle particulate mass is plotted as a function of Φ. The total mass of fuel carbon returned was determined by integrating the total mass returned for each case from CA90 to EVO, and multiplying that mass by the fraction that was fuel carbon. The total mass of particulate formed in the cycle was determined by multiplying the calculated particulate mass concentration by the cylinder volume, then correcting the total for the difference between the exhaust temperature and pressure and the SMPS temperature and pressure. Ratio values greater than 1.0 mean that the total mass of fuel carbon returned was greater than the total particulate mass, so it is conceivable that all of the particulate mass could come from crevice gasses. Ratio values lower than 1.0 mean that the total mass of fuel carbon returned was lower than the total particulate mass, so some portion of the particles must be from another source.

Two results are noteworthy in Figure 6.19. First, although the fuel carbon mass returned is three orders of magnitude greater than the particulate mass at $\Phi < \Phi_C$, the balance shifts exponentially for $\Phi > \Phi_C$. This is in agreement with the thermodynamic and PSD results that show carbon crevice mass increasing linearly with Φ while particulate number and mass increase exponentially. Second, The ratio decreases as load increases. If increased particles were the direct result of carbon crevice mass, the ratio should be constant between loads. The fact that the ratio decreases with load suggests that the effect of pressure is the primary driver of increased particulate.

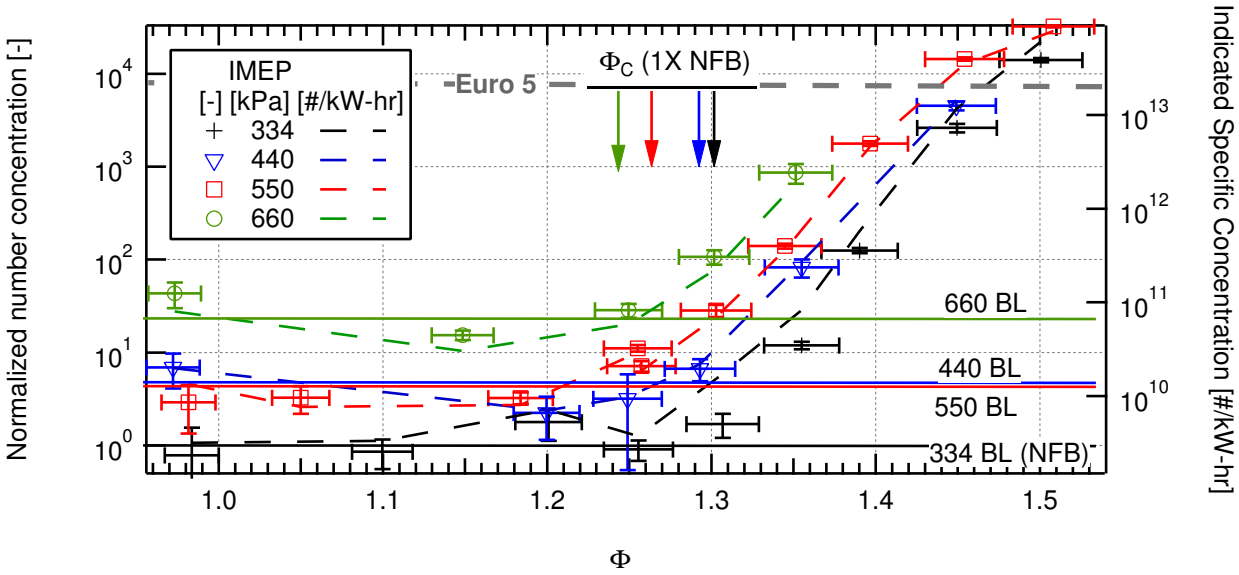

Figure 6.16: Integrated particulate number concentrations normalized by the non-fuel baseline (left axis, symbols) and indicated specific particulate number emissions (right axis, dashed lines) vs Φ as a function of load (IMEP). Vertical arrows denote location of Φ_C based on 1X NFB results. Solid horizontal lines denote the baseline particle number for each load. For graph clarity, uncertainty bounds are only applied to the concentration data.

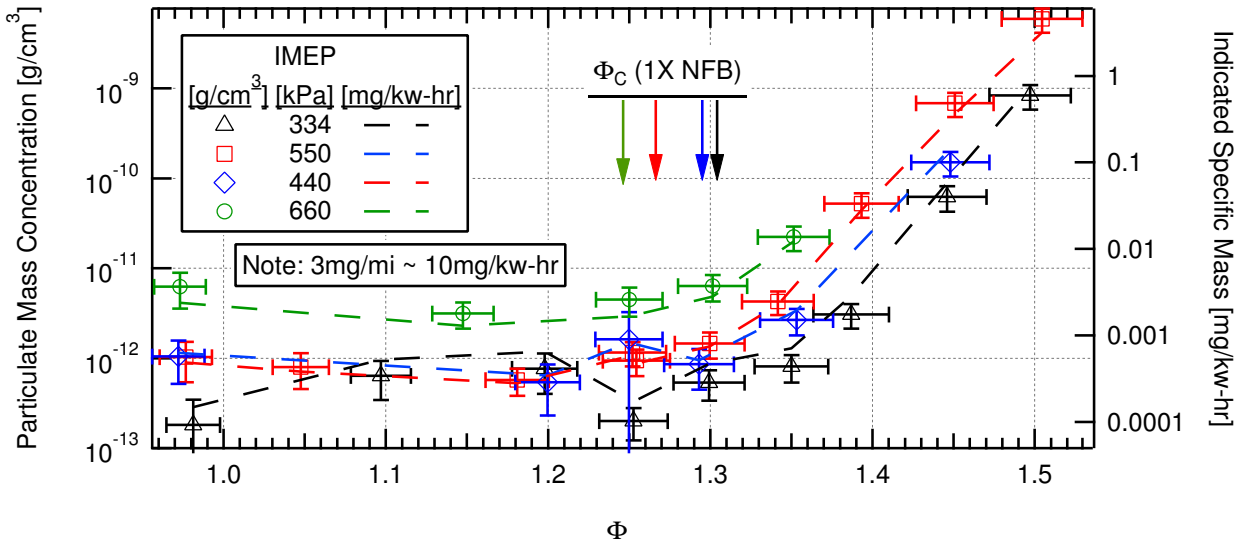

Figure 6.17: Integrated particulate mass concentrations (left axis, symbols) and indicated specific particulate mass emissions (right axis, dashed lines) vs Φ as a function of load (IMEP). Note that values are absolute, rather than normalized. Vertical arrows denote location of Φ_C based on 1X NFB results. For graph clarity, uncertainty bounds are only applied to the concentration data.

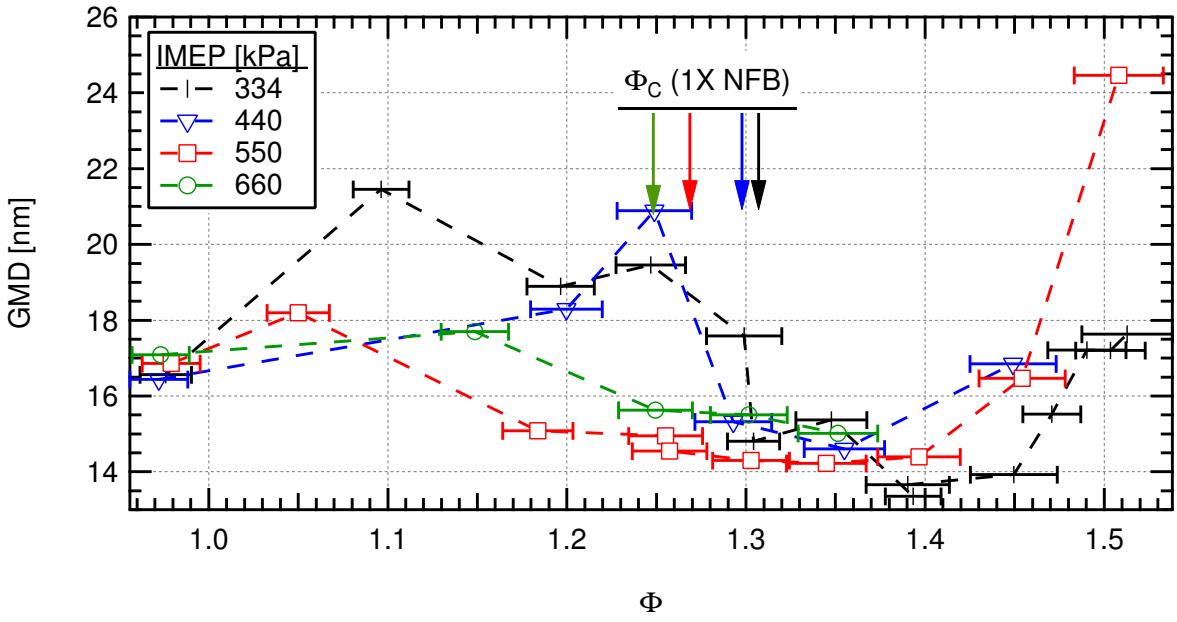

Figure 6.18: Geometric Mean Diameter (GMD) as a function of Φ for all engine loads. Dashed lines are intended only to guide the eye.

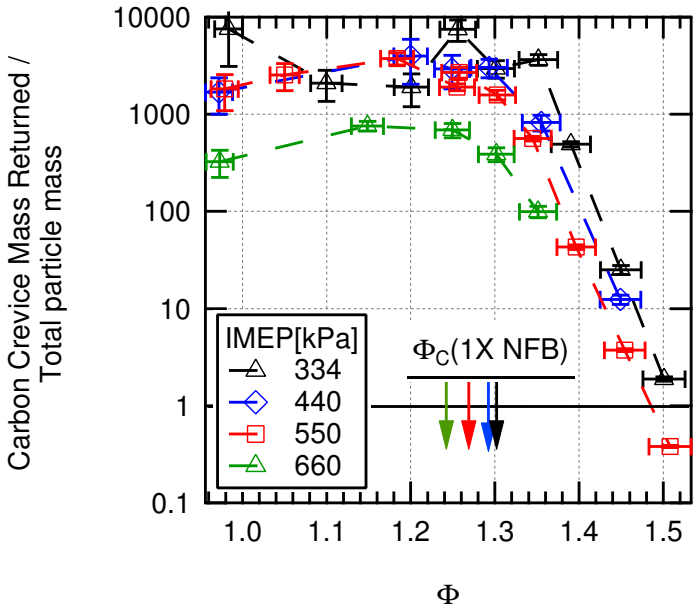

Figure 6.19: Ratio of total fuel carbon returned from the crevice after CA90 to the total mass of particles formed in the cycle as a function of Φ. Dashed lines are intended only to guide the eye.

6.2.3 Discussion

The literature agrees that the dependence on pressure of soot volume fraction for C_2H_4-air flames below 10 bar is between $f_v \propto P^1$ and $f_v \propto P^2$, and that different mechanisms determine the effect of pressure above and below 10 bar [16, 19, 51, 76]. Below 10 bar, soot inception and early-stage growth reactions dominate causing both particulate number and size to increase [76]. Wagner and coworkers [16, 19] experimentally established a $f_v^\infty \propto P^2$ dependence for C_2H_4-air flat flames, while Mauss and Bockhorn predicted a pressure dependence of $f_v^\infty \propto P^2$ up to 3 bar, $P^{1.3}$ from 3-5 bar, and P^1 above 5 bar. Each of these studies acknowledged that $f_v^\infty \propto P^n$ varies with flame temperature, and the P^2 dependence in [16] was found for C_2H_4 at $0.66 \leqslant C/O \leqslant 0.76$, $P \leqslant 10$ bar, and T = 1700 K. It is also important to note that f_v^∞ is generally measured at heights above the burner that correspond to timescales on the order of 100 ms [76]. Although fuel chemistry might be expected to affect the dependence as well, Böhm and Hesse found the C_6H_6 pressure dependence to be nearly the same as the C_2H_4 dependence [19]. In addition to increased f_v^∞ with pressure, C/O_C has been shown to decrease as pressure increases [16]. Both these trends are present in the current data set as a function of IMEP, but the strength of the dependence appears to be different.

A direct comparison of pressure dependence to the premixed flame literature is difficult because the metric for particulate formation is different, the pressure and temperature are variable, and a multi-component fuel was used here. However, an approximate final soot volume fraction can be estimated from the particulate number data by dividing the calculated particle mass by an assumed primary particle density of 2 g/cm^3. Additionally, an approximate late cycle pressure dependence can be determined using a pressure averaged from the time spent between 1900 K and 1400 K. Therefore, it is possible to determine the dependence of soot volume fraction on late cycle pressure as a function of Φ, and compare that to the laboratory results. This dependence is shown in Figure 6.20. Best-fit curves based on a power-law curve fit were applied to the Φ = 0.98, 1.30, 1.35, and 1.45 load sweeps.

The n exponent was determined to be between 6 and 8 for each of these fits. The $\Phi = 1.5$ data could not be fitted because there were only two points.

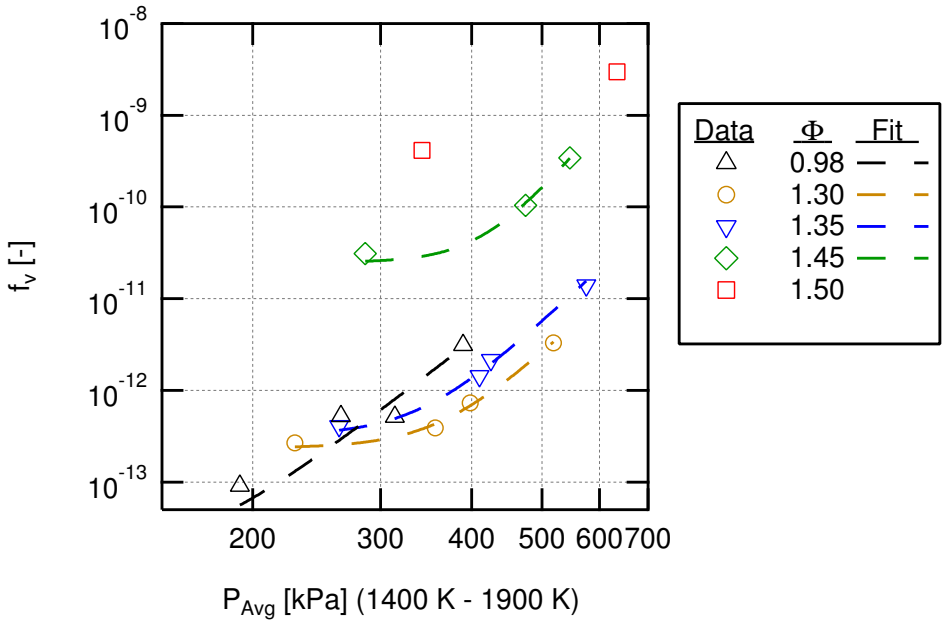

Figure 6.20: Soot volume fraction (f_v) dependence on IMEP, assuming a $f_v \propto P^n$ relationship, as a function of Φ.

Cylinder pressure at 1900 K increased from 300 to 600 kPa in increments of about 100 kPa from the lowest to the highest load, and decreased with CAD to between 200 kPa and 300 kPa at EVO, depending on load. Therefore, the pressure dependence based on references [16] and [76] would be expected to be between $P^{1.3}$ and P^2. The dependence calculated here is much stronger than what was expected. However, note that although the temperature traces are well-matched between loads at a given CAD, the temperature at any given pressure varies significantly between loads, and the pressure drop is quicker for the higher load cases. Based on the temperature dependencies presented earlier for premixed flames, the temperature at which the system reaches a given pressure is likely to influence the apparent pressure dependence. Additionally, the total residence time in the critical temperature range is less than 10 ms, which is far shorter than the time allowed for laboratory flame measurements, so reactions with longer time constants and those that

appear later in the mechanism that determines the P^2 dependence may not be a factor in-cylinder.

This discussion has so far ignored the potential effects of peak cylinder pressure on particulate formation, based on the combustion phasing study. It is worth noting that premixed flames studies have shown that above 10 bar, the high-pressure limit of gas-phase reactions may be reached [76], and particulate coagulation slows [51]. Hannisch et al. [20, 51] noted that at pressures $>$ 15 bar, the growth of soot volume fraction is due to an increase in smaller particles, rather than due to particulate surface growth. This suggests that a dependence on peak pressure (25 bar - 35 bar in this study) should be characterized by an increase in small particles, not increased particle size. Here, increased f_v is due to both increased particulate number and particle growth. This is additional evidence that particles are formed at pressures below peak pressure.

6.3 Engine Speed Effects on Thermodynamics and Particles

To study the impact of engine speed and available reaction time, additional measurements were performed at an engine speed one-half the speed of the standard operating condition. The low-speed condition was operated at a speed of 1050 rpm, a CA50 of +8 CAD, and a fuel mass per cycle ($\dot{m}_{fuel}$) matched at each Φ to the corresponding 2100 rpm case. Matching of the CA50 between speeds resulted in the best thermodynamic matching throughout the cycle. Matching fuel mass per cycle rather than IMEP provided identical charge mass, resulting in well-matched peak temperature and pressure, and the closest matching between late-cycle pressures at the same temperature. This provided good isolation of the effect of reaction time. Maintaining a constant fuel flow and combustion phasing between the two speeds resulted in engine loads in the low rpm case that were slightly different from one Φ

to the next, and slightly lower than the 2100 rpm IMEP. The gIMEP for the low rpm cases varied between 305-320 kPa, and was dependent on Φ.

6.3.1 Thermodynamic Results

The average late cycle temperatures and time between 1900 K and 1400 K as a function of Φ for both speeds are plotted in Figure 6.21. At 2100 rpm, the temperature spends between 5 ms and 7 ms between 1400 K and 1900 K, and during this time the pressure drops from 300 kPa to below 130 kPa. At 1050 rpm, temperature spends about twice as much time in the critical temperature range for most Φs. Because the temperature reaches 1900 K at an earlier crank angle, pressure is about 60 kPa higher at the same temperatures in the 1050 rpm case. The difference in the average late-cycle temperature for all Φs above Φ_C is less than 20 K. The comparison of 1050 rpm and 2100 rpm thermodynamics is shown for the $\Phi = 0.98$ case in Figure 6.22. There is no need for an expanded view of the late cycle thermodynamics because late cycle pressure, crevice flows, and AHRR are identical on a crank-angle basis, and the primary difference in the late-cycle temperatures is apparent from Figure 6.22.

The 1050 rpm case successfully extends the time spent in the temperature range of interest. Maintaining the fuel mass between the two engine speeds results in well-matched peak temperature and well-matched CAD-resolved temperature and pressure. The peak apparent heat release rate is about 2.5 J/CAD higher in the 1050 rpm case, which is expected due to the longer time available for flame propagation per CAD. Although turbulence helps offset this effect with higher engine speed, the increase in turbulence does not quite augment the flame speed enough to match the 1050 rpm condition. The temperature decreases more quickly with CAD for the 1050 rpm case because there is twice as much time for heat transfer than in the 2100 rpm case. Similarly, although the crevice flow rate is lower for the 1050 rpm case, the total crevice mass is nearly the same because the flow rate is integrated over twice as much time. The close thermodynamic matching between

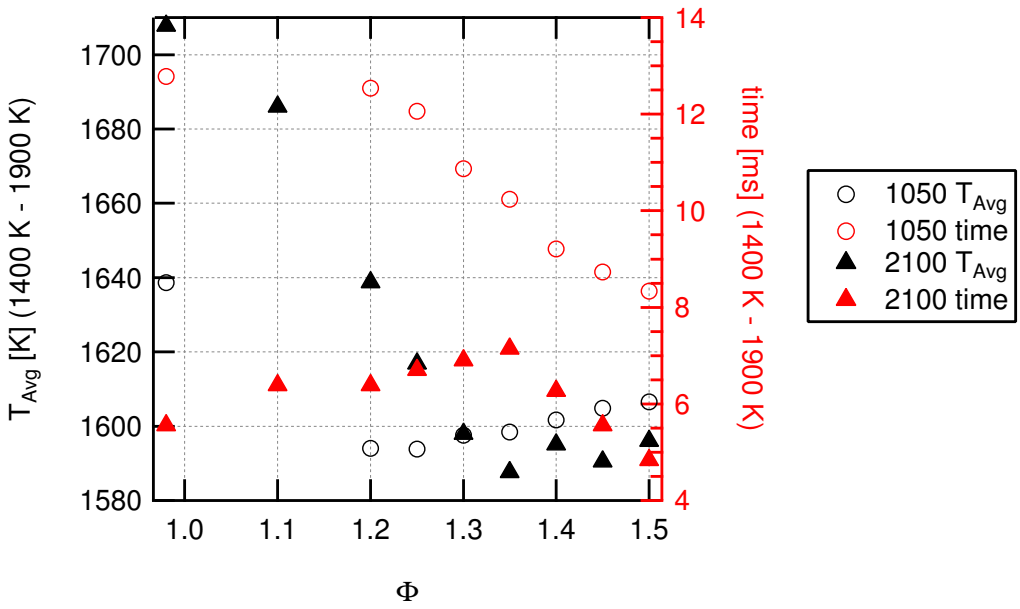

Figure 6.21: Average temperature (left axis) and time spent (right axis) between 1900 K and 1400 K late in the cycle as a function of Φ for the speed study. For cases where temperatures did not reach 1400 K before EVO, the times and average temperatures recorded are those between 1900 K and EVO.

cases makes the rpm study a useful method for quantifying the effect of timescale and temperature late in the cycle.

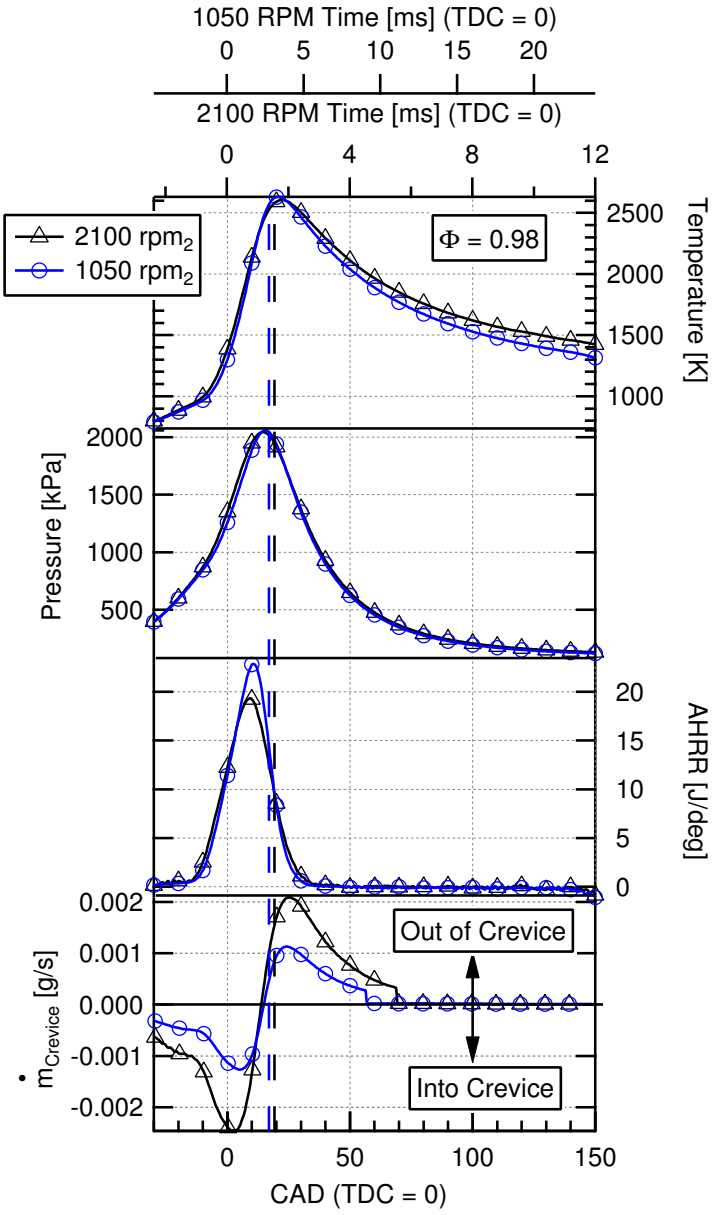

Figure 6.22: Averaged thermodynamic data from $\leqslant 3$ runs of the 1050 rpm and 2100 rpm cases. Markers are drawn every 20 data points. Vertical dashed lines represent approximate location of CA90 for each case. Data comparison for the $\Phi = 0.98$ case is representative of the matching achieved at all Φ.

6.3.2 Particulate Results

Comparisons of the 2100 rpm and 1050 rpm cases at selected Φs are shown in Figure 6.23. The first trend to note in Figure 6.23 is that the effect of reduced rpm under PMPV operation is the opposite of what has been shown for both PFI [59, 60] and SIDI [71] engines, where particles were shown to increase with an increase in rpm. Reducing rpm by half has the effect of increasing particulate in all cases. The NFB PSD is slightly higher at 1050 rpm than at 2100 rpm, although the difference between the two speeds is likely within the day-to-day repeatability of the NFB (note that the 2100 rpm data show here is the average of 7 scans from a single day). The speed study was performed at the same time as the load study, so the 2100 rpm data is the same for both, and the decreased 2100 rpm baseline is used for critical enrichment calculations for both speeds here. The critical enrichment thresholds are given in Table 6.3.

Above Φ_C, for the lower rpm condition both the GMD and total particulate number increase quickly above the critical equivalence ratio. Once the small particle dN/dlog(Dp) reaches approximately 10^8 for a D_m of 10 nm the large rate of agglomeration begins to flatten out the PSD. At the highest equivalence ratio the number of small particles decreases due to agglomeration and the total concentration levels off with increasing Φ although the total mass continues to grow. Comparison of PSDs for 1050 rpm vs. 2100 rpm at $\Phi = 1.5$ demonstrates the important distinction between particle number and particle mass. The total number is similar between the two cases, but due to the higher GMD, the total mass

Table 6.3: Speed-dependent critical sooting thresholds

Speed	Ψ_C^{1X}	Ψ_C^{10X}	Φ_C^{1X}	Φ_C^{10X}	C/O_C^{1X}	C/O_C^{10X}
2100	0.856	0.885	1.30	1.35	0.446	0.461
1050	0.808	0.832	1.23	1.27	0.421	0.433

The NFB total particulate number used for all graph normalizations is 27,863 [$1/cm^3$].
Superscript "1X" refers to 1X NFB results.
Superscript "10X" refers to 10X NFB results.

produced at low rpm is much higher. The 2100 rpm and 1050 rpm GMD comparison for all Φs can be found in Figure 6.26.

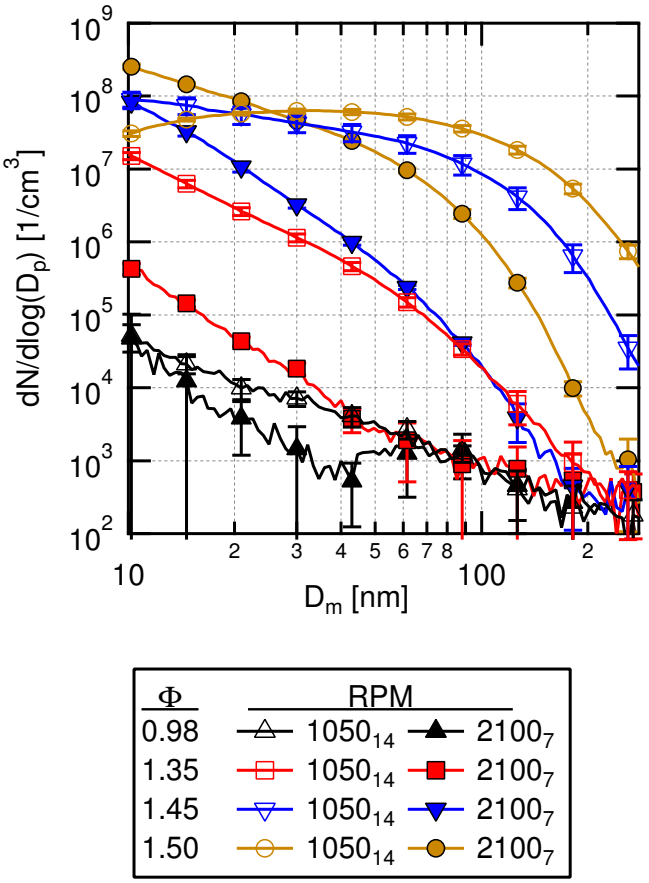

Figure 6.23: Averaged PSDs from ⩽ 21 scans of 2100 rpm and 1050 rpm cases at selected Φ. Markers are drawn every 10 data points.

The normalized total particle number concentrations and indicated specific particle number emissions at every Φ for the 2100 rpm and 1050 rpm conditions are shown in Figure 6.24. At low rpm Φ_C decreases. The shift from inception dominated PSDs to agglomeration dominated PSDs occurs at lower Φ for the lower speed condition, as seen in the GMD plot in Figure 6.26. Due to this shift, the mass concentration continues to increase approximately exponentially as shown by the approximately linear increase with Φ on the log-linear plot in Figure 6.25, despite the decreased dependence of particulate number on Φ at high Φ.

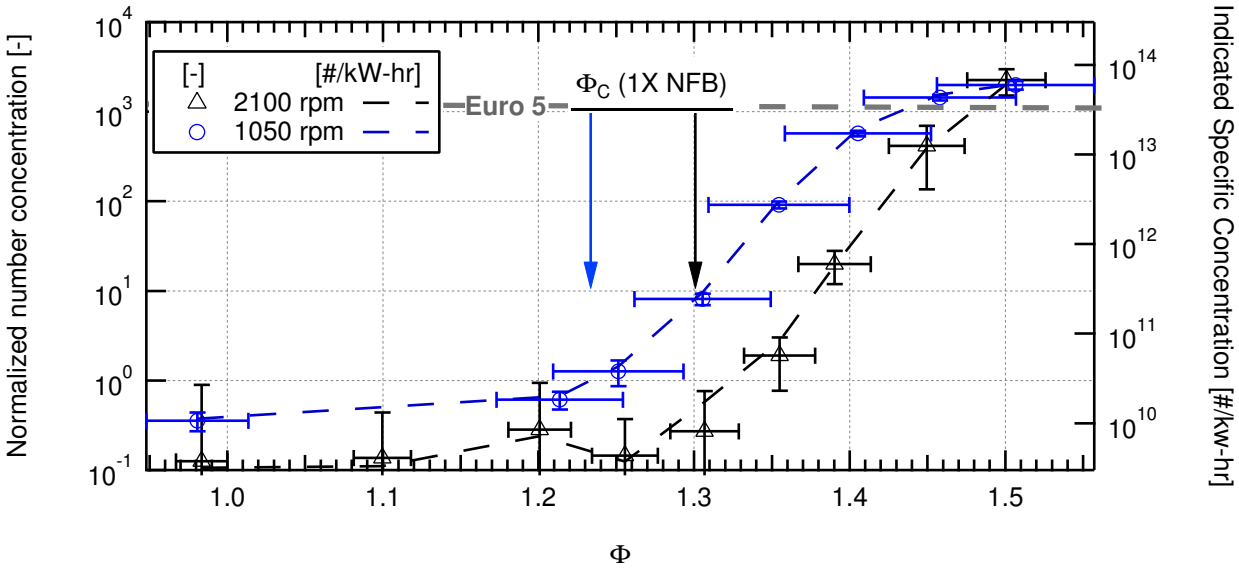

Figure 6.24: Integrated particulate number concentrations normalized by the NFB (left axis, symbols) and indicated specific particulate number emissions (right axis, dashed lines) vs Φ for the 2100 rpm and 1050 rpm cases. Vertical arrows denote approximate x-axis locations of Φ_C based on 1X NFB results. For graph clarity, uncertainty bounds are only applied to the concentration data.

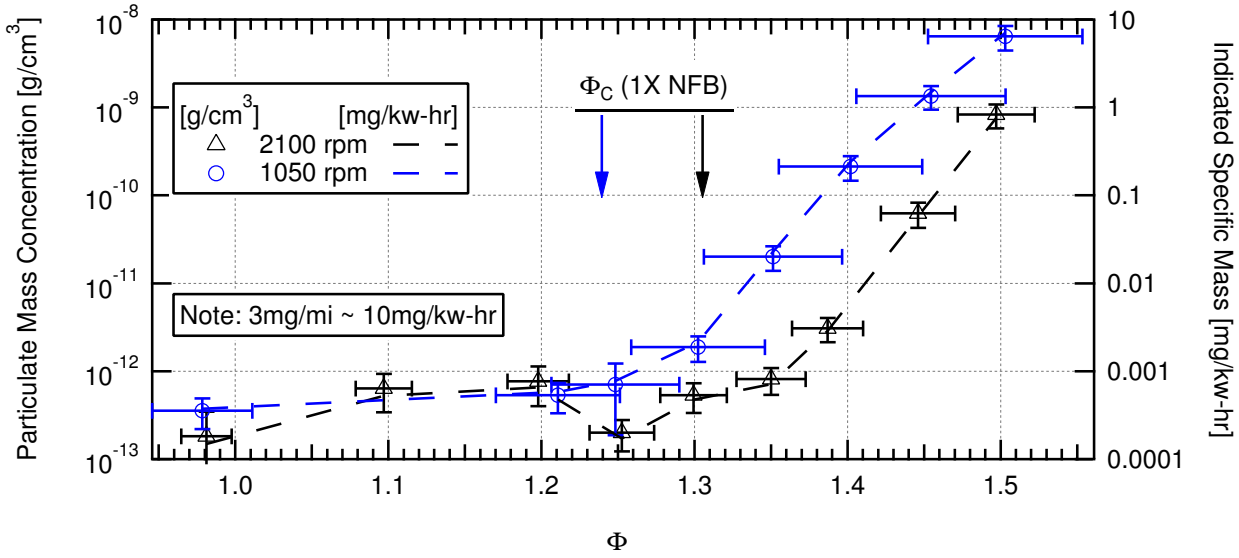

Figure 6.25: Integrated particulate mass concentrations (left axis, symbols) and indicated specific particulate mass emissions (right axis, dashed lines) vs Φ for the 2100 rpm and 1050 rpm cases. Note that values are absolute, rather than normalized. Vertical arrows denote location of Φ_C based on 1X NFB results. For graph clarity, uncertainty bounds are only applied to the concentration data.

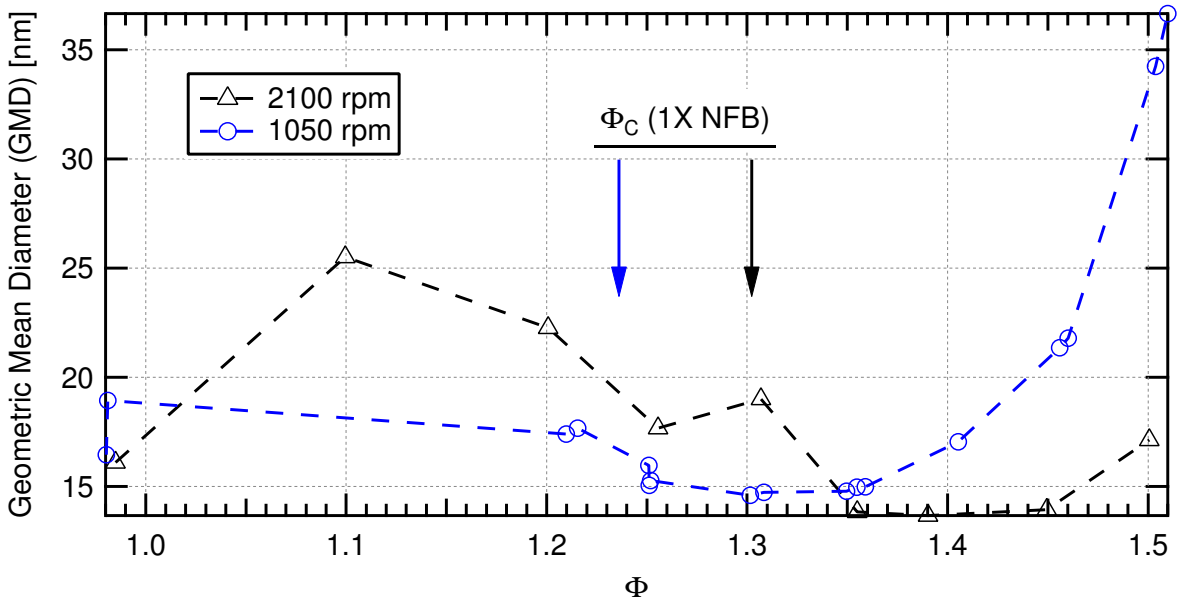

Figure 6.26: Geometric Mean Diameter (GMD) as a function of Φ for both engine speeds

6.3.3 Discussion

The substantial impact of time available for particulate formation on soot onset and soot yield indicates that soot formation is kinetically limited in the engine as compared to premixed laboratory flames. The strong dependence on time for the engine data correlates well with the rapid increase in soot volume fraction near the main reaction zone under sooting conditions in premixed laminar flames which occurs at similar time scales to those in the engine [16, 75]. However, the dependence on time appears to be somewhat stronger than in laboratory laminar flames. To fully characterize the time dependence and to compare with laboratory flames, a wider range of engine speeds should be tested in the future.

While the particles spend twice as much time in the engine, it is also worth noting that the volumetric flow rate was effectively cut in half, so they also spent twice as much time between the exhaust port and sample point. Between these points the temperature drops from about 773 K to 523 K. It is possible that particulate agglomeration could continue during this period. The fact that the trend with rpm for PMPV is the opposite of the trends with rpm under DI supports earlier conclusions that the reduced mixing and evaporation time is the driving factor for particulate with increasing engine speed under DI operation. However, this study also shows that the effect of reduced residence time in this rpm range is to reduce particulate formation from a premixed flame. This effect would be in direct competition with the effect of reduced evaporation and mixing time during DI operation.

Finally, Figure 6.27 shows the ratio of fuel carbon crevice mass returned after CA90 to the total particulate mass as a function of Φ for the two speeds. Although the crevice mass flow rate in the 1050 rpm case is lower than in the 2100 rpm case, the total carbon mass from the crevice is very similar for both cases. Additionally, the ratio drops below 1.0 for the highest Φ cases for both speeds. This suggests that the difference between the sooting tendencies for these two speeds is not due to differences in crevice mass flows.

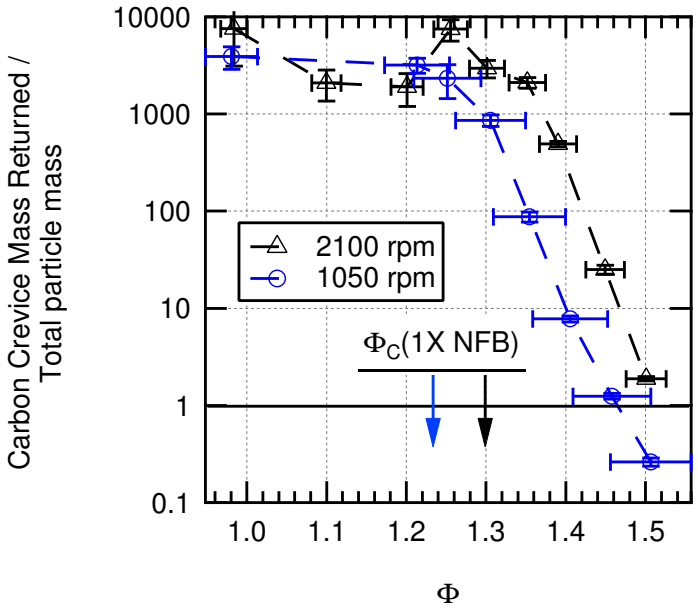

Figure 6.27: Ratio of the fuel carbon crevice mass returned after CA90 to the total particulate mass per cycle as a function of Φ for the 1050 rpm and 2100 rpm cases. Dashed lines are intended only to guide the eye.

7 SPARK-IGNITION DIRECT-INJECTION ENGINE OPERATION: EFFECTS OF FUEL PHYSICAL PROPERTIES

The PMPV results helped to: establish the minimum achievable levels of particulate for this engine, establish the minimum level of enrichment for soot formation, and characterize the effects of thermodynamic conditions, kinetic timescale, and fuel chemistry on particulate formation under premixed conditions. In this chapter, the focus is shifted to direct-injection operation where soot formation will be influenced not only by the fuel chemistry and thermodynamic conditions, but also by the presence of the spray and as a result the fuel's physical properties. The results of the PMPV investigations provide a framework for interpreting results under SIDI operation and allow the influence of fuel physical properties on particulate formation to be studied.

An end of injection (EOI) sweep under SIDI operation was performed for EEE and TRF30. This study had four main goals: first, to view the differences in sooting under SIDI conditions relative to those under PMPV operation, second, to test the ability of TRF30 to duplicate EEE sooting under SIDI operation, third, to use differences in the physical properties of TRF30 and EEE to determine the relative importance of physical sooting effects versus chemical sooting effects, and fourth, to attempt to separate soot formation due to charge heterogeneity from soot formation due to non-premixed combustion of in-cylinder liquid films and droplets.

7.1 Fuel Properties and Operating Conditions

TRF30 was shown in the PMPV studies to be an appropriate chemical surrogate for EEE. With this background it is hypothesized that any differences in sooting tendencies between the two fuels under SIDI operation can be attributed to the differences in physical fuel properties, resulting in differences in in-cylinder mixture formation. This hypothesis is

Table 7.1: EEE, surrogate component, and TRF30 physical properties

Fuel	Abs. Viscosity [N s/m^2]	Density [kg/l]	ΔH_v [kJ/kmol]	RVP [kPa]
EEE	6.00E-4 [9]	0.742[a]	34900[99]	62.74[a]
iso-octane	5.00E-4[d,e]	0.691[a]	30790[c]	5.47[a]
n-heptane	3.76E-4[d]	0.684[a]	31785[c]	11.10[109]
toluene	5.50E-4[d]	0.867[a]	33319[c]	7.12[109]
TRF30	5.00E-4[18]	0.742[d]	31499[f]	7.49[b]

[a] Data from manufacturer's data sheets
[b] Calculated using Rault's Law
[c] Calculated in EES
[d] From www.engineeringtoolbox.com
[e] value is for octane
[f] calculated using a linear molar blending assumption

further supported by the fact that Witkowski et al. [122] demonstrated the matching of sooting tendencies for TRF30 and EEE in a laminar co-flow diffusion flame. So from a chemical sooting tendency perspective TRF30 has been validated as a suitable surrogate for EEE under both premixed and non-premixed conditions.

Although the chemical sooting tendencies of the two fuels are well matched, the volatility properties are not. The volatility properties are expected to play a primary role in soot formation under SIDI operation. Comparison of the two fuels under carefully selected SIDI conditions is useful in determining the relative importance of the differences in volatility properties. The volatility properties of interest for the two fuels and the SIDI operating conditions used to test the influence of those properties are discussed here before moving on to the discussion of the results.

Table 7.1 lists physical fuel properties for both EEE and TRF30 along with the properties of the pure fuel components. All the physical properties of TRF30 are based on ideal mixing assumptions. Although the viscosity and enthalpy of vaporization for EEE are not listed in the manufacturer's data sheet, general values are listed from other sources. The density, Reid Vapor Pressure (RVP), and distillation results are listed in the data sheet, and can be compared to the calculations for TRF30.

The viscosity and density of EEE and TRF30 are similar, but the volatility properties are quite different. EEE has a much higher RVP than TRF30, but also has a much wider boiling point range than TRF30. The distillation curves shown in Figure 7.1 display a more complex vaporization process for EEE than for TRF30. The TRF30 distillation is close to a flat line, reflecting the fact that the three components in the mixture all have similar boiling points. EEE has an initial boiling point slightly greater than room temperature and an end boiling point of over 200 °C. The 40% recovery temperature is approximately the same as the boiling points of the components of TRF30. Since the enthalpy of vaporization is similar for EEE and TRF30, 40% of the components of EEE will vaporize more easily than TRF30, but the remaining 60% may require higher temperatures to completely vaporize. These heavier components could represent a source for soot due to their lower volatility.

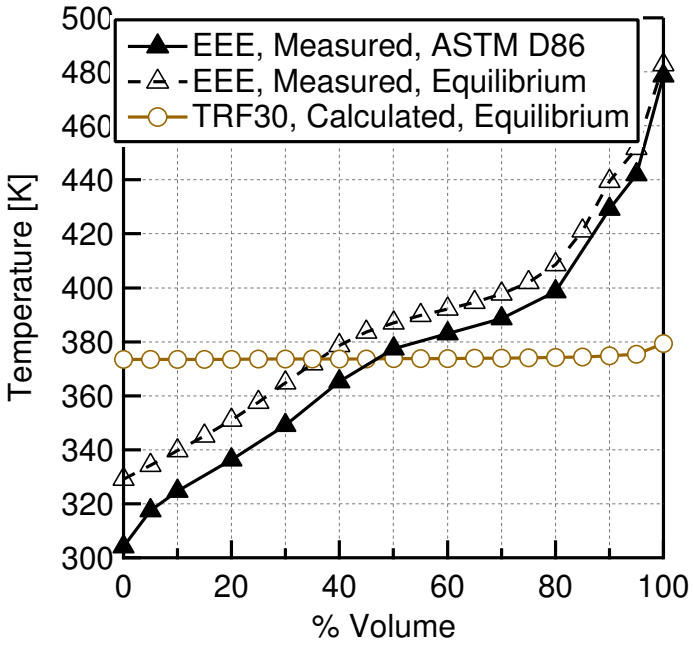

Figure 7.1: Comparison of EEE and TRF30 distillation curve comparison. EEE curves are measured using both equilibrium and ASTM D86 methods [37]. TRF30 curve is calculated according to an equilibrium method.

To test for the influence of wall wetting and incomplete mixing during SIDI operation, a range of injection timings at an equivalence ratio of 0.98 were tested for both EEE and

TRF30. Since the chemical sooting properties of the fuels are matched under both premixed and diffusion flame conditions differences in sooting can be attributed to physical property differences causing differences in fuel impingement and vaporization or differences in in-cylinder fuel mixing. Fuel impingement is more likely for earlier timings and may contribute to diffusion-limited burning of liquid films [88] but mixing time is also maximized for earlier injection times which is expected to contribute to a more homogeneous bulk-gas charge [23].

The EOI timings tested for both fuels were -340 CAD, -250 CAD, -220 CAD, and -140 CAD. The piston positions for these cases and two additional EOI timing cases that were run for EEE only are depicted in Figure 7.2. The EOI = -340 CAD case was chosen because it is expected to have a high level of fuel impingement and a long available mixing time, so soot formation above the NFB is assumed to be dominated by the liquid film generated on the piston during the injection process. The EOI -250 CAD case was expected to generate a low number of particles because it has close to the optimal tradeoff between maximized mixing time and minimized wall wetting due to the distance of the piston from the injector and the bulk in-cylinder tumble motion limiting penetration to the cylinder liner. Charge motion is expected to deflect the fuel plume away from the wall as injection timing is retarded [73], due to stronger intake flow at higher piston speeds. The maximum piston speed occurs at -270 CAD. The EOI = -220 CAD and -140 CAD cases were chosen because they represent identical piston positions with different mixing conditions. The EOI -220 CAD condition has significantly greater mixing time available before the time of spark and likely has higher in-cylinder flow than the -140 CAD condition. Table 7.2 summarizes the test conditions for this study. All conditions were characterized by a speed of 2100 rpm, an IMEP of 334 kPa, a CA50 of +8 CAD, and $\Phi = 0.98$.

Maintaining speed, load, and combustion phasing between fuels resulted in similar temperature, pressure, AHRR, and crevice mass flows between the two fuels for a given injection timing. Although the load, speed, and combustion phasing were also maintained

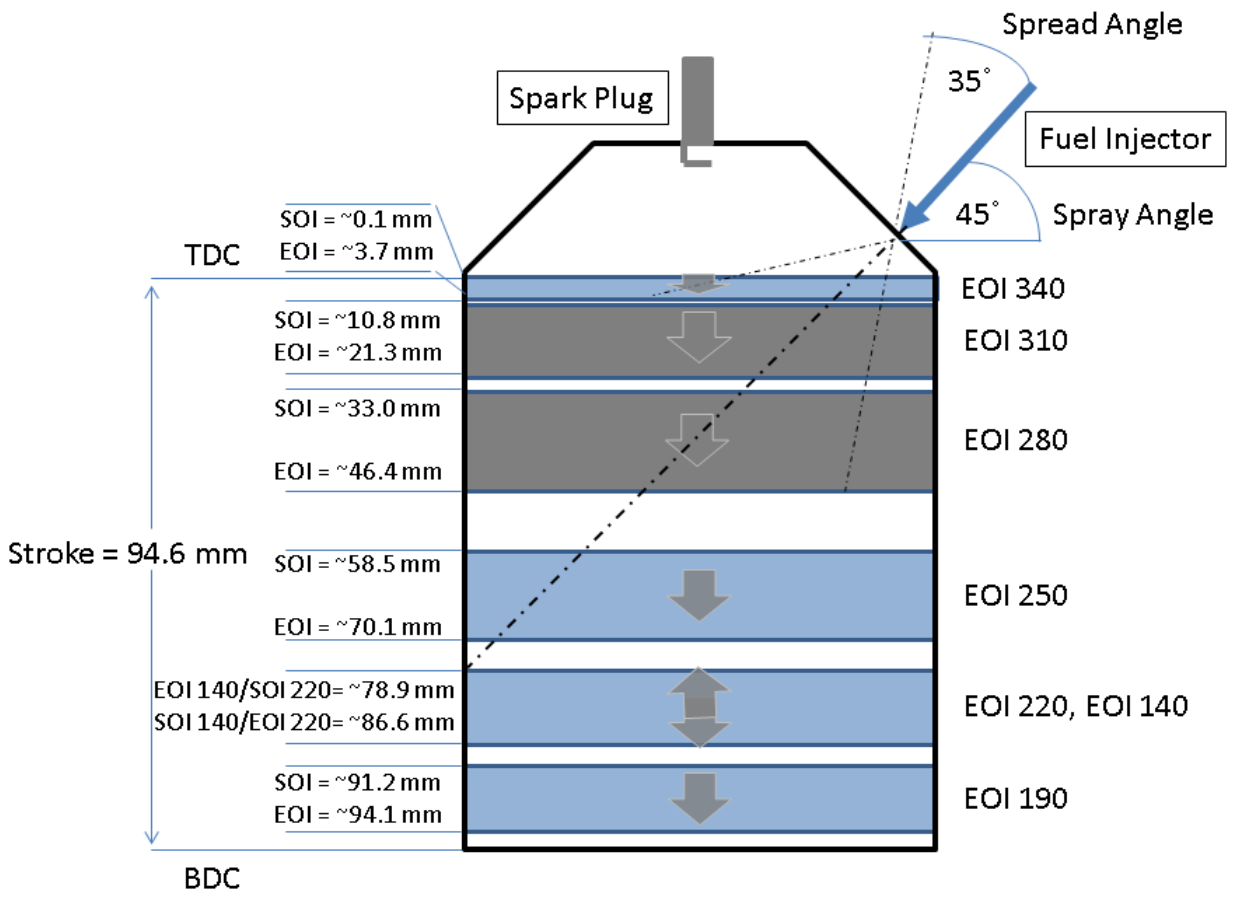

Figure 7.2: Approximate piston surface positions for the EOI timings studied here. For a downward moving piston the top of the rectangles represent the top of the piston surface at SOI, and the bottom of the rectangles represent the piston position at EOI. Distances quoted are distance from the position of the piston face at the top of its stroke. Gray rectangles represent cases where only EEE was tested. Blue rectangles represent cases where EEE and TRF30 were tested.

for all injection timings, the peak temperature decreased as injection timing was retarded from -340 CAD to -140 CAD. The TRF30 thermodynamics for each EOI were nearly identical to those of EEE. The thermodynamic parameters at each EOI are compared for EEE and TRF30 in Figures 7.3 and 7.4. The average late cycle temperatures and times spent between 1900 K and 1400 K for EEE and TRF30 are plotted in Figure 7.5. Although the average temperatures vary by as much as 60 K for the two EOI extremes, the time spent in the critical temperature range is very similar between the two fuels at every EOI.

Table 7.2: SIDI injection timing and fuel effects study parameters

EOI [CAD]	Fuel1	Fuel2
-340	EEE	TRF30
-310	EEE	-
-280	EEE	-
-250	EEE	TRF30
-220	EEE	TRF30
-190	EEE	-
-140	EEE	TRF30

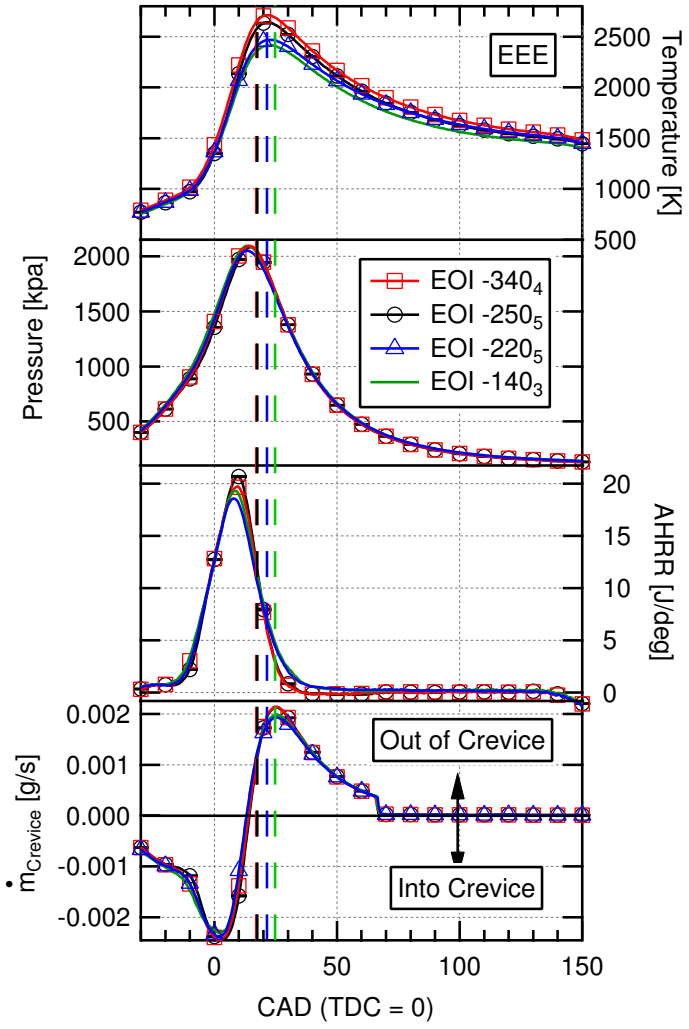

Figure 7.3: EEE comparisons of thermodynamic parameters for the four EOI cases that were matched with TRF30 EOI cases. Markers are drawn every 20 data points. Vertical dashed lines represent approximate location of CA90 for each case.

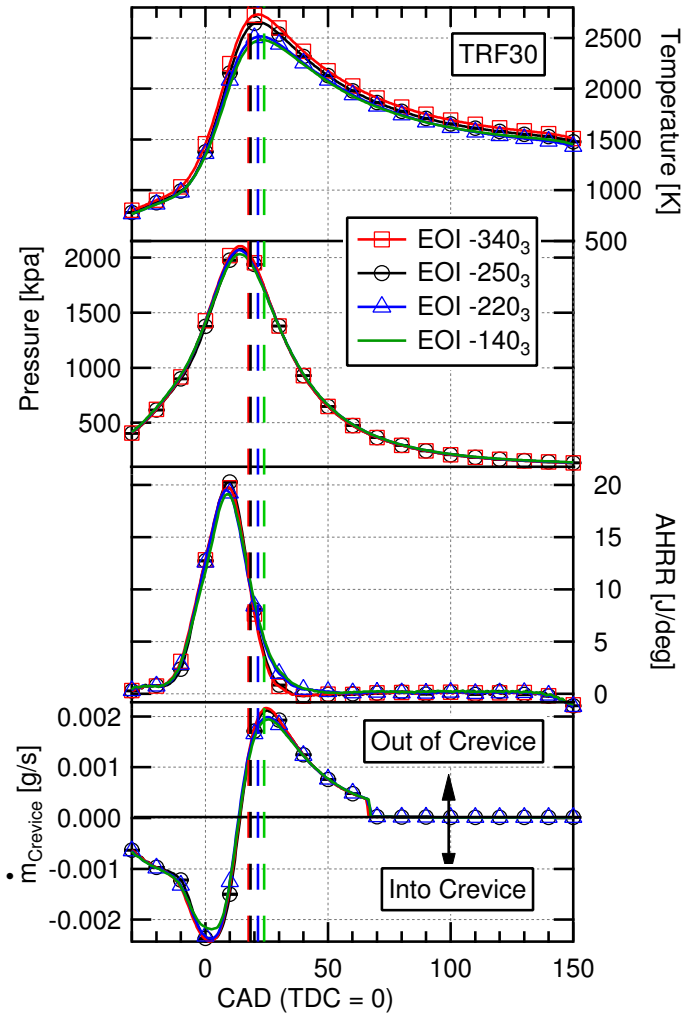

Figure 7.4: TRF30 comparisons of thermodynamic parameters for the four EOI cases that were matched with TRF30 EOI cases. Markers are drawn every 20 data points. Vertical dashed lines represent approximate location of CA90 for each case.

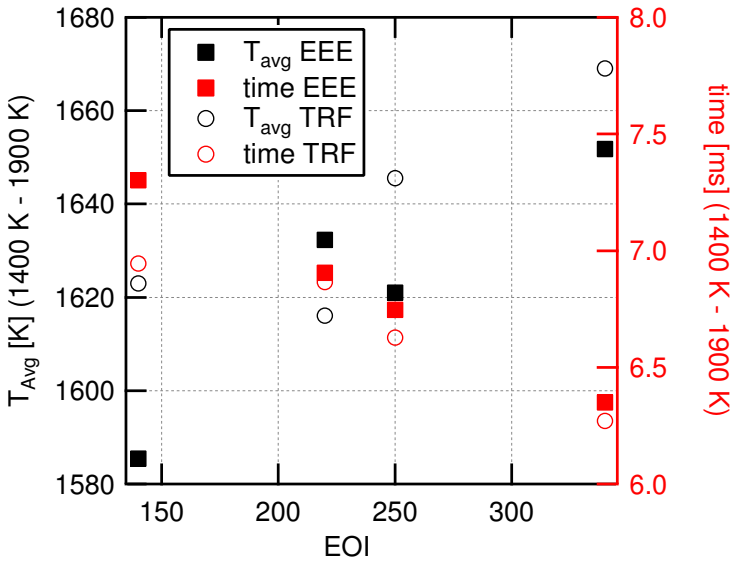

Figure 7.5: Average temperature (left axis) and time spent (right axis) between 1900 K and 1400 K late in the cycle as a function of EOI for TRF30 and EEE. For cases where temperatures did not reach 1400 K before EVO, the times and average temperatures recorded are those between 1900 K and EVO.

7.2 EEE PMPV vs. EEE SIDI Particulate Data

The first goal of this study (stated at the beginning of the chapter) was to view the differences in sooting under SIDI conditions relative to those under PMPV operation, and the fourth goal was to separate soot formation due to charge heterogeneity from soot formation due to non-premixed combustion of in-cylinder liquid films and droplets. Both goals are addressed in Figure 7.6 where the EEE SIDI EOI sweep PSD results are compared against the bounds of the EEE PMPV Φ sweep results. Recall that both the SIDI EOI sweep and the PMPV Φ sweep were run at 334 kPa IMEP and CA50 = +8 CAD, and are relatively comparable from a thermodynamics standpoint.

All the SIDI cases were run at $\Phi = 0.98$, so particle numbers above the NFB are either the result of charge inhomogeneities and locally rich premixed flames or the result of non-premixed combustion of in-cylinder liquid films and droplets. Comparison of the rich PMPV PSD to the SIDI PSDs gives an indication of which type of combustion likely dominates. Rich EEE PMPV operation at an equivalence ratio of 1.47 produces several orders of magnitude lower number of large particles ($D_m > 100$ nm) and more than an order of magnitude more small particles than the EOI -140 SIDI condition. This is significant given the fact that the entire in-cylinder charge under PMPV operation is at a high equivalence ratio, whereas, for SIDI operation the overall equivalence ratio is slightly lean. This suggests that the PSD for the EOI -140 condition is likely dominated by diffusion-limited burning of liquid films and droplets or very rich partially-premixed regions resulting from liquid films and droplets. As injection timing is advanced the SIDI distributions initially become less dominated by accumulation mode particles and the distribution shape more closely resembles those for PMPV operation, suggesting that some of the particulate is the result of rich premixed regions. As injection timing is further advanced to -340 CAD the accumulation mode particles increase suggesting that the impingement of the fuel spray on the piston and potential splashing of the fuel off the piston onto the cylinder head and valves results in increased liquid films and diffusive

combustion. The overall observation from Figure 7.6 is that the presence of a significant number of accumulation mode particles that result from growth of soot via agglomeration is a good indication of very rich, likely diffusive, combustion resulting from impingement of the fuel spray or the presence of droplets at the start of combustion.

Figure 7.7 presents the same data as Figure 7.6, but each PSD is normalized by its respective peak particle number. The y-axis has also been changed to a linear scale. This treatment makes the dominant particle diameters for each case more recognizable. The cases that are most likely to have diffusion limited burning are characterized by peak particle numbers between 60 nm and 70 nm, while the cases that are less likely to have diffusion-limited burning have peak concentrations at the smallest measurable particle size.

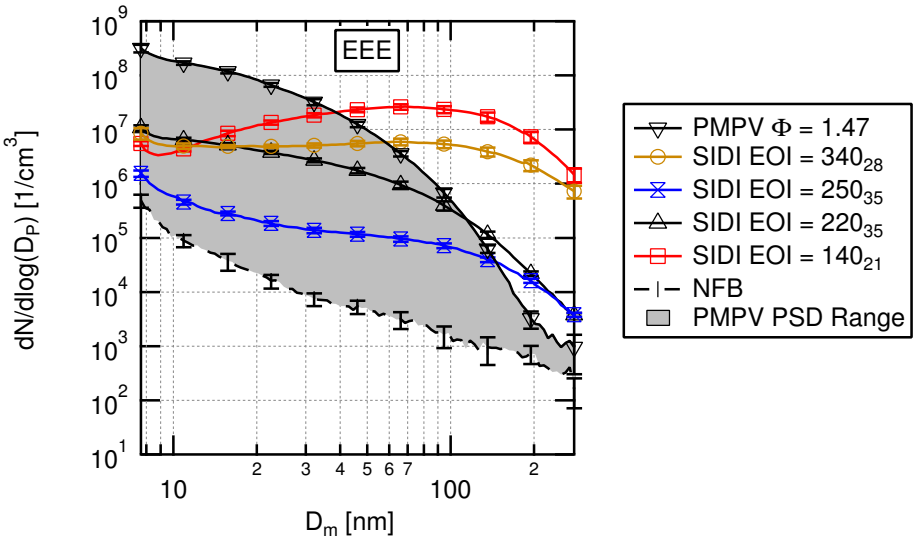

Figure 7.6: EEE SIDI EOI sweep cases plotted along with the extremes of the EEE PMPV Φ sweep. Few PMPV cases resulted in PSDs outside of the NFB or the $\Phi = 1.47$ PSD. Therefore, the gray area between the two marks the range of PSDs present for PMPV cases when operating using EEE with Φ between 0.98 and 1.47. Markers are drawn every 10 data points.

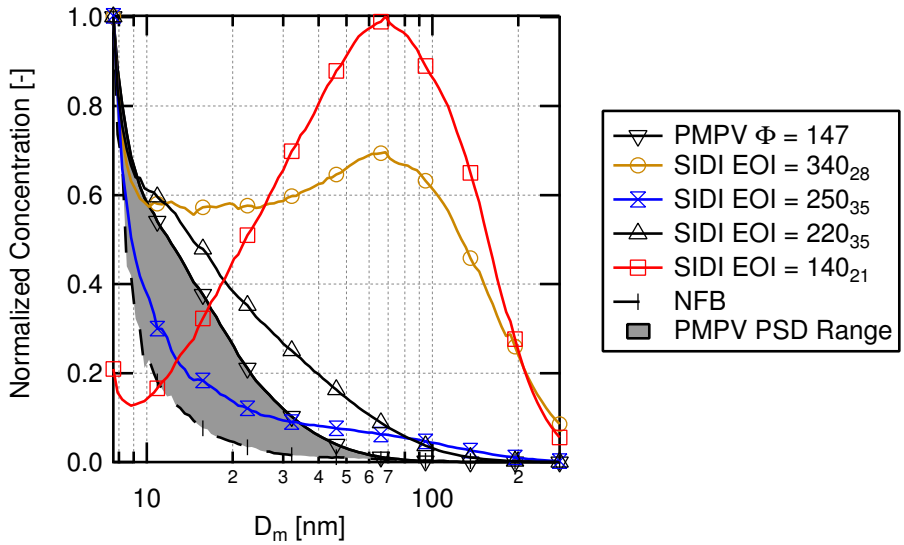

Figure 7.7: PSDs for EEE SIDI EOI sweep cases and EEE PMPV Φ sweep extreme cases normalized by their respective peak particulate numbers . A y-axis value of 1.0 denotes the location of the peak particulate number for each case. The gray area between the two PMPV cases marks the range of PSDs present for PMPV cases when operating using EEE with Φ between 0.98 and 1.47. Markers are drawn every 10 data points.

7.3 TRF30 SIDI vs. EEE SIDI Particulate Data

The second and third goals of this study were to test the ability of TRF30 to duplicate EEE sooting under SIDI operation, and to use differences in the physical properties of TRF30 and EEE to determine the relative importance of physical fuel property effects versus chemical sooting effects. These goals were addressed by comparing TRF30 and EEE over the range of SIDI injection timings.

The total particle numbers and indicated specific particle number emissions for all the cases are shown in Figure 7.8. The corresponding total mass concentrations and indicated specific particulate mass emissions are shown in Figure 7.9. Two interesting results are worth noting based on Figures 7.8 and 7.9. First, there appears to be a tradeoff between the effects of mixture homogeneity and wall wetting when using EEE as the fuel. The earliest injection timing (EOI -340) is guaranteed to have a significant level of piston wetting, but also a long time for evaporation and mixing. As the piston travels downward, piston wetting should decrease, but mixing time also decreases. Near the bottom of the piston travel, piston wetting is unlikely but cylinder wall wetting is more likely to be due to reduced intake flow. At the late injection timings the time available for evaporation and mixing following injection is reduced. This combination of factors explains the increase in particles for more retarded injection times. The latest injection timing (EOI -140 CAD) has significantly decreased mixing time and some wall wetting is likely. This is the likely reason that the EOI -140 case produces the largest number of particles. The best tradeoff between wall wetting and mixing time appears to occur for EEE around an EOI = -310 CAD simultaneous with the high in-cylinder flow motion and a relatively long time for evaporation and mixing prior to combustion.

The most interesting finding is that the TRF30 and EEE results become very different as injection timing is advanced, and there does not seem to be a tradeoff between the effects of wall wetting and mixing time for TRF30 at the earliest injection timing. Most notably, at an EOI of -340 CAD, where the EEE particle number increases sharply, theTRF30 particle

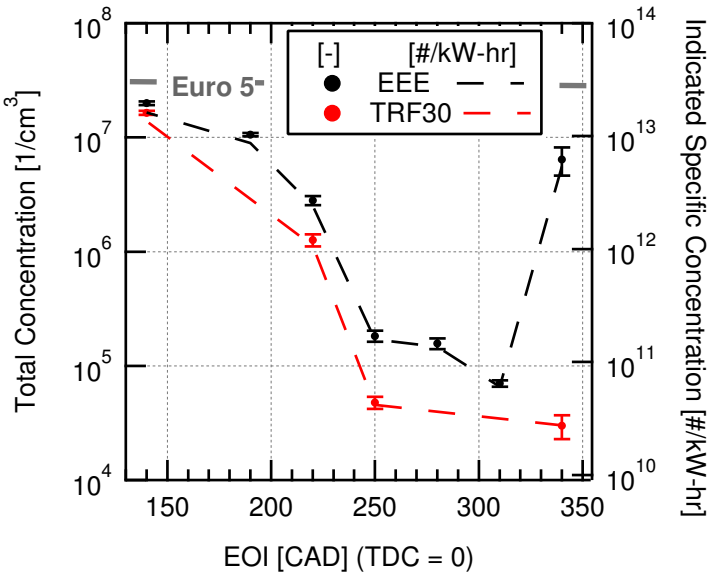

Figure 7.8: Integrated particulate number concentrations (left axis, symbols) and indicated specific particulate number emissions (right axis, dashed lines) vs. EOI for TRF30 and EEE SIDI cases. For graph clarity, uncertainty bounds are only applied to the concentration data.

number continues to drop. Piston wetting is insured at this injection time for both fuels, but time for evaporation and mixing is maximized. Therefore, it is likely that EEE does not evaporate completely off the in-cylinder surfaces or fails to mix significantly prior to ignition. Optical SIDI studies have shown piston impingement resulting in pool fires for gasoline [88, 100] providing further support for the conclusion that EEE is not fully evaporating prior to combustion. On the other hand, TRF 30 must evaporate completely and mix well prior to ignition. A likely explanation is that the large amount of fuel impingement reduces the piston temperature for both fuels, but due to the lower end boiling point of TRF30 it is able to fully evaporate from the piston, whereas the high end boiling point of EEE prevents complete evaporation at the depressed piston temperatures caused by the severe wetting of the piston surface.

The corresponding PSDs are shown for EEE in Figure 7.10 and for TRF30 in Figure 7.11. Two interesting results are noteworthy. First, the TRF30 -340 CAD EOI condition PSD is only slightly higher than the NFB, confirming the assertion that the charge is almost fully

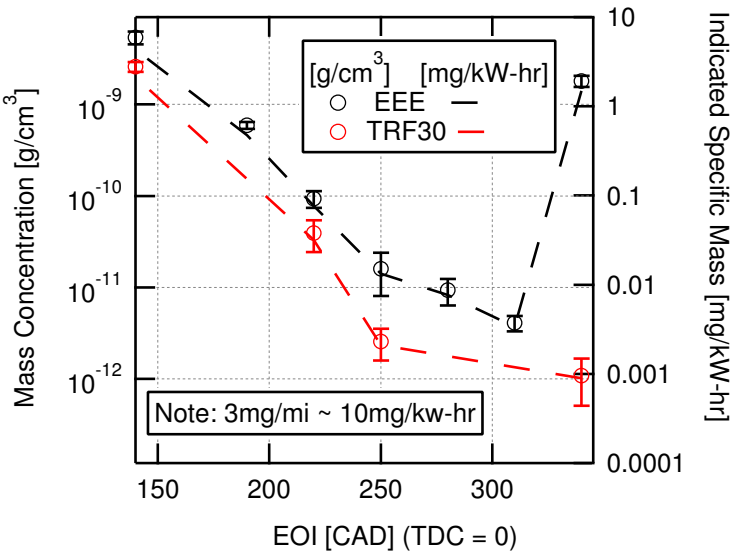

Figure 7.9: Integrated particulate mass concentrations (left axis, symbols) and indicated specific particulate mass emissions (right axis, dashed lines) vs. EOI for TRF30 and EEE SIDI cases. For graph clarity, uncertainty bounds are only applied to the concentration data.

mixed and vaporized at ignition. The thermodynamic conditions for the TRF30 EOI = -340 CAD case and a TRF30 PMPV, $\Phi = 0.98$ case are compared in Figure 7.13. Note that the thermodynamic conditions for both cases match well, suggesting that the difference between the two results is likely due to slightly more mixture heterogeneity for the DI case. Second, note that the TRF30 and EEE results are similar for EOI = -140 CAD and EOI = -220 CAD, and begin to diverge as the timing is advanced earlier than EOI = -250 CAD. Based on the previous conclusion that agglomeration-dominated PSDs appear to be a marker of non-premixed burning or very rich regions resulting from liquid films and droplets, it is likely that the EOI cases later than EOI -250 are progressively more dominated by regions that have liquid fuel present or are very poorly mixed when they combust. At EOI = -140 CAD there is little time following the end of injection before the piston sweeps over the wall region where fuel impingement may have occurred, trapping this fuel in the crevice region until it is released during the expansion stroke, making the crevice region very rich. This phenomenon may explain why the later injection conditions (EOI -140 and -220 CAD)

seem to have results that are converging for EEE and TRF30 even though the two fuels have much different vaporization characteristics as determined from the -340 CAD EOI case.

The emissions trends with EOI for the two fuels provide some additional insight, and are shown in Figure 7.12. Note in Figure 7.12 that the concentrations have been normalized so that the trends for CO, O_2, CO_2 and HC could be plotted on the same graph. Each species was normalized against the EEE EOI -340 CAD value. While CO_2 and HC trends are similar between the fuels, note that at EOI -340 CAD, the TRF fuel produces lower CO, and although it is not plotted here, the combustion efficiency is about 2% higher than the EEE case. Absolute measurements of these emissions for these cases are given in Figures G.24 and G.25 in Appendix G.

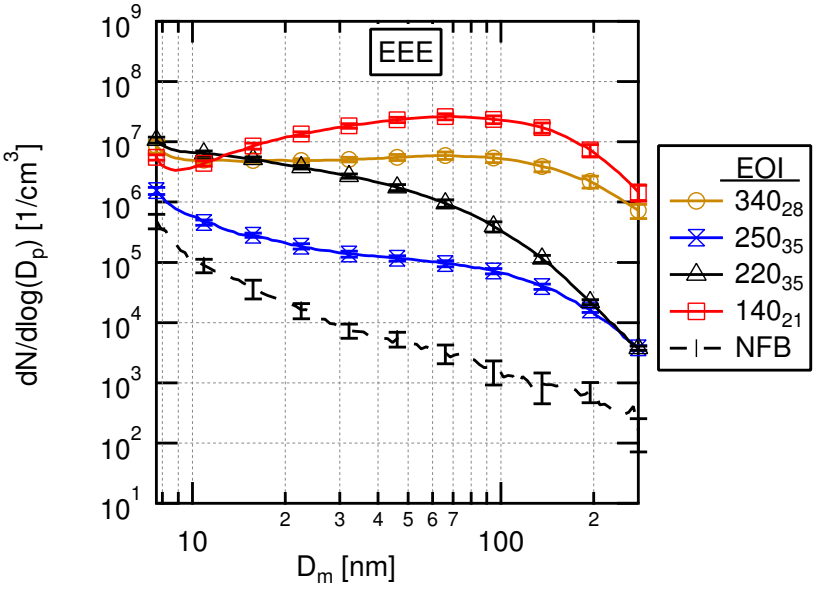

Figure 7.10: EEE PSDs as a function of EOI. Markers are drawn every 10 data points. NFB trace matches that from [50].

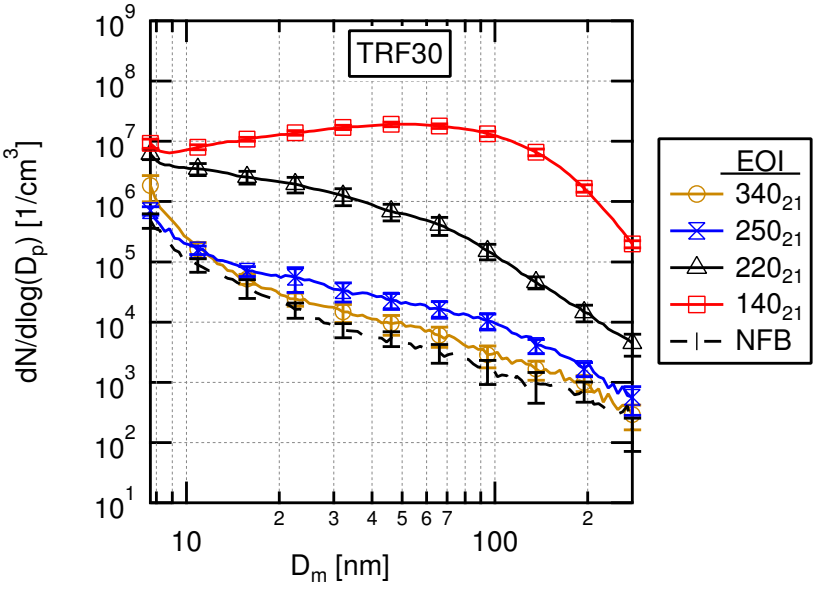

Figure 7.11: TRF30 PSDs as a function of EOI. Markers are drawn every 10 data points. NFB trace matches that from [50].

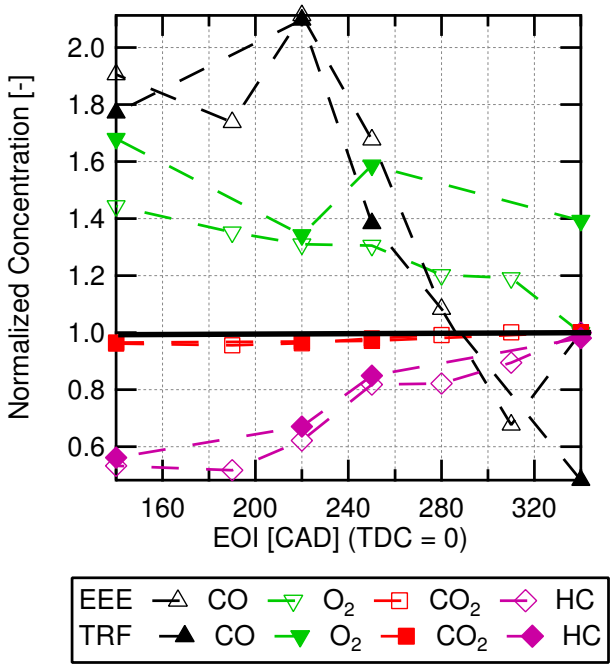

Figure 7.12: EEE and TRF normalized gaseous emissions concentrations as a function of EOI timing. Each species is normalized by the EEE TRF -340 CAD case concentration.

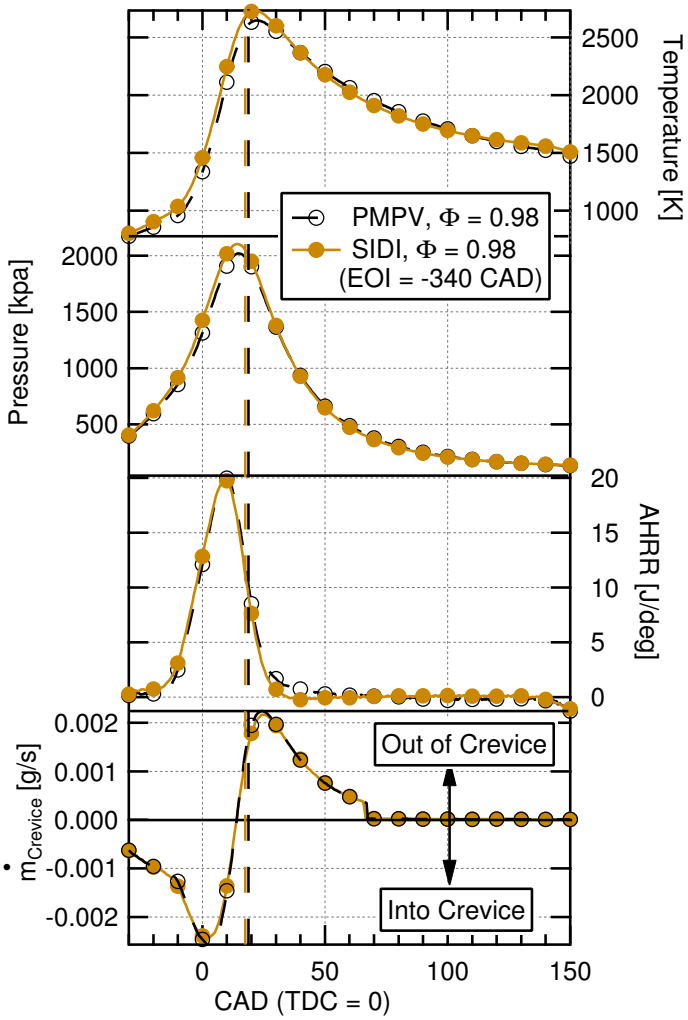

Figure 7.13: TRF30 PMPV Φ = 0.98, and SIDI EOI = - 340 CAD Φ = 0.98 thermodynamic comparisons. Markers are drawn every 20 data points. Vertical dashed lines represent approximate location of CA90 for each case.

7.4 Discussion

The current work and the literature both show that EOI timing has a strong effect on particulate formation. The magnitude of the effect is a function of injection pressure, fuel type, and charge motion. Optimized injection pressure and higher fuel volatility both reduce particulate formation, which may overshadow the effects of changes in EOI [90]. Intake charge motion can reduce fuel impingement by deflecting the fuel spray [73] and compression charge motion promotes pre-ignition mixing [83]. Differences in these three variables cause the optimal injection timing to be engine and operating condition dependent. The optimal injection timing therefore differs between studies, but is commonly found occur during the middle of the intake stroke [35, 54, 68, 86, 90, 92].

Four questions regarding the effects of injection timing, fuel properties, and non-premixed combustion were addressed in this chapter:

1. What is the effect of removing pool fires on particulate formation under DI operation?
2. What are the potential effects of fuel volatility on particulate formation?
3. How can the effects of non-premixed combustion be distinguished from the effects of rich premixed combustion in a PSD?
4. What are the most important factors that determine the optimal injection timing?

The first two questions were addressed by the observed differences in the PSD and total particle number at the EOI -340 timing for EEE and TRF30. For the current circumstance more than 50% of the components in EEE have a boiling point greater than the end boiling point for the TRF30 mixture. These components will be more difficult to vaporize from the piston surface (as compared to TRF30 which appears to have vaporized almost completely) during the time available and are responsible for the increased particle number for EEE at an EOI of -340 CAD. This conclusion is supported by the fact that the two fuels have been shown to have matched sooting tendency for both premixed and non-premixed combustion

conditions. The similarity of the PSD for TRF30 at the EOI -340 condition and the NFB PSD suggests that the equivalence ratio everywhere within the engine cylinder is at or below the critical equivalence ratio for TRF30 determined from the PMPV measurements. The large increase in accumulation mode particles for EEE at the same conditions indicates pool fires as the likely cause of the increase in particulate based on the expected high level of fuel impingement and the supporting results in the literature. In particular, pool fires from a gasoline SIDI engine have been shown in previous work to occur for an SOI timing of -320 CAD, and disappear at a SOI of -260 CAD with a centrally mounted injector [100]. This behavior also appears to be present in the current engine data set.

The fuel properties that most directly influence evaporation are the RVP and the distillation curve (assuming that the enthalpy of vaporization is similar). In a study of fuel chemistry and volatility effects, Vuk et al [118] tested fuels with variations in both the distillation curve and in the RVP. They cited high boiling points as a primary factor for increased particulate formation between fuels. More rapid vaporization reduces diffusive burning of in-cylinder liquid fuel and improves mixture homogeneity [86, 90]. This conclusion is supported by the current work based on the fact that TRF30 has approximately matched chemical sooting tendency and enthalpy of vaporization with EEE, but has a lower RVP and much lower end boiling point. It is important to note that the role of enthalpy of vaporization is not explored here but this will have a strong impact for fuels with significantly different enthalpy of vaporization than gasoline, e.g., ethanol and ethanol-gasoline blends.

The third question was addressed by the comparison between PMPV and SIDI PSDs. The high Φ PMPV cases did not produce the same number of large particles that the slightly lean SIDI cases produced, suggesting that a shift to accumulation mode particles was a sign of non-premixed combustion rather than slightly or moderately rich premixed combustion.

To answer the fourth question, injection pressure, charge motion, and fuel physical properties must all be considered simultaneously. This is easier now that the effects of fuel physical properties are well-understood. Injection pressure affects fuel atomization, spray

impingement, and mixture heterogeneity. High injection pressures improve atomization and mixture homogeneity [90]. Although higher injection pressure may lead to greater spray impingement, it has been shown that piston impingement alone does not increase particulate formation if conditions are favorable for small droplet sizes and fast evaporation from the piston [86]. Because of this, higher injection pressure has been consistently shown to reduce particles due to the improved fuel atomization [35, 83, 90, 92]. Injection pressures below 10 MPa have been shown to significantly increase particulate formation [35], and the particulate reduction with injection pressure becomes lower above 15 MPa [90]. The injection pressure used here (11 MPa) is in the middle of this range. This ensures that the effect of fuel volatility was neither overshadowed by excessive liquid fuel at low injection pressure, nor eliminated due to improved atomization at high injection pressure.

Charge motion is affected by the injection event, engine speed, engine geometry, and piston position [83, 92]. This engine has a flat-top piston and no wall-guiding for the spray. The side-mounted injector may cause wetting of the cylinder liner on the opposite of the injector location, which is expected to decrease at higher piston speeds [83]. Because the rpm is maintained for all EOI timings, the only factor affecting piston speed is the piston position. Therefore, the greatest spray deflection is expected when the piston is at -270 CAD, which is halfway down the cylinder. Charge motion during compression induces mixing, and becomes more effective as the piston nears TDC, which is one explanation that has been offered for why later ignition timings under direct-injection conditions result in lower particles [89, 90, 92, 107].

Based on the above arguments, it is possible to predict which variables were most critical in the EOI sweeps for each fuel. In the case of EEE, spray impingement is important because the fuel does not necessarily fully evaporate from in-cylinder surfaces under the conditions studied. Particulate is minimized through the tradeoff of mixing time and piston wetting at an injection timing of -310 CAD. Because TRF30 appears to evaporate fully from the piston, maximizing mixing time is the most critical factor in minimizing particles. Therefore, the

earliest injection timing produces the fewest particles for the current engine conditions. Under cold start conditions, where the piston temperature is much lower, TRF30 might behave more like EEE and early injection times where piston impingement is significant would be expected to also have increased particulate production.

8 SIDI STUDY OF PRESSURE AND SPEED EFFECTS

Using knowledge from the characterization of load and speed effects under PMPV operation, the effects of load and speed under SIDI operation were studied. The comparisons were used to interpret the relative importance of pressure and residence time on premixed and non-premixed in-cylinder combustion.

8.1 Effects of Engine Load Under Direct Injection

The study of SIDI engine load effects included only two operating points. For both points, the engine was run at 2100 rpm, Φ = 0.98, an injection pressure of 11 MPa, and EOI = -220 CAD. The low-load case is the same as the EOI 220 case from the injection timing sweep. This case is characterized by gIMEP = 334 kPa and CA50 = +8 CAD. As in the PMPV load study, close late-cycle temperature matching was desired. However, in this case acceptable temperature matching throughout the cycle was achieved at the same combustion phasing as for the low load case. Therefore, the high load case is characterized here by gIMEP = 550 kPa and CA50 = +8 CAD.

8.1.1 Results

The resulting thermodynamics from the 334 kPa and 550 kPa cases can be seen in Figure 8.2. The differences between the two cases are similar to the differences between the PMPV 334 and 550 kPa IMEPcases. The resulting PSDs can be seen in Figure 8.1. As expected, the higher load case produces a larger number of particles than the low load case. As in the PMPV study, the higher load also causes a slight shift to larger particles. Note from Table 8.4 that the CO and HC emissions are higher and the O_2 emissions are lower for the 550 kPa case than for the 334 kPa case. This corresponds to a 1% lower combustion efficiency for the 550 kPa case as compared to the 334 kPa case. The pressure dependence

of the PSDs for the two load cases shown here is similar to the dependence at very rich conditions under PMPV, suggesting that charge heterogeneity is likely. Additionally, some level of diffusion burning is also expected at this injection timing.

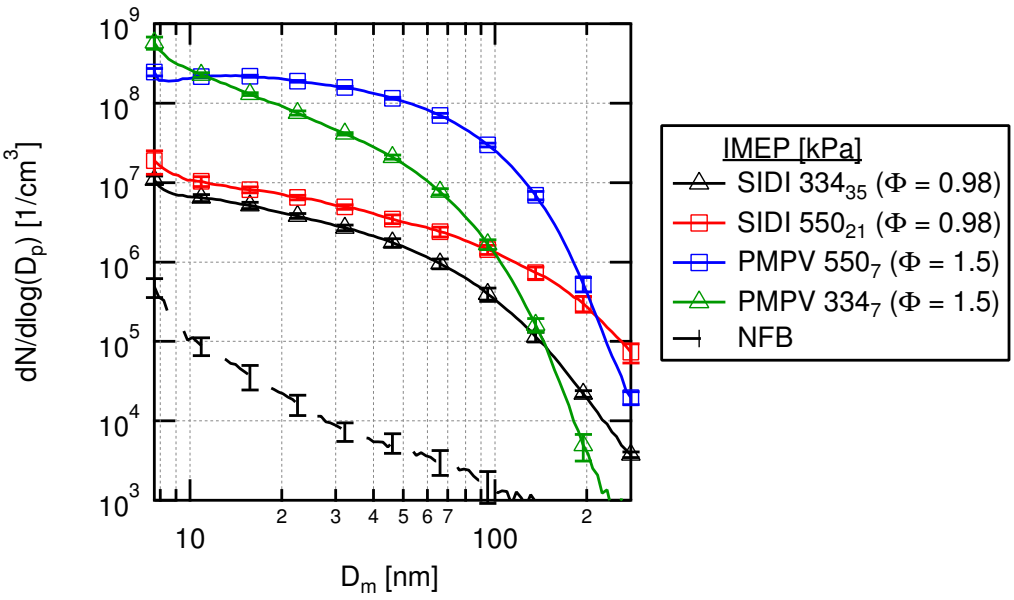

Figure 8.1: EOI 220 (334 kPa) vs 550 kPa case PSDs. Markers are drawn every 10 data points. NFB trace matches that from [50].

Table 8.1: Gaseous emissions comparisons between 334 kPa and 550 kPa cases

Load [kPa]	CO_2 [mol%]	CO [mol%]	O_2 [mol%]	H_2 [mol%]	H_2O [mol%]	HC [mol%]	NO_X [mol%]	N_2 [mol%]
334	13.7	1.0	1.2	0.03	13.2	0.19	0.12	70.6
550	13.4	1.8	1.0	0.07	13.1	0.22	0.15	70.3

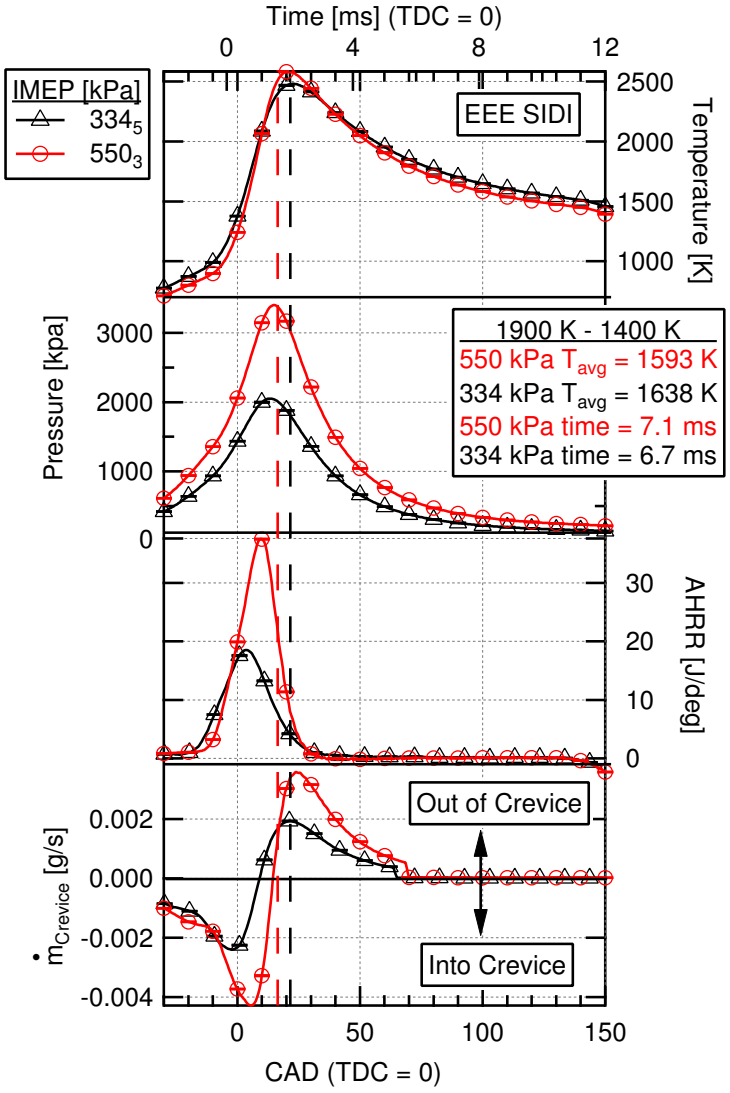

Figure 8.2: EEE 550 kPa IMEP and 334 kPa IMEP thermodynamic parameters at EOI = -220 CAD, and 2100 rpm. Markers are drawn every 20 data points. Vertical dashed lines represent approximate location of CA90 for each case.

8.1.2 Discussion

It is important to recognize that the effects of increased load may be different under DI operation than under PMPV operation. Under PMPV operation the air and fuel is premixed so changes in in-cylinder pressure do not influence the mixture formation process. However, for DI operation the increased in-cylinder density, longer required injection duration and

different temperature during the intake stroke are likely to result in differences in fuel evaporation, wall wetting, and mixture heterogeneity. Additionally, the effect of pressure on premixed flame soot formation at the high equivalence ratios used in the PMPV method is potentially different than the effect of pressure on diffusion flame sooting. Finally, rich premixed burning is only expected to occur locally under DI operation and the overall number concentrations resulting from a local mixture enrichment would be significantly less than a PMPV condition with a global mixture at the same level of enrichment.

Although main combustion event thermodynamics are not controlling parameters in premixed operation, the same has not been proven for DI operation. Therefore, it is important to understand the expected pressure dependence for diffusion burning from 100 kPa up to 3500 kPa (0.1 MPa to 3.5 MPa). Soot formation dependence on pressure in this range has so far only been studied for low carbon number fuels such as ethane, ethylene, methane, and propane (C_1 - C_3 hydrocarbons). A few methods for describing the pressure dependence are common. All studies referenced here noted a $[soot] \propto P^n$ dependence on pressure, where the quantity $[soot]$ may be the path-integrated soot volume fraction, some local soot volume fraction defined at a given height above the burner, or the fraction of the fuel carbon that is converted to soot. The dependence of any of these metrics on pressure is quantified by the exponent n. Table 8.2 lists n values using various measurement techniques from several sources.

From Table 8.2, a few common results are noticeable. First, soot formation consistently increases as a function of pressure. Second, the pressure dependence decreases as pressure increases. Finally, it appears that larger hydrocarbons have a greater dependence on pressure than smaller hydrocarbons. In this study the late-cycle pressure range of interest is approximately 0.2 MPa to 0.45 MPa, and the peak pressure range of interest is approximately 2.0-3.5 MPa. The fuel is EEE, which is a complex mixture of small to large hydrocarbons so the exponent n is difficult to predict. However, based on the above results, it is reasonable to believe that the n exponent of soot volume fraction should fall between 1.0 and 2.0 between

Table 8.2: Summary of literature results for dependence of soot formation in diffusion flames

Source	Fuel	Measurement Technique	Pressure Range [MPa]	Exponent n for P^n		
				Path-integrated f_v^{max}	local f_v^{max}	% fuel carbon conv. to soot
[77]	methane (CH_4)	LII	0.1-2.5	1.0	1.2	-
[114]	methane (CH_4)	SSE & LOSA	0.5-2.0	1.3	2.0	1.0
[114]	methane (CH_4)	SSE & LOSA	2.0-4.0	0.9	1.2	0.1
[38]	ethylene (C_2H_4)	LOSA	0.1-1.0	1.2	-	-
[77]	ethylene (C_2H_4)	LII	0.1-1.6	1.2	1.7	-
[70]	ethane (C_2H_6)	SSE	0.2-0.51	-	-	2.2
[70]	ethane (C_2H_6)	SSE	0.51-1.52	-	-	1.1
[70]	ethane (C_2H_6)	SSE	1.52-3.34	-	-	0.4
[17]	propane (C_3H_8)	SSE	0.1-0.2	3.4	-	3.3
[17]	propane (C_3H_8)	SSE	0.2-0.73	1.4	1.8	1.1

LOSA = Line of sight attenuation
LII = Laser induced incandescence
SSE = Spectral soot emission

0.2 MPa and 0.45 MPa, and closer to 1.0 above 2.0 MPa. The n exponent for premixed combustion for similar fuels in the late-cycle pressure range is expected to be ≈ 1.3, so the late-cycle pressure dependence for either flame type is similar.

Recall that under PMPV operation the n exponent as a function of IMEP was found to be between 6.0 and 8.0, which is much higher than these predicted values. Because only two cases were studied under SIDI conditions the n exponent cannot be calculated. However, the difference between the two loads here is similar to the difference noted for the PMPV $\Phi = 1.5$ case, suggesting that the dependence is similar. The high number of large particles is also similar to the PMPV $\Phi = 1.5$ case, but the global Φ is 0.98, which suggests the presence of local pockets of $\Phi \geqslant 1.5$ and potentially some diffusion-limited combustion, particularly at the higher load condition. Because the pressure dependence is similar to the PMPV results, it is unlikely that main-combustion temperature and pressure significantly influence particulate formation for DI operation. .

8.2 Effects of Engine Speed Under Direct Injection

The effect of speed under SIDI operation was studied using the results of the corresponding PMPV study to aid in interpretation of the results. Like the PMPV study, engine speeds of 2100 rpm and 1050 rpm were tested. For both speeds, Φ = 0.98, EOI = -220 CAD, injection pressure = 11 MPa, $m_{fuel} \approx 11.69$ mg/cycle. The 2100 rpm case used here is the same as the EOI 220 case used for both the SIDI load study and the injection timing sweep. The fuel mass per cycle for the 1050 rpm case was matched to the 2100 rpm case instead of matching IMEP. This is the same strategy that was used in the PMPV engine speed study, and it resulted in similarly good thermodynamics matching on a crank-angle-resolved basis between the two cases.

8.2.1 Results

The resulting thermodynamics from the 1050 rpm and 2100 rpm cases can be seen in Figure 8.4. The differences between the two cases are similar to the differences between the PMPV 1050 rpm and 2100 rpm cases. In particular, the crank-angle-resolved AHRR is higher for the 1050 rpm case. The temperature and pressure traces are well matched, and the total crevice flow is similar, although the end of crevice flow occurs at slightly different crank-angles. Note that the different time scales for the 2100 rpm and 1050 rpm cases are shown on the top axis, and the crevice flow rate is in [g/s] as a function of crank angle. Therefore, although the crevice flow rate is higher for the high rpm case, when integrated over time, the total crevice mass becomes nearly the same between the two cases.

The PSDs for the two speed cases are compared in Figure 8.3. It is interesting to note that the lower engine speed not only reduced the total particulate number, but also significantly changed the PSD shape. The lower speed PSD has an increase in large particles greater than 120 nm in mobility diameter, but has significantly lower particle concentrations below this diameter. Because the global Φ is well below Φ_C, but the PSD is at least an order

of magnitude higher than the NFB, it is clear that mixture heterogeneities still exist at ignition. The PMPV speed study results showed an increase in particulate formation for decreasing speed. Considering that result here suggests that the fuel mass tied up in rich regions for the 1050 rpm condition is lower than at 2100 rpm, i.e., the in-cylinder charge is more uniformly mixed. However, due to the increase in particulate mass with increased residence time the total mass of particulate formed is relatively similar. The comparison of total particulate number and mass between the two cases is shown in Table 8.4.

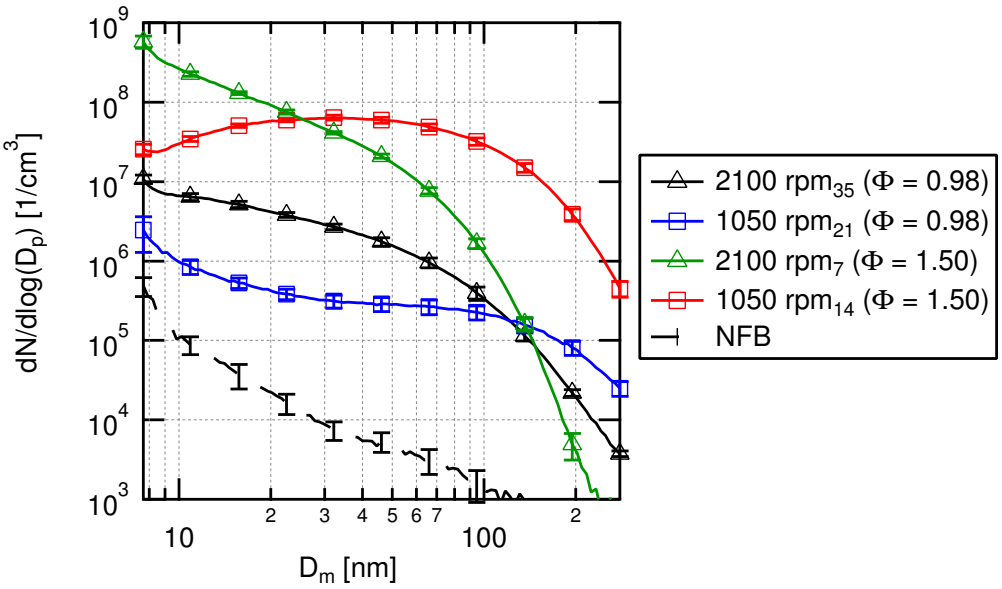

Figure 8.3: EOI 220 (2100 rpm) vs 1050 rpm case PSDs. Markers are drawn every 10 data points. NFB trace matches that from [50].

Table 8.3: Total particulate comparisons between 1050 rpm and 2100 rpm cases

Case	Fuel Mass In [mg/cycle]	Number ± 95% conf [1/cm^3]	Mass ± 95% conf [g/cm^3]
2100 rpm	11.53	$(28.591 \pm 2.3)10^5$	$(9.1 \pm 2.8)10^{-11}$
1050 rpm	11.67	$(4.173 \pm 0.8)10^5$	$(6.8 \pm 2.4)10^{-11}$

The 1050 rpm case produced slightly lower particulate mass, but the particulate masses of the two cases are within each other's 95% confidence bounds. The higher speed case produced about 7 times the number of particles. As shown in the PMPV results the

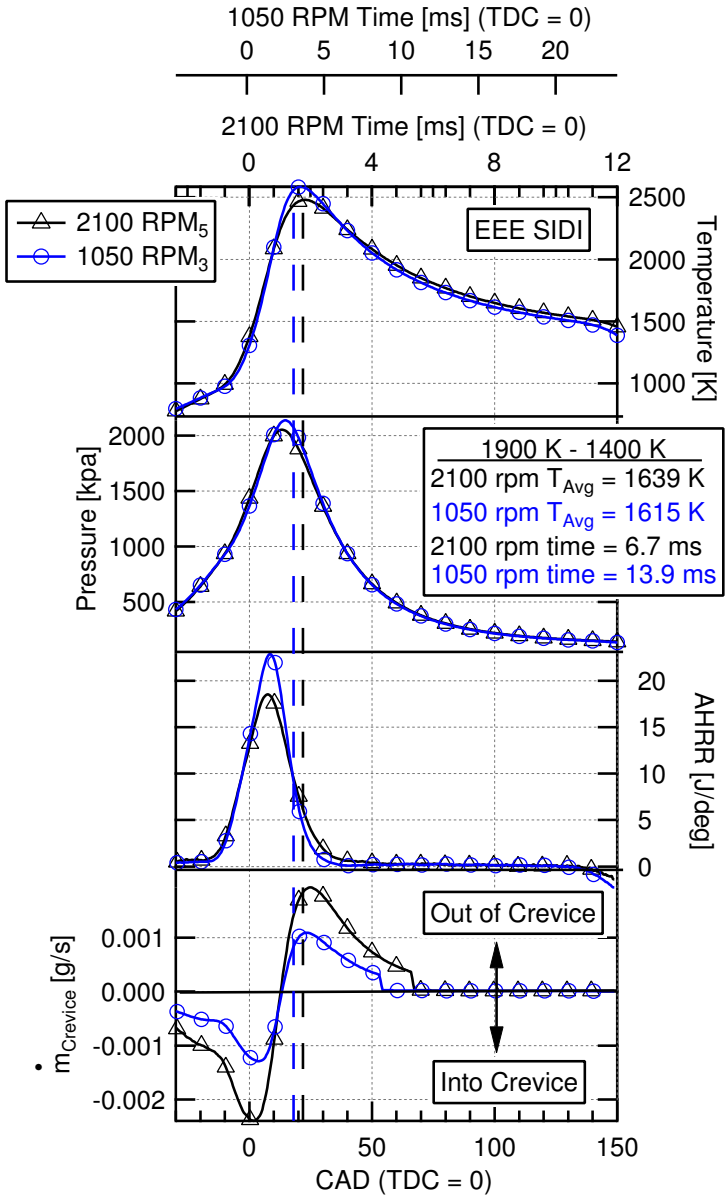

Figure 8.4: EEE 1050 rpm and 2100 rpm thermodynamic parameters at EOI = -220 CAD. Markers are drawn every 20 data points. Vertical dashed lines represent approximate location of CA90 for each case.

longer residence time associated with lower rpm results in an increase in particle size. This explains in part the change in PSD shape for the lower engine speed. Also note that the gaseous HC emissions are tripled from the 2100 rpm condition to the 1050 rpm condition. The decreased charge heterogeneity at the lower engine speed may help explain the existence of a larger than anticipated number of small particles (D_m <20) for the

Table 8.4: Gaseous emissions comparisons between 334 kPa and 550 kPa cases

Speed [rpm]	CO_2 [mol%]	CO [mol%]	O_2 [mol%]	H_2 [mol%]	H_2O [mol%]	HC [mol%]	NO_X [mol%]	N_2 [mol%]
2100	13.7	1.0	1.2	0.03	13.2	0.19	0.12	70.6
1050	13.5	0.8	1.6	0.03	12.52	0.61	0.09	70.8

1050 rpm PSD. Although the approximation of mass based on the PSD may be imperfect, the result highlights the importance of considering both particulate mass and number concentration when interpreting the particulate formation trends.

8.2.2 Discussion

Previous studies of particulate dependence on engine speed [59, 71] identified the critical variables to be temperature which affects reaction rates, pre-ignition mixing time which affects fuel evaporation, and post-flame residence time which affects available reaction time. A unique element of the current study is that in-cylinder pressure and temperature were well matched. Additionally, the PMPV investigation characterized the effects of residence time on soot formation and growth reactions for the residence times at the two engine speeds studied under SIDI operation. Therefore, the effect of residence time on vaporization and mixing is the primary variable remaining.

Recall that the effect of lower speed under PMPV operation for rich mixtures was to increase the total particulate number and mass due to increased post-flame residence time. Additionally, increases in residence time for PMPV operation increased the amount of agglomeration and surface growth resulting in distributions with larger geometric mean diameters. Here, the same increase in late-cycle residence time is provided, but the total particulate number decreases by nearly an order of magnitude and the mass reduces slightly. Although the particles in these DI cases are likely due to a combination of locally rich mixture pockets and diffusive combustion of in-cylinder liquid fuel, the global Φ is slightly lean, so there is enough oxygen to fully oxidize the PM if a long enough residence time and sufficient mixing is provided.

Increased reaction time in the premixed flame experiments also caused a shift to accumulation mode particles. A similar shift to larger particles at the lower speed SIDI case was demonstrated here. The shape of the 1050 rpm SIDI PSD is very similar to a combination of the PMPV Φ = 1.35 and 1.5 1050 rpm PSDs, but the total particulate numbers are about three orders of magnitude lower at the large particle sizes. This is suggestive of a globally lean bulk gas with locally rich mixture pockets that produce the majority of the particles from a tiny fraction of the overall charge mass. The occurrence of these locally rich pockets is likely reduced at low rpm due to the longer mixing time. This argument is supported by optical engine measurements of fuel mixture inhomogeneity by Rothamer and Ghandhi [98] in a SIDI engine. Their measurements indicate a significant increase in flame-front mixture equivalence ratio inhomogeneity with increasing engine speed when increasing speed from 600 rpm to 1200 rpm. If the same increase in mixture stratification is assumed for the results here, this could explain the lower particle number for the lower engine speed and the lower engine speed having a similar mass as the higher engine speed, even though the PMPV results would suggest both a higher number and mass for the lower engine speed. This is a good example of how both an understanding of the sooting dependence under premixed conditions and an understanding of the influence of mixture formation are needed to understand sooting trends for DI operation.

At a lower speed, reduced droplet burning is expected due to increased time for evaporation. Kayes and Hochgreb [61] predicted a 90% lower concentration of liquid fuel at a 1500 rpm condition than at a comparable 2500 rpm condition in a PFI engine due to a greater available time for vaporization. However, this was a prediction for a PFI engine where no in cylinder injection event occurs. The 1050 rpm case is more likely to experience wall wetting because lower in-cylinder charge motion from the slower moving piston is likely to result in less spray deflection. There are therefore two competing factors affecting the mixing and fuel vaporization as a function of engine speed: spray impingement depending on charge motion, and fuel evaporation depending on mixing time. The effects of lower

rpm based on the current results appear to be enhanced pre-ignition bulk gas mixture homogeneity, and increased post-flame residence time resulting in increased soot growth via agglomeration and surface growth. Unfortunately, it is difficult to determine from this data the fraction of soot that originates from liquid fuel versus the fraction that originates from locally rich gaseous A/F mixtures.

Dynamometer limitations prevented engine operation at significantly higher engine speeds, but additional speed points would enhance the validity of these observations. Recent work dedicated to the effects of engine speed is limited, and the increase in particulate number with speed may not be monotonic. Kayes and Hochgreb [59] noted a significant increase in both particle mass and number from 1500 rpm to 2000 rpm, but then a slight decrease from 2000 rpm to 2500 rpm. This result was repeatable for three different engine loads. Maricq [71] noted an increase in particulate number for a speed increase from 1500 rpm to 2750 rpm, with no intermediate data point. Additional studies [54, 86] investigated soot formation at various speeds with mixed results, but additional operating parameters were simultaneously varied so the effect of speed in these investigations is uncertain. The PMPV results presented here suggest that increasing engine speed will decrease particulate formation due to decreased kinetic time scales for soot growth. However, this will generally be counteracted by decreased time for mixing and evaporation. Therefore, the individual engine design will strongly influence particulate formation, suggesting that mixed results can be anticipated from different engines.

9 CONCLUSIONS AND FUTURE WORK

9.1 Conclusions

9.1.1 Premixed Combustion Threshold Sooting Behavior

Premixed pre-vaporized operation of a SI engine was detailed. The PMPV technique was applied to measure critical sooting behavior of gasoline. Successful use of the technique required careful conditioning of the intake and exhaust streams. Intake conditioning was needed to fully vaporize the fuel and to avoid condensation. Careful exhaust sample conditioning was needed to avoid formation of volatile particles. PMPV operation was used to identify and characterize the NFB PSD. The NFB PSD was shown to be independent of fuel type over a range of Φs for methanol, E100, and EEE. The NFB represents the minimum level of PM achievable for this engine under the conditions tested and establishes a baseline from which to determine the onset of fuel-borne soot due to mixture chemistry and thermodynamic factors. It was found to be similar for all fuels and both engine speeds studied, but increased with engine load. The NFB PSD is likely due to particles generated from engine oil and engine wear particles.

With the NFB established, PMPV operation was first used to demonstrate the critical enrichment threshold sooting behavior of a certification gasoline, and the sooting characteristics above the critical enrichment threshold. A method was developed for determining the critical enrichment threshold from the integrated particulate data, and used to show that the critical threshold for EEE is between $\Phi = 1.32$ and $\Phi = 1.36$. This threshold behavior was also observed for all fuels and operating conditions, but was shown to decrease as fuel aromatic fraction increased, as engine speed decreased, and as load increased. The PSD showed a marked increase in small diameter particles at Φ = 1.35 with increases at all diameters for higher Φs. There appeared to be a transition to higher rates of agglomeration, due to the large number of small particles, as Φ was increased. Again, this transition was

observed for all fuels and operating conditions. The transition occurred at lower mixture enrichment levels for fuels with higher aromatic fraction, for EEE at higher loads, and for EEE at lower speeds.

Based on premixed flame literature, it is hypothesized that at Φ_C soot formation occurs in the periphery of the engine cylinder at the end of combustion or slightly after combustion. The earliest location of soot formation is anticipated to move towards the center of the engine cylinder as Φ is increased above Φ_C. The air-fuel mixture forced in the crevices during the compression process will begin to flow back into the cylinder once the pressure begins to decrease, and is a potential source of late-cycle particle formation. However, the PMPV speed and load studies showed that at high Φ, all the particulate mass cannot possibly come from this one source.

9.1.2 Premixed Combustion Fuel Chemistry Effects

Increasing aromatic fraction simultaneously increases the C/H ratio, the number of C-C bonds, and the number of carbon atoms for all the fuel blends studied here. Although this makes it difficult to determine which elements of fuel structure are most critical, a few predictions may be made based on the literature and the current results. Aromatics in the fuel are likely to lead more quickly to resonantly stabilized radicals, which accelerate soot formation, so it is likely that this element of fuel structure is a controlling factor. The HACA mechanism is likely present in the combustion of all the fuels, and is likely to be the dominant path to soot formation for the non-aromatic fuels. Synergistic mixing effects were not noted in this study.

The agreement in particulate formation trends between EEE and TRF30 reported for atmospheric pressure, laminar co-flow diffusion flames by Witkowski et al. [122] has been extended here to premixed flames in a SI engine, suggesting that the TRF30 mixture is an appropriate chemical surrogate for use in SI engine particulate modeling applications. Although the correlations between the critical fuel chemistry parameters and sooting

tendency are not fully isolated, matching the C/H and aromatic fraction of TRF30 to EEE without knowing the EEE C-C bond number was sufficient to give close agreement in the sooting trends between the two fuels regardless of enrichment or the metric used for comparison.

Finally, both the enrichment metric and the particle formation metric were shown to be important for accurate interpretation of particulate formation tendencies. Each metric presented for comparing the enrichment level between hydrocarbon fuels had benefits and drawbacks for the experimental method used here, based on matching of fuel carbon, thermodynamics, and chemistry assumptions. Additionally, due to the transition to agglomeration mode particles with increasing enrichment, particulate formation should be compared on both a number and mass basis.

9.1.3 Premixed Combustion Thermodynamic Effects

The PMPV combustion phasing sweep gave strong evidence that soot formation has low sensitivity to the main combustion event thermodynamics, which provides a stronger case for the suggestion that the time spent between 1400 K and 1900 K is the most important variable. This range is met for all conditions late in the cycle near the end of combustion or after the main combustion.

The PMPV load sweep successfully isolated the effect of late-cycle cylinder pressure from residence time and temperature, although crevice mass returned also increased with load. The effect of the returned crevice mass was shown to be less important than the effect of cylinder pressure because at high Φ, the ratio of crevice mass to particulate mass was < 1, and was dependent on cylinder pressure. This shows that the decreased Φ_C and increased total particulate that occurs with increased load are most likely due to late-cycle pressure differences that affect the reaction rates. The dependence of soot volume fraction on the average pressure between 1900 K and 1400 K for the cases studied was estimated to have an n exponent of 6.0 to 8.0, which is much higher than the n value recorded for

laboratory premixed flames. This may be due to a combination of factors including the variable temperature/pressure history, and the lower available reaction time in-cylinder.

Matching the combustion phasing and fuel mass per cycle between two engine speeds effectively isolated the effect of late-cycle residence time from temperature and pressure for premixed operation. The lower critical enrichment threshold, higher particle number, and higher particle mass resulting from the lower speed conditions indicates that soot formation is kinetically limited in the engine as compared to premixed laboratory flames. The trend under PMPV is the opposite of the trends under DI operation, suggesting that the reduced mixing time is the driving factor of higher particulate from speed changes under DI operation. The effect of reduced residence time in this rpm range is to reduce particulate formation from a premixed flame, which would be in direct competition with the effect of reduced mixing time under DI operation.

9.1.4 Interpreting Differences Between SIDI and PMPV Results

Comparisons between the EEE PMPV Φ sweep and the EEE SIDI EOI sweep indicated that the presence of a significant number of accumulation mode particles that result from growth of soot via agglomeration is a good indication of very rich, likely diffusive, combustion resulting from impingement of the fuel spray or the presence of droplets at the start of combustion. The fact that TRF30 produced nearly the same level of particulates as the NFB at EOI -340 CAD while EEE produced very high particulate number and mass at the same condition suggests that the TRF30 evaporated from chamber surfaces, and the difference between the two fuels at this condition quantifies the effect of pool fires. The difference between the distillation curves of the two fuels is expected to be the fuel physical property that is responsible for the PSD differences. Fuel that wets the cylinder liner may be swept into the crevice region, creating a very rich unburnt crevice charge. At late injection timings, there is less time for evaporation from the walls before this occurs, which may explain why the TRF30 and EEE results converge at the latest timings.

SIDI operation was found to have a similar dependence on load to PMPV operation. The high levels of particulates at $\Phi = 0.98$ at both loads suggests the existence of very rich, potentially diffusion-limited combustion areas in the SIDI case. The similar load dependence also suggests that main-combustion thermodynamics play a similarly small role in SIDI particle formation as they do in PMPV particle formation. The PSD differences between the two SIDI engine speed cases suggest that the lower rpm case favors agglomeration due to longer late-cycle residence time while the 2100 rpm case favors new particle formation due to incomplete pre-ignition mixing and short late-cycle residence time. The resemblance of the slightly lean 1050 rpm SIDI PSD to the PMPV $\Phi = 1.5$ case suggests that the 1050 SIDI PSD could be coming from a small fraction of $\Phi \geqslant 1.5$ pockets of rich premixed combustion.

9.1.5 Summary of Conclusions

A major contribution of this work was the development and validation of the PMPV method, which allowed isolation of fundamental parameters leading to particulate formation in SI engines. The experiments spanned both PMPV and SIDI operating conditions, and the PMPV results aided significantly in the interpretation of the SIDI results. SIDI operation is characterized by a combination of both premixed and diffusion-limited combustion. The sooting tendencies of an in-cylinder premixed flame were shown here to increase with mixture enrichment, fuel aromatic content, late cycle pressure, and late-cycle residence time in a temperature range between 1400 k and 1900 K. The main combustion event thermodynamics were shown to have little effect on particle formation.

The PMPV results were compared against thermodynamically similar SIDI cases to make several important discoveries. First, the prevalence of particle agglomeration is a potential sign of diffusion-limited burning in an SIDI engine. Second, the high boiling point of the heaviest species in a real fuel are a likely cause of pool fires in SIDI operation, which result in several orders of magnitude higher particle number and mass. Third,

the effects of pressure under SIDI operation are similar to those under PMPV operation, suggesting a similar dependence on pressure for soot formation from in-cylinder premixed and diffusion flames. Finally, the effect of lower engine speed under SIDI operation is to increase pre-ignition mixture homogeneity, but also leave more time for late-cycle soot formation, resulting in lower particle number, but a similar particle mass for the conditions tested.

The exact dependence of premixed and diffusion flames on pressure in-cylinder is still unknown. The exact temperature dependence and the critical chemical timescales are also uncertain. This is largely due to the fact that the in-cylinder thermodynamics are continuously variable so it is difficult to pinpoint the critical CAD windows. Additionally, while aromatic fraction appears to be a critical fuel chemistry property contributing to soot formation, the relative importance of C/H ratio, number of C-C bonds, and unique pathways for large hydrocarbon fuels are still uncertain. The composition and sources of the NFB are also uncertain, although data has been collected that may help to clarify that question. Finally, although the crevice gases have potential to produce some particulate, the highest Φ PMPV cases showed that all of the particulate cannot possibly be from this source. The relative contribution of the crevice gases has not been characterized. These are issues that could be addressed in future work. The improvements to the understanding of SI engine particulate formation as a function of various parameters are summarized in Table 9.1.

Table 9.1: Effects of engine operating parameters on particulate formation in SI engines

Engine parameter	**Parameter change**	**Particulate response**	**Known effects**	**Improvements to understanding of parametric effects**
Load	Increase	Increase	Increased fuel mass	-Diffusion n still unknown -Premixed $n \approx 6-8$
Speed	Increase	Increase	Less mixing time	-Increased residence.time = increased particulate
Combustion Phasing	Advanced	Increase	Less mixing time	-Low sensitivity to main comb. thermodynamics -High sensitivity to postflame thermodynamics -Some sensitivity to postflame residence time
Injection Pressure	Increase	Depends on Pressure & injection strategy	-Small droplets (low soot) -Good mixing (low soot) -Fuel impingement (high soot)	-Mixing / impingement tradeoff shown to be fuel-volatility dependent
Injection Timing	TDC to -280CAD -280 CAD to ≈BDC ≈BDC to Ignition	High Low High	Fuel impingement vs. charge mixing tradeoff	-Fuel volatility effect characterized -Turbulence effect not studied
Number of Injections	2 or 3 (rather than 1)	Decrease	Fuel impingement vs. mixing tradeoff	heterogeneity / diffusion signals characterized
Injection Targeting	Strategies vary	Depends on Strategy	Mixture distribution	-Diffusion signals characterized
Mixture Enrichment	Increase	Increase	Lower oxygen availability	-Enrichment effects characterized
Fuel Chemistry	Various Parameters	Parameter Dependent	Fuel-bound oxygen reduces soot	-Effect of aromatics fraction characterized -Gasoline surrogate demonstrated
Fuel Physical Properties	High volatility	Low	Improved mixing	-Fuel volatility effects characterized

9.2 Future Work

While it has been concluded that the particles that make up the NFB do not originate from the fuel, their source is still unknown. Compositional information for these particles would be very useful in determining their origins. For example, particles from oil films are expected to be composed of both hydrocarbon species and metallic species due to the additives mentioned earlier. Compositional information for NFB particles of $D_m > 50$ nm was collected using the SPLAT during the 2014 collaboration with PNNL. This data is expected to help determine the likely sources of the NFB particles, but it has not yet been fully processed. Compositional information was also collected for selected cases where volatile particles were present, so that more information on the composition of those particles is also anticipated soon.

With regard to the effects of fuel chemistry, the relative importance of aromatic fraction, C/H, C-C bond number, and unique chemical pathways associated with individual species pathways have not been characterized by this study. Better characterization of each of these parameters might be possible through PMPV testing of other surrogate fuel blends. For example another alkyl-benzene aromatic such as one of the xylene isomers or ethylbenzene could be substituted for toluene. Each of the xylene isomers and ethylbenzene have a yield soot index (YSI) between 50 and 54 whereas that of toluene is 43.5 [78]. Use of one of these fuels would allow the same aromatic fraction to be tested in the surrogate, and a similar molecular structure to be used but with a different C/H ratio. This would likely be possible while maintaining the octane number because the octane numbers (RON) of these fuels range from 107.4 (ethylbenzene) to 145 (m-xylene), and o-xylene has nearly the same octane number as toluene (120.1 vs 120.0).

A 3-component TRF blend has been demonstrated here as an appropriate chemical surrogate fuel for gasoline, but the physical volatility properties caused significant differences in the particulate-related performance of the two fuels under DI operation. Backhaus et. al. developed a voaltility model for surrogate fuel blends and showed that at least

four components are needed to accurately reproduce the volatility characteristics of a real gasoline [14]. The volatility properties of interest in that model are the four properties specified in ASTM D4814, which outlines gasoline volatility property requirements for different regions and times of year in the U.S. These four properties are the distillation curve, RVP, temperature for a vapor-liquid ratio of 20 ($T_{V/L=20}$), and driveability index. The distillation curve is used to define the driveability index [37]. Using this model as a guide, it may be possible to match both the chemical and physical particulate affecting properties of EEE with a four or five component surrogate.

While high loads were clearly demonstrated to produce both a higher baseline PSD and soot formation at lower Φ, the baseline PSD at loads higher than 334 kPa was not demonstrated to be a NFB. To demonstrate a NFB at the higher loads, methanol and E100 should be tested at a range of Φ at each load point, just as was done for the demonstration of the 334 kPa IMEP NFB.

Comparisons between the SIDI and PMPV speed changes provided significant insight into the different effects of speed on particulate formation. However, with only two speed points for each operating mode, it is difficult to characterize the exact dependence of particle formation on residence time and mixing time. To better understand the trends, a wider range of speeds and a finer resolution between speeds should be studied. Adding 800 rpm, 1500 rpm, and 2500 rpm points for both the SIDI and PMPV modes would accomplish both these needs.

Finally, the effect of engine load under SIDI operation appeared to be similar at $\Phi = 0.98$ as the effect of load under PMPV operation at high Φ ($\Phi \approx 1.5$). However, only two load cases were compared under SIDI operation whereas four load cases were compared under PMPV operation. Therefore the effect of load on premixed combustion is relatively clear, whereas a trend under SIDI operation is uncertain. Data at 440 kPa IMEP and 660 kPa IMEP under SIDI operation would strengthen the conclusions drawn here regarding the effect of load for cases where diffusion-limited burning is possible.

A.1 Introduction

A small fraction of the fuel and air mixture introduced in each engine cycle becomes trapped in the crevice volumes formed by the piston rings and the clearance between the piston and the cylinder wall. The flame does not propagate into the crevice because the high surface-to-volume ratio keeps the temperature too low, and the mass trapped in the crevice escapes the main combustion event. Some portion of the initial trapped mass escapes before the main combustion event has passed and is burned normally with the rest of the bulk cylinder gasses. However, that portion that remains in the crevice past the main combustion event returns to the main cylinder volume late in the cycle and mixes with combustion products that are still hot enough for fuel decomposition, but low in oxygen. This limits the potential for the oxidation of pyrolysis products and increases the fraction of fuel that forms pollutants. Although the trapped crevice mass makes up a small fraction of the overall charge mass, the environment into which it is released makes it a potentially significant particulate source. Estimations for the magnitudes and directions of the mass flows into and out of the three piston ring gaps on a crank-angle-resolved basis are formulated here.

A.2 Assumptions

Several assumptions are common for all the calculations in this discussion, so it is appropriate to list them first. First, both the crevice mass (m_{crev}) and the total cylinder trapped mass (m_T) were treated as **ideal gasses** whether they were composed of reactants, products, or both. An **isothermal boundary condition** was imposed on the system wall, at a wall temperature (T_W) of 400 K. The temperature, pressure and composition were assumed to be **spatially uniform in the bulk gas** for each instantaneous position in the cycle, which is

consistent with a **single zone heat release model**. Because the crevice is extremely narrow, heat transfer from the crevice gas to the wall is very fast, so the **crevice volume temperature was assumed to equal the wall temperature** ($T_{Crev} = T_W$).

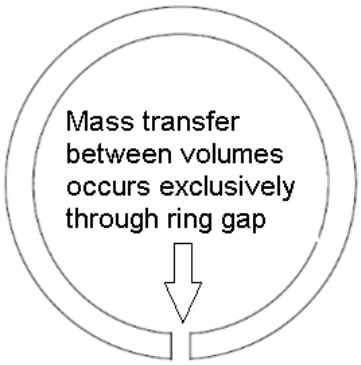

Figure A.1: Sample ring geometry depicting ring gap where mass flow occurs. Modified from [103].

The piston rings were assumed to seal completely against the cylinder walls and the piston lands, so that mass is only able to flow through the piston ring end-gap, which was approximated as a constant-area orifice. The ring gap is depicted in Figure 1. Finally, the formulations of $MW_{products}$ and $MW_{reactants}$ developed in the heat release appendix apply here. Additional assumptions are stated as they are encountered in the discussion of the specific situations for which they were used.

A.3 Model Geometry

The basic crevice volume model discussed here followed the model proposed by Salazar [103]. The model accounted for the three gaps (V_1, V_2 & V_3) formed by the space between the piston radius (r_{Pist}) and the cylinder bore radius (r_{Bore}) and the gaps cut for the two compression rings and the oil ring ("1^{st} Ring", "2^{nd} Ring", & "Oil Ring"). The volumes interact through the piston ring end-gaps on the basis of mass flows and pressure changes. The mass flow between V_1 and the bulk cylinder volume was the primary variable of interest here. For all three gap volumes (V_1, V_2 & V_3) the **composition of the mixture was**

assumed to be that of the fresh intake charge reactants. A simplified schematic of the piston, bore, and ring gaps from [103] is presented in Figure A.2, and shows the spatial relationships between the volumes, pressures, and mass flows.

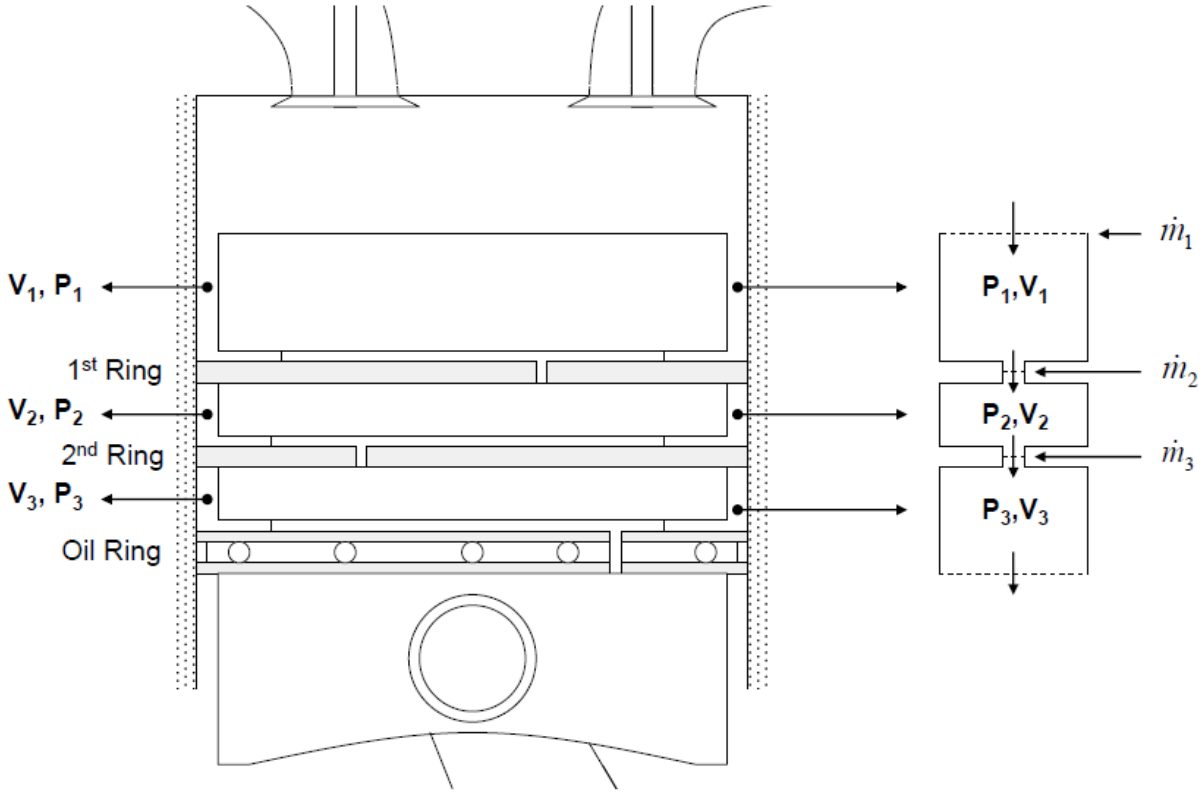

Figure A.2: Generic schematic of volumes formed between the piston and cylinder bore and separated by the piston rings and the associated pressures and mass flows (not to scale) [103].

A.4 Volume Definitions

The volumes V_1, V_2, and V_3 each represent the total volume between their respective piston rings. These total volumes are composed of the crevice volume, ($V_{crev(m)}$) , the gap volume ($V_{gap(m)}$), and some combination of ring land volumes ($V_{land(m)}$). The subscript "m" refers to the mass flow rate (1, 2, or 3) that is affected. The crevice volumes $V_{crev(m)}$ are formed

between the outside diameter of the piston and the cylinder wall. They were defined by the land height (H) and the difference in piston and bore diameters.

$$V_{crev(m)} = \pi \left(r_{Bore}^2 - r_{Pist}^2 \right) * H_{(m)} \tag{A.1}$$

The ring land volumes ($V_{land(m)}$), are formed in the space between the ring and the ring land, which is formed by the ring clearance height (H_{cl}), and extends from the piston radius inside the ring gap ($r_{gap(m)}$) to the cylinder bore radius (r_{bore}).

$$V_{land(m)} = \pi \left(r_{Bore}^2 - r_{gap(m)}^2 \right) * H_{cl(m)} \tag{A.2}$$

The ring gap volumes are formed in the space between the ring inside diameter and the ring gap outside diameter and defined by the gap height

$$V_{gap(m)} = \pi \left(r_{ring(m)}^2 - r_{gap(m)}^2 \right) * H_{gap(m)} \tag{A.3}$$

The values of V_1, V_2, and V_3 change depending on the position of the piston rings. To simplify the analysis, **it was assumed that each ring sits against either its respective bottom crevice land or its top crevice land, but never in the middle of the gap**. The ring positions were determined by the pressure balance, and when the balance changes the ring position undergoes an instantaneous step change from one side of the gap to the other. Four potential pressure balance combinations exist among the pressures P_1, P_2, and P_3 that correspond to the respective V_m. These combinations are listed in Table A.1 along with the resulting V_m calculations. For reference, Pressure Balance 1 in Table A.1 corresponds to the ring positions depicted in Figure A.2. Also, a position of "Bottom" means that the ring sits against the lower ring land of its respective crevice, "Top" means it sits against the upper ring land, and the numbers correspond to the crevices in which the rings sit. It was **assumed that the oil ring does not restrict mass flow**, so V_3 was treated as an extension

of the crank case volume. Therefore, the dimensions of V_3 were unimportant and left out of Table A.1.

Table A.1: Possible combinations of the pressure balance in the ring gaps.

Pressure Balance	Ring 1 Position	Ring 2 Position	V1	V2
1. $P_1 > P_2 > P_3$	Bottom 1	Bottom 2	$V_{crev1} + V_{land1} + V_{gap1}$	$V_{crev2} + V_{land2} + V_{gap2}$
2. $P_1 > P_2 > P_3$	Bottom 1	Top 2	$V_{crev1} + V_{land1} + V_{gap1}$	V_{crev2}
3. $P_1 < P_2 < P_3$	Top 1	Top 2	V_{crev1}	$V_{crev2} + V_{land1} + V_{gap1}$
4. $P_1 < P_2 < P_3$	Top 1	Bottom 2	V_{crev1}	$V_{crev2} + V_{land1} + V_{land2} + V_{gap1} + V_{gap2}$

A.5 Pressure Definitions

Each of the crevice pressures required approximation. Figure A.2 shows that V_1 is directly connected to the bulk cylinder volume, so it is a good approximation that

$$P_{1,\theta} = P_\theta \tag{A.4}$$

The subscript "θ" refers to an iteration of the calculation based on the crank angle degree, and P_θ is the measured cylinder volume averaged over 500 cycles. Similarly, because V_3 is approximated as an extension of the crankcase pressure, P_3 was treated as constant and equal to the crankcase pressure. Because the SIDI engine does not have a crankcase pressure transducer, **the crankcase pressure was assumed to be constant and equal to ambient pressure**.

$$P_3 = P_{crankcase} = P_{ambient} = 101.25\text{kPa} \tag{A.5}$$

The pressure in the middle ring gap (P_2) was calculated based on the interaction between V_2 and the other two gap volumes. This interaction is defined by the mass flows between the crevices, which were determined by the pressure balance. Therefore, P_2 and the mass flows are codependent and it is prudent to define the positions and directions of the mass

flows before continuing with the development of the P_2 calculation. Briefly, $[+]\dot{m}_m$ flows from V_{m-1} to V_m and $[-]\dot{m}_m$ flows from V_m to V_{m-1}. Table 2 summarizes the positions and sign conventions for the mass flow rates $\dot{m}_m$ associated with the volumes V_m.

Table A.2: Sign conventions for mass flow rates

Flow Rate	Interacting Volumes	Sign Convention	Flow Direction	Local Pressure Balance
$\dot{m}_1$	$V_{Bulk} \Leftrightarrow V_1$	+	$V_{Bulk} \Rightarrow V_1$	$dP_{Bulk} = dP_1 < 0$
		-	$V_{Bulk} \Leftarrow V_1$	$dP_{Bulk} = dP_1 > 0$
$\dot{m}_2$	$V_1 \Leftrightarrow V_2$	+	$V_1 \Rightarrow V_2$	$P_1 > P_2$
		-	$V_1 \Leftarrow V_2$	$P_1 < P_2$
$\dot{m}_3$	$V_2 \Leftrightarrow V_3$	+	$V_2 \Rightarrow V_3$	$P_2 > P_3$
		-	$V_2 \Leftarrow V_3$	$P_2 < P_3$

If the mass flow rates are known, the change in P_2 follows the ideal gas law, and $P_{2,i}$ can be found if $P_{2,(i-1)}$ is known:

$$P_{2,i} = P_{2(i-1)} + \frac{T_W \left(\dot{m}_{2,i} - \dot{m}_{3,i}\right) \Delta t}{V_{2,i}} \left(\frac{R_{Universal}}{MW_{Reactants}}\right) \tag{A.6}$$

The subscript "i" is a numeric index that corresponds to θ. For $i = 1$, $P_{2,i}$ was unknown, so a guess value was needed. Calculations began at BDC (θ = -180). At BDC $P_3 = 101.25\,kPa$ & $P_{1,1} = IMAP$, which was normally below atmospheric pressure. It is sensible to **assume that** $P_{2,1}$ **is between** P_3 **and** $P_{1,1}$. To check the sensitivity of the model to the guess value of $P_{2,1}$, the affected mass flow rate was compared at the two most extreme possible values. These extremes are $P_{2,1} = P_3$ and $P_{2,1} = P_{1,1}$. Slightly higher mass flow was calculated from V_2 to V_1 when $P_{2,1} = P_3$, but the difference in the mass returned to the cylinder was less than 0.02%. Therefore, the choice of $P_{2,1}$ is not critical, but to achieve the minimum difference in error among all cases, $P_{2,1}$ was calculated as the average between $P_{1,1}$ and P_3.

$$P_{2,1} = \frac{P_{1,1} + P_3}{2} \tag{A.7}$$

This ensured that $P_{2,1}$ remained between P_3 and $P_{1,1}$ whether the engine was naturally aspirated ($P_{1,1} < P_3$) or boosted ($P_{1,1} > P_3$).

An example of pressure traces for the three crevices throughout the cycle resulting from the above equations is shown in Figure A.3. As previously specified, P_1 is equal to the measured cylinder pressure, P_3 is constant at 101.25 kPa, and P_2 begins between P_1 and P_3 and increases as a function of P_1 and the flow rates through the ring gaps. The lower rate of change in P_2 compared to P_1 is due to the tight tolerances in the piston components that restrict mass flow rates. As discussed next, the ring gaps are actually quite small, and very little mass flowed past the first ring. The effects of these pressures on mass flow rates into and out of the rings are discussed next.

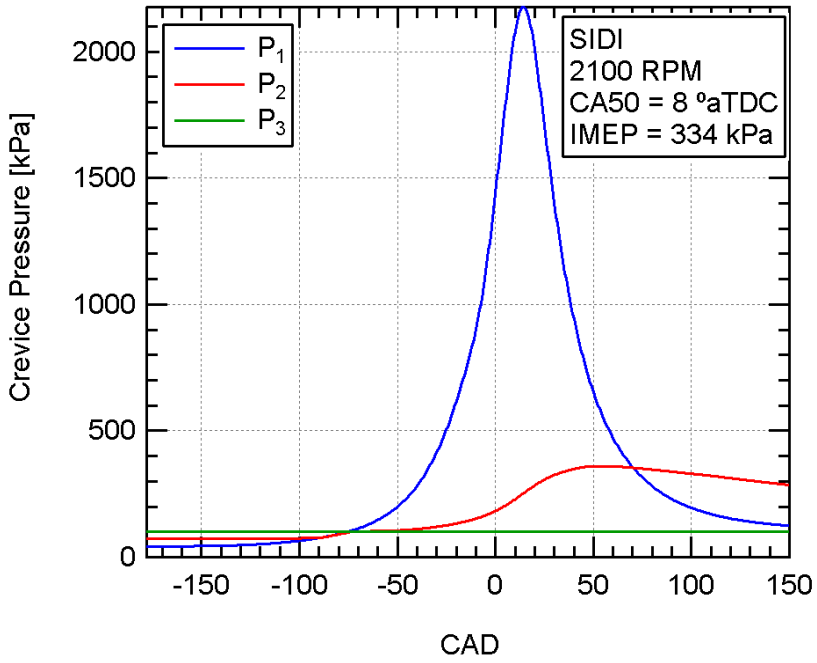

Figure A.3: Selected example of crevice pressure balances.

A.6 Mass Flow Directions and Magnitudes

The direction of the flows between the crevice volumes are dependent on the pressure balances. Table A.1 showed the potential pressure balance combinations, while Table A.2 suggested the flow directions that would result from those pressure balances. For each flow an upstream pressure ($P_{U,m}$) and a downstream pressure ($P_{D,m}$) were defined, where P_1, P_2, and P_3 can all play the role of either $P_{U,m}$ or $P_{D,m}$ depending on the pressure balance. The roles of the three crevice pressures are defined in Table A.3 for each situation.

Table A.3: Crevice pressure roles for pressure balance combinations

Pressure Balance	P_1	P_2	P_3
1. $P_1 > P_2 > P_3$	$P_{U,2}$	$P_{D,2}$, $P_{U,3}$	$P_{D,3}$
2. $P_1 > P_2 > P_3$	$P_{U,2}$	$P_{D,2}$, $P_{D,3}$	$P_{U,3}$
3. $P_1 < P_2 < P_3$	$P_{D,2}$	$P_{U,2}$, $P_{D,3}$	$P_{U,3}$
4. $P_1 < P_2 < P_3$	$P_{D,2}$	$P_{U,2}$, $P_{U,3}$	$P_{D,3}$

Again, it was assumed that the flow can only travel between the crevice volumes through the ring end gaps. The pressure difference determines whether the flow through the end gap is subsonic or choked, and this was determined before calculating the mass flow rate. The criteria defined in [43] for choked flow is:

$$\frac{P_D}{P_U} < 0.52 \rightarrow \text{Choked Flow} \tag{A.8}$$

Otherwise, the flow is subsonic. For both choked and subsonic flow, the flow rate is [104]:

$$\dot{m}_i = C_D * A_{eg} * \sqrt{\frac{\gamma}{R * T_W} * P_U} * \eta_{Comp} \tag{A.9}$$

$$C_D = 0.85 \ (\text{Discharge Coefficient})$$

$$A_{eg} = \text{Ring Endgap Area}$$

$$\eta_{comp} = \text{Compressibility Factor}$$

In Equation A.9, η_{comp} depends on whether the flow is choked or subsonic (see Equations A.12 and A.13). A_{eg} was approximated as a rectangle and calculated as:

$$A_{eg} = w_{endgap} * (r_{bore} - r_{piston}) \tag{A.10}$$
$$w_{endgap} = 4.3\left(10^{-4}\right)\,[m]$$

The crevice gas specific heat ratio (γ_{crev}) and ideal gas constant (R) were calculated assuming the compostion of the crevice mixture was equal to the composition of the original mixture of reactants (fuel and air). The formula used for γ_{crev} was that specified by Ghandhi [43]:

$$\gamma_{crev} = 1.426\Phi - 0.0459 + T_W\left(1\left(10^{-5}\right) * 1.02\Phi^2 - 3.3\Phi - 9.44\right) \tag{A.11}$$

For both the $\dot{m}_i$ and γ_{crev} calculation, the term T_W refers to the temperature of the wall, but was substituted in these formulas as the gas temperature due to the assumption that the crevice gas temperature was equal to the wall temperature. The compressibility factor depends on whether the flow is choked or subsonic. The equations for both cases are:

$$\eta_{comp} = \left(\frac{2}{\gamma+1}\right)^{\frac{\gamma+1}{2(\gamma-1)}} \quad (Choked) \tag{A.12}$$

$$\eta_{comp} = \left(\frac{2}{\gamma-1}\left(\left(\frac{P_D}{P_u}\right)^{\frac{2}{\gamma}} - \left(\frac{P_D}{P_u}\right)^{\frac{\gamma+1}{\gamma}}\right)\right)^{0.5} \quad (Subsonic) \tag{A.13}$$

This completes the equation set required for finding $\dot{m}_2$, $\dot{m}_3$ and $P_{2,i}$. As seen in Table A.2, $\dot{m}_1$ is determined from dP_{Bulk}.

$$\boxed{\dot{m}_1 = \dot{m}_2 + \dot{m}_{CV} = \dot{m}_2 + \left(\frac{dP_1}{dt}\right) * \frac{V_1}{RT_W}} \tag{A.14}$$

In Equation A.14, $dP_1 = dP_{Bulk}$ and $\dot{m}_{CV}$ refers to the rate of change of the mass in the control volume bounded by V_1.

An example of the three crevice mass flow rates throughout the cycle resulting from the above equations is shown in Figure A.4. The piston schematics in Figure A.4 display the approximate flow directions as they change with piston travel. As shown in the graph and pictures, mass generally flows from the combustion chamber towards the crankcase (into the crevices) as the piston moves up towards TDC ($\theta = 0$). Flow continues into the crevice after TDC due to the high chamber pressure caused by the main combustion event. Mass begins to flow back towards the combustion chamber as the piston moves down after the main combustion when the chamber pressure is dropping rapidly. As the graph shows, $\dot{m}_1$, $\dot{m}_2$, and $\dot{m}_3$, do not change directions simultaneously. The individual directions of flow are determined by the pressure balances from Figure A.3. The flow directions in the piston schematics are drawn to provide a general idea of the flow direction. The relative magnitudes of the flows agree well with the relative magnitudes of the pressures in Figure A.3. Both results show that very little mass flows into the 2^{nd} or 3^{rd} crevices.

A schematic of the dimensions used to determine crevice volumes and endgap areas is shown in Figure A.5. The scaling is inflated to show the details of interest. The values and uncertainties for the measurements depicted in Figure A.5 are listed in Table A.4. In Table A.4, linear dimensions were measured with a calipers, and the uncertainty in these measurements is equal to that calipers' rated accuracy of 0.02 mm. Radial measurements were provided by the shops that machined the piston and cylinder liner. The machine shops did not provide uncertainties for their measurements, so the uncertainty was estimated as half of the lowest significant figure. Finally, areas and volumes in Table A.4 were calculated from the linear and radial measurements, so propagation of error was used to determine these uncertainties.

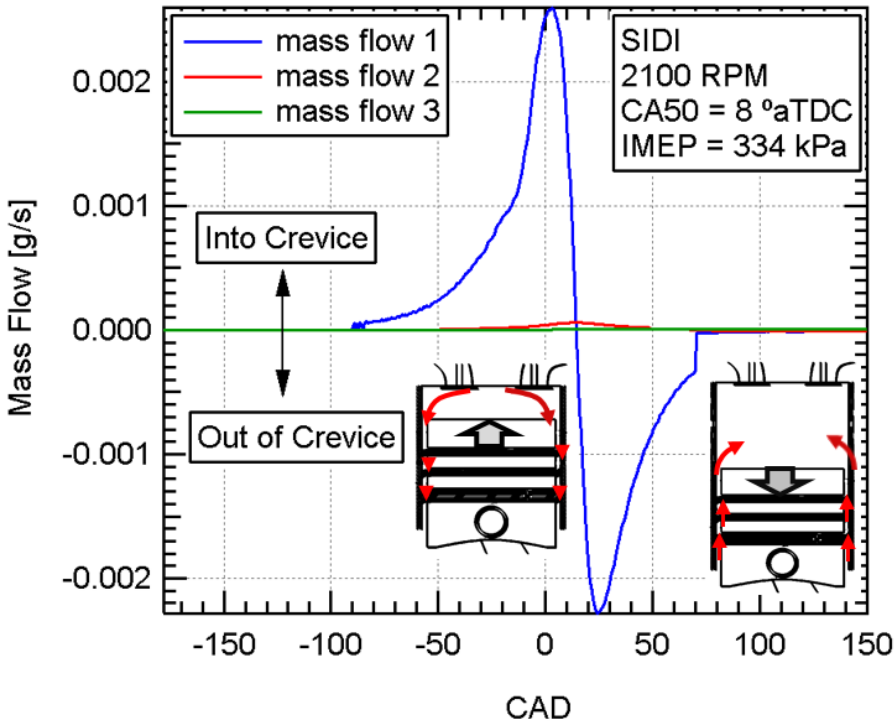

Figure A.4: Selected example of flow rates from all three crevices.

Table A.4: Measured crevice dimensions

Name	Value	Uncertainty	[Units]
Bore	86.00	± 0.005	[mm]
r_{pist}	42.95	± 0.005	[mm]
r_{ring}	39.74	± 0.005	[mm]
r_{groove}	38.95	± 0.005	[mm]
H_1	2.719	± 0.02	[mm]
H_2	3.8	± 0.02	[mm]
H_{rg1}	1.219	± 0.02	[mm]
H_{rg2}	1.473	± 0.02	[mm]
H_{ring1}	1.15	± 0.02	[mm]
H_{ring2}	1.46	± 0.02	[mm]
w_{endgap}	0.33	± 0.005	[mm]
A_{eg}	0.0165	± 2E-6	[mm^2]
V_{crev1}	22.0	± 0.0298	[mm^3]
V_{crev2}	30.8	± 0.0213	[mm^3]
V_{land1}	71.6	± 0.1739	[mm^3]
V_{land2}	13.5	± 0.1404	[mm^3]
V_{rg1}	225	± 0.0043	[mm^3]
V_{rg2}	285	± 0.0034	[mm^3]

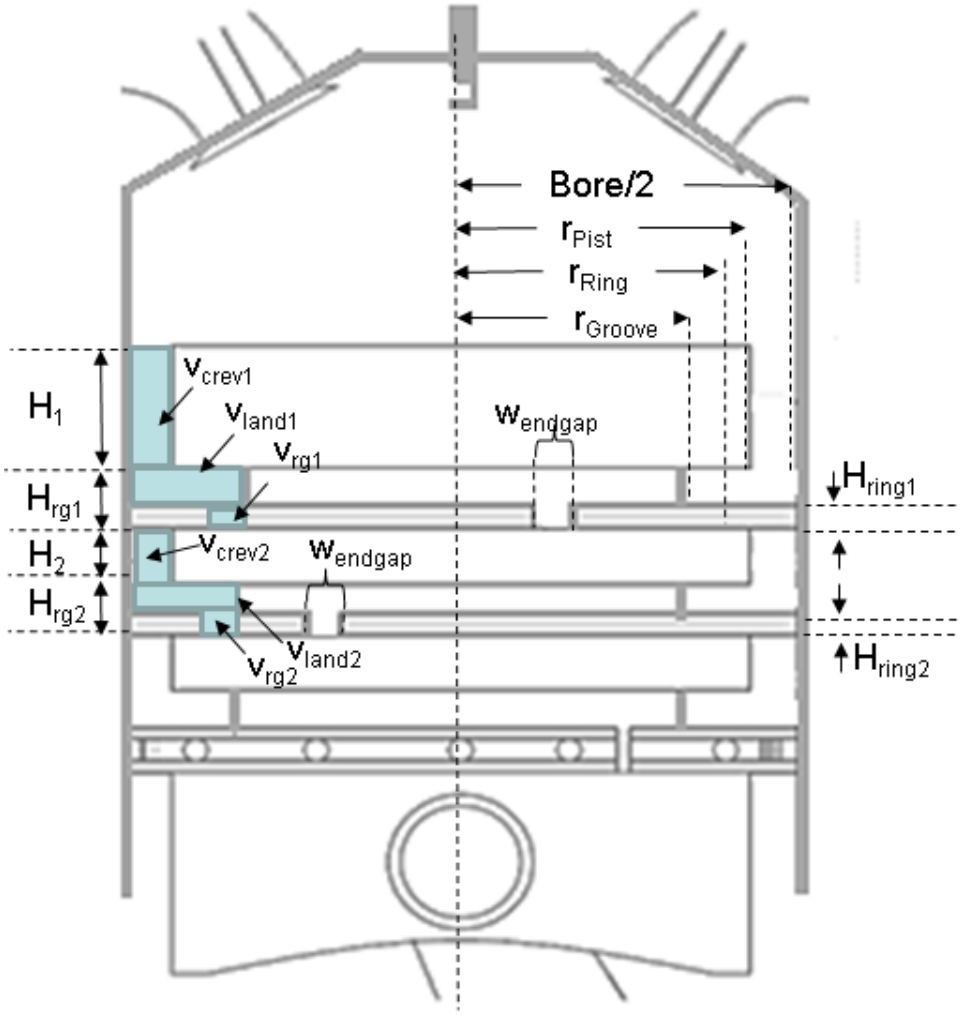

Figure A.5: Measured chamber and crevice dimensions for the engine used in this study.

B CALCULATING CRANK-ANGLE-RESOLVED THERMODYNAMIC PARAMETERS FROM IN-CYLINDER PRESSURE DATA

The 720 tooth crankshaft encoder and Kistler pressure transducer provided 1440 crank-angle-resolved pressure readings per cycle for 500 cycles via the high speed DAQ channel. The 500 cycles were averaged in the post-processor to produce a single column of 1440 crank-angle resolved pressure readings (P_θ). These P_θ were used to approximate additional in-cylinder thermodynamic parameters including temperature (T), apparent heat release rate (AHRR), and cumulative heat release (Q_{cum}). These three parameters can only be accurately calculated if the cylinder is a closed system. Therefore, the calculations presented here are not valid after Exhaust Valve Open (EVO), or before Intake Valve Closed (IVC) crank angle positions. The subscript θ is used throughout this document to denote that a variable changes as a function of crank angle (θ).

B.1 Assumptions

The calculations relied on several assumptions and approximations. First, the fuel and air mixture inside the cylinder, referred to here as the trapped mass (m_T) was treated as an **ideal gas**. The ideal gas law was used to determine T_θ from P_θ as shown in Equation B.1.

$$P_\theta V_\theta = m_T R T_\theta \tag{B.1}$$

There was also an **isothermal boundary condition** imposed on the system wall, and the resulting constant cylinder wall temperature (T_W) was set to 400 K. Mixture composition, T_θ and P_θ were assumed to be **spatially uniform** for each instantaneous position in the cycle, which is consistent with a **single zone heat release** model. Therefore, T_θ in Equation B.1 was the average bulk gas temperature ($T_{B,\theta}$). The closed-system model assumes **no blowby**.

Additionally, the **crevice volume was ignored**.

To summarize, the main assumptions were:

1. ideal gas
2. isothermal boundary (400 K)
3. closed system (no blowby)
4. spatially uniform T ($T_{B,\theta}$)
5. single-zone heat release
6. no crevice volume

Additional assumptions were made that were applicable only to small groups of calculations. These are discussed here as they are used. All **assumptions are presented in boldface**. Also, multiple steps in derivations of key parameters are presented. The final solutions of these derivations are $\boxed{\texttt{boxed}}$.

B.2 Volume

The crank-angle-varying volume of the system was determined using bore (B), clearance volume (V_C), crankshaft length (a), connecting rod length (l), and the instantaneous crank angle (θ) in Equation B.2.

$$\boxed{V_\theta = V_C + \frac{\pi}{4}B^2(l + a - s)} \tag{B.2}$$

In Equation B.2, s is the instantaneous distance between the crank axis and the piston pin axis:

$$s = \left[\left(l^2 - a^2 sin^2\theta\right)^{\frac{1}{2}} + a\cos\theta\right] \tag{B.3}$$

The quantity $(l + a - s)$ is the instantaneous stroke. These parameters are defined in [55], and can be seen in Figure B.1.

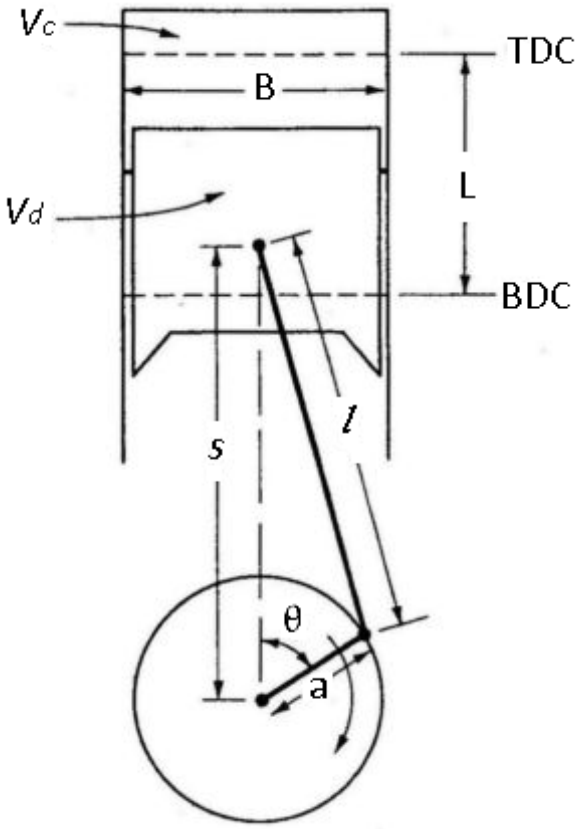

Figure B.1: Generic cylinder geometry. Modified from [55].

B.3 Trapped Mass

Trapped mass is composed of the mass flow in (m_{in}) and a small mass of residual exhaust components that remain in the cylinder after each cycle (m_{res}).

$$m_T = m_{in} + m_{res} \tag{B.4}$$

In this study, m_{in} was the sum of the fuel mass injected per cycle (m_f), the air mass injected per cycle (m_a), and the mass of exhaust gas intentionally recirculated using the exhaust gas recirculation system (m_{EGR}).

$$m_{in} = m_a + m_f + m_{EGR} \tag{B.5}$$

No experiments used EGR, so this expression simplifies to:

$$m_{in} = m_a + m_f \tag{B.6}$$

The residual portion of the trapped mass was estimated by **assuming polytropic compression and expansion processes** for the compression and exhaust strokes, respectively. To begin, two points between IVC and ignition were chosen from the compression stroke. Point 1 needed to be long enough after IVC that pressure fluctuations caused by the closing of the intake valve were negligible, but close enough to IVC to maximize the crank angle window between Point 1 and Point 2. Similarly, Point 2 needed to be long enough before ignition to guarantee no early combustion during the crank angle window bounded by Points 1 and 2, but close enough to ignition to maximize the window. Point 1 was set to 5 CAD after IVC, and Point 2 was set to 30 CAD before TDC. The polytropic exponent for the compression (n_c) was determined from the pressures and volumes at these two points using Equation B.7

$$P_1 V_1^{n_c} = P_2 V_2^{n_c} \therefore \boxed{n_c = \frac{\ln \frac{P_2}{P_1}}{\ln \frac{V_1}{V_2}}} \tag{B.7}$$

It was **assumed that n_c remained constant** throughout compression, ignition, combustion, and exhaust. With the assumption of constant n_c, the fraction of residual mass left in the cylinder after the exhaust stroke was determined using the n_c calculated from the compression stroke. For a polytropic process:

$$P\left(\frac{V}{m}\right)^{n_c} = Constant \tag{B.8}$$

In a closed system like the compression stroke, the distinction of specific volume that separates Equations B.8 and B.7 is irrelevant because the mass does not change. However, a **polytropic expansion was also assumed for the exhaust stroke** beginning at Exhaust Valve Open (EVO), where all of the original mass was still present, and ending at Exhaust Valve Closed (EVC), where some unknown residual mass was left in the cylinder. In this case, n_c was defined by the conditions at EVO and EVC.

$$n_c = \frac{\ln \frac{P_{EVC}}{P_{EVO}}}{\ln \frac{V_{EVO}/m_{EVO}}{V_{EVC}/m_{EVC}}} \tag{B.9}$$

In Equation B.9, the unknown quantity is m_{EVC}, and $m_{EVC} = m_{res}$. Similarly, $m_{EVO} = m_T$. Acknowledging these equalities and rearranging B.9 gives the equation for the residual mass fraction (y_{res}).

$$\frac{m_{res}}{m_T} = \frac{m_{EVC}}{m_{EVO}} = \frac{V_{EVC}}{V_{EVO}}\left(\frac{P_{EVC}}{P_{EVO}}\right)^{\frac{1}{n_c}} = y_{res} \tag{B.10}$$

Because $m_{res} = 0$ for the very first cycle, Equation B.4 simplifies to

$$m_{T(1)} = m_{in(1)} \tag{B.11}$$

and

$$y_{res(1)} = \frac{m_{res(1)}}{m_{T(1)}} \tag{B.12}$$

$$\therefore$$

$$m_{res(1)} = m_{T(1)} * y_{res}$$

The trapped mass for each subsequent cycle (cycle i) is the sum of the residual mass from the previous cycle ($m_{res(i-1)}$) and the current cycle's mass flow in ($m_{in(i)}$) and can be determined using the value of the previous cycle's residual mass fraction ($y_{res(i-1)}$).

$$\boxed{m_{T(i)} = \frac{m_{in(i)}}{1 - y_{res(i-1)}}} \tag{B.13}$$

Recall that this formulation depended on the assumption that n_c remained constant. This assumption has the potential to introduce discernible error. During the compression stroke where n_c was determined, the charge is mostly air and fuel. In the exhaust stroke, the charge has transformed into products including CO_2, CO, NO_X, H_2O, O_2, N_2, and unburned hydrocarbons. It is unlikely that n_c remains constant throughout this process. However, this is currently the best method of determining n_c for these types of calculations.

B.4 Temperature

The crank-angle-resolved average bulk gas temperature ($T_{B,\theta}$) was estimated using the ideal gas law directly from known values of P_θ, V_θ, R, and m_T.

$$\boxed{T_{B,\theta} = \frac{P_\theta * V_\theta}{\frac{R_u}{MW_{mix,\theta}} * m_T}} \tag{B.14}$$

The approximation of $MW_{mix,\theta}$ required to solve for $T_{B,\theta}$ is an important consideration. In any engine $MW_{mix,\theta}$ changes with charge composition as combustion progresses. Before ignition, the charge is composed of unburned fuel and air (the reactants) and after combustion the charge is composed of combustion products. During combustion the composition is less certain. Additionally, The approximation of $MW_{mix,\theta}$ depends on the choice of a single zone or multiple zone combustion model. Two choices of combustion models are discussed here: a single zone model, and a two zone model. Once the choice of combustion model is explained, the discussion of $MW_{mix,\theta}$ will continue.

A two zone model consists of a burned gas zone and a unburned gas zone. In this case, $MW_{mix,\theta} = MW_{reactants}$ is used for the unburned portion, and $MW_{mix,\theta} = MW_{products}$ is used for the burned portion. The two-zone model accounts for the significant temperature differences between the burned and unburned gasses, but adds computational complexity to post-processing. Here, it was **assumed that by CA90, only the burned zone remains**. With this assumption, a single zone model and a two zone model are equivalent before ignition and after CA90. Because late cycle temperatures were of most interest here, the single zone model was used. Therefore, the two zone model will not be discussed further, and the following derivations are for the single zone model.

For the single zone model, the cumulative heat release ($Q_{cum,\theta}$) was used to provide an estimate of the burned and unburned mixture fractions, which have $MW_{products}$ and $MW_{reactants}$, respectively. $MW_{mix,\theta}$ was calculated as the average of these fractions.

$MW_{products}$ was approximated using the measured exhaust gas concentrations and applying the following simple formula.

$$MW_{products} = \sum (MW_X * [X]) \tag{B.15}$$
$$[X] = Concentration\ of\ product\ X$$

The **products (X) are assumed to be CO_2, O_2, CO, NO_X, HC, H_2, H_2O, and N_2**. The concentrations [CO_2], [O_2], and [CO] are measured directly by the Horiba emissions bench. Similarly, NO ppm and HC ppm are measured and can be converted to [NO] and [HC] by dividing the ppm readings by 1000. The Horiba bench measurements are taken on a "dry" basis. For dry measurements, H_2 concentration can be approximated as

$$[H_2] = \frac{n_{CO} * n_{H2O}/n_{CO2}}{3.8 * n_{dry-exhaust}} \tag{B.16}$$

In Equation B.16, n stands for the number of moles, and the subscripts are the species. The H_2O concentration can be approximated as

$$[H_2O] = \left(\frac{H}{C}\right)_{fuel} * (0.5 * [CO_2] + 0.25 * [CO]) \tag{B.17}$$

Finally, it was **assumed that N_2 makes up the balance** of the remaining products.

$$[N_2] = 1 - [H_2] - [CO_2] - [H_2O] - [O_2] - [CO] - [HC] - [NO] \tag{B.18}$$

The molecular weights of CO_2, CO, H_2, H_2O, and O_2 are known. The **molecular weight of NO_X was assumed to be equal to NO**, and the **molecular weight of HC was approximated as MW_{HC} = 41.625kg/kmol** according to a test code provided by General Motors. In the calculation of $MW_{reactants}$ the reactants are the fuel and air, and the combined molecular weight can be determined using the measured air and fuel mass for each engine cycle.

$$MW_{reactants} = \frac{m_f + m_a}{\frac{m_f}{MW_f} + \frac{m_a}{MW_a}} \tag{B.19}$$

Finally, $MW_{mix,\theta}$ was calculated as a weighted average of $MW_{products}$ and $MW_{reactants}$ based on the normalized cumulative heat release ($\hat{Q}_{cum,\theta}$). Because $\hat{Q}_{cum,\theta}$ is proportional to the mass fraction burned (MFB), it was **assumed that $\hat{Q}_{cum,\theta} = MFB_\theta$**. Then, the proportion of the cylinder contents with $MW_{products}$ is $\hat{Q}_{cum,\theta}$, and the proportion with $MW_{reactants}$ is (1-$\hat{Q}_{cum,\theta}$). The calculation of $MW_{mix,\theta}$ follows.

$$\boxed{MW_{mix,\theta} = MW_{products}\hat{Q}_{cum,\theta} + MW_{reactants}\left(1 - \hat{Q}_{cum,\theta}\right)} \tag{B.20}$$

Note that $MW_{mix,\theta}$ was used for approximations of $T_{B,\theta}$, $dQ/d\theta$, and $Q_{cum,\theta}$, so $MW_{mix,\theta}$ and $Q_{cum,\theta}$ were mutually dependent. Therefore, an iterative process was used for each θ where the first iteration used $MW_{mix,\theta} = MW_{reactants}$ to calculate $\hat{Q}_{cum,\theta}$,

which was used in the second iteration to provide a better estimation of $MW_{\mathrm{mix},\theta}$ from Equation B.20. This completes the formulation for $MW_{\mathrm{mix},\theta}$. For completeness, it is worth discussing additional options for the estimation of $MW_{\mathrm{mix},\theta}$ and why they were not used here.

The simplest approximation is $MW_{\mathrm{mix},\theta} = MW_{\mathrm{air}} = 28.97\,\mathrm{kg/kmol}$. This may be sufficient if early and late cycle accuracy are of equal importance, there are no cases with significantly rich mixtures, and ≈10% error is acceptable throughout the cycle. This approximation requires no additional calculations. Because greater accuracy was desired here and many PMPV cases are very rich, this option was not used.

If early cycle accuracy is of the greatest importance, $MW_{\mathrm{reactants}}$ can be used, but this introduces significant inaccuracy late in the cycle. Conversely, if late cycle accuracy is of the greatest importance, MW_{products} can be used, but this introduces inaccuracies early in the cycle. Figure B.2 from Ghandhi [43] shows the difference between $MW_{\mathrm{reactants}}$ and MW_{products} for a range of Φ using a mixture of iso-octane and air. MW_{air} is not shown, but it is a constant 28.97 kg/kmol, and therefore approximately splits the difference between the other two calculations. The difference between the two methods increases for richer mixtures, and at $\Phi = 1.4$, the difference is about 17%. Because T depends directly on MW through the ideal gas law, a 17% difference in MW corresponds to a 17% difference in temperature.

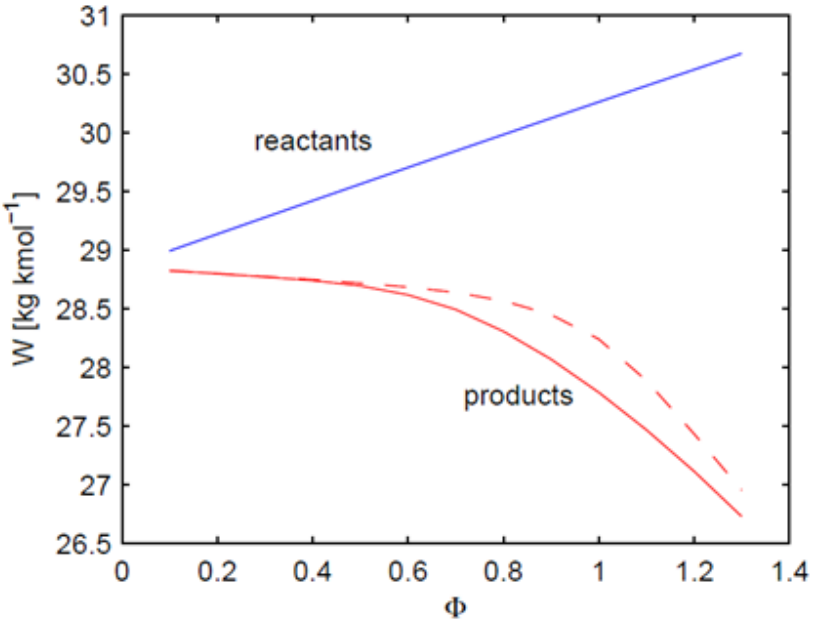

Figure B.2: Calculation of average MW (W here) resulting from use of reactant species MW and product species MW for an air/iso-octane mix [43].

B.5 Heat Release

B.5.1 Closed System Energy Balance

The heat release model employed here for the combustion event was a single zone model. There are two methods of implementing a single zone heat release model [43]. One method assumes a fuel mass addition to the system, which employs a changing mixture composition that is a function of the mass addition. This is suitable for diesel combustion, but it does not describe spark-ignition combustion well and will not be discussed further here. The method used here models the combustion event as a heat addition across the system boundary. The **rate of heat addition was assumed to be the rate of conversion of chemical energy (Q_{chem}) to sensible internal energy (Q_{sens})**. Additional heat transfer to the system from the surroundings was also considered. All external heat additions are lumped here into a single term, defined as the wall heat transfer (Q_w). These heat additions are shown in the simple closed system model shown in Figure B.3 and Equation B.21.

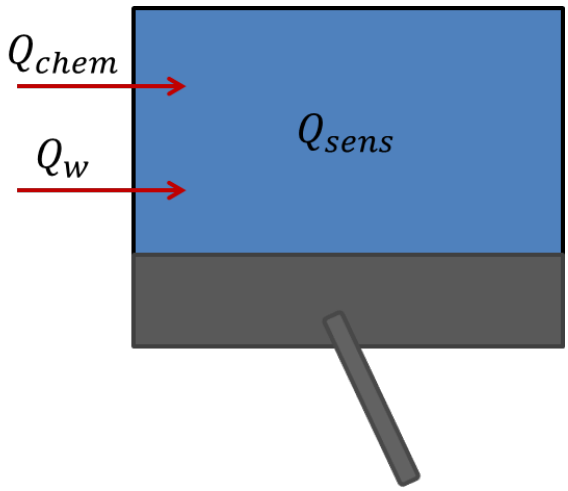

Figure B.3: Closed system cylinder energy flows.

$$Q_{sens} = Q_{chem} + Q_w \tag{B.21}$$

Q_{chem} is a function of the flow of fuel into the cylinder and the combustion efficiency (η_C).

$$Q_{chem} = m_f * LHV * \eta_c \tag{B.22}$$

The calculation for the combustion efficiency was dependent on measured emissions data and will be discussed later. Here, η_C was a known quantity. Because the fuel mass flow rate and LHV of the fuel are also known, Q_{chem} was easily calculated, and restating the equation for sensible enthalpy, the total chemical energy released must be the difference between the system's total sensible energy and the wall heat transfer:

$$Q_{chem} = Q_{sens} - Q_w \tag{B.23}$$

Because this is a time varying system, the differential form of this equation must be solved on either a time or θ basis, then integrated. Ignoring heat transfer from the walls for a moment simplifies the closed system differential energy equation and allows for a

quicker solution for Q_{sens}. The generic form of the differential energy equation for a closed system is:

$$\begin{aligned} \delta Q - \delta W &= dU \\ \delta W &= P dV \\ dU &= m\, c_v\, dT \\ \therefore \delta Q - P dV &= m\, c_v\, dT \end{aligned} \tag{B.24}$$

Here, δQ is Q_{chem}, and $dU + \delta W$ represents Q_{sens}. The ideal gas equation in differential form is [36]

$$m dT = \frac{1}{R}\left(P dv + V dP\right) \tag{B.25}$$

Solving for δQ and applying the ideal gas specific heat relations, the solution for δQ can be written in terms of the specific heat ratio (γ).

$$\delta Q = \left(1 + \frac{c_v}{R}\right) P dV + \frac{c_v}{R} V dP \tag{B.26}$$

$$\frac{c_v}{R} = \frac{1}{\gamma - 1} \tag{B.27}$$

$$\frac{c_p}{R} = \frac{\gamma}{\gamma - 1} \tag{B.28}$$

$$\gamma = \frac{c_p}{c_v} \tag{B.29}$$

$$\delta Q = \left(\frac{\gamma}{\gamma - 1}\right) P dV + \left(\frac{1}{\gamma - 1}\right) V dP \tag{B.30}$$

The differential form of Q_{sens} is therefore:

$$\delta Q_{sens} = \left(\frac{\gamma}{\gamma - 1}\right) P dV + \left(\frac{1}{\gamma - 1}\right) V dP \tag{B.31}$$

Reinserting the wall heat transfer term and acknowledging that $\delta Q = \delta Q_{chem}$:

$$\delta Q_{chem} = \left(\frac{\gamma}{\gamma - 1}\right) P dV + \left(\frac{1}{\gamma - 1}\right) V dP - \delta Q_W \tag{B.32}$$

The instantaneous values and changes in pressure and volume are known. The two unknowns left to be solved in this equation are γ and δQ_W. These are treated separately next.

B.5.2 Approximation of γ

The time-varying gas composition makes the value of γ difficult to define, and a few options exist for its calculation. A correlation that has been shown to have reasonable agreement with experimental results is the Gatowski correlation [2]. Equation B.33 defines the calculation of γ from this correlation (γ_{Gat}).

$$\gamma_{Gat} = 1.392 - 0.000075 T_B \theta \tag{B.33}$$

However, γ_{Gat} ignores the variation in composition with combustion, and does not account for differences in fuel chemistry. A two part correlation gives γ_{2P}, which is discussed in [43] and shown in Equation B.34.

$$\gamma_{2P} = \begin{cases} \gamma_0 + \gamma_1 T[K] \\ \gamma_{HT} \end{cases} \tag{B.34}$$

$$\gamma_0 = 1.426\Phi - 0.459$$

$$\gamma_1 = 10^{-5}\left(1.02\Phi^2 - 3.30\Phi - 9.44\right)$$

$$\gamma_{HT} = 0.0386\Phi^2 - 0.838\Phi + 1.33$$

In Equation B.34 γ_0 & γ_1 are part of the T-dependent reactant mixture, and γ_{HT} corresponds to the plateau region of the products. A drawback of both the two part and Gatowski correlations are that they are only valid for Φ close to one. In the PMPV experiments of this study, where $1.2 < \Phi < 1.6$, both correlations are inaccurate. Additionally γ is a function of fuel, which is not addressed by either correlation.

For these reasons, neither γ_{Gat} nor γ_{2P} was used here. Instead, γ was determined independently as a function of fuel and Φ from a chemical equilibrium calculation in Cantera using a detailed chemical mechanism. The equilibrium value (γ_{eq}) for each fuel and Φ was taken as an average of values calculated at a range of temperatures from 1200 K to 2700 K and a pressure of 20 bar. Because **γ_{eq} assumes chemical equilibrium under engine thermodynamic conditions,** the results are least accurate early in the cycle, and become more accurate as combustion progresses. Results of the γ_{eq} vs Φ calculation for the fuels of interest are shown in Figure B.4. The results for TRF30 are an acceptable approximation for EEE, and γ_{eq} for any ethanol blend or TRF blend can be interpolated from the results for Ethanol and TRF30 or iso-octane and TRF30, respectively.

The results from Figure B.4 were tabulated, called into the post-processor for the specified fuel type, and interpolated according to the measured Φ, ethanol blend fraction, and TRF number to determine the case-specific γ_{eq}. This treatment assumed **γ_{eq} was constant with θ**.

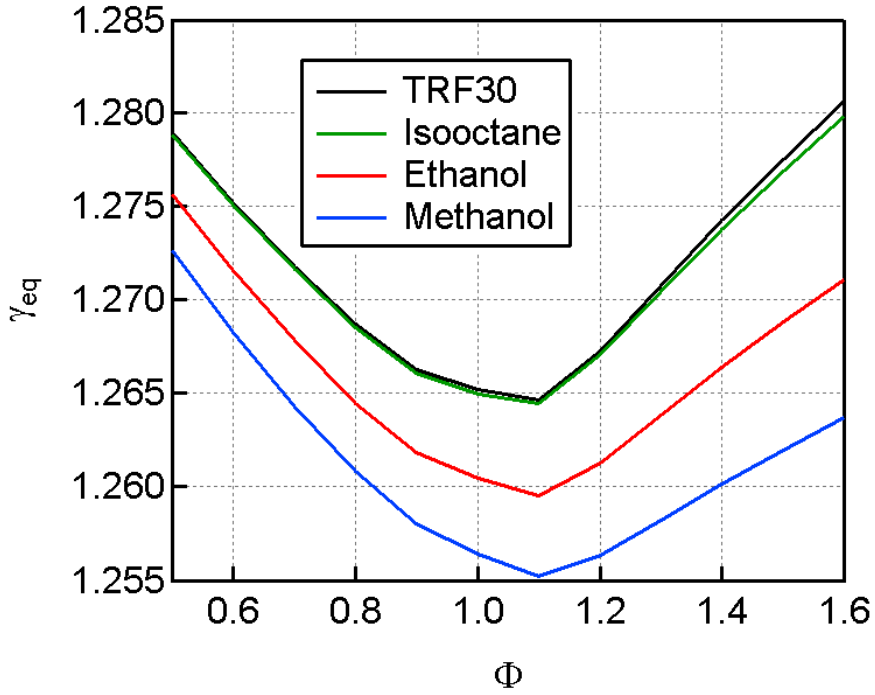

Figure B.4: Approximations of γ_{eq} for various fuels as a function of Φ. Calculations and plot courtesy of Prof. David Rothamer.

B.5.3 Approximation of δQ_W

Heat transfer to cylinder walls is spatially variable and difficult to measure. It was not measured here. Instead, Equation B.35 was used. Utilizing an analogy to turbulent pipe flows, Equation B.35 is a convective heat-transfer correlation developed by Annand [11, 55] that matches previously published experimental instantaneous heat flux data.

$$\frac{h_{c,\theta}B}{k} = a\left(\frac{\rho\bar{S}_{p,\theta}B}{\mu}\right)^{b} \tag{B.35}$$

$h_c = Convective\ Heat\ Transfer\ Coefficient$

$B = Engine\ Bore$

$k = Thermal\ Conductivity$

$\bar{S}_p = Mean\ Piston\ Speed$

$\mu = Dynamic\ Viscosity$

$a\ \&\ b = Constants$

Assuming ideal gas behavior and the correlations in Equations B.36 & B.37, Woschni [55, 123] developed the semi-empirical correlation in Equation B.38.

$$k \propto T^{0.75} \tag{B.36}$$

$$\mu \propto T^{0.62} \tag{B.37}$$

$$h_{c,\theta} = CB^{m-1}P^{m}w_{\theta}^{m}T_{B,\theta}^{0.75-1.62m} \tag{B.38}$$

In Equation B.38, w is the average cylinder gas velocity [m/s]. This was estimated as

$$w_{\theta} = C_1\bar{S}_{p,\theta} + \frac{C_2V_{disp}T_{ref}}{P_{ref}V_{ref}}\left(P_{\theta} - P_{motor,\theta}\right) \tag{B.39}$$

$C_1 = 2.28\ (Combustion\ \&\ Expansion)$

$C_2 = 3.24\left(10^{-3}\right)\ (Combustion\ \&\ Expansion)$

Here, $P_{motor,\theta}$ is calculated using n_c calculated in Equation B.7 and the instantaneous volume.

$$P_{motor,\theta} = P_{IVC}\left(\frac{V_{IVC}}{V_{,\theta}}\right)^{n_c} \tag{B.40}$$

The subscript "ref" is used to specify a property at a reference state. Here, the reference state was chosen as IVC. The constants C_1 and C_2 depend on the geometry of the engine and the portion of the cycle being considered. Although the above expression for gas velocity was originally developed for a direct-injection CI engine without swirl, spark ignition tests have shown that the constants specified are acceptable for use with SI operation as well [55]. Combustion and expansion was the period of interest for heat release, and the constants were chosen accordingly.

Heywood [55] sets the exponent $m = 0.8$ in the formulation of the Woschni correlation, resulting in the more directly useful correlation:

$$\boxed{h_{c,\theta}\left[\frac{W}{(m^2K}\right] = (3.26B[m])^{-0.2}\,(P_\theta[kPa])^{0.8}\,(T_{B,\theta}[K])^{-0.55}\left(w_\theta\left[\frac{m}{s}\right]\right)^{0.8}} \tag{B.41}$$

This can be utilized in the general expression for convection heat transfer to the wall:

$$\dot{Q}_{HT} = \frac{dQ_{HT}}{dt} = h_c A\,(T_B - T_w)$$

$$\therefore \tag{B.42}$$

$$dQ_{HT} = h_c A\,(T_B - T_w)\,dt$$

The variable "A" is the wall area. As a function of crank angle, these questions become:

$$\frac{dQ_{HT}}{d\theta} = h_{c,\theta} A_\theta\,(T_{B,\theta} - T_w)\,\frac{dt}{d\theta}$$

$$\therefore \tag{B.43}$$

$$\boxed{\frac{dQ_{HT}}{d\theta} = h_{c,\theta} A_\theta \left(T_{B,\theta} - T_w\right) \bar{S}_{p,\theta}}$$

Note that **radiation heat transfer was ignored**. Also, because $T_{B,\theta}$ is greater than T_w during combustion, the heat is transferred to the cylinder walls, changing the sign convention for $\dot{Q}_{HT}$. The crank-angle resolved sensible energy can be expressed as

$$\frac{dQ_{sens}}{d\theta} = \left(\frac{\gamma}{\gamma - 1}\right) P \frac{dV}{d\theta} + \left(\frac{1}{\gamma - 1}\right) V \frac{dP}{d\theta} \tag{B.44}$$

The total heat release is the sum of the sensible and convective heat transfers, and equal to the chemical heat release:

$$Q_{total} = Q_{Chem} = \int_{SA}^{EA} \left(Q_{sens} + Q_{HT}\right) d\theta \tag{B.45}$$

SA (Start Angle) and EA (End Angle) were normally defined as -40 CAD and EVO, respectively. As cited by Ghandhi [43], this heat transfer model does not accurately predict the absolute magnitude of the heat release rate. This error is corrected by applying an overall energy balance that sets the integrated heat release equal to the total fuel energy, $\int Q_{chem} = \eta_{cm} f LHV$ by multiplying the wall heat transfer term by a scaling factor that is determined as follows:

$$f_{HT} = \frac{Q_{total} - Q_{HR}}{Q_{HT}} \tag{B.46}$$

The correction is applied so that the equality between Q_{total}, Q_{chem}, and $Q_{sens} + Q_{HT}$, is obeyed, and then solves for all the thermodynamic data in a second iteration using the corrected values.

C CALCULATIONS FROM THE MEASURED PARTICLE SIZE DISTRIBUTION (PSD)

C.1 Introduction

The primary diagnostic used to determine particle formation tendencies was the engine-out measured particle size distribution (PSD). The SMPS provides particle number concentrations for each D_m from 7.64 nm up to 289 nm. These measured concentrations were used to calculate a number of other useful metrics. The PSD was integrated across all size ranges to give the total number concentration (PN). The geometric mean diameter (GMD) was the concentration-weighted average of all the particle diameters. Finally, an assumed particle density was multiplied by the concentration and D_m at each D_m and integrated across the PSD, producing a total particle mass (PM). The assumptions, calculations, and error sources for each of these metrics will be discussed here. Because the errors in the PSD propagate into the rest of the metrics, the measurement and errors associated with the PSD will be discussed first. Because the calculation of GMD and PN require straightforward mathematical methods with no additional assumptions, these two calculations will be discussed second. The assumptions, calculations and errors associated with the total particle mass will be discussed last.

C.2 Errors Associated With Particle Size: D_m

The reported D_m is the channel midpoint on range of D_m whose size is determined by the user-defined bin size resolution. All particles with D_m within this range are counted in the same "bin." The bin size resolution was maintained between all experiments performed here and used to define the uncertainty in the D_m reading. the uncertainty for any reported D_m is assumed to be half the bin width. Past studies have shown the uncertainty in the

mobility diameter of a standard reference material measured by this system to be within 1% of the particle size [7]. Because this is lower than half the bin width, it suggests that using half the bin width is a sufficient measure of the uncertainty in D_m. Figure C.1 shows how this uncertainty increases with D_m for the range and resolution used for the SMPS data used throughout this study.

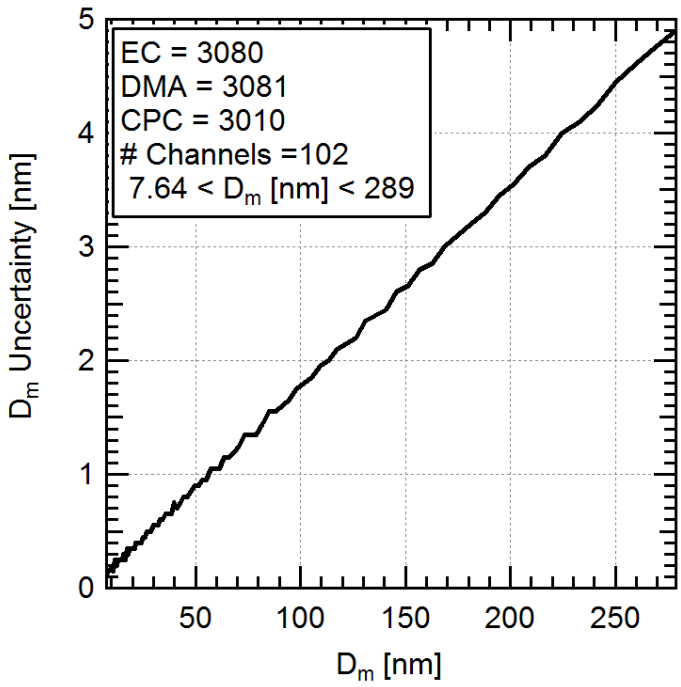

Figure C.1: Uncertainty in D_m as a function of D_m for the SPMS range and resolution used for this study.

C.3 Uncertainties in Particle Counting Techniques

The particle number in any particle D_m bin is subject to several types of error including instrument error, measurement error, uncertainty from data corrections, repeatability and reproducibility. Measurement error refers to changes in the particulate sample due to characteristics of the sampling system such as sample line length, temperature changes, and imperfections in the dilution process. Instrument error refers to any systematic errors

associated with the chosen measurement system, which is the SMPS in this case. Repeatability and reproducibility are determined by taking measurements on separate occasions using separate operators and preferably, separate laboratories. The sources of measurement and instrument error are discussed here. Although there are several sources of uncertainty inherent in the sampling technique and the instrument, they are not quantifiable and are left out of the determination of uncertainty. The particulate data were therefore interpreted with the understanding that the measured sample is an imperfect representation of the engine-out sample. Reproducibility is not discussed here because no attempt was made to prove the reproducibility of the data. Therefore, the reported particulate data represent the sample measured at the SMPS inlet, and the calculated uncertainty is a representation only of the repeatability of the data.

Although their contributions are not quantified, the potential errors that arise from the sampling technique and the instrument are important to understand so that the reported PSDs may be interpreted more accurately. These potential error sources are discussed at length in this section. Then the calculation of confidence bounds from the measurement repeatability is discussed.

C.3.1 Sampling Technique Error Sources

The best practices listed in the PMP protocol provide a good benchmark from which to determine potential error sources in a sampling apparatus. Best practices include minimizing sample line length, minimizing sharp bends in the sample line, minimizing residence time, and utilizing careful temperature control. Most of these guidelines are followed where possible in this setup, but a few deviations are worth mentioning.

First, the sample point is located downstream of the exhaust surge tank to minimize pressure fluctuations from the engine that may otherwise reach the SMPS and disrupt the steady flow of aerosol through the system. Additionally, an isothermal first stage dilution is desired, and this sample location allows the exhaust to cool sufficiently so that

the primary dilution air heater is capable of matching the dilution air temperature to the sample temperature. The caveat to this technique is that it significantly increases the residence time before dilution, and continued pyrolysis, oxidation, and agglomeration may be possible in the surge tank during this time.

Second, although the sample length is minimized for the current setup, diffusion losses are still possible in all the sample lines. Although the SMPS applies a diffusion loss correction for internal SMPS sampling lines, there is no correction for losses in the sample line upstream of the SMPS. Therefore, diffusion losses may occur in the sample lines, and are not accounted for by the data presented here.

Finally, although an isothermal first stage dilution is desired, it is not always perfectly achievable. The primary diluter temperature is set to 250 °C, but naturally fluctuates by as much as 15 °C. similarly, The exhaust system is warmed up to a minimum of 250 °C before taking samples, but it may reach as high as 300 °C for high exhaust port temperature cases, such as high load. Additionally, the low RPM sample point temperature may sometimes drop slightly below 250 °C because the exhaust temperature for that case is so low. Therefore, the first stage dilution is not perfectly isothermal. Wider deviations between the sample and dilution air temperatures were tested for familiar cases, and they did not affect the data substantially. Therefore, the deviations mentioned here were considered acceptable for this study.

C.3.2 Instrument Error Sources

Instrument error is associated with the corrections built into the AIM software, as well as the capabilities and errors associated with each of the SMPS system components. The raw particle count data from the CPC undergoes a complex data inversion to convert the counts to a size distribution. Several internal algorithms are used for the systematic corrections, and data is not available for all of these algorithms at the sampling conditions used here.

The software accounts for the following variables [7]:

1. DMA voltage
2. CPC & DMA flow rates
3. Scan time
4. Charge distribution
5. CPC counting efficiency
6. DMA transfer function
7. Working gas parameters
8. Diffusion Losses

The interdependence of all these factors within the data inversion is not well-defined, so even if their individual uncertainties were known, a mathematical propagation of uncertainty accounting for the entire system and data inversion process would be extremely difficult . Therefore, instrument uncertainty was also not considered in the final calculation. However, the effect of each of these variables on the reported PSD is worth mentioning briefly here to clarify the interpretation of the data.

C.3.2.1 DMA Voltage

The size distribution of a static aerosol was originally measured by stepping the voltage linearly. The modern DMA including the one used here utilizes exponential voltage increases in the range 5-10,000 volts, which decreases measurement time, covers the size range of interest, and allows real-time aerosol measurements. Any discrepancy in the actual and reported DMA voltage would cause the actual and reported D_m to disagree. This is not a concern here because the DMA voltage is calibrated with NIST traceable meters [7].

C.3.2.2 CPC & DMA Flow Rates

Errors in the flow measurement can significantly reduce the measurement accuracy. The inlet and exit sheath flows must match in order to ensure laminar flow in the DMA, which is required for the actual and calculated migration velocities to match. The monodisperse flow rate must also match the incoming aerosol flow rate, which is achieved by recirculating the sheath air as needed. All flow control is achieved using NIST traceable flow meters that adjust for differences in atmospheric pressure and temperature [7]. In addition, the accuracy of the sheath flow reading is periodically calibrated in-house using a NIST traceable independent volumetric bubble flow meter.

C.3.2.3 Scan Time

A longer scan time will result in a more accurate measurement. Short scans can result in a tail toward large particle sizes, which may be due to turbulent mixing between the DMA and CPC. The best accuracy is achieved for 300 second scans, but this would make data collection impractically slow. Therefore, the scan time of 90 seconds used for this study is a compromise that achieves both good data repeatability and reasonable sample time.

C.3.2.4 Charge Distribution

A predictable bipolar charge distribution is applied to the aerosol before it enters the DMA. Historically, the beta-emitter Krypton-85 was used to apply this distribution, but the strength of the emission declines slowly over time with this source, making it difficult to determine when the useful life has expired. All the data taken in this study utilized an X-ray source to apply the charge distribution. This source has been shown to produce equivalent accuracy to the Kr-85 source, with a more abrupt and easily recognizable end of life. A new X-ray source was installed approximately two years before the writing of this document, and the lifespan is considered to be near seven years with continuous use.

Another issue to be considered in the charge distribution is the tendency for multiple charges to be applied to single particles. As mentioned in the Experimental Setup section, multiple charge correction corrects for the potential of large particles obtaining a greater polarity from the charging mechanism and being counted as smaller particles due to their increased mobility. This issue is most pronounced for particles above 100 nm. The correction uses an internal algorithm [5]. After the concentration in a given bin is measured, the algorithm subtracts the fraction believed to have multiple charges. The algorithm assumes a 64-channel resolution when applying the correction, while the data here was taken using 102 channels. Additionally, the impactor is assumed to remove particles with an aerodynamic size that is equivalent to the geometric diameter. That is, the particle density is assumed to be 1.0. For particle densities $\neq 1.0$, the correction is less accurate.

C.3.2.5 CPC Counting Efficiency

The CPC condenses butanol onto particles in the sample flow, which creates particles large enough to be detected by light scattering. The sample first passes through a saturator block, where the butanol evaporates into the sample stream, saturating the flow. Then, the flow passes through a cooled condenser tube where the butanol supersaturates and condenses onto nearly all particles, regardless of chemical composition. Finally, the supersaturated droplets pass through a ribbon of laser light, and the resulting light scattering is collected by optics and focused onto a photodetector. This converts the signal to an electrical pulse, that records a particle count. A correction is required for this process because not every particle that enters the CPC is saturated with butanol and counted. The fraction of particles counted to those in the sample is referred to as the counting efficiency. Although the counting efficiency is very high and approaches 1.0 for large particles, it decreases quickly for particles below 10 nm.

The counting efficiency of the CPC is characterized and used to correct for the missed particles. The efficiency curve is shown in Figure C.2. Note that the counting efficiency

approaches 0.0 below 7 nm, and is very low below 10 nm. This means that the correction below 10 nm is much larger, and the raw particle count used for data collection is lower, so the signal to noise ratio will be greater. The manufacturer specifies that the minimum size for accurate particle counts is the size at which the counting efficiency reaches 50% [7]. For this model, the counting efficiency reaches 50% at 10 nm [2]. This is why all the data shown here begins at $D_m = 10nm$.

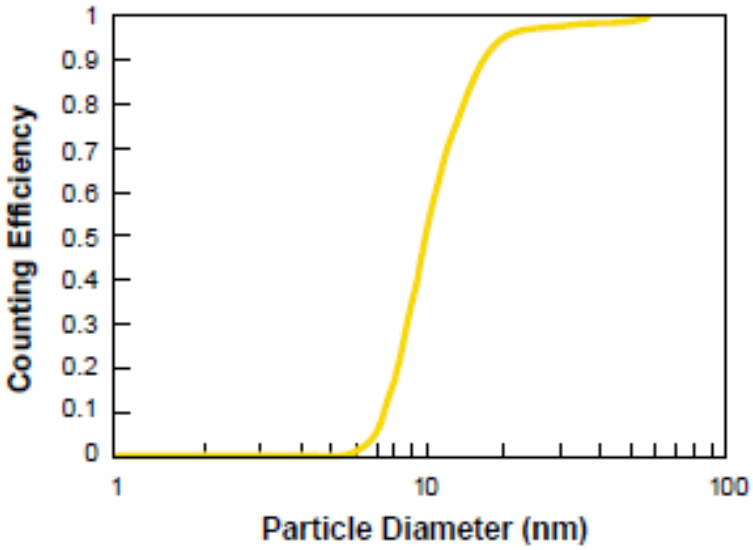

Figure C.2: Counting efficiency curve for CPC model 3010 [2].

C.3.2.6 DMA Transfer Function

The transfer function is the probability that a particle with electrical mobility Z will have the correct trajectory to reach the sampling slit. A small range of particle sizes are capable of exiting through the slit for a given setting. The range is narrowed by using a high ratio of sheath air to sample air. TSI recommends a sheath to aerosol ratio of 10:1. This is the default setting and was used throughout the study.

C.3.2.7 Working Gas Parameters

The equations used for the internal algorithms were nearly all validated using air at standard temperature and pressure, and the flow meters are calibrated using air. Particle diffusion and velocity are both functions of the working gas. It is possible to change the parameters of the working gas in the software, but the flow meters would then need to be calibrated with this gas. In this study, the carrier gas is composed of the products of combustion, which have similar properties to air. The exhaust gas composition changes with operating condition, and the accuracy of the instrument may change slightly because of this.

C.3.2.8 Diffusion Losses

Loss of particles via diffusion to the walls is accounted for with diffusion correction. When particles collide with the flow path walls, they adhere du to van der Walls force, electrostatic force, and surface tension. This is the primary transport mechanism for particles of $D_m < 100nm$, and the smaller the particle, the more rapid the diffusion [5]. The diffusion correction option approximates the particle penetration in critical sections of the SMPS sample flow utilizing modeling, experimental, and published data as appropriate [5]. The uncertainty associated with this correction is a function of the CPC, DMA, and EC models used, the flow rate, and the working gas. The working gas is assumed to be air at standard temperature and pressure. It is possible to input gas properties in the software to increase accuracy, but this was not done for any of the experiments performed here, and the resulting error is unknown. Furthermore, although the corrections for some flow rates and components are given in the literature, others are not readily available, so the uncertainty associated with the diffusion correction was not determined. Therefore, no error associated with this correction is applied to the uncertainty analysis of the data presented in this work. However, it is worthwhile to provide a brief overview of which particles are most affected by the diffusion correction option.

First, diffusion losses are described by the fraction of particles that penetrate both ends of a tube, rather than diffusing. Therefore, diffusion losses are inversely proportional to Penetration. Penetration (P_p) is defined by Equation C.1

$$P = \frac{n_{out}}{n_{in}} \tag{C.1}$$

Penetration depends on tube length (L), a diffusion coefficient (D) and the volumetric flow rate (Q). This relationship was characterized by Gormley and Kennedy [49], and can be seen in Figure C.3. The diffusion coefficient is smaller for larger particles. Therefore, Figure C.3 shows that diffusion losses will increase (Penetration decreases) for small particles (high D), low flow rates (low Q), and long tube lengths (high L).

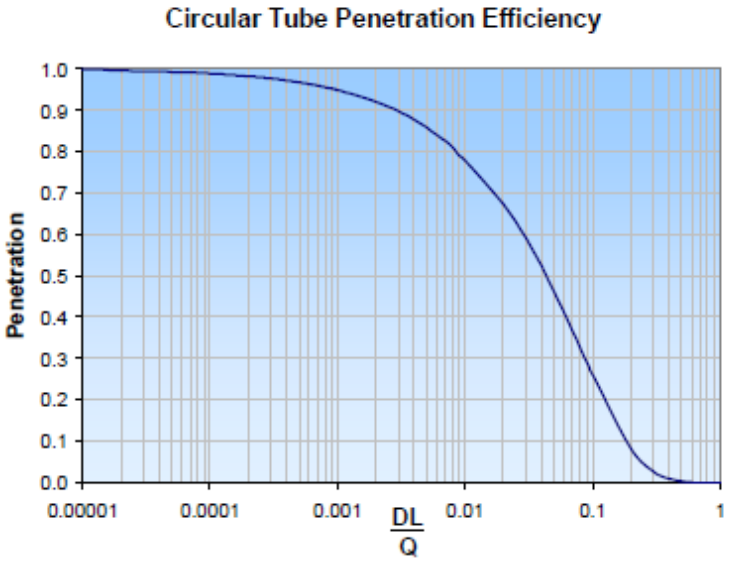

Figure C.3: Penetration of particles through a circular tube as a function of tube length, diffusion coefficient, and flow rate [49].

The diffusion losses associated with just the SMPS system used here are automatically calculated and applied in the AIM software. The flow paths considered for the total penetration are depicted in the SMPS schematic of Figure C.4. Five flow paths are considered:

the impactor inlet (P_1), the neutralizer and internal plumbing (P_2), the tubing to the DMA and CPC (P_3), the DMA (P_4), and the CPC (P_5).

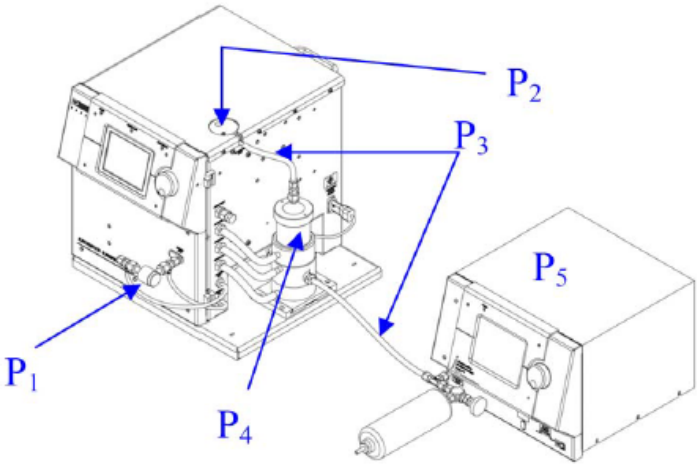

Figure C.4: SMPS flow paths considered in the AIM calculation of diffusion losses through the SMPS system [5].

The total penetration through the SMPS is the production of these five individual penetrations:

$$P_{total} = P_1 P_2 P_3 P_4 P_5 \tag{C.2}$$

A more in-depth discussion of the diffusion correction and multiple charge correction can be found in the AIM software user's manual. A large portion of the discussion here was taken from Application Note SMPS-003 [7], which provides a more in-depth discussion of all the factors affecting the accuracy of the measurements.

C.3.3 Thermodenuder Correction

The thermodenuder is designed to remove volatile and semi-volatile compounds from the sample. When it is used, it is located downstream of the microdiluter because the sample must be cooled and diluted before entering the thermodenuder. The thermodenuder is composed of two sections. The first section is an aerosol heater that vaporizes the volatile

and semi-volatile compounds. The second section is an activated charcoal adsorber that both cools the sample and adsorbs the volatile particles. The volatile particles are assumed to have a much higher diffusion velocity (≈ 100 times higher) than the nonvolatile particles, which is why the volatile particles are collected in the adsorber section while the nonvolatile particles escape [3]. A cross-section of the sample path is shown in Figure C.5.

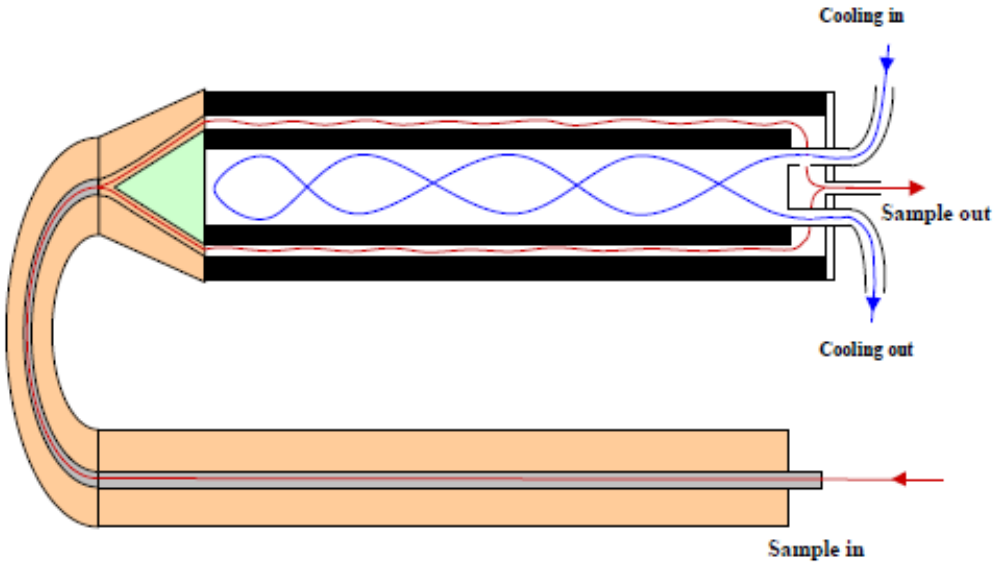

Figure C.5: Sample flow path cross-section of the Dekati thermodenuder [3].

The heater section heats the sample to 250 °C, and the resulting vaporized particles are assumed to be composed primarily of volatile hydrocarbons. The thermodenuder is designed to be used at flow rates of 10-20 lpm, and at 15 lpm, it removes approximately 90% of the volatile organic compounds. At lower flow rates nonvolatile compounds begin to diffuse, while at higher flow rates, the volatile compounds do not have enough time to diffuse. Because some diffusional losses of non-volatile particles will occur, a correction to the resulting data must be applied. The correction is size dependent, and specified in Equation C.3[3].

$$1-\eta = 9.7 * \ln(D_p) - 0.5 * Q + 68 \ (D_p < 170\,nm \tag{C.3}$$

$$1-\eta = 0.5 * Q + 28 \ (70\,nm \leqslant D_p \leqslant 500\,nm)$$

$$\eta = particle\,penetration$$

$$D_p = particle\,size\,[nm]$$

$$Q = flow\,rate\,[lpm]$$

No discussion of uncertainty is given in the product literature for these corrections, so the added uncertainty from thermodenuder use has not been quantified. Therefore, the thermodenuder was used only for a small set of data to verify procedures for removing volatile particles. Once it was confirmed that a high dilution ratio had the same effect on the volatiles seen here, the thermodenuder was not used again. Unless otherwise stated, all the data shown in this work was taken without the thermodenuder.

C.3.4 Dilution Ratio Correction

A final type of correction is applied in postprocessing to account for dilution of the sample before it reaches the SMPS. The upstream dilution of the sample by the Dekati Microdiluter system was measured both internally by pressure readings and critical flow orifices inside the microdiluter controller, and by comparison of CO_2 measurements made by Horiba emissions bench upstream and downstream of the microdiluter. The internal DR readings were used during operation as a check against the CO_2 based DR. Within the range of DR used for most experiments, the two readings agreed within 15% for normal operation. The CO_2 based DR was more accurate so the internal DR readings were not used to correct particulate readings. Therefore, only the errors associated with the CO_2 based DR readings will be discussed here.

The DR was a 1 Hz signal recorded by the DAQ for a given data point. The number of DR readings was therefore dependent on the length of sampling time, but generally fell between 600 and 900 readings. In post-processing, the average of these readings was used to correct for the associated SMPS data. The concentration at every particle size was multiplied by the dilution ratio for each individual SMPS scan. This treatment assumes that the DR affected each particle size and each SMPS scan equally.

The error associated with the DR correction includes the error in both CO_2 measurements, and the variation in the DR over the length of the scan. There may also be some error associated with particle losses in the flow path between the engine exhaust port and the SMPS inlet, particle losses due to the dilution process, and from the assumption that all particle sizes are affected equally. However, these errors cannot be quantified so they are ignored here.

Although the upstream and downstream CO_2 analyzers are identical, the errors associated with each will be different because the CO_2 concentrations, analyzer range settings, span gas concentrations, and calibration curves are different between the two analyzers. The error for these readings were determined in the same fashion as the rest of the emissions measurements, then propagated through the SMPS calculations. Because the DR error is the only quantifiable source of measurement error in the SMPS reading, it is directly applied to each individual scan, then combined with repeatability using the root-sum-squares method to determine the total uncertainty for a group of measurements.

C.4 Total Number Concentration

The calculation of the total number concentration is an integration of the particle size distribution, accounting for the logarithmic particle diameter increase. The Matlab post-processor applies a trapezoidal integration scheme (trapz). The integration reported in all the data used here spans from 10.2 nm up to 278.8 nm. These are the size bins that

are above the CPC 50% counting efficiency cutoff. The integration is performed for each individual scan, and the uncertainty in the reported value is the 95% confidence interval calculated from the mean and standard deviation of all the scan integrations.

C.5 Geometric Mean Diameter

The geometric mean diameter (GMD) is a weighted average diameter based on the particle number counts from the PSD. Equation C.4 is implemented in the postprocessor for this calculation.

$$GMD = exp\left[\frac{\sum ln(D_p) * n}{N}\right] \tag{C.4}$$

$$n = number\,at\,D_p$$

$$N = total\,number$$

Like the total number concentration, the GMD is calculated for each individual scan, and the uncertainty in the reported value is the 95% confidence interval calculated from the mean and standard deviation of all the scans.

C.6 Total Mass Concentration

The total mass concentration was approximated from the PSD using the mass vs. D_m relationship discussed in Appendix D. For each D_m the corresponding particle mass multiplied by the particle number. The process was repeated for all size bins from 10.2 nm to 278.8 nm, providing the total integrated particle mass, as shown in Equation C.5

$$mass = \sum n_{D_m} * mass_{D_m} \tag{C.5}$$

Like GMD and total number, the mass is calculated for each scan, and the uncertainty in the reported value is the 95% confidence interval calculated from the mean and standard deviation of all the scans. There is additional uncertainty in this calculation due to the assumption that all conditions have the same mass vs. D_m relationship.

C.7 Soot Volume Fraction

The soot volume fraction (f_v^∞) was also approximated from the SMPS data. The volume of a soot particle is simply the particle mass divided by the density of the material that composes the particle. In this case, all particles are assumed to be composed of some number of primary particles, and an assumed primary particle density of 2 g/cm^3 is used. The soot volume as a fraction of the total sample volume was calculated for each D_m and summed over all the size bins using the same integration method as was used for the total particle number concentration and total particle mass concentration. This is shown in Equation C.6

$$f_v^\infty = \sum n_{D_m} * \frac{mass_{D_m}}{2g/cm^3} \tag{C.6}$$

D MASS VS MOBILITY DIAMETER (D_m) RELATIONSHIP

During a two week collaboration with PNNL, both SIDI and PMPV cases were run with a variety of fuels and operating conditions. For these studies, an SMPS system was connected in series with an aerosol particle mass analyzer (APM). The SMPS was used to sample the particles at selected mobility diameters. This size-selected sample was then sent to the APM, which determined the particle mass. The process was repeated for several mobility diameters throughout the D_m range of interest, providing a mass vs D_m relationship that allows more accurate approximation of the mass based on the PSD. The conditions for which the mass vs D_m relationship was determined include both PMPV and SIDI operation, six fuels, and nine operating conditions. This resulted in 29 unique data sets, which are listed in Table D.1.

The mass vs D_m relationships for all the cases are shown in Figure D.1. Due to the large number of cases and the close agreement between cases, the legend only gives general marker and color trends. Figure D.1 shows that the mass vs D_m relationship appears linear on a log-log scale for all conditions, and the relationship is nearly the same regardless of fuel or operating condition. Because of this, the data points from all the listed conditions were pooled into a single data set, and used to calculate mass as a function of D_m from a curve fit of the data. The pooled data and the curve fit are plotted on a linear scale in Figure D.2. Note that particle mass in Figure D.2 is listed in grams, whereas the mass in Figure D.1 is in femtograms.

The curve fit equation shown in Figure D.2 was used to approximate the mass at every D_m used for the standard PSD in this work. However, the mass vs D_m data became unreliable at D_m below 20 nm, and was not fully trustworthy between $D_m = 20$ nm and $D_m = 30$ nm. Therefore, below $D_m = 30nm$ a constant particle density of 2 g/cm^3 was used along with the assumption of a spherical particle to determine the particle mass from the particle D_m. This combination of the measured mass vs D_m relationship above

Table D.1: Conditions for which particle mass vs D_m relationship was measured

Operating Mode	Operating Condition	Φ	Fuel	Operator
PMPV	1050 rpm	1.5	EEE	MDH
PMPV	1050 rpm	1.4	EEE	MDH
PMPV	2100 rpm, 550 kPa IMEP	1.4	EEE	MDH
PMPV	2100 rpm, 334 kpa	1.5	E10	SSS
PMPV	2100 rpm, 334 kpa	1.46	E20	SSS
PMPV	2100 rpm, 334 kpa	1.52	E20	SSS
PMPV	2100 rpm, 334 kpa	1.50	TRF	MDH
SIDI	EOI -140 CAD	0.98	EEE	MDH
SIDI	EOI -220 CAD	0.98	EEE	MDH
SIDI	EOI -250 CAD	0.98	EEE	MDH
SIDI	EOI -340 CAD	0.98	EEE	MDH
SIDI	EOI -140 CAD	0.98	TRF	MDH
SIDI	EOI -220 CAD	0.98	TRF	MDH
SIDI	EOI -250 CAD	0.98	TRF	MDH
SIDI	EOI -190 CAD	0.98	E20	SSS
SIDI	EOI -220 CAD	0.98	E20	SSS
SIDI	EOI -250 CAD	0.98	E20	SSS
SIDI	EOI -280 CAD	0.98	E20	SSS
SIDI	EOI -310 CAD	0.98	E20	SSS
SIDI	EOI -190 CAD	0.98	E30	SSS
SIDI	EOI -220 CAD	0.98	E30	SSS
SIDI	EOI -250 CAD	0.98	E30	SSS
SIDI	EOI -280 CAD	0.98	E30	SSS
SIDI	EOI -310 CAD	0.98	E30	SSS
SIDI	EOI -190 CAD	0.98	E50	SSS
SIDI	EOI -220 CAD	0.98	E50	SSS
SIDI	EOI -250 CAD	0.98	E50	SSS
SIDI	EOI -280 CAD	0.98	E50	SSS
SIDI	EOI -310 CAD	0.98	E50	SSS

Operator initials: MDH = Mitchell D. Hageman, SSS = Steven S. Sakai

$D_m = 30$ nm and the constant particle density below $D_m = 30$ nm produced the mass vs D_m approximation that was used to calculate the particle mass from the PSD for every case studied. This relationship is plotted in Figure D.3.

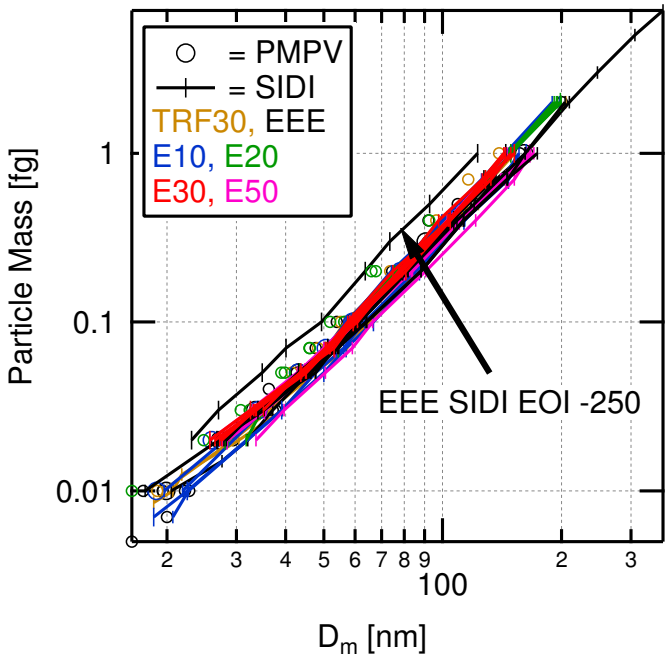

Figure D.1: Particle mass measurements [fg] at a range of D_m [nm] for all fuels and conditions. PMPV cases are marked by symbols while SIDI cases are marked by lines with a | at each data point. Fuel name text colors indicate the color used to mark each fuel. No further distinctions are made between cases due to the number of cases and the close agreement between cases. The exception is the EEE SIDI EOI -250 CAD case, which is marked here because it is a slight outlier compared to the remaining data.

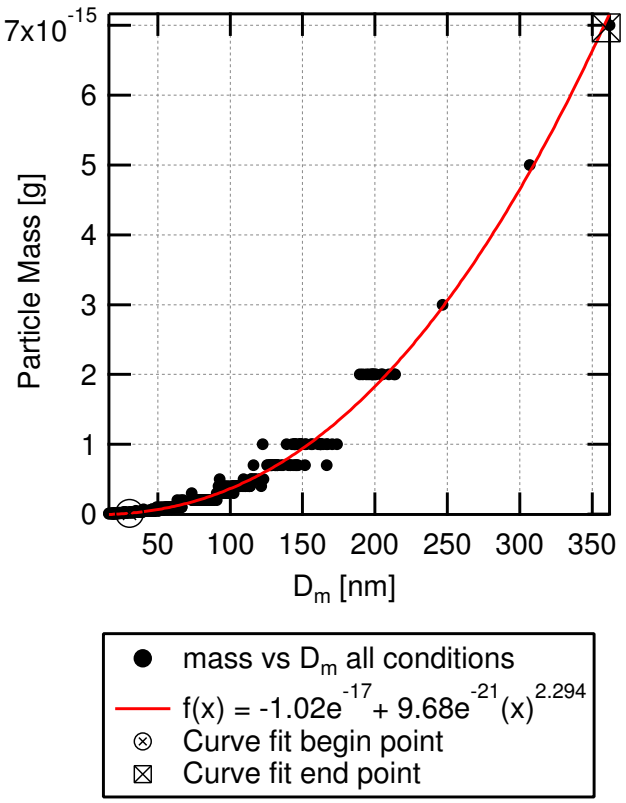

Figure D.2: Pooled particle mass measurements [g] vs D_m [nm] measured data plotted with a curve fit to the data. Note that the curve is fit to the data beginning at $D_m = 30$ nm because the measurements became less reliable below this range.

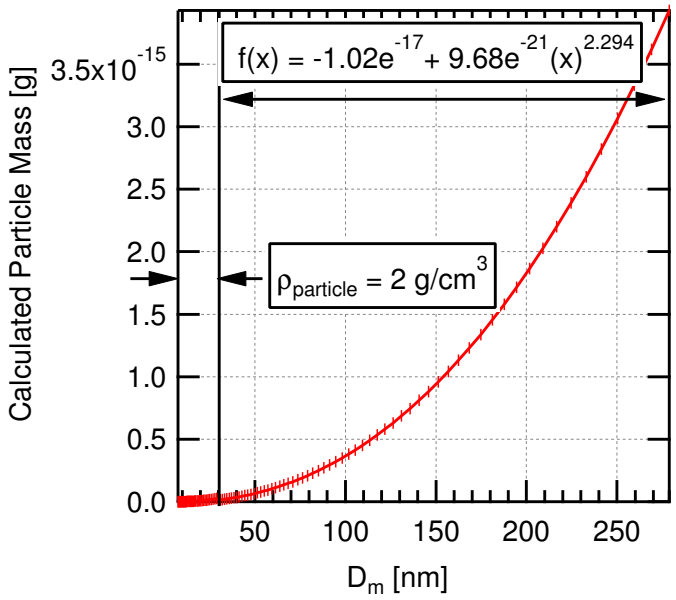

Figure D.3: Pooled particle mass calculations [g] vs D_m [nm] used for calculations of particle mass from the PSD. Note that the curve is fit from the measured data is used for $D_m \geqslant 30$ nm, and $\rho_{particle} = 2$ g/cm^3 is used for $D_m < 30$ nm because the measurements became less reliable below this range.

E.1 Introduction

In this study, multiple measurements of most variables were recorded in each run. Then, the same condition was repeated over multiple days or runs to provide a metric of repeatability/reproducibility for the data. The final reported value was averaged from the repetitions, and a determination of that value's uncertainty is required. The value of uncertainty must account for measurement error, variation within a run, and variation between runs. This appendix discusses how that uncertainty was determined for the various types of data reported here.

Uncertainties in the reported data were assessed according to three criteria:

1. Measurement error (AKA: systematic error/bias/inaccuracy)
2. Measurement repeatability within a run (AKA: random error/imprecision)
3. Day-to-day repeatability

Measurement error was assesed based on the known accuracies of the measurement equipment and measurement techniques, and was taken from manufacturers' specifications, calibration data, and standard operating procedures. Measurement repeatability refers to how well several measurements of the same quantity taken within a single run agreed. For example, approximately 600-900 measurements of gaseous emissions values were taken for each run. A 95% confidence interval based on the average and standard deviation of those 600-900 measurements defined the repeatability of the measurements for those runs.

Finally, nearly all the conditions that were reported here were repeated at least once. Because nearly all of the data collected here was taken by the same operator in the same laboratory on the same apparatus, a true test of reproducibility was not made, and no attempt is made here to quantify the uncertainty using reproducibility. The time between

tests was often many days or weeks, the engine was rebuilt at least twice over the course of the experiments, and some data was repeated by separate operators, so the data does have many of the required elements of reproducibility, but there was no formal reproducibility study. Instead, item 3 uses a method for a "pooled" 95% confidence interval that accounts for uncertainty both within a run and from one day of operation to the next.

A broad summary of how these three criteria for uncertainty were combined to provide a final measure of uncertainty is as follows:

1. A measurement error, or bias (B_I) was determined for each independent variable, and the 95% confidence interval (P_I) of the measurement population was determined using the student's-t method. For the 1 HZ data, these metrics were based on $\approx$ 600-900 measurements, for the SMPS data they were based on 7 SMPS scans, for the crank-angle-resolved data they were based on the 500 in-cylinder pressure traces, and for the manually tabulated data no repeatability metric could be determined because only one data point was recorded. The total uncertainties of the independent variables were taken as the root-sum-of-squares (RSS) of B_I and P_I.

2. Propagation of error was determined for the dependent variables and combined using RSS.

3. The pooled average ($\hat{L}$) and 95% confidence interval for L were calculated by combining the measurements from repetitions of the same condition.

E.2 Independent Variable Uncertainty Calculation

Some quantities reported in this study were measured directly, and are referred to here as independent variables because the determination of their error is not dependent on

any other variables. Many variables were calculated from measured quantities and are referred to here as dependent variables because they are a function of a set of independent variables. All dependent variables require a calculation of propagation of error from independent variables. Examples of directly measured quantities (independent variables) include fuel flow, gaseous emissions, temperatures, pressures, engine dimensions and raw particulate counts. The determination of measurement error for many of these quantities is as simple as directly using the manufacturer's accuracy specifications. For example,the standard error on a k-type thermocouple is 2.2 °C or 0.75% FS (T $>$ 0 °C) to 2.0% FS (T $<$ 0 °C), whichever is greater, so this rule is applied to determine errors in the appropriate temperature measurements. Other determinations of independent variable error are more complicated. Emissions errors, for example are based on calibrations that must be performed approximately every six months. Finally, some measurement equipment does not have a manufacturer's stated accuracy and is impractical to calibrate. In these cases, error is approximated based on experience. Engine RPM is a good example of this. RPM is measured by both the dynamometer controller and the shaft encoder. No documentation is available for either of these pieces of equipment and no equipment is available to calibrate them. However, the maximum difference between the measured RPM at 2100 RPM that has ever been noted is 14 RPM, so this is used as the measurement error at that RPM. The uncertainty (U_I) in an independent variable is a function of the measurement error (B_I) and the precision (P_I) which are combined through the root-sum-squares method.

$$\boxed{U_I = \sqrt{B_I^2 + P_I^2}} \tag{E.1}$$

Some ambiguity exists with regard to what qualifies as an independent variable. For example, in calculations concerning emissions concentrations the individual gas concentrations reported by the DAQ were treated here as independent variables, and their B_I were determined from the calibration curves. However, one could argue that because the Horiba bench outputs a voltage that is then converted to a concentration by the DAQ, the

voltage is the independent variable and error propagation should be peformed on the conversion from voltage to concentration. Furthermore, the calibration curve is dependent on errors in gas bottle concentrations and flow rates through the gas divider. However, the DAQ does not record voltages, so the post-processor could not treat voltage as an independent variable. To standardize the error propagation process, DAQ outputs are treated as independent variables in the postprocessor, and error propagation begins with these values.

Determination of the P_I of these values was based on a student's-t distribution with a 95% two-sided confidence interval:

$$P_I = t_{95}\frac{\sigma_s}{\sqrt{n}} \tag{E.2}$$

where the test statistic (t_{95}) is determined by the number of degrees of freedom (ν), which is determined from the sample size (n) by $\nu = n - 1$. For sample sizes greater than 120, $t = 1.96$.

E.3 Dependent Variable Uncertainty Calculation

The equations presented here are consistent with those presented by Dempsey [30]. The first step in calculating uncertainty propagation for a dependent variable (D) is to define the variable purely as a function of independent variables (I_i):

$$D = f(I_1, I_2, ..., I_J) \tag{E.3}$$

For any single measurement, the difference between the actual and measured values ($D - D_{actual}$) is the sum of all the differences between the actual and measured values of the independent variables ($I - I_{actual}$) weighted by the partial derivative of D with respect to I_i.

$$\delta D \equiv D - D_{actual} = \sum_{i=1}^{J} \frac{\partial D}{\partial I_1}(I_i - I_{i,actual}) \tag{E.4}$$

For a large number (N) of measurements, the variance in δD becomes

$$\sigma_{\delta D}^2 = \lim_{n\to\infty}\left(\frac{1}{N}\sum_{k=1}^{N}(\delta I_k)^2\right) \tag{E.5}$$

Substituting the definition of δD from Equation E.4 into Equation E.5 and ignoring cross terms results in the following relationship:

$$\sigma_{\delta D}^2 = \sum_{i=1}^{J}\left(\frac{\partial D}{\partial I_i}\right)^2 \sigma_{I_i}^2 \tag{E.6}$$

In Equation E.6, σ_{I_i} is the uncertainty in the measured independent variable(U_I) determined earlier from P_I and B_I. Taking the square root of Equation E.6 gives the final solution for the uncertainty in the calculated dependent variable U_D.

$$\boxed{U_D = \sqrt{\sum_{i=1}^{J}\left(\frac{\partial D}{\partial I_i}U_I\right)^2}} \tag{E.7}$$

At this point, the uncertainties of the independent and dependent variables have been calculated based on both systematic and random errors for a single run. The next step is to determine the statistical uncertainty in a value averaged from multiple runs.

E.4 Uncertainty in the Average of Multiple Runs

To determine repeatability from multiple runs, the formulation from Vardeman and Jobe [117] for a confidence interval in a multisample study was used. This method is appropriate when r samples of sizes n_1, n_2, ... ,n_r are independent samples from normal underlying distributions with sample variances σ_1^2, σ_2^2, ... ,σ_r^2. The distinction of varying sample sizes (n) and variances (σ^2) allows for the determination of a pooled standard deviation σ_P for

the entire population calculated from the individual σ_i and weighted by n_i. This was important here because variations in sampling times of 1 HZ data produce sample sizes that vary to some degree, the number of SMPS scans is sometimes variable, and data variability differs slightly between days.

For the formulation from [117], the total number of observations from all r samples(n) is:

$$n = \sum_{i=1}^{r} n_i \tag{E.8}$$

The pooled sample variance (σ_p^2) is the weighted average of the individual sample variances where the weights are the sample sizes minus 1.

$$\sigma_p^2 = \frac{\sum_{i=1}^{r}(n_i - 1)\sigma_i^2}{\sum_{i=1}^{r}(n_i - 1)} \tag{E.9}$$

Of course, the standard deviation (σ_p) is just the square root of the sample variance.

Using the same model, it is possible to calculate a linear combination $\hat{L}$ of the individual means y_i:

$$\hat{L} = C_1\bar{y}_1 + C_2\bar{y}_2 + ... + C_r\bar{y}_r \tag{E.10}$$
$$\bar{y}_i = mean\,of\,sample\,i$$

Equation E.10 is a general formula that can be used to determine various quantities from statistical data. For example, if $C_1 = 1$, $C_2 = -1$, and all other $C_i = 0$, $\hat{L}$ represents the difference in mean responses from samples 1 and 2. In this study, the average of the averages was desired, so a common formula was specified for C_i

$$C_i = \frac{n_i}{n} \tag{E.11}$$

Substituting Equation E.11 into Equation E.10 gives the formula for $\hat{L}$ used for this study.

$$\hat{L} = \sum_{i=1}^{r} \frac{n_i}{n} \bar{y}_i \tag{E.12}$$

The result of Equation E.12 is the same as pooling all the individual readings from all the days and taking the average as a single large sample.

Uncertainty in the actual value of L is determined using a 2-sided student's-t 95% confidence interval where the test statistic ($t = t_{n-r}$). That is, there are $n - r$ degrees of freedom. The confidence limits for L are:

$$L = \hat{L} \pm t\sigma_p \sqrt{\frac{C_1^2}{n_1} + \frac{C_2^2}{n_2} + ... + \frac{C_r^2}{n_r}} \tag{E.13}$$

Substituting E.11 into Equation E.13 gives:

$$L = \hat{L} \pm t\sigma_p \sqrt{\frac{n_1}{n^2} + \frac{n_2}{n^2} + ... + \frac{n_r}{n^2}}$$

$$\therefore \tag{E.14}$$

$$\boxed{L = \hat{L} \pm \frac{t\sigma_p}{\sqrt{n}}}$$

The final form of Equation E.14 is the pooled 95% confidence interval for all runs. It takes the the same form as Equation E.2 except that it uses a pooled form of the standard deviation. Accounting for B_I and error propagation in σ_p is built in through the use of σ_i as calculated in Section E.3, so that averaging values from multiple runs does not require additional error propagation.

F INDICATED SPECIFIC PARTICULATE NUMBER EMISSIONS CALCULATED FOR $D_m \geqslant 23$ NM

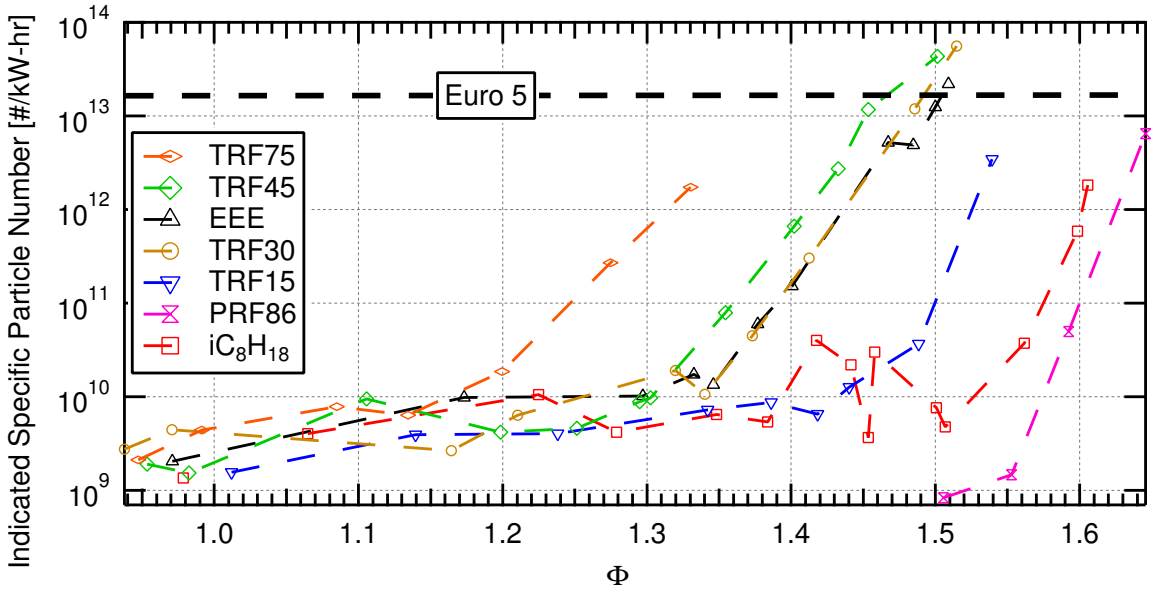

Figure F.1: Indicated specific particulate number emissions as a function of Φ for all fuels under PMPV operation. Horizontal dashed line denotes the Euro 5 number standard ($6(10^{13})$ particles/km) converted to particles/kw-hr based on the assumption of a 4000 lb vehicle traveling at 50 mph.

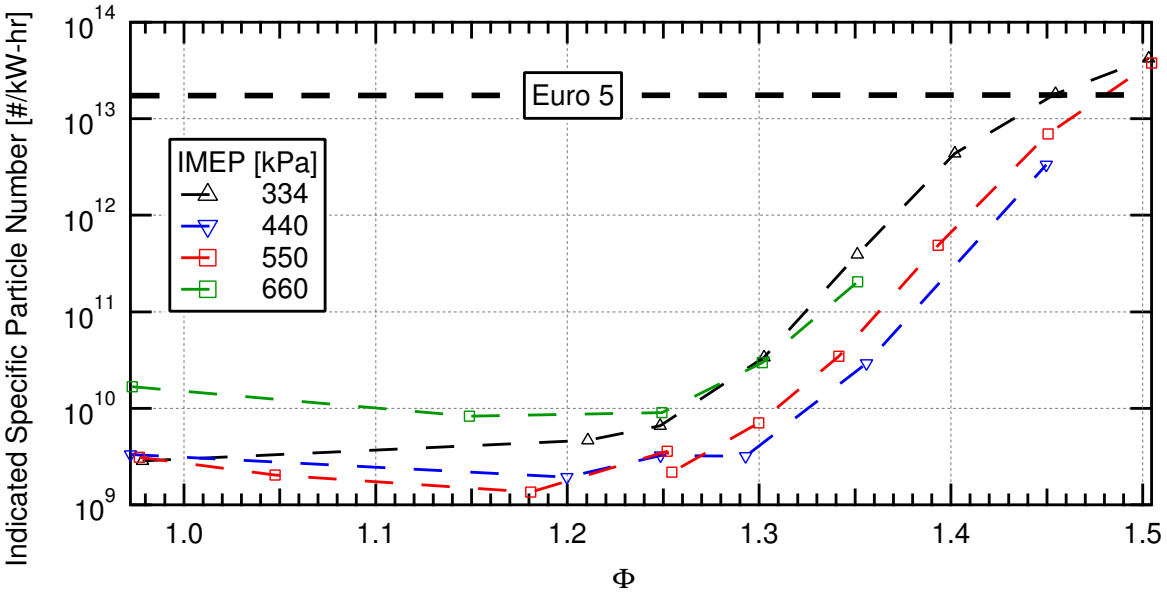

Figure F.2: Indicated specific particulate number emissions as a function of Φ for all loads under PMPV operation. Horizontal dashed line denotes the Euro 5 number standard ($6(10^{13})$ particles/km) converted to particles/kw-hr based on the assumption of a 4000 lb vehicle traveling at 50 mph.

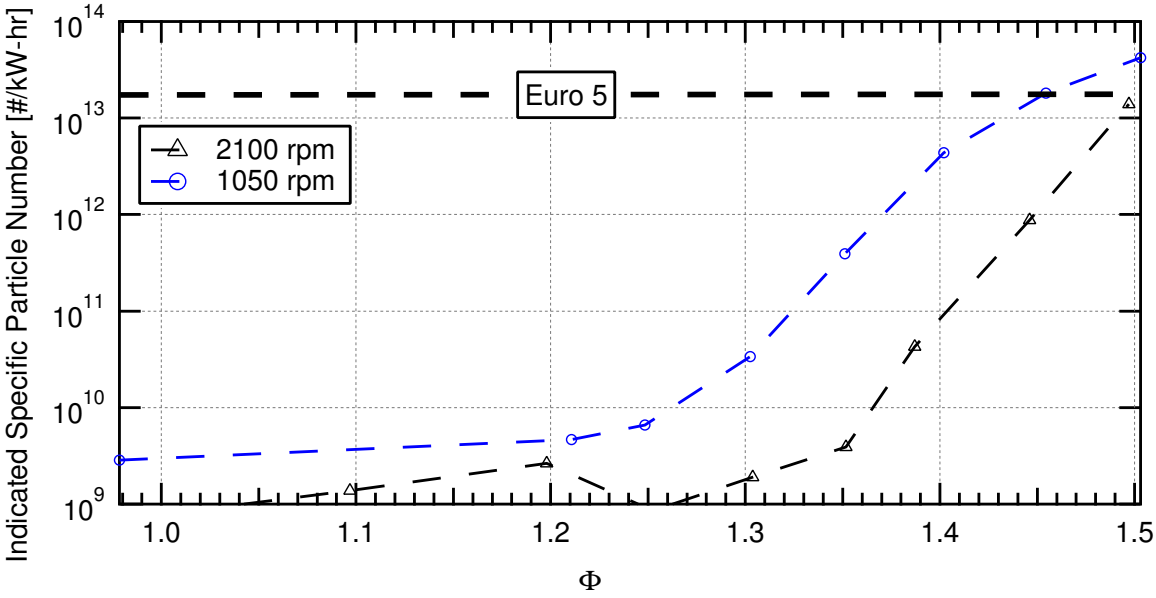

Figure F.3: Indicated specific particulate number emissions as a function of Φ for the 2100 rpm and 1050 rpm cases under PMPV operation. Horizontal dashed line denotes the Euro 5 number standard ($6(10^{13})$ particles/km) converted to particles/kw-hr based on the assumption of a 4000 lb vehicle traveling at 50 mph.

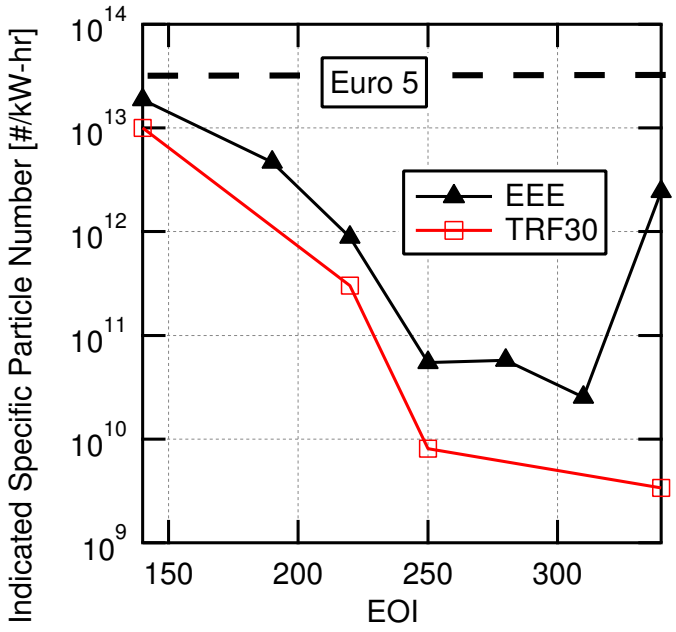

Figure F.4: Indicated specific particulate number emissions as a function of EOI for the EEE and TRF30 cases under SIDI operation. Horizontal dashed line denotes the Euro 5 number standard ($6(10^{13})$ particles/km) converted to particles/kw-hr based on the assumption of a 4000 lb vehicle traveling at 50 mph.

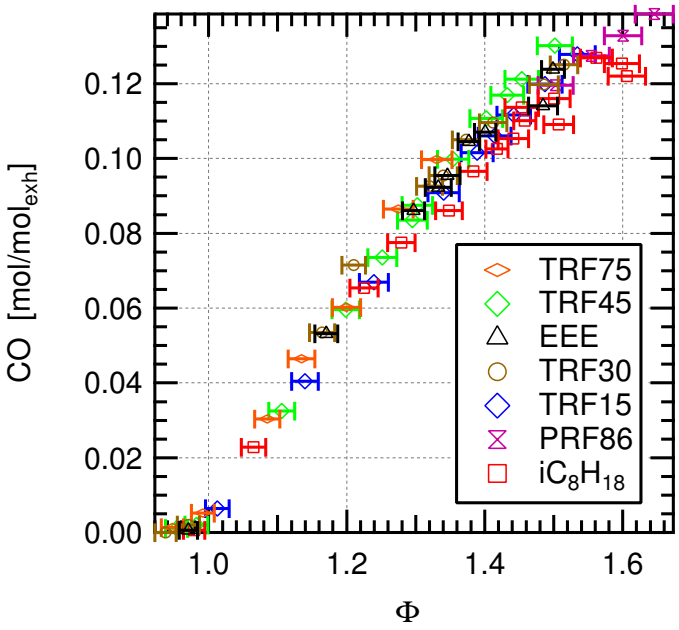

Figure G.1: CO emissions as a function of Φ for all fuels under PMPV operation.

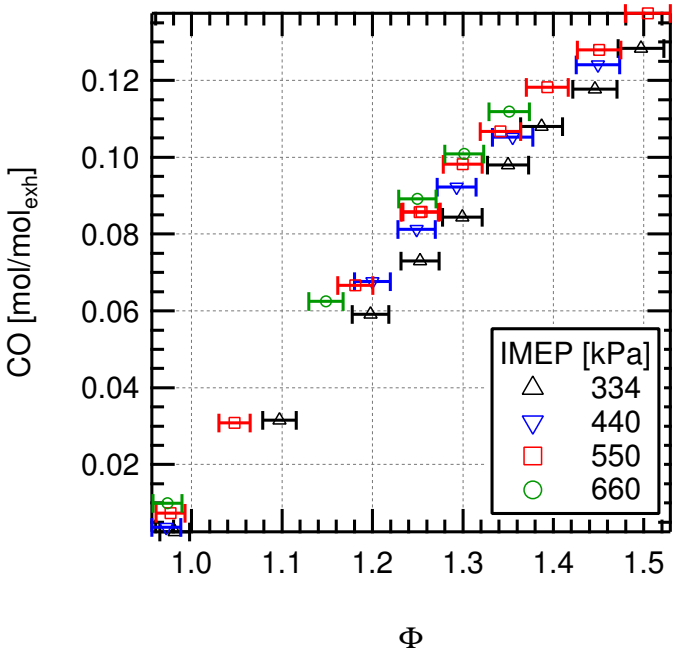

Figure G.2: CO emissions as a function of Φ for all loads under PMPV operation.

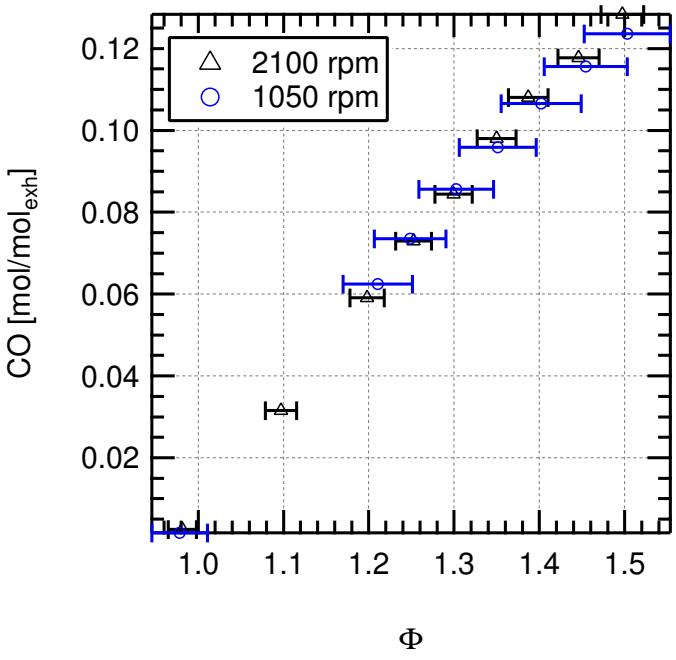

Figure G.3: CO emissions as a function of Φ for 2100 rpm and 1050 rpm under PMPV operation.

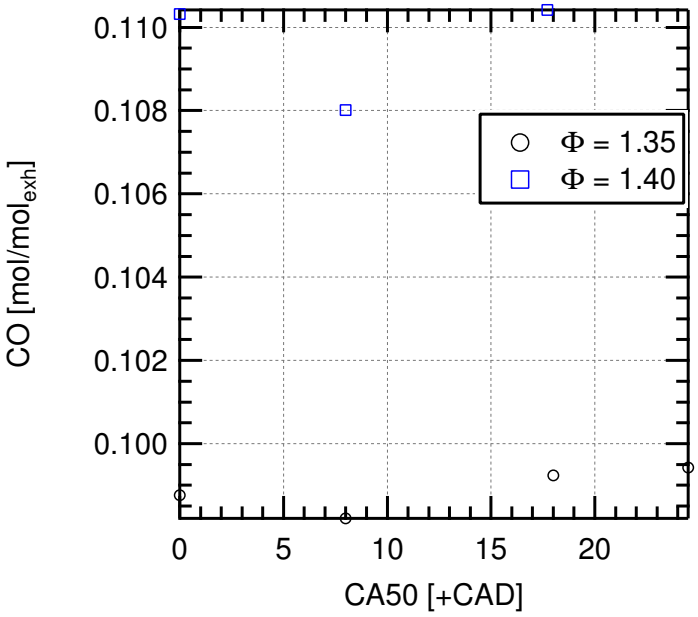

Figure G.4: CO emissions as a function of CA50 for $\Phi = 1.35$ and $\Phi = 1.40$ under PMPV operation.

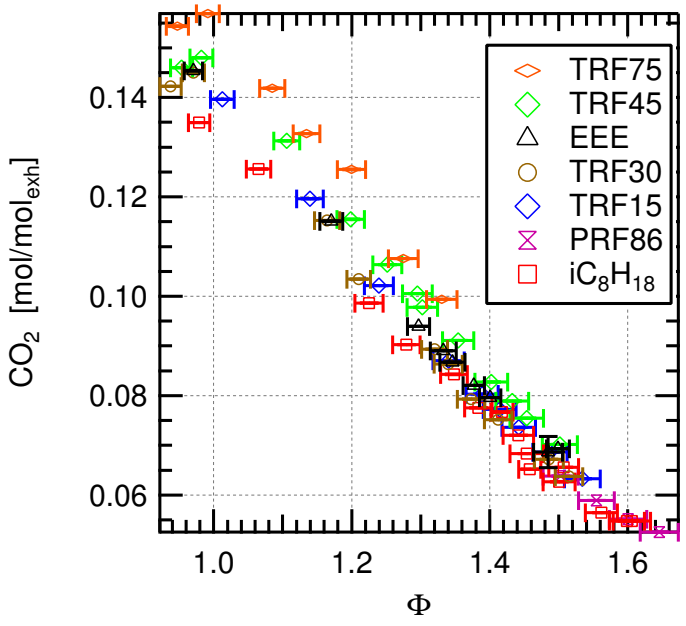

Figure G.5: CO_2 emissions as a function of Φ for all fuels under PMPV operation.

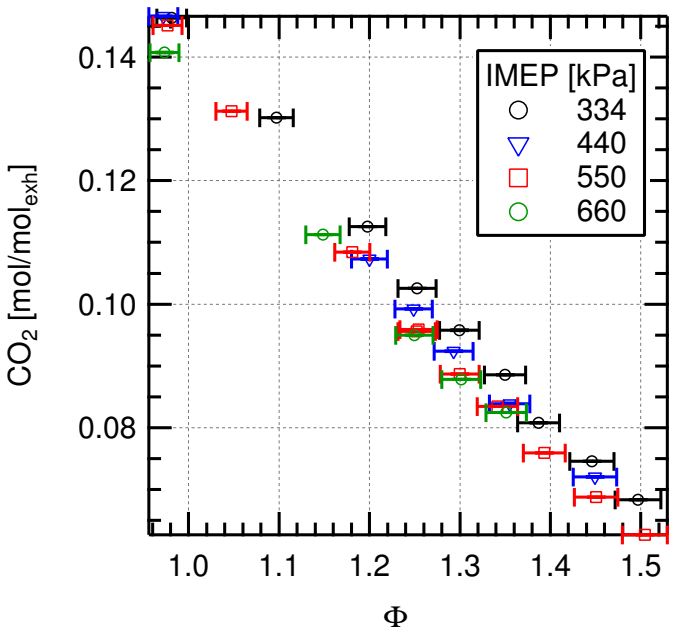

Figure G.6: CO_2 emissions as a function of Φ for all loads under PMPV operation.

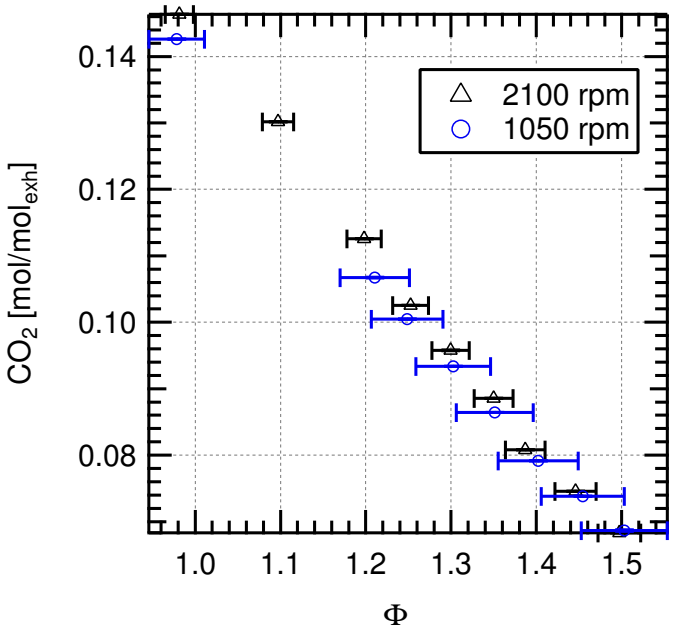

Figure G.7: CO_2 emissions as a function of Φ for 2100 rpm and 1050 rpm under PMPV operation.

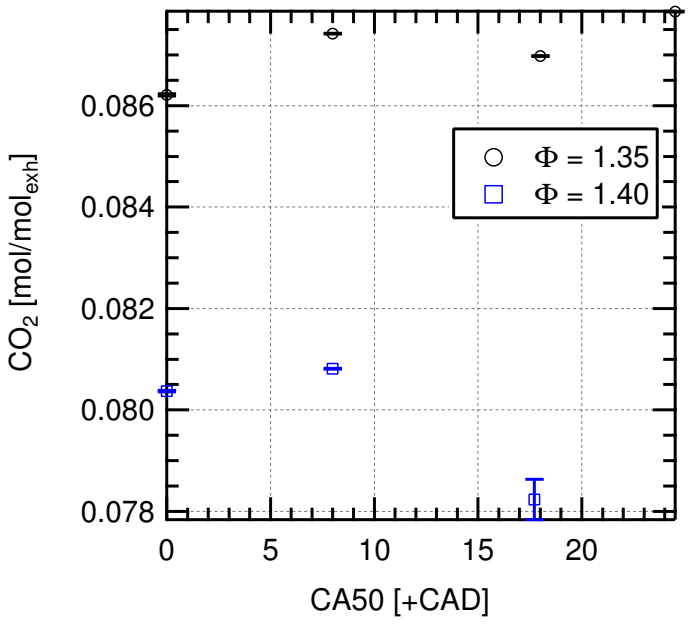

Figure G.8: CO2 emissions as a function of CA50 for $\Phi = 1.35$ and $\Phi = 1.40$ under PMPV operation.

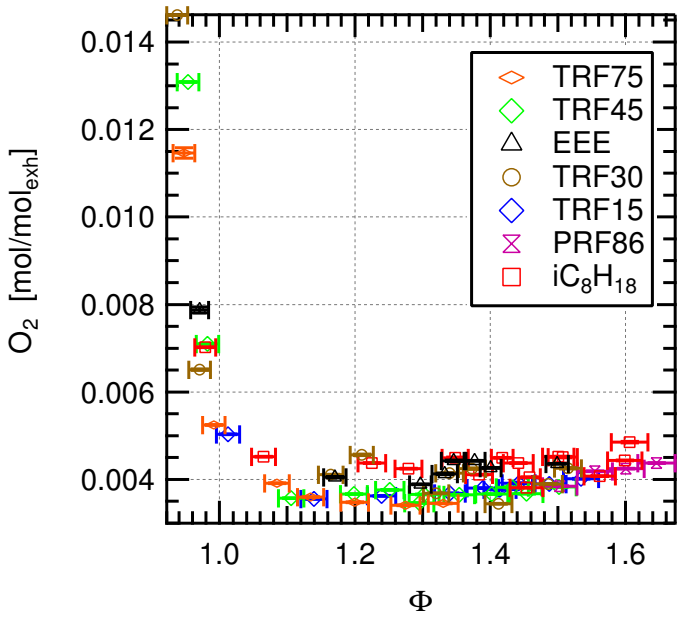

Figure G.9: O_2 emissions as a function of Φ for all fuels under PMPV operation.

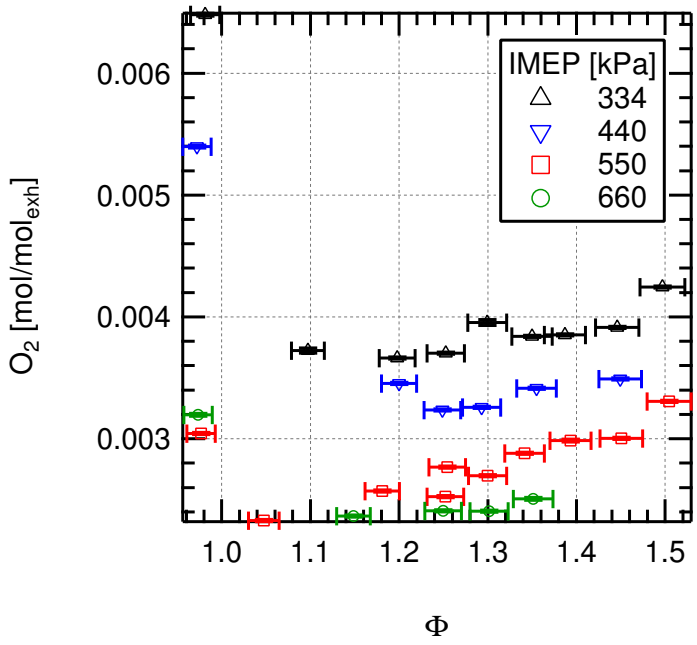

Figure G.10: O_2 emissions as a function of Φ for all loads under PMPV operation.

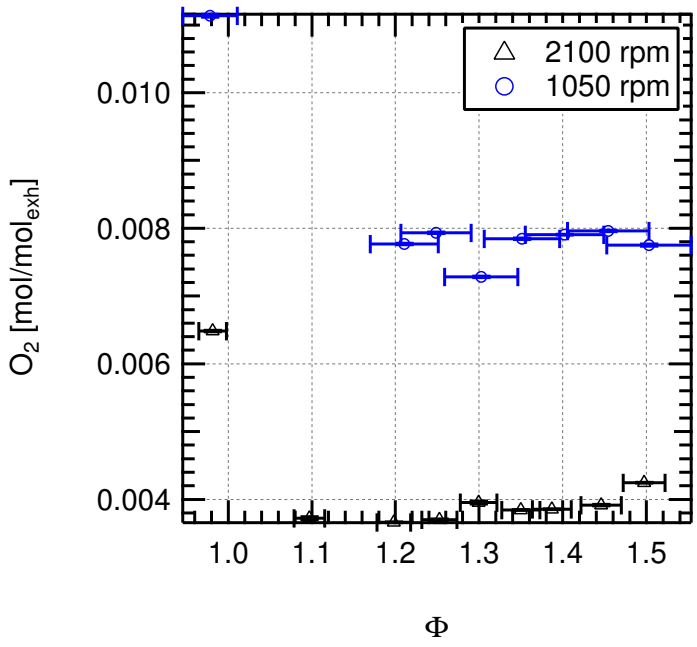

Figure G.11: O_2 emissions as a function of Φ for 2100 rpm and 1050 rpm under PMPV operation.

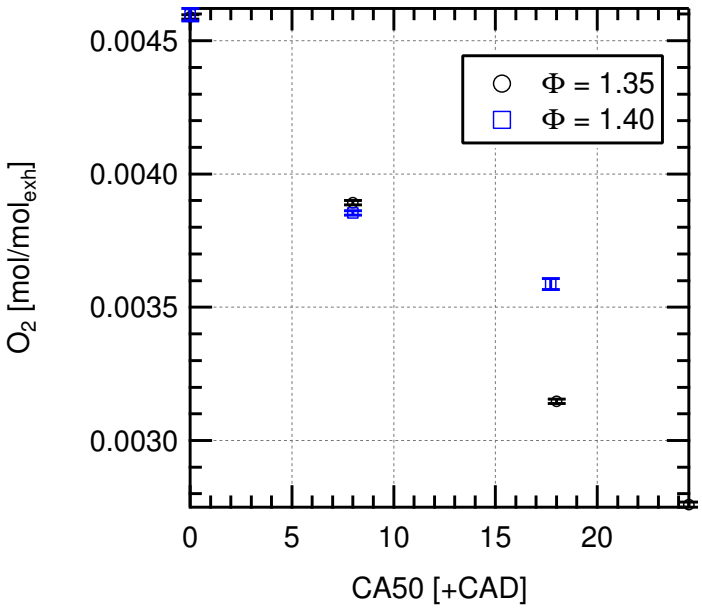

Figure G.12: O_2 emissions as a function of CA50 for $\Phi = 1.35$ and $\Phi = 1.40$ under PMPV operation.

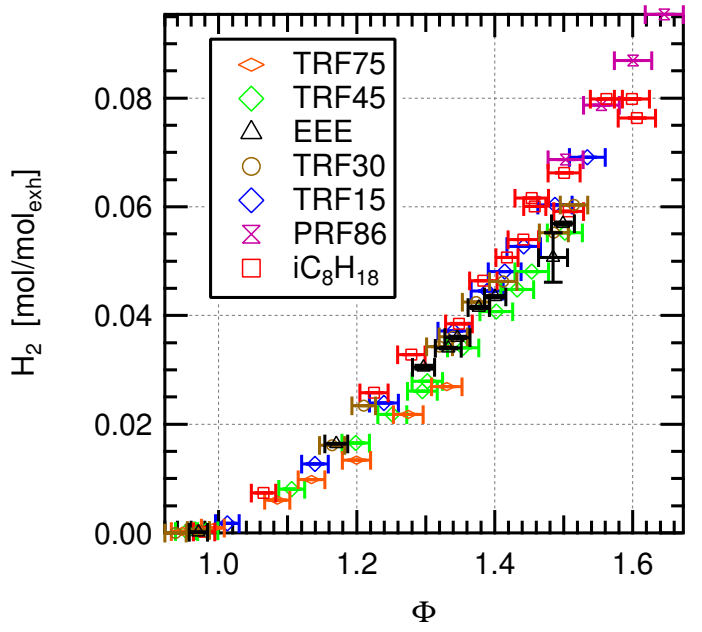

Figure G.13: H_2 emissions as a function of Φ for all fuels under PMPV operation.

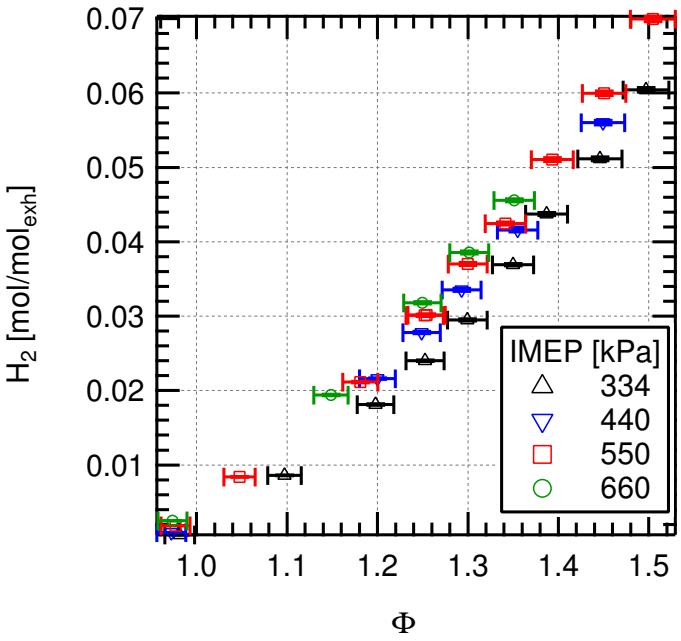

Figure G.14: H_2 emissions as a function of Φ for all loads under PMPV operation.

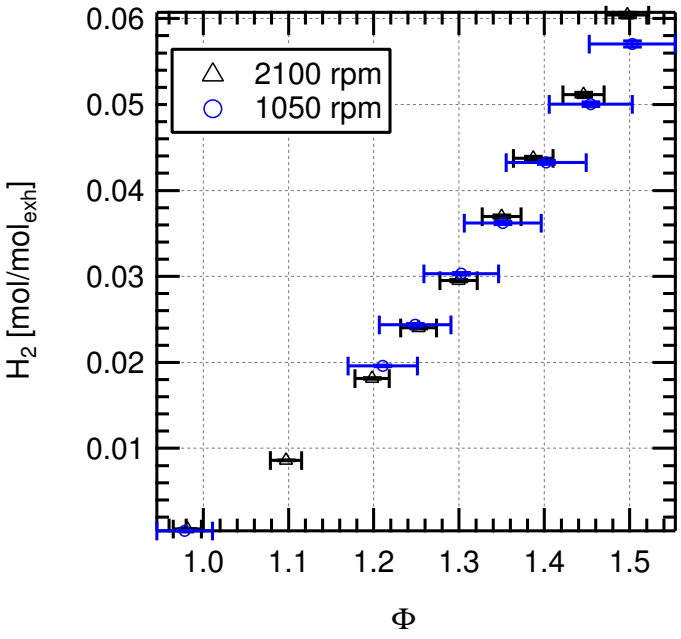

Figure G.15: H_2 emissions as a function of Φ for 2100 rpm and 1050 rpm under PMPV operation.

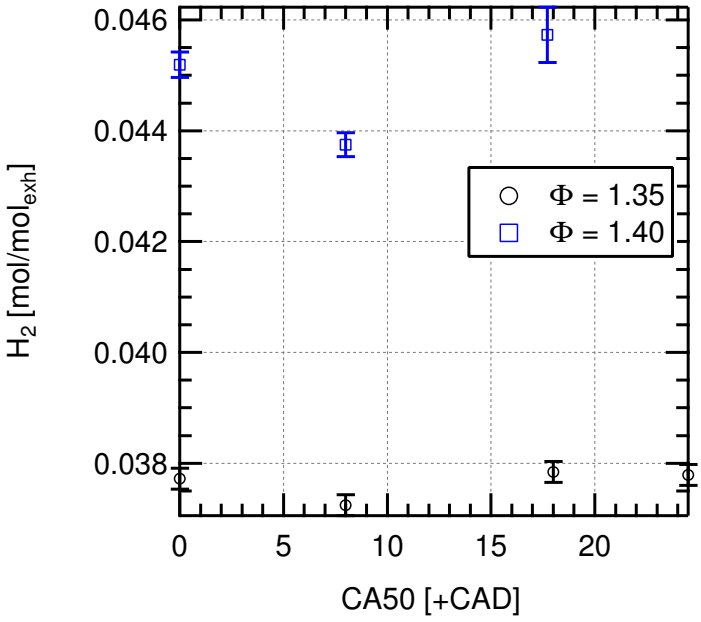

Figure G.16: H_2 emissions as a function of CA50 for $\Phi = 1.35$ and $\Phi = 1.40$ under PMPV operation.

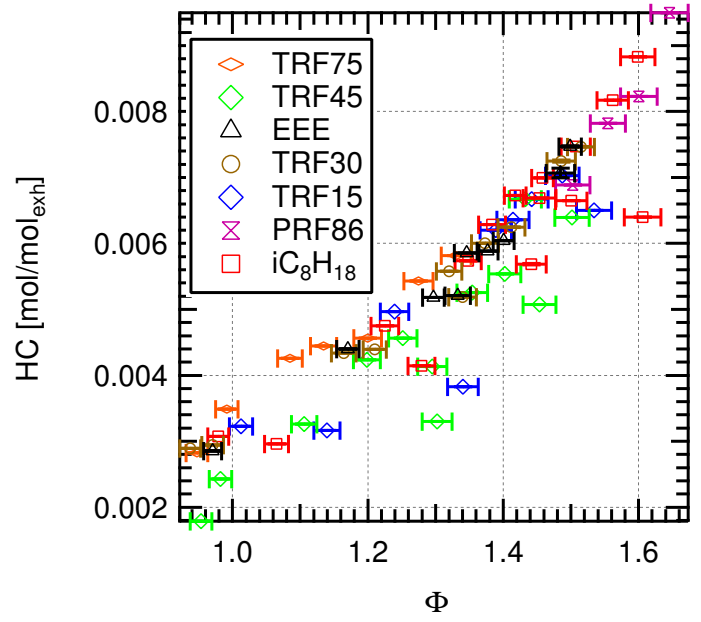

Figure G.17: HC emissions as a function of Φ for all fuels under PMPV operation.

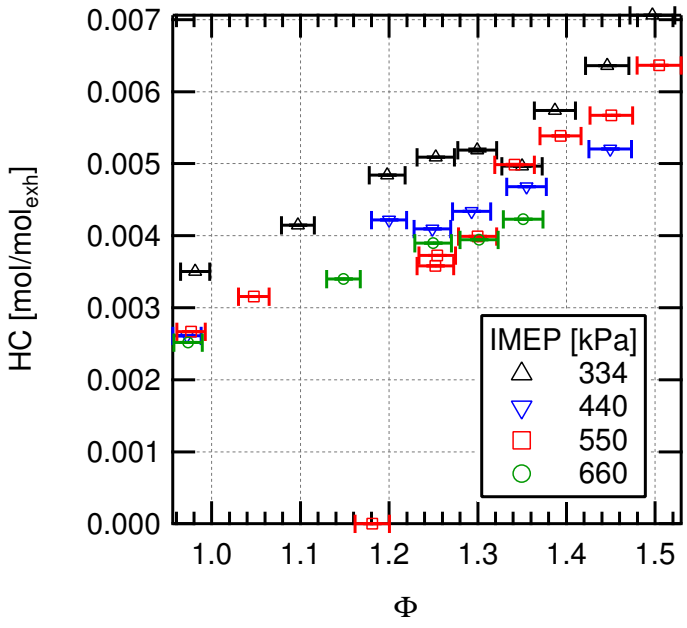

Figure G.18: HC emissions as a function of Φ for all loads under PMPV operation.

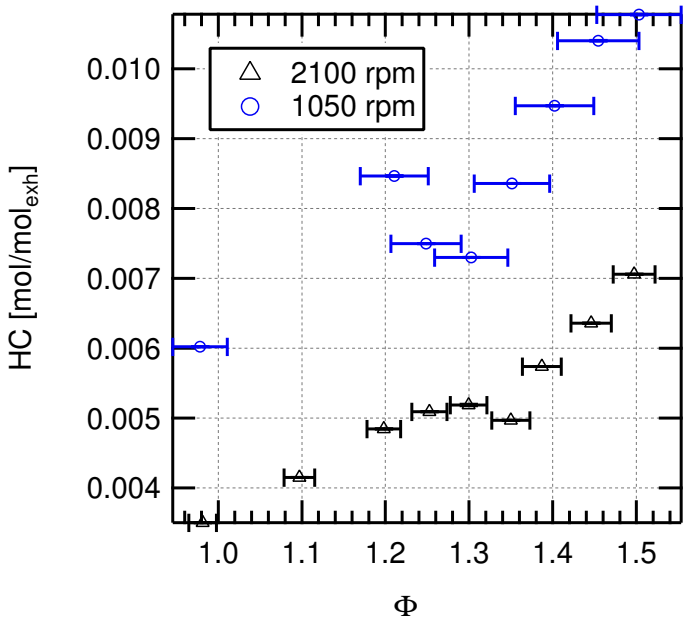

Figure G.19: HC emissions as a function of Φ for 2100 rpm and 1050 rpm under PMPV operation.

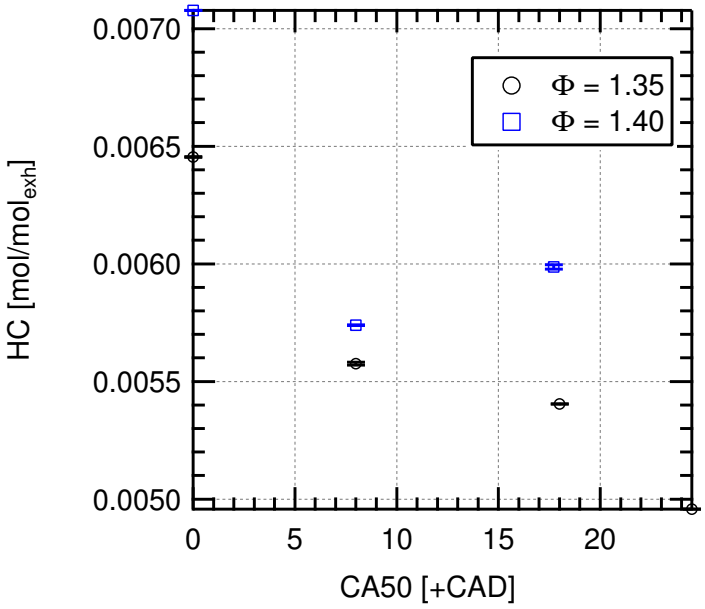

Figure G.20: HC emissions as a function of CA50 for $\Phi = 1.35$ and $\Phi = 1.40$ under PMPV operation.

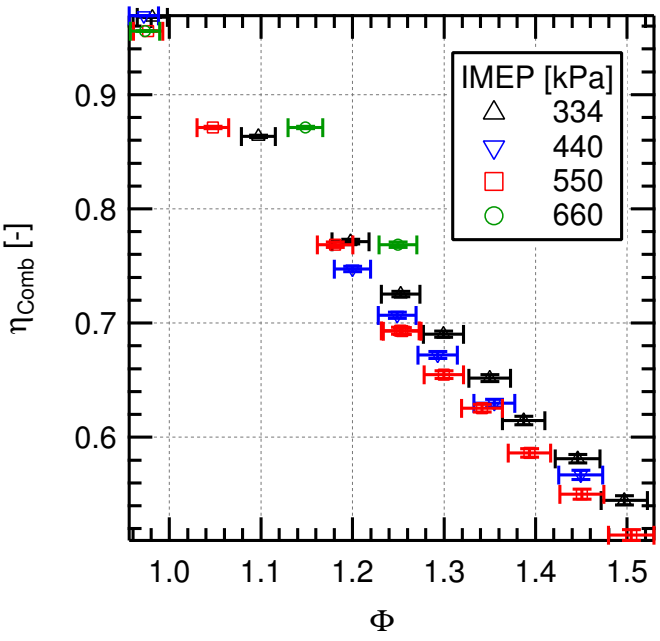

Figure G.21: Combustion efficiency as a function of Φ for all loads under PMPV operation.

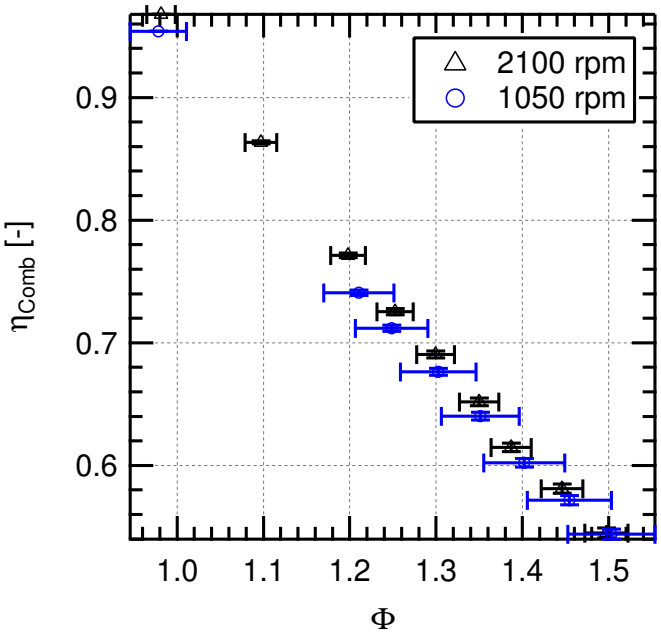

Figure G.22: Combustion efficiency as a function of Φ for 2100 rpm and 1050 rpm under PMPV operation.

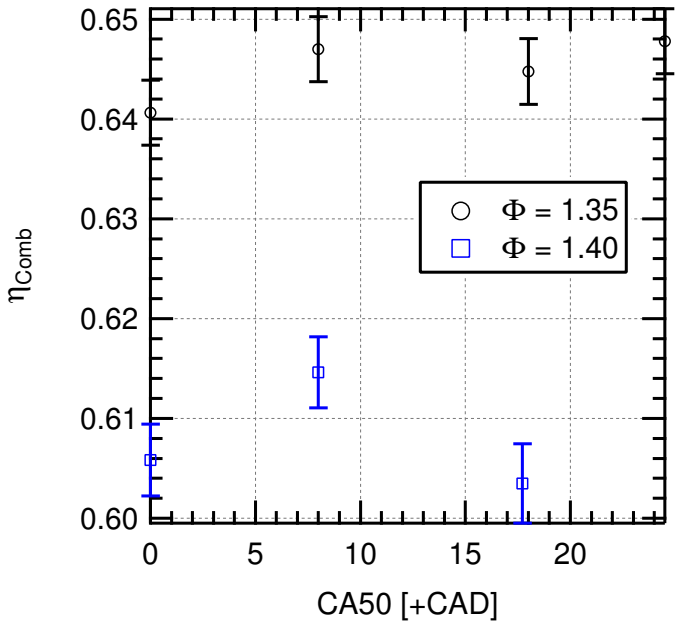

Figure G.23: Combustion efficiency as a function of CA50 for $\Phi = 1.35$ and $\Phi = 1.40$ under PMPV operation.

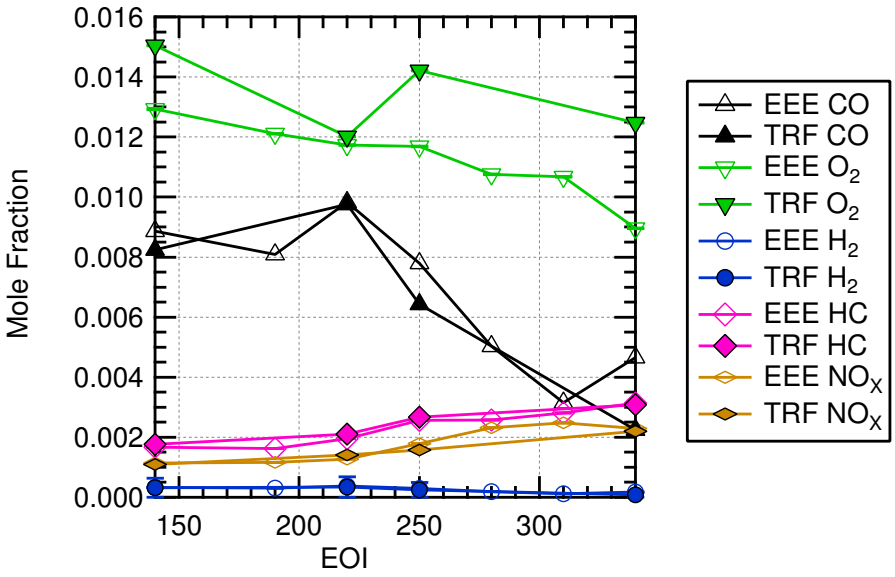

Figure G.24: Gaseous emissions as a function of EOI for EEE and TRF under SIDI operation.

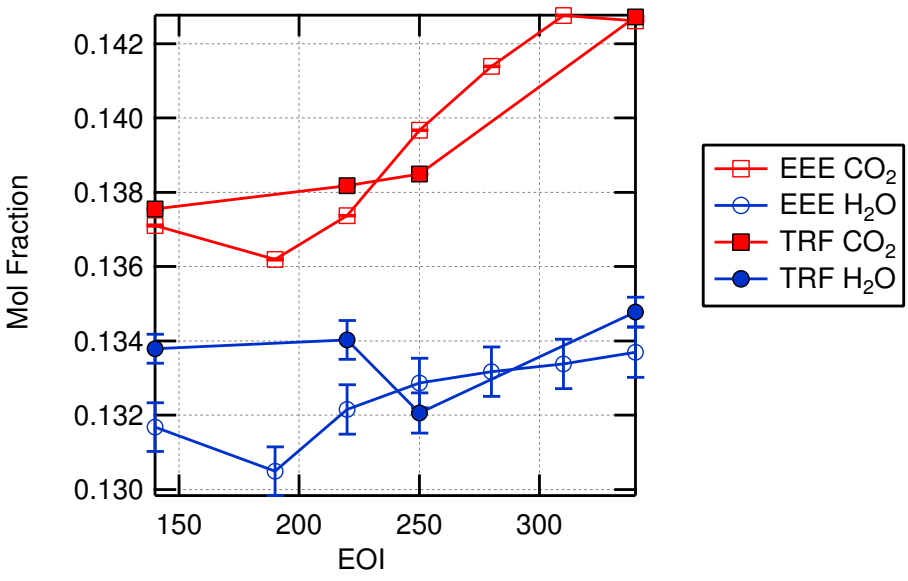

Figure G.25: Gaseous emissions as a function of EOI for EEE and TRF under SIDI operation.

H PMPV THERMODYNAMICS PLOTS

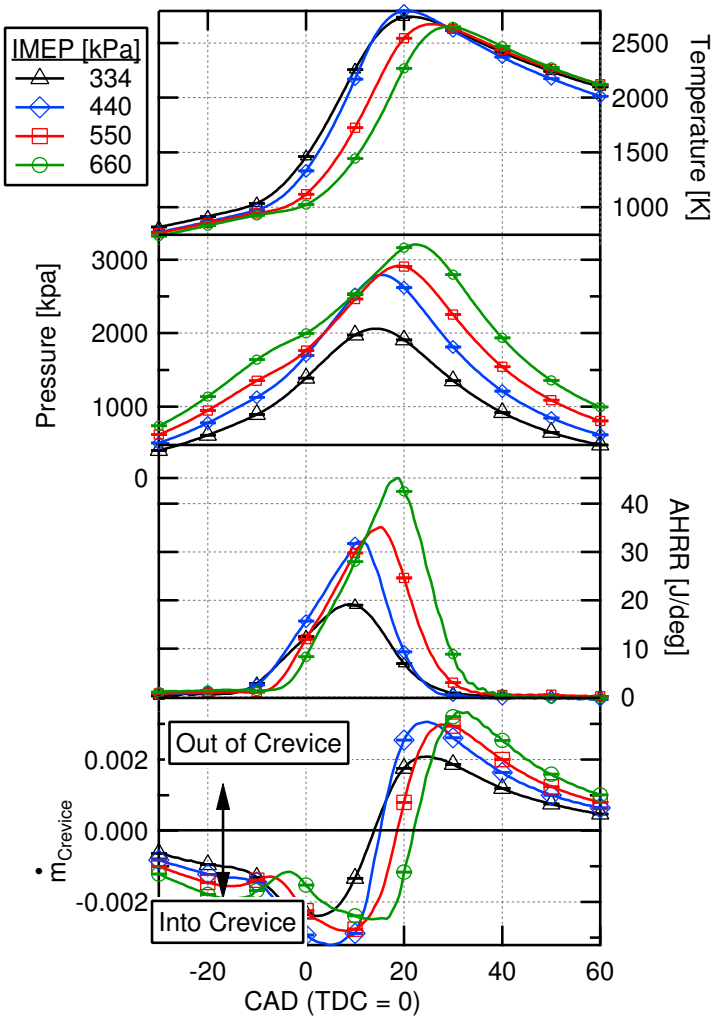

Figure H.1: Averaged main combustion event thermodynamic data for all PMPV loads at $\Phi = 0.98$. Markers are drawn every 20 data points.

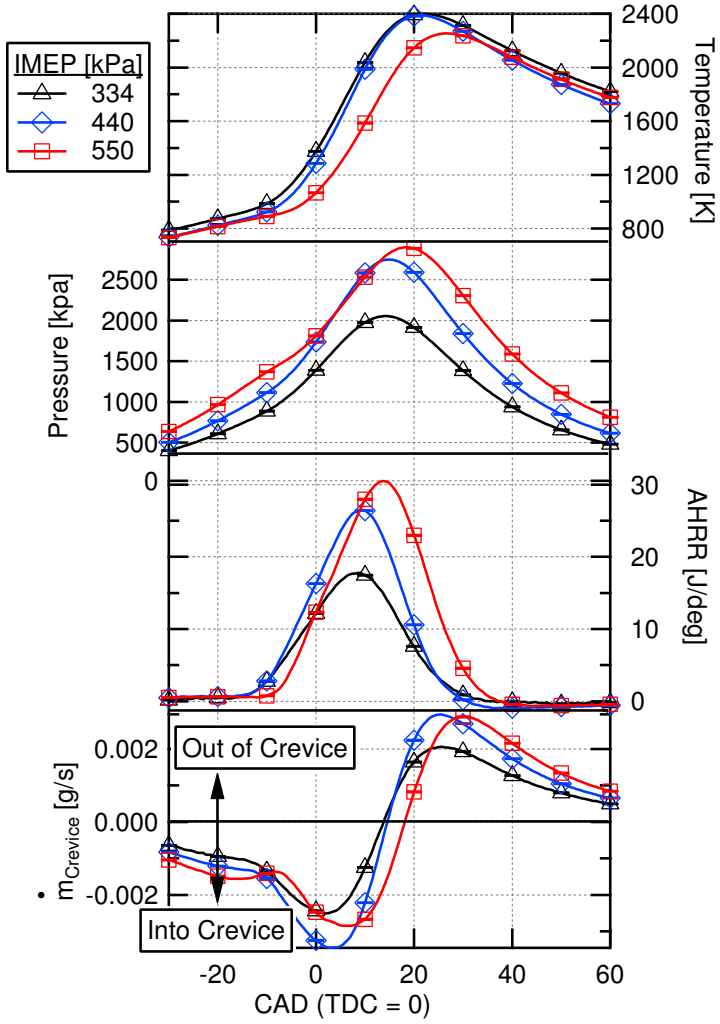

Figure H.2: Averaged main combustion event thermodynamic data for all PMPV loads at $\Phi = 1.45$. Markers are drawn every 20 data points.

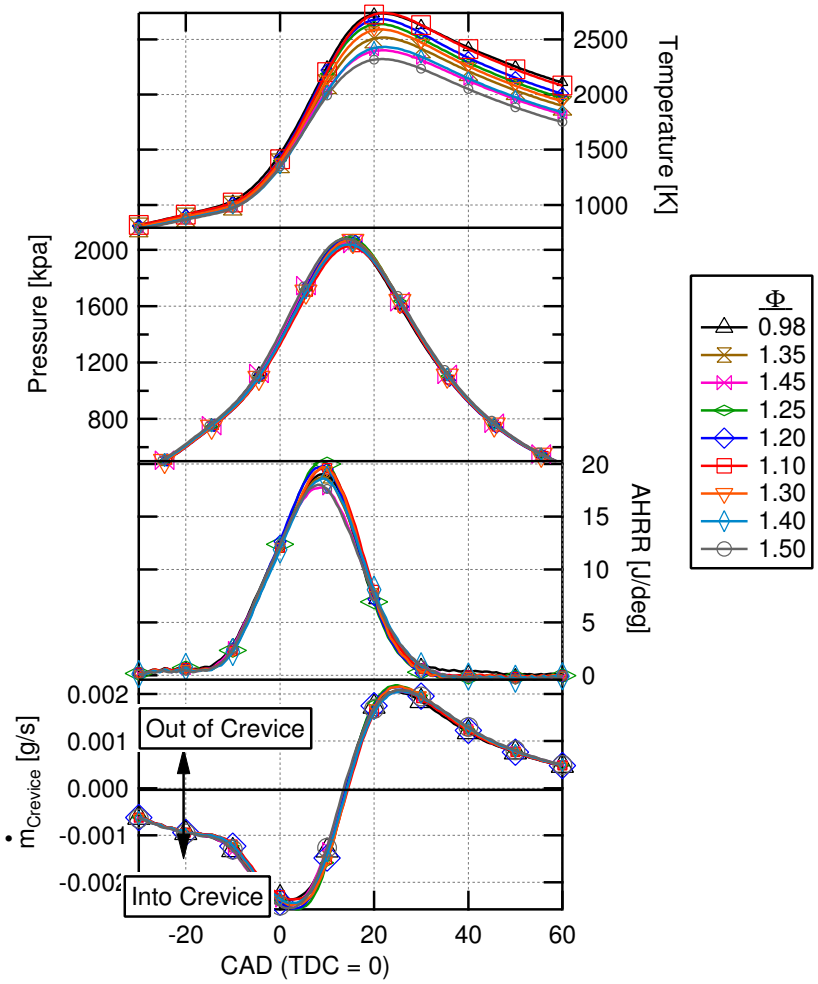

Figure H.3: Averaged main combustion event thermodynamic data for all Φs for EEE at the standard operating condition (334 kPa, 2100 rpm and CA50 = 8). Markers are drawn every 20 data points.

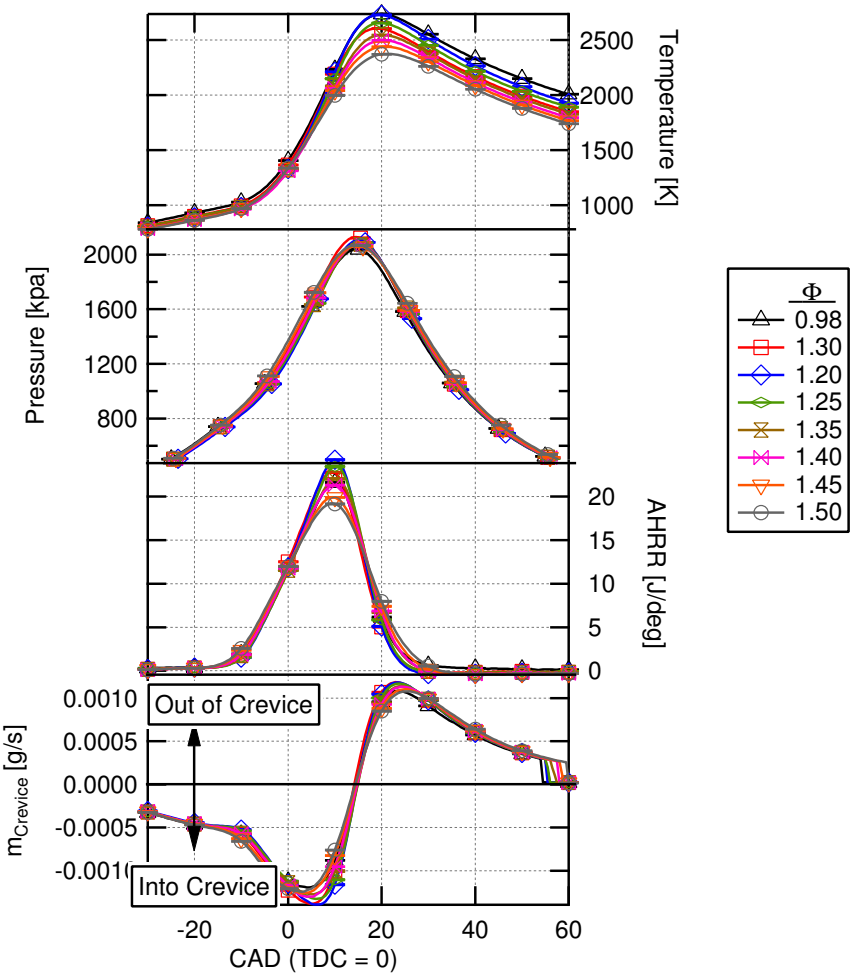

Figure H.4: Averaged main combustion event thermodynamic data for all Φs for EEE at the low speed condition (334 kPa, 1050 rpm and CA50 = 8). Markers are drawn every 20 data points.

I BLANK DATA SHEET

UW - GM CRL Gasoline DISI Laboratory Data Collection Sheet

Date:		**Page Number:**	1	**Test by:**	
Comments:					
Fuel					
Run Number					
Engine Settings					
Engine Speed	RPM				
Intake Orifice	#				
Torque	Nm				
Time of Day	-				
Dyno Hours	hours				
Engine Hours	hours				
Temperatures					
Intake	C				
Exh. Port	C				
Exh Sample	C				
Coolant In	C				
Coolant Mid	C				
Coolant Out	C				
Oil In	C				
Oil Out	C				
Pressures					
Ambient Pres	psia				
Oil Pres	psig				
Fuel Rail Pres	MPa				
Exhaust Pres	kPa				
IMAP	kPa				
Orifice Pressure	kPa				

Controlling Params					
Air Flow Rate (orif)	mg/cycle				
Fuel Flow (Meas.)	mg/cycle				
Fuel Flow (Calc.)	mg/cycle				
Spark Timing	°BTDC				
Spark Dwell	ms				
Injection Timing	°BTDC				
Injection Duration	ms				
Comb. Parameters					
IMEP Avg	kPa				
IMEP COV	%				
PP Avg	kPa				
LPP Avg	deg				
MRPR Avg	kPa/dCA				
NMEP Avg	kPa				
CA-50 Avg	°ATDC				
Emissions Bench					
AF (carbon)	-				
AF (oxygen)	-				
AF (mass)	-				
CO2	% Vol				
O2	% Vol				
CO	% Vol				
HC	ppm				
NO	ppm				
EGR-CO2	%				
Dilution Ratio (CO2)	-				
Particulate Cart					
Dilution Ratio	-				
Valve Combination	P/S				
Probe Heater Temp	C				
Primary Dil. Temp	C				
External Line Temp	C				
SMPS Begin	#				
SMPS Finish	#				
Sample Flowrate	lpm				
SMPS Inlet Pressure	mBar				
Bypass Flow	lpm				
T1	C				
T3	C				

Ambient CO2	% Vol				
TD cooling temp	C				
EvCh Pre 2nd Dilution	C				
EvCh 2nd Dilution Press					
Sample Cooling Flow	gpm				
Emissions bench bath temp (33F-40F)	F				
Thermodenuder?	Y/N				
Operation type	PMPV or DI				
Liquid Fuel?	Y/N				
Zero & Span before?	Y/N				
Comments:					

J HALTERMANN FUEL DATA SHEETS

haltermannsolutions

fueling the world, one solution at a time

Product Information

Telephone: (800) 969-2542

FAX: (281) 457-1469

Johann Haltermann Ltd.

PRODUCT: EPA TIER II EEE FEDERAL REGISTER

PRODUCT CODE: HF0437

Batch No.: ZE3121LT10

Tank No.: 107

Date: 6/1/2011

TEST	METHOD	UNITS	HALTERMANN Specs			RESULTS
			MIN	TARGET	MAX	
Distillation - IBP	ASTM D86	°F	75		95	87
5%		°F				112
10%		°F	120		135	127
20%		°F				149
30%		°F				175
40%		°F				205
50%		°F	200		230	224
60%		°F				234
70%		°F				245
80%		°F				267
90%		°F	305		325	321
95%		°F				339
Distillation - EP		°F			415	399
Recovery		vol %		Report		97.2
Residue		vol %		Report		1.1
Loss		vol %		Report		1.7
Gravity	ASTM D4052	°API	58.7		61.2	58.7
Density	ASTM D4052	kg/l	0.734		0.744	0.744
Reid Vapor Pressure	ASTM D5191	psi	8.7		9.2	8.9
Carbon	ASTM D3343	wt fraction		Report		0.8657
Carbon	ASTM E191	wt fraction		Report		0.8621
Hydrogen	ASTM E191	wt fraction		Report		0.1361
Hydrogen/Carbon ratio	ASTM E191	mole/mole		Report		1.880
Stoichiometric Air/Fuel Ratio				Report		14.627
Oxygen	ASTM D4815	wt %			0.05	None Detected
Sulfur	ASTM D5453	wt %	0.0025		0.0035	0.0030
Lead	ASTM D3237	g/gal			0.01	None Detected
Phosphorous	ASTM D3231	g/gal			0.005	None Detected
Silicon	ASTM 5184	mg/kg			4	None Detected
Composition, aromatics	ASTM D1319	vol %			35	29
Composition, olefins	ASTM D1319	vol %			10	1
Composition, saturates	ASTM D1319	vol %		Report		70
Particulate matter	ASTM D5452	mg/l			1	0.7
Oxidation Stability	ASTM D525	minutes	240			1000+
Copper Corrosion	ASTM D130				1	1a
Gum content, washed	ASTM D381	mg/100mls			5	1.0
Fuel Economy Numerator/C Density	ASTM E191		2401		2441	2427
C Factor	ASTM E191			Report		1.0059
Research Octane Number	ASTM D2699		96.0			97.2
Motor Octane Number	ASTM D2700			Report		88.4
Sensitivity			7.5			8.8
Net Heating Value, btu/lb	ASTM D3338	btu/lb		Report		18466
Net Heating Value, btu/lb	ASTM D240	btu/lb		Report		18267
Color	VISUAL			Report		Undyed

APPROVED BY:

haltermannsolutions
fueling the world, one solution at a time
Telephone: (800) 969-2542

Product Information

FAX: (281) 457-1469
Johann Haltermann Ltd.

PRODUCT: EPA TIER II EEE FEDERAL REGISTER

PRODUCT CODE: HF0437

Batch No.: ZL0121LT10

Tank No.: 106

Date: 12/4/2011

TEST	METHOD	UNITS	HALTERMANN Specs			RESULTS
			MIN	TARGET	MAX	
Distillation - IBP	ASTM D86	°F	75		95	86
5%		°F				109
10%		°F	120		135	125
20%		°F				147
30%		°F				172
40%		°F				202
50%		°F	200		230	224
60%		°F				235
70%		°F				247
80%		°F				269
90%		°F	305		325	321
95%		°F				341
Distillation - EP		°F			415	402
Recovery		vol %		Report		97.4
Residue		vol %		Report		1.1
Loss		vol %		Report		1.5
Gravity	ASTM D4052	°API	58.7		61.2	59.2
Density	ASTM D4052	kg/l	0.734		0.744	0.742
Reid Vapor Pressure	ASTM D5191	psi	8.7		9.2	9.0
Carbon	ASTM D3343	wt fraction		Report		0.8647
Carbon	ASTM E191	wt fraction		Report		0.8619
Hydrogen	ASTM E191	wt fraction		Report		0.1355
Hydrogen/Carbon ratio	ASTM E191	mole/mole		Report		1.873
Stoichiometric Air/Fuel Ratio				Report		14.616
Oxygen	ASTM D4815	wt %			0.05	None Detected
Sulfur	ASTM D5453	wt %	0.0025		0.0035	0.0031
Lead	ASTM D3237	g/gal			0.01	None Detected
Phosphorous	ASTM D3231	g/gal			0.005	None Detected
Silicon	ASTM 5184	mg/kg			4	None Detected
Composition, aromatics	ASTM D1319	vol %			35	28
Composition, olefins	ASTM D1319	vol %			10	1
Composition, saturates	ASTM D1319	vol %		Report		71
Particulate matter	ASTM D5452	mg/l			1	0.7
Oxidation Stability	ASTM D525	minutes	240			1000+
Copper Corrosion	ASTM D130				1	1a
Gum content, washed	ASTM D381	mg/100mls			5	<0.5
Fuel Economy Numerator/C Density	ASTM E191		2401		2441	2422
C Factor	ASTM E191			Report		1.0005
Research Octane Number	ASTM D2699		96.0			97.0
Motor Octane Number	ASTM D2700			Report		88.1
Sensitivity			7.5			8.9
Net Heating Value, btu/lb	ASTM D3338	btu/lb		Report		18490
Net Heating Value, btu/lb	ASTM D240	btu/lb		Report		18395
Color	VISUAL			Report		Undyed

APPROVED BY:

haltermannsolutions
fueling the world, one solution at a time

Telephone: (800) 969-2542

FAX: (281) 457-1469

Johann Haltermann Ltd.

Product Information

PRODUCT: EPA TIER II EEE FEDERAL REGISTER

PRODUCT CODE: HF0437

Batch No.: AJ0221LT10

Tank No.: 105

Date: 10/3/2012

TEST	METHOD	UNITS	HALTERMANN Specs			RESULTS
			MIN	TARGET	MAX	
Distillation - IBP	ASTM D86	°F	75		95	87
5%		°F				110
10%		°F	120		135	126
20%		°F				149
30%		°F				175
40%		°F				204
50%		°F	200		230	223
60%		°F				234
70%		°F				244
80%		°F				263
90%		°F	305		325	319
95%		°F				342
Distillation - EP		°F			415	411
Recovery		vol %		Report		96.9
Residue		vol %		Report		1.1
Loss		vol %		Report		2.0
Gravity	ASTM D4052	°API	58.7		61.2	59.2
Density	ASTM D4052	kg/l	0.734		0.744	0.742
Reid Vapor Pressure	ASTM D5191	psi	8.7		9.2	9.2
Carbon	ASTM D3343	wt fraction		Report		0.8646
Carbon	ASTM E191	wt fraction		Report		0.8631
Hydrogen	ASTM E191	wt fraction		Report		0.1339
Hydrogen/Carbon ratio	ASTM E191	mole/mole		Report		1.847
Stoichiometric Air/Fuel Ratio				Report		14.580
Oxygen	ASTM D4815	wt %			0.05	None Detected
Sulfur	ASTM D5453	wt %	0.0025		0.0035	0.0031
Lead	ASTM D3237	g/gal			0.01	None Detected
Phosphorous	ASTM D3231	g/gal			0.005	None Detected
Silicon	ASTM 5184	mg/kg			4	<1
Composition, aromatics	ASTM D1319	vol %			35	28
Composition, olefins	ASTM D1319	vol %			10	1
Composition, saturates	ASTM D1319	vol %		Report		71
Particulate matter	ASTM D5452	mg/l			1	0.6
Oxidation Stability	ASTM D525	minutes	240			1000+
Copper Corrosion	ASTM D130				1	1a
Gum content, washed	ASTM D381	mg/100mls			5	<0.5
Fuel Economy Numerator/C Density	ASTM E191		2401		2441	2426
C Factor	ASTM E191			Report		0.9991
Research Octane Number	ASTM D2699		96.0			96.5
Motor Octane Number	ASTM D2700			Report		88.6
Sensitivity			7.5			7.9
Net Heating Value, btu/lb	ASTM D3338	btu/lb		Report		18492
Net Heating Value, btu/lb	ASTM D240	btu/lb		Report		18475
Color	VISUAL			Report		Undyed

APPROVED BY:

haltermannsolutions
fueling the world, one solution at a time

Telephone: (800) 969-2542

FAX: (281) 457-1469

Johann Haltermann Ltd.

Product Information

PRODUCT: EPA TIER II EEE FEDERAL REGISTER

PRODUCT CODE: HF0437

Batch No.: BB2521LT10

Tank No.: 105

Date: 2/27/2013

TEST	METHOD	UNITS	HALTERMANN Specs			RESULTS
			MIN	TARGET	MAX	
Distillation - IBP	ASTM D86	°F	75		95	88
5%		°F				112
10%		°F	120		135	125
20%		°F				146
30%		°F				169
40%		°F				198
50%		°F	200		230	220
60%		°F				230
70%		°F				240
80%		°F				258
90%		°F	305		325	313
95%		°F				336
Distillation - EP		°F			415	402
Recovery		vol %		Report		96.7
Residue		vol %		Report		1.0
Loss		vol %		Report		2.0
Gravity	ASTM D4052	°API	58.7		61.2	59.3
Density	ASTM D4052	kg/l	0.734		0.744	0.741
Reid Vapor Pressure	ASTM D5191	psi	8.7		9.2	9.1
Carbon	ASTM D3343	wt fraction		Report		0.8646
Carbon	ASTM E191	wt fraction		Report		0.8598
Hydrogen	ASTM E191	wt fraction		Report		0.1347
Hydrogen/Carbon ratio	ASTM E191	mole/mole		Report		1.860
Stoichiometric Air/Fuel Ratio				Report		14.606
Oxygen	ASTM D4815	wt %			0.05	None Detected
Sulfur	ASTM D5453	wt %	0.0025		0.0035	0.0034
Lead	ASTM D3237	g/gal			0.01	None Detected
Phosphorous	ASTM D3231	g/gal			0.005	None Detected
Silicon	ASTM 5184	mg/kg			4	None Detected
Composition, aromatics	ASTM D1319	vol %			35	28
Composition, olefins	ASTM D1319	vol %			10	1
Composition, saturates	ASTM D1319	vol %		Report		71
Particulate matter	ASTM D5452	mg/l			1	0.3
Oxidation Stability	ASTM D525	minutes	240			1000+
Copper Corrosion	ASTM D130				1	1a
Gum content, washed	ASTM D381	mg/100mls			5	<0.5
Fuel Economy Numerator/C Density	ASTM E191		2401		2441	2421
C Factor	ASTM E191			Report		0.9989
Research Octane Number	ASTM D2699		96.0			96.6
Motor Octane Number	ASTM D2700			Report		88.5
Sensitivity			7.5			8.1
Net Heating Value, btu/lb	ASTM D3338	btu/lb		Report		18489
Net Heating Value, btu/lb	ASTM D240	btu/lb		Report		18359
Color	VISUAL			Report		Undyed

APPROVED BY:

haltermannsolutions
linking the world, one solution at a time

Telephone: (800) 969-2542 FAX: (281) 457-1469

Johann Haltermann Ltd.

Product Information

PRODUCT: EPA TIER II EEE FEDERAL REGISTER

PRODUCT CODE: HF0437

Batch No.: BI0921LT10

Tank No.: 105

Date: 9/13/2013

TEST	METHOD	UNITS	HALTERMANN Specs			RESULTS
			MIN	TARGET	MAX	
Distillation - IBP	ASTM D86	°F	75		95	88
5%		°F				111
10%		°F	120		135	124
20%		°F				144
30%		°F				167
40%		°F				196
50%		°F	200		230	218
60%		°F				230
70%		°F				239
80%		°F				257
90%		°F	305		325	314
95%		°F				339
Distillation - EP		°F			415	400
Recovery		vol %		Report		97.4
Residue		vol %		Report		1.1
Loss		vol %		Report		1.5
Gravity	ASTM D4052	°API	58.7		61.2	59.2
Density	ASTM D4052	kg/l	0.734		0.744	0.742
Reid Vapor Pressure	ASTM D5191	psi	8.7		9.2	9.1
Carbon	ASTM D3343	wt fraction		Report		0.8650
Carbon	ASTM E191	wt fraction		Report		0.8642
Hydrogen	ASTM E191	wt fraction		Report		0.1334
Hydrogen/Carbon ratio	ASTM E191	mole/mole		Report		1.840
Stoichiometric Air/Fuel Ratio				Report		14.568
Oxygen	ASTM D4815	wt %			0.05	None Detected
Sulfur	ASTM D5453	wt %.	0.0025		0.0035	0.0029
Lead	ASTM D3237	g/gal			0.01	None Detected
Phosphorous	ASTM D3231	g/gal			0.005	None Detected
Silicon	ASTM 5184	mg/kg			4	None Detected
Composition, aromatics	ASTM D1319	vol %			35	28
Composition, olefins	ASTM D1319	vol %			10	2
Composition, saturates	ASTM D1319	vol %		Report		70
Particulate matter	ASTM D5452	mg/l			1	0.8
Oxidation Stability	ASTM D525	minutes	240			1000+
Copper Corrosion	ASTM D130				1	1a
Gum content, washed	ASTM D381	mg/100mls			5	<0.5
Fuel Economy Numerator/C Density	ASTM E191		2401		2441	2428
C Factor	ASTM E191			Report		1.0059
Research Octane Number	ASTM D2699		96.0			96.8
Motor Octane Number	ASTM D2700			Report		88.3
Sensitivity			7.5			8.5
Net Heating Value, btu/lb	ASTM D3338	btu/lb		Report		18480
Net Heating Value, btu/lb	ASTM D240	btu/lb		Report		18312
Color	VISUAL			Report		Undyed

APPROVED BY:

haltermannsolutions
fueling the world, one solution at a time

Report of Analysis

Telephone: (800) 969-2542 **FAX: (281) 457-1469**

Johann Haltermann Ltd.

PRODUCT: Dry Ethanol ASTM D4806

PRODUCT CODE: BS-158

Batch No:. AA0921GP01

Date: 11/14/11

TEST	METHOD	UNITS	SPECIFICATIONS			RESULTS
			MIN	TARGET	MAX	
API Gravity	ASTM D4052	-		Report		48.39
Ethanol content	ASTM D5501	vol %	92.1			96.18
Methanol content	ASTM D5501	vol %			0.5	0.000
Hydrocarbon denaturant	GC	vol %	1.96		5.0	3.27
Inorganic Chlorides	ASTM D7328	ppm wt			10	0.01
Copper content	ASTM D1688A	mg/kg			0.1	<0.05
Acidity, as Acidic acid	ASTM D1613	wt %			0.007	0.002
pHe	ASTM D6423		6.5		9.0	7.88
Water content	ASTM E203	vol %			1.0	0.55
Washed gum	ASTM D381	mg/100mls			5.0	<0.5
Sulfur	ASTM D5453	ppm wt			30	1.5
Sulfates	ASTM D7328	ppm wt			4	0.24
Appearance		visual		Clear,Bright & Free		CBF

APPROVED BY: Kenneth Smith

K EEE COMPOSITION ANALYSIS

SOUTHWEST RESEARCH INSTITUTE®

6220 CULEBRA ROAD 78238-5166 • P.O. DRAWER 28510 78228-0510 • SAN ANTONIO, TEXAS, USA • (210) 684-5111 • WWW.SWRI.ORG

OFFICE OF AUTOMOTIVE ENGINEERING

December 5, 2013

Mr. Mitchell D. Hageman
Engine Research Center
The University of Wisconsin – Madison
1500 Engineering Dr.
Madison, WI 53706
Phone: 515-451-7425
E-Mail: mhageman@wisc.edu

Re: Test Summary Report
SwRI WO# 69499

Dear Mr. Hageman:

The sample received on November 20, 2013 has been analyzed as requested. The sample was received in a gallon metal container in good condition. Test results and methods are shown in the attached table.

Testing was performed through December 5, 2013. Analysis was performed according to the listed ASTM test procedures with no modifications or deviations. Precision should be consistent with those stated in the ASTM test procedures. Sample aliquots were taken in accordance with the various ASTM test procedures. The analyses above pertain only to the sample received by Southwest Research Institute and represent only that sampling lot. This report shall not be reproduced except in full without the express written permission of Southwest Research Institute.

If there are questions concerning these analyses, or if you have further instructions, please contact me at (210) 522-2181.

Sincerely,

Mary R. Nelson

Mary R. Nelson
Senior Research Scientist
Fuels and Lubricants Laboratory
Petroleum Products Research Department
Office of Automotive Engineering

OMRRDLE13

SOUTHWEST RESEARCH INSTITUTE®

6220 CULEBRA ROAD 78238-5166 • P.O. DRAWER 28510 78228-0510 • SAN ANTONIO, TEXAS, USA • (210) 684-5111 • WWW.SWRI.ORG

OFFICE OF AUTOMOTIVE ENGINEERING

Southwest Research Institute

Test Summary Report

for

University of Wisconsin - Madison

December 5, 2013

DATA TABLE ATTACHED

Note 1: The information contained in this document is legally privileged and/or proprietary business information intended only for the use of the individual or the entity named above. If the reader of this document is not the intended recipient, you are hereby notified that any dissemination, distribution, or copy of this document is strictly prohibited. If you have received this document in error, please immediately notify us by telephone at 210/522-2964 and return the original document to the sender at the return address via the United States Postal Service.

Note 2: Institute shall not publish or make known to others the subject matter or results of the Project or any information obtained in connection therewith which is proprietary and confidential to Client without Client's written approval. No advertising or publicity containing any reference to Institute or any of its employees, either directly or by implication, shall be made use of by Client or on Client's behalf without Institute's written approval. In the event Client distributes any report issued by Institute on this Project outside its own organization, such report shall be used in its entirety, unless Institute approves a summary or abridgement for distribution.

Benefiting government, industry and the public through innovative science and technology

Data Summary			
University of Wisconsin-Madison			
SWRI Work Order #69499			
	LabNum	20616	
	PSponCd	recd 11-20-13	
	SSponCd	GASOLINE	
D4052	API@60F	62.5	
	SPGr@60F	0.7295	
	Dens@15C	0.7293 g/ml	
D5769Vol	ValDate	Volume %	Weight %
	Benzene	0.28	0.34
	Toluene	20.99	25.09
	TtlAroma	33.08	39.73
	EthBenz	<0.1	<0.1
	mpXylene	0.1	0.12
	Oxylene	0.42	0.51
	IPrpBnz	0.19	0.22
	nPrpBnz	0.67	0.8
	1m3eBenz	1.83	2.18
	1m4eBenz	1.07	1.27
	135tmBnz	1.04	1.24
	1m2eBenz	0.78	0.95
	124tmBnz	3.7	4.46
	123tmBnz	0.67	0.82
	Indan	0.17	0.23
	14deBenz	0.26	0.3
	nbutBenz	<0.1	<0.1
	12deBenz	<0.1	<0.1
	1245tmBz	<0.1	<0.1
	1235tmBz	<0.1	<0.1
	Napthaln	<0.1	0.12
	pmBenz	<0.1	<0.1
	2mNaptha	0.24	0.34
	1mNaptha	0.13	0.18
	C10Benz	0.22	0.26
	C11Benz	<0.1	<0.1
	C12Benz	<0.1	<0.1
	AlkIndan	<0.1	<0.1

BIBLIOGRAPHY

[1] Regulation no. 83, uniform provisions concerning the approval of vehicles with regard to the emission of pollutants according to engine fuel requirements.

[2] Product information; model 3010 condensation particle counter, 1999.

[3] Dekati thermodenuder user manual, 2003.

[4] Model 3090 engine exhaust particle sizer^{TM} spectrometer; operation and service manual, 2004.

[5] Aerosol Instrument Manager software for scanning mobility particle sizer (SMPS^{TM}) spectrometer; user's manual, 2006.

[6] Fps-4000; user's manual, 2010.

[7] Measuring nanoparticle size distributions in real-time: Key factors for accuracy, 2012.

[8] Control of air pollution from motor vehicles: Tier 3 motor vehicle emission and fuel standards; final rule, 2014.

[9] Viscosity of liquids and gases, accessed: 08-11-2014.

[10] Series 3080 electrostatic classifiers; instruction manual, March 2005.

[11] W.J.D. Annand. Heat transfer in the cylinders of reciprocating internal combustion engines. *Proc. Instn Mech. Engrs*,, 177(36):973–990, 1963.

[12] J. Appel, H. Bockhorn, and M. Frenklach. Kinetic modeling of soot formation with detailed chemistry and physics: Laminar premixed flames of c-2 hydrocarbons. *Combustion and Flame*, 121(1-2):122–136. ISSN 0010-2180.

[13] Jörg Appel, Henning Bockhorn, and Michael Wulkow. A detailed numerical study of the evolution of soot particle size distributions in laminar premixed flames. *Chemosphere*, 42:635–645, 2001.

[14] A. Backhaus, J.and Ferris and D. Rothamer. Design of bioderived gasoline fuels: Volatility modeling, 2014.

[15] T.L. Barone, J.M.E. Storey, A.D. Youngquist, and J.P. Szybist. An analysis of direct-injection spark-ignition (disi) soot morphology. *Atmospheric Environment*, 49:268–274, 2012.

[16] M. Bönig, ChR. Felderman, H. Jander, B. Lüers, G. Rudolph, and H.Gg. Wagner. Soot formation in premixed C_2H_4 flat flames at elevated pressure. *The Combustion Institute*, Twenty-Third Symposium (International) on Combustion:1581–1587, 1990.

[17] D. S. Bento, K. A. Thomson, and O. L. Gulder. Soot formation and temperature field structure in laminar propane-air diffusion flames at elevated pressures. *Combustion and Flame*, 145(4):765–778. ISSN 0010-2180.

[18] Victor A Bloomfield and R.K. Dewan. Viscosity of liquid mixtures. *Journal of Physical Chemistry*, 75(20):3113–3119.

[19] H. Böhm, D. Hesse, H. Jander, B. Lüers, J. Pietscher, H. G. G. Wagner, and M. Weiss. The influence of pressure and temperature on soot formation in premixed flames. *Twenty-Second Symposium (International) on Combustion*, pages 403–411, 1989.

[20] H. Böhm, Chr. Feldermann, Th. Heidermann, H. Jander, B. Lüers, and H.Gg. Wagner. Soot formation in premixed c_2h_2-air flames for pressures up to 100 bar. *Twenty-Fourth Symposium (International) on Combustion*, pages 991–998, 1992.

[21] Tak W. Chan, Eric Meloche, Joseph Kubsh, Deborah Rosenblatt, Rasto Brezny, and Greg Rideout. Evaluation of a gasoline particulate filter to reduce particle emissions from a gasoline direct injection vehicle. *SAE paper 2012-01-1727*, pages 1277–1290, 2012.

[22] M. Chaos, Z. Zhao, A. Kazakov, P. Gokulakrishnan, M. Angioletti, and F.L. Dryer. A prf+ toluene surrogate fuel model for simulating gasoline kinetics, March 25-282007.

[23] Longfei Chen, Mike Braisher, Alison Crossley, Richard Stone, and Dave Richardson. The influence of ethanol blends on particulate matter emissions from gasoline direct injection engines.

[24] B.C. Choi, S.K. Choi, and S.H. Chung. Soot formation characteristics of gasoline surrogate fuels in counterflow diffusion flames. *Proceedings of the Combustion Institute*, 33:609–616, 2010.

[25] A. Ciajolo, A. D'Anna, R. Barbella, A. Tregrossi, and A Violi. The effect of temperature on soot inception in premixed ethylene flames. In *26th Symposium (Intl) on Combustion*. The Combustion Institute, 1996.

[26] M.B. Colket and D.J. Seery. Reaction mechanisms for toluene pyrolysis. In *25th Symposium (Intl) on Combustion*, pages 883–891. The Combustion Institute, 1994.

[27] Diegel Susan Moore Sheila Davis, Stacy and Robert Boundy. Vehicle technologies' fact of the week 2012, 2012.

[28] Theo M.C.M. De Kok, Hermen A.L. Driece, Janneke G.F. Hogervorst, and Jacob J. Briede Hogervorst b. Toxicological assessment of ambient and traffic-related particulate matter: A review of recent studies. 613:103âŁ“122, 2006.

[29] P. F. DeCarlo, J. G. Slowik, D. R. Worsnop, P. Davidovits, and J. L. Jimenez. Particle morphology and density characterization by combined mobility and aerodynamic diameter measurements. part 1: Theory. *Aerosol Science and Technology*, 38(12):1185–1205.

[30] A.B. Dempsey. *Dual-Fuel Reactivity Controlled Compression Ignition (RCCI) with Alternative Fuels*. Thesis, 2013.

[31] Silvana Di Iorio, Maurizio Lazzaro, Paolo Sementa, Bianca Maria Vaglieco, and Francesco Catapano. Use of renewable oxygenated fuels in order to reduce particle emissions from a gdi high performance engine.

[32] Peter Eastwood. *Particulate Emissions from Vehicles*. Wiley-PEPublishing Series. John Wiley & Sons Ltd, West Sussex, England, 1st edition, 2008.

[33] A. Ergut, R.J. Therrien, Y. A. Levendis, H. Richter, J. B. Howard, and J. Carlson. Chemical speciation of premixed ethylbenzene flames at the soot onset limit at various (phi, t) pairs. *Combustion and Flame*, 156:1014–1022, 2009.

[34] Kathy Erickson, Markus Galli, Brian Osmondson, Hans-Georg Horn, Rob Caldow, and Tim Johnson. 2010 new product introduction; tsi's new advance aerosol neutralizer (ppt), 2010.

[35] Carolyn Farron, Nicholas Matthias, David Foster, Michael Andrie, Roger Krieger, Paul Najt, Kushal Narayanaswamy, Arun Solomon, and Alla Zelenyuk. Particulate characteristics for varying engine operation in a gasoline spark ignited, direct injection engine.

[36] Colin R. Ferguson and Allan T. Kirkpatrick. *Internal Combustion Engines, Applied Thermosciences*. John Wiley & Sons, Inc., 2nd edition, 2001.

[37] A Ferris. *Development of Volatility and Anti-Knock Characterization Tools for the Design of Gasoline-Like Drop-in Fuels*. Ms thesis, 2014.

[38] W. L. Flower and C. T. Bowman. Soot production in axisymmetric laminar diffusion flames at pressures frome one to ten atmospheres. *Proc. Combust. Inst.*, 21(1986): 1115–1124, 1986.

[39] M. Frenklach. Reaction mechanism of soot formation in flames. *Physical Chemistry Chemical Physics*, 4(11):2028–2037.

[40] M. Frenklach and H. Wang. Detailed modeling of soot particle nucleation and growth. *Proceedings of the Combustion Institute*, 21:1559–1566.

[41] Michael Frenklach, David W. Clary, William C. Jr. Gardiner, and Stephen E. Stein. Detailed kinetic modeling of soot formation in shock-tube pyrolysis of acetylene. *Twentieth International Symposium on Combustion / The Combustion Institute*, pages 887–901, 1984.

[42] J. A. Gatowski, E. N. Balles, K. M. Chun, F. E. Nelson, J. A. Ekchian, and J. B. Heywood. Heat release analysis of engine pressure data. *SAE Technical Paper*, 841359.

[43] Jaal B. Ghandhi. Heat release analysis. 2012.

[44] Tim Gilles. Comparison of dynamometer power absorption characteristics and vehicle road load measurements, 2011.

[45] Irvin Glassman. Soot formation in combustion processes. *Symposium (International) on Combustion*, 22(1):295–311. ISSN 0082-0784.

[46] Irvin Glassman. Sooting laminar diffusion flames: Effect of dilution, additives, pressure, and microgravity. *Twenty-Seventh Symposium (International) on Combustion/ The Combustion Institute*, pages 1589–1596, 1998.

[47] Irvin Glassman and Richard A Yetter. *Combustion*. Academic Press, United States of America, fourth edition, 2008.

[48] A. Gomez, M. G. Littman, and I. Glassman. Comparative-study of soot formation on the centerline of axisymmetrical laminar diffusion flames - fuel and temperature effects. *Combustion and Flame*, 70(2):225–241, 1987.

[49] P. G. Gormley and M. Kennedy. Diffusion from a stream flowing through a cylindrical tube. *Proceedings of the Royal Irish Academy. Section A: Mathematical and Physical Sciences*, 52:163–169.

[50] Mitchell Hageman, David Rothamer, and Steven Sakai. Identification of soot onset and background particulate levels in a spark-ignition engine, 2014.

[51] S. Hanisch, H. Jander, Th. Pape, and H. Gg. Wagner. Soot mass growth and coagulation of soot particles in c_2h_4/air-flames at 15 bar. *The Combustion Institute*, Twenty-Fifth Symposium (International) on Combustion:577–584, 1994.

[52] Nils Hansen, Terrill A. Cool, Phillip R. Westmoreland, and Katharina Kohse–Höinghaus. Recent contributions of flame-sampling molecular-beam mas spectrometry to a fundamental understanding of combustion chemistry. *Progress in Energy and Combustion Science*, 35:168–191, 2009.

[53] B. S. Haynes and H. G. Wagner. Soot formation. *Progress in Energy & Combustion Science*, 7(4):229–273.

[54] Xin He, Matthew A. Ratcliff, and Bradley T. Zigler. Effects of gasoline direct injection engine operating parameters on particle number emissions. *Energy & Fuels*, 26: 2014–2027, 2012.

[55] J. B. Heywood. *Internal Combustion Engine Fundamentals*. McGraw-Hill, Inc., New York, 1988.

[56] I. Hunwartzen. Modification of cfr test engine unit to determine octane numbers of pure alcohols and gasoline-alcohol blends. *SAE Technical Paper*, 820002, 1982.

[57] Qi Jiao and Rolf Reitz. Modeling of equivalence ratio effects on particulate formation in a spark-ignition engine under premixed conditions. *SAE Paper*, 2014-01-1607, 2014.

[58] H. I. Joo and Ö. L. Gülder. Soot formation and temperature field structure in co-flow laminar methane-air diffusion flames at pressures from 10 to 60 atm. *Proceedings of the Combustion Institute*, 32:769–775.

[59] D. Kayes and S. Hochgreb. Mechanisms of particulate matter formation in spark-ignition engines. 1. effect of engine operating conditions. *Environmental Science & Technology*, 33(22):3957–3967, . ISSN 0013-936X.

[60] D. Kayes and S. Hochgreb. Mechanisms of particulate matter formation in spark-ignition engines. 2. effect of fuel, oil, and catalyst parameters. *Environmental Science & Technology*, 33(22):3968–3977, . ISSN 0013-936X.

[61] D. Kayes and S. Hochgreb. Mechanism of particulate matter formation in spark-ignition engines. 3. model of pm formation. *Environmental Science & Technology*, 33 (22):3978–3992, . ISSN 0013-936X.

[62] T. Kitamura, T. Ito, J. Senda, and H. Fujimoto. Detailed chemical kinetic modeling of diesel spray combustion with oxygenated fuels. *SAE Paper*, 2001-01-1262, 2001.

[63] David B Kittelson. Engines and nanoparticles: A review. *Journal of Awerosol Science*, 29(5/6):575–588, 1998.

[64] A. Kowalewicz. Methanol as a fuel for spark ignition engines: A review and analysis. *Proceedings of the Institution of Mechanical Engineers, Part D: Journal of Automobile Engineering*, 207:43–52, 1993.

[65] B.M. Kumfer, S.A Skeen, and R.L. Axelbaum. Soot inception limits in laminar diffusion flames with application to oxy-fuel combustion. *Combustion and Flame*, 154: 546–556, 2008.

[66] T.H. Lake, J. Stokes, P.A. Whitaker, and J.V. Crump. Comparison of direct injection gasoline combustion systems. *SAE Technical Paper No. 980154*, 1998.

[67] J. Lee, R. Patel, A. Schönborn, N. Ladommatos, and C. Bae. Effect of biofuels on nanoparticle emissions from spark- and compression-ignited single-cylinder engines with same exhaust displacement volume. *Energy & Fuels*, 23:4363–4369.

[68] K. Lee, H.J. Seong, S. Sakai, M Hageman, and D. Rothamer. Detailed morphological properties of nanoparticles from gasoline direct injection engine combustion of ethanol blends. *SAE Technical Paper*, 2013-24-0185, 2013.

[69] F. S. Liu, K. A. Thomson, H. S. Guo, and G. J. Smallwood. Numerical and experimental study of an axisymmetric coflow laminar methane-air diffusion flame at pressures between 5 and 40 atmospheres. *Combustion and Flame*, 146(3):456–471.

[70] Paul M. Mandatori and Ömer L. Gülder. Soot formation in laminar ethane diffusion flames at pressures from 0.2 to 3.3 MPa. *Proceedings of the Combustion Institute*, 33: 577–584, 2011.

[71] M. Matti Maricq, Diane H. Podsiadlik, Diana D. Brehob, and Mohammad Haghgooie. Particulate emissions from a direct-injection spark-ignition (DISI) engine.

[72] P. Markatou, H. Wang, and M. Frenklach. A computational study of sooting limits in laminar premixed flames of ethane, ethylene, and acetylene. *Combustion and Flame*, 93(4):467–482, 1993.

[73] Atsushi Matsumoto, yi Zheng, Xingbin Xie, and Ming-Chia Lai. Interactions of multi-hole di sprays with charge motion and their implications to flexible vale-trained engine performance. *SAE Technical Paper*, 2011-01-1883, 2011.

[74] N. Matthias, C. Farron, D. Foster, M. Andrie, and R. Krieger. Particulate matter sampling and volatile organic compound removal for characterization of spark ignited direct injection engine emissions. *SAE Technical Paper*, 2011-01-2100, 2011.

[75] H. Mätzing and H. Gg Wagner. Measurements about the influence of pressure on carbon formation in premixed laminar c2h4-air flames. *Symposium (International) on Combustion*, 21(1):1047–1055, 1988.

[76] F. Mauss and H Bockhorn. Soot formation in premixed hydrocarbon flames: Prediction of temperature and pressure dependence. *Zeitschrift für physikalische Chemie, Bd.*, 188:45–60, 1995.

[77] L. L. McCrain and W. L. Roberts. Measurements of the soot volume field in laminar diffusion flames at elevated pressures. *Combustion and Flame*, 140(1-2):60–69. ISSN 0010-2180.

[78] C. S. McEnally and L. D. Pfefferle. Improved sooting tendency measurements for aromatic hydrocarbons and their implications for naphthalene formation pathways. *Combustion and Flame*, 148(4):210–222.

[79] C. S. McEnally, L. D. Pfefferle, B. Atakan, and K. Kohse–Höinghaus. Studies of aromatic hydrocarbon formation mechanisms in flames: Progress towards closing the fuel gap. *Progress in Energy and Combustion Science*, 32(3):247–294.

[80] Tyler Melton, Fikret Inal, and Selim Senkan. The effects of equivalence ratio on the formation of polycyclic aromatic hydrocarbons and soot in premixed ethane flames. *Combustion and Flame*, 121:671–678, 2000.

[81] R. C. Millikan. Non-equilibrium soot formation in premixed flames. *Journal of Chemical Physics*, 66:794–799, 1961.

[82] N. Morgan, A. Smallbone, A. Bhave, M. Kraft, R. Cracknell, and G. Kalghatgi. Mapping surrogate gasoline compositions into ron/mon space. *Combustion and Flame*, 157(6):1122–1131.

[83] C. L. Myung and S. Park. Exhaust nanoparticle emissions from internal combustion engines: A review. *International Journal of Automotive Technology*, 13(1):9–22, 2012.

[84] André Nel. Air pollution– related illness:effects of particles. *Science*, 308:804–805, 2005.

[85] Thomas S. Norton and Frederick L. Dryer. The flow reactor oxidation of C_1-C_4 alcohols and MTBE. In The Combustion Institute, editor, *Twenty-Third Symposium (International) on Combustion*, pages 179–185, 1990.

[86] Takahiro Noyori. Experimental study of smoke emission on small-displacement spark-ignition direct-injection engine. *SAE Technical Paper*, 2006-32-0105, JSAE20666605, 2006.

[87] State of California Air Resources Board (CARB). Preliminary discussion paper - proposed amendments to california's low-emission vehicle regulations - particulate matter mass, ultrafine solid particle number, and black carbon emissions, 2010.

[88] G. Pilla and L. de Francqueville. Investigation of particle formation processes in a GDI engine in catalyst heating operation, 2011.

[89] G.L. Pilla and L. de Francqueville. Investigation of particle formation mechanisms in GDI engines during transient heating operation, 2013.

[90] W. Piock, G. Hoffmann, A. Berndorfer, P. Salemi, and B. Fusshoeller. Strategies towards meeting future particulate matter emission requirements in homogeneous gasoline direct injection engine. *SAE Technical Paper*, 2011-01-1212.

[91] W. J. Pitz, N. P. Cernansky, F. L. Dryer, F. N. Egolfopoulos, J. T. Farrell, D. G. Friend, and H. Pitsch. Development of an experimental database and chemical kinetic models for surrogate gasoline fuels. *SAE Technical Paper*, 2007-01-0175, 2007.

[92] Philip Price, Richard Stone, Tony Collier, and Marcus Davies. Particulate matter and hydrocarbon emissions measurements: Comparing first and second generation DISI with PFI in single cylinder optical engines. .

[93] Philip Price, Richard Stone, Dave OudeNijeweme, and Xiangdong Chen. Cold start particulate emissions from a second generation DI gasoline engine. .

[94] Philip Price, Ben Twiney, Richard Stone, Kenneth Kar, and Harold Walmsley. Particulate and hydrocarbon emissions from a spray guided direct injection spark ignition engine with oxygenate fuel blends. .

[95] Y. Ra and R. D. Reitz. A combustion model for multi-component fuels using physical surrogate group chemistry representation (psgcr). *In Preparation*, 2014.

[96] Samuel W. Radcliffe and John P. Appleton. Shock-tube measurements of carbon to oxygen atom ratios for incipient soot formation with C_2H_2, C_2H_4, and C_4H_6 fuels. *Combustion Science and Technology*, 3(6):255–262, 1971.

[97] A. Raj, I.D.C Prada, A.A. Amer, and S.H. Chung. A reaction mechanism for gasoline surrogate fuels for large polycyclic aromatic hydrocarbons. *Combustion and Flame*, 159:500–515, 2012.

[98] D. A. Rothamer and J. B. Ghandhi. Determination of flame-front equivalence ratio during stratified combustion. *SAE Transactions Journal of Engines*, 112 (SAE Technical Paper 2003-01-0069)(3):282–292, 2003.

[99] D. A. Rothamer and J. H. Jennings. Study of the knocking propensity of 2,5-dimethylfuran-gasoline and ethanol-gasoline blends. *Fuel*, 2012.

[100] Daniel Sabathil, Achim Koenigstein, Peter Schaffner, Jan Fritzsche, and Arndt Doehler. The influence of DISI engine operating parameters on particle number emissions. *SAE Technical Paper*, 2011-01-0143, 2011.

[101] Steven Sakai, Mitchell Hageman, and David Rothamer. Effect of equivalence ratio on the particulate emissions from a spark-ignited, direct-injected gasoline engine. *SAE Technical Paper*, 2013-01-1560, 2013.

[102] Y. Sakai, A. Miyoshi, M. Koshi, and W. J. Pitz. A kinetic modeling study on the oxidation of primary reference fuel-toluene mixtures including cross reactions between aromatics and aliphatics. *Proceedings of the Combustion Institute*, 32:411–418.

[103] Victor M. Salazar. *Unburned Hydrocarbon Emission Mechanisms in Small Engines*. Thesis, 2008.

[104] V.M. Salazar and J.B. Ghandhi. Ring pack crevice effects on the hydrocarbon emissions from an air-cooled utility engine. *SAE Int. J. Engines*, 1(1):1319–1331, 2008.

[105] R. J. Santoro, T. T. Yeh, J. J. Horvath, and H. G. Semerjian. The transport and growth of soot particles in laminar diffusion flames. *Combustion Science and Technology*, 53 (2-3):89–115.

[106] MD Seaton, Anthony, MD Godden, David, MD MacNee, William, and PhD Donaldson, Kenneth. Particulate air pollution and acute health effects. *The Lancet*, 345(8943): 176–178, 1995.

[107] Masayuki Shimizu, Kazunori Yageta, Yoshinori Matsui, and Takahiro Yoshida. Development of new 1.6 liter four cylinder turbocharged direct injection gasoline engine with intake and exhaust valve timing control system. *SAE Technical Paper*, 2011-01-0419, 2011.

[108] Jasdeep Singh, Michael Balthasar, Markus Kraft, and Wolfgang Wagner. Stochastic modeling of soot particle size and age distributions in laminar premixed flames. *Proceedings of the Combustion Institute*, 30:1457–1465, 2005.

[109] James G. Speight. Lange's handbook of chemistry, 2005.

[110] B. R. Stanmore, J. F. Brilhac, and P. Gilot. The oxidation of soot: a review of experiments, mechanisms and models. *Carbon*, 39(15):2247–2268.

[111] J. C. Street and A. Thomas. Carbon formation in pre-mixed flames. *Fuel*, 34:4–36, 1955.

[112] F. Takahashi and I Glassman. Sooting correlations for premixed flames. *Combustion Science and Technology*, 37:1–18, 1984.

[113] Glenn Thompson and Myriam Torres. Automotive service: Inspection, maintenance, repair, 1977.

[114] K. A. Thomson, O. L. Gulder, E. J. Weckman, R. A. Fraser, G. J. Smallwood, and D. R. Snelling. Soot concentration and temperature measurements in co-annular, nonpremixed ch4/air laminar flames at pressures up to 4 mpa. *Combustion and Flame*, 140(3):222–232.

[115] Stephen R Turns. *An Introduction to Combustion*. Mcgraw-Hill Higher Education, Singapore, second edition, 2000.

[116] A Ulrich, A. Wichser, A. Hess, N. Heeb, L. Emmenegger, J. Czerwinski, M. Kasper, J. Mooney, and A. Mayer. Particle and metal emissions of diesel and gasoline engines - are particle filters appropriate measures?

[117] Stephen B. Vardeman and J. Marcus Jobe. *Basic Engineering Data Collection and Analysis*. Duxbury, Pacific Grove, CA, 2001.

[118] Carl Vuk and Steven J. Vander Griend. Fuel property effects on particulates in spark ignition engines. *SAE paper 2013-01-1124*, 2013.

[119] H. Wang. Formation of nascent soot and other condensed-phase materials in flames. *Proceedings of the Combustion Institute*, 33:41–67. ISSN 1540-7489.

[120] Simon A.G. Watson. *Lubricant-Derived Ash - in-Engine Sources and Opportunities for Reduction*. Phd thesis, 2010.

[121] Phillip R. Westmoreland, Jack B. Howard, and John P. Longwell. Tests of published mechanisms by comparison with measured laminar flame structure in fuel-rich acetylene combustion. *Twenty-first Symposium (International) on Combustion*, 21:773–782, 1986.

[122] Dustin Witkowski, Katsufumi Kondo, Gokul Vishwanathan, and David Rothamer. Evaluation of the sooting properties of real fuels and their commonly used surrogates in a laminar co-flow diffusion flame. *Combustion and Flame*, 160:1129–1141, 2013.

[123] G. Woschni. A universally applicable equation for instantaneous heat transfer coefficient in the internal combustion engine. *SAE Technical Paper*, 670931, 1967.

[124] B Zhao, Z. Yang, Johnston M. Li, Z, and H. Wang. Particle size distribution function of inceipient soot in laminar premixed ethylene flames: effect of flame temperature. *Proceedings of the Combustion Institute*, 30:1441–1448, 2005.

[125] F. Zhao, M.C. Lai, and D.L. Harrington. Automotive spark-ignited direct-injection gasoline engines. *Progress in Energy and Combustion Science*, 25:437–562, 1999.